Mechatronic guidance of rail vehicles through switches and crossings to enable vehicle-based switching

by

Nabilah Farhat

A doctoral thesis submitted in partial fulfillment of the requirements for the award of

Doctor of Philosophy

Loughborough University

February 2019

Acknowledgements

Arguably one of the most difficult bits to write in a thesis, is the ‘acknowledgements’ because so often gratitude is more than can be expressed in words. I couldn’t start in any other way than to firstly thank my principal supervisor, Chris Ward, for offering the opportunity. He has always been very helpful, approachable and honest. I am incredibly lucky to have had his unwavering support and the chance to learn a tremendous amount from him. I am certain that all of my struggles would have been a lot bigger if it weren’t for his generosity with his time and advice. A huge thanks would have to go to Roger Goodall for always making himself available and offering his words of wisdom. It’s been a privilege to work with him. Thanks also to my secondary supervisor, Roger Dixon for his help, especially with the PIP controllers.

On a personal front, a massive thanks goes to my better half, Paul for always encouraging and supporting me. I wouldn’t really be able to finish this PhD without him. A big thanks to this ‘weird and wonderful’ bunch of people I call family - Dina, Anton, Jas, Jackie, Malcolm, Nana, Steve and Rachel. Thanks for doing all the things with me that families do and for giving me a sense of normality through everything.

Lastly, I would like to thank my office colleagues/ friends for always allowing me to pick their brains - George, Emma, Hasma, Tim, Pete, Precious and Sam. Thank you all for our technical chats and for sharing your stories of the PhD life.

Abstract

The research presented in this thesis demonstrates the theory that a mechatronic rail vehicle could be used on conventional switches and crossings (S&Cs) to reduce wear. Railway track switches withstand high vertical and lateral forces leading to wear and damage. This necessitates a disproportionately high level of maintenance of over 10 % of total maintenance costs, despite accounting for less than 0.1 % of the network length.

Mechatronically-guided rail vehicles are of paramount importance in addressing the increasing interest in reducing wheel-rail wear across the network and improving guidance and steering. Conventional passively-guided rail vehicles are limited by the mechanical constraints of the suspension elements. Currently, a typical rail vehicle suspension needs to be sufficiently stiff to stabilize the wheelsets while being complaint enough to negotiate curved track profiles. The suspension is therefore a compromise for the contradictory requirements of curving and stability. In mechatronic vehicles, actuators are used with the conventional suspension components to provide pseudo stiffness or damping forces needed to optimise a vehicle for a wide variety of scenarios, which can be positive or negative. This means that the vehicle is not reliant on a sub-optimal combination of passive components.

Previous research in the area of mechatronic rail vehicles has shown the performance improvement in different straight or curved track profiles compared to a conventional vehicle. In this thesis, three vehicle configurations discussed previously in the literature, are evaluated on several different track profiles. These are the secondary yaw control (SYC), actuated solid-axle wheelset (ASW) and driven independently-rotating wheelsets (DIRW) steering mechanisms. The vehicle models are implemented in a multi-body simulation software Simpack to obtain high fidelity simulations that are comparable to a real rail vehicle. The DIRW vehicle showed the best performance in terms of reduced wear and minimal flange contact and was therefore chosen for studying its performance on a conventional S&C.

The DIRW vehicle was simulated on a C switch which is the most common on the UK mainline and on a high speed H switch. The results show that the DIRW vehicle gives a significant reduction in wear and reduces flange contact on the through and diverging routes of both S&Cs. This proves the theory that active vehicles could be used to reduce impact forces at conventional S&Cs. This could be an intermediate step towards a longer term vision

of having a track switch without any moving parts where the switching is vehicle-based instead of track-based.

Ultimately, if active elements on the vehicle could fully control the route while the track switch was completely passive i.e. had no moving parts, the reliability of the railways as a transport system would increase significantly. The technology could be combined with electronically-coupled vehicles which could form longer trains on busier routes and decouple to serve intermediary routes.

Table of contents

List of figures

List of tables

Chapter 1

Introduction

1.1 Introduction

Railways as a means of transportation rely on a well-connected rail network. The development of a rail network with multiple routes is enabled by track switches. A conventional track switch, illustrated in Figure 1.1 consists of two stock rails that are securely fixed and two switch rails that displace laterally to form the selected route for the rail vehicle. The arrangement is called a switch and crossing (S&C), also known as a point or a turnout and consists of a through route and a diverging route as shown. The guidance of a vehicle through a track switch is a purely passive mechanical concept where the track forms a fixed configuration depending on the intended route. In other words, the switching is purely track-based.

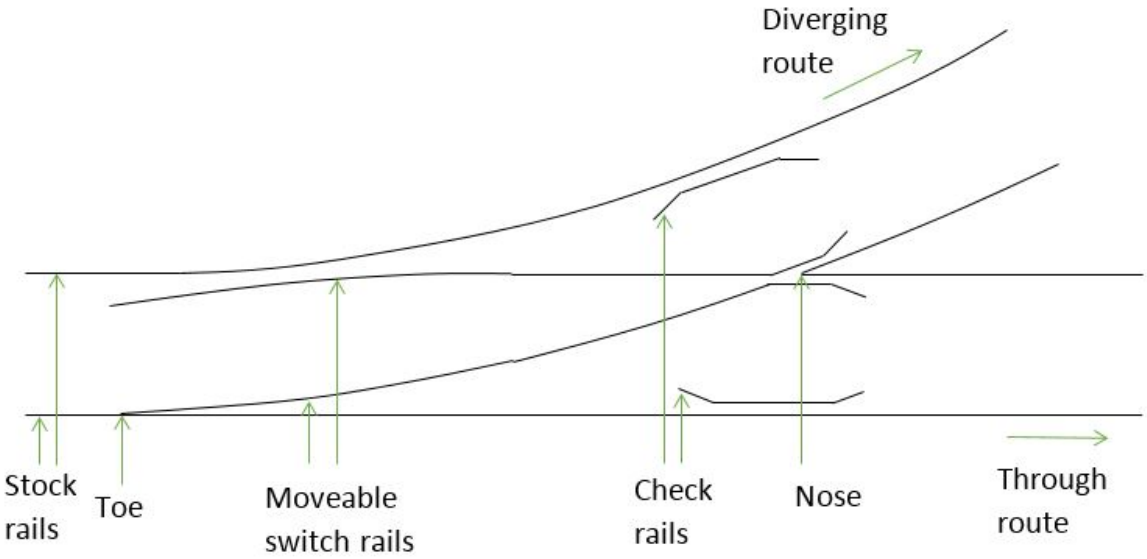

Figure 1.1: Conventional track switch configuration (set to diverging route)

Although track switches make up less than 0.1% of the route length on the UK rail network, more than 10% of total maintenance costs is spent towards replacing or re-profiling worn switches [2]. This is due to high impact forces from the wheel onto the switch rails. Vehicle-based switching (VBS) is a concept that considers the possibility of performing the switching function from on-board the vehicle. The possible outcomes of VBS range from relatively modest changes in keeping with industrial reality through to a complete redesign which harnesses the theoretical benefits of VBS. The aim of this PhD work is to show that an actively-controlled vehicle can reduce impact forces on a conventional track switch to increase its lifetime. The intention is to motivate a radical change of both the vehicle and track architecture which facilitates a continuous rail network without any moving parts on all diversionary routes. This could be combined with electronically-coupled trains to facilitate an operational change in railways where individual vehicles could be combined on busy routes or detached when required to optimise the throughput of the rail network.

Figure 1.2 shows the broad technology route-map. The top left corner represents the current technology where a conventional track switch is designed for a conventional vehicle. The ultimate long term goal is to reach the bottom right corner where a completely redesigned vehicle performs the switching function on a new track switch infrastructure without any moving components. This PhD study shows that a part VBS vehicle could be used on a conventional track switch to reduce impact and resulting wear. This research is of great topical interest due to the development of high speed lines HS1 and HS2 [3] in the UK where track switch wear is accelerated at higher speeds. Several ongoing European projects under the Shift2rail [4] initiative are investigating novel switch designs for conventional vehicles. New materials capable of self-healing and lubricating rail steel and different manufacturing techniques are being investigated with a view to reducing failures and maintenance costs [5]. Previous studies into optimal track geometry [6], rail profile [7] and track support stiffness [8] at S%Cs have been undertaken to improve vehicle stability and reduce material degradation. The work in this thesis addresses at the switch wear problem from the vehicle suspension level instead of the track level.

The next phase would be to redesign track switches using the existing research on track geometry optimisation to support a VBS vehicle. Conventional track switches have been developed for many years to work optimally with a passive vehicle. A redesign would be necessary to achieve the maximum potential benefits of active vehicles. The results from this study support the theory that a purely mechanical track switching approach which is several hundred years old could be seen in a new light where the switching is from on-board the vehicle, in other words vehicle-based instead of track-based.

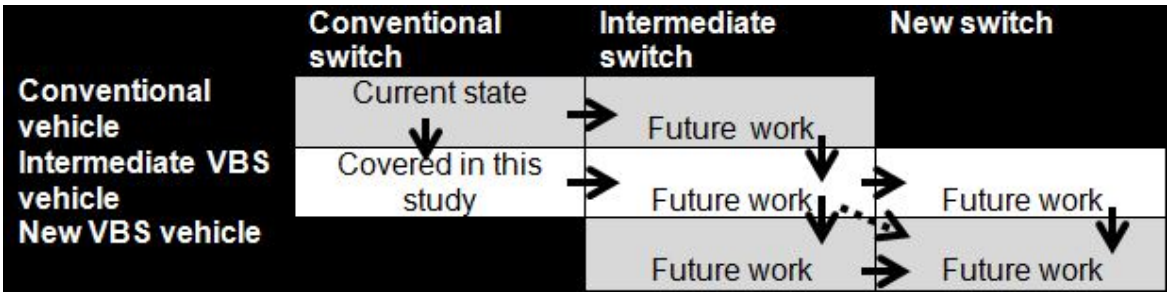

Figure 1.2: VBS technology route map

1.2 Background and research question

Data published from the Office of Road and Rail (ORR) [9] show that track switches are the second biggest contributor of delay minutes and consequent compensation after track faults, costing ≈£26m per financial year. The delay minutes represent the total delay to all services as a direct result of a track switch failure. The cost accounts for the compensation paid to the train operators for unscheduled down-time but does not include any subsequent effect on the economy as a result of the failure [10].

There are several reasons why track switches account for a disproportionately high cost of maintenance and renewals. The switching mechanism requires the switch rails to mate with the stock rails at the toe resulting in a rapid change in wheel-rail contact conditions when the rails are changing shape. The switch rail width is also very small at the toe which means that high impact forces are imposed on the thin switch blades. This leads to rapid wear and degradation of support structures under the rail. High wear is also seen at crossings where there is a discontinuity or gap in the running rail to allow the flange to pass through.

Statistical analysis of switch failure data has shown that the 75 - 80% of switch failures are due to electrical faults in the Points Operating Equipment (POE) incurred from high frequency excitations when a vehicle traverses a switch [11]. This failure mode will likely not be eliminated as long as the use of POEs is continued. The development of a passive track switch without moving parts, which is the ultimate vision for VBS, would remove the need for POE. Amongst permanent way assets i.e. rails, sleepers, ballast and adjoining assets, switch blades are the highest failed component accounting for over half the failures. The two main modes of switch blade failure are plastic deformation (where the rail profile gets deformed due to high contact stress) and wear of the rails. The results presented in this thesis show a significant reduction in wear of the rails using active vehicles on moderate and high speed switches.

There have been several efforts in industry and academia to reduce the impact forces at points to increase their lifetime such as a movable crossing nose to remove the gap at the

crossing for high speed turnouts which have a shallow divergence angle [12], which is the angle of the diverging route. Flange bearing crossings allow wheels to ride on their flange which are supported from underneath [13]. Optimisation of wheel transfer at high speed crossings through changes in the check rail geometry and proper machining of the nose has been shown to significantly reduce wear [14]. The Run2Rail project [15] is investigating the use of unconventional materials and manufacturing methods such as 3D printing for active rail vehicles and track switch components to increase the lifetime of running gear and infrastructure. However the fundamental problem of a rapid change in contact points from the stock to the switch rails still exists because the basic mechanism of track switches has not changed.

VBS proposes a fundamental shift of the switching mechanism from track-based to vehicle-based. This thesis shows that active vehicle could be used to reduce the wear on current switching technology. In the future active vehicles can be used to allow for a completely different track switch that has no moving components. As a consequence, switch reliability would be improved as the turnout has a permanent position and does not require locking or detection mechanisms. They would also not need to be controlled from an external operations centre, reducing the human factor elements of track switch operation.

1.3 Scope of thesis

A conventional rail vehicle usually has a purely mechanical suspension consisting of springs and dampers. Their performance is determined principally by the spring stiffnesses, damper coefficients and their masses. With the introduction of active components in the suspension, the performance depends on sensors, actuators and the controller design. VBS is heavily reliant on active elements providing the required guidance forces to negotiate a track switch. This means that sensing the feedback signals and providing the required actuator forces are crucial. Another challenge is to detect and isolate faults to improve safety against failure.

From the technology route map of VBS in Figure 1.1 it can be seen that there are several possible paths to the ultimate vision. Each stage has many research challenges that need to be studied in order to make VBS a safe and reliable technology. The research presented in this thesis is intended to provide an incremental solution in keeping with the challenges of industrial reality. Active strategies, such as the Secondary Yaw Control (SYC) and the Actuated Solid-axle Wheelset (ASW), where the actuators can be retrofitted onto conventional vehicles are compared against a conventional vehicle as the first step. They are tested on several different track profiles with stochastic disturbances and curves of different radii. This is followed by studying an active steering concept involving Driven Independently-

Rotating Wheelsets (DIRW) which requires a complete redesign of a rail vehicle. Finally, the performance of the DIRW mechanism is compared to that of a passive vehicle on a moderate speed switch and a high speed switch. This provides proof to the theory that active vehicles could reduce impact forces at conventional switches, which is an intermediary solution to the ultimate goal of having purely passive turnout.

Ideal sensing is assumed with a view that the performance benefits need to be established before the practicalities of sensing can be considered at a later stage. In practice, the feedback signals could be measured from non-contacting sensors or estimated from inertial sensors mounted on the bogie. At present, New Measurement Trains used by Network Rail have laser-based systems to record measurements of track geometry for the purpose of rail maintenance [16]. In this study, a brief look is taken into the power consumption of the actuation mechanism to show that the required control is achievable using readily available actuators of reasonable power consumption. Actuator dynamics are not taken into consideration as the aim is to quantify the benefits for an ideal scenario. A further extension of this work could be to assess the sensing and actuation requirements of each of the schemes in more detail, taking into account actuator dynamics. In reality, the actuator dynamics are not likely to be a major problem because of the availability of high bandwidth actuators as is used in test rigs for commercial vehicles to simulate road conditions. Sensing is more likely to be a problem due to the difficulty of measuring at the wheel-rail interface which is a high vibration environment.

1.4 Thesis outline

This thesis consists of seven chapters and can be broadly considered in two parts. The first part describes the vehicle and controller modelling of the passive vehicle and the three active vehicles. The active schemes are compared against the passive vehicle and relative to each other on a variety of track profiles. The second part applies the active vehicle with the best performance on track switches with different maximum speed restrictions to analyse its performance against that of a conventional passive vehicle.

Chapter 2 provides detailed background on current rail vehicle topology, track switch architecture and the conventional guidance mechanism. It explains the use of active guidance to achieve VBS and provides a review of relevant literature on different active guidance mechanisms and radical track switching innovations.

Chapter 3 explains the modelling of the passive vehicle and each of the active vehicles in detail. Two sets of models are produced for each vehicle where non-linear ‘simulation’

models are developed in Simpack and a linear 'design' model is developed using system identification methods.

The linear models allow the use of frequency-based methods for designing controllers which is discussed in chapter 4. A classical controller and a more advanced controller is designed for each active vehicle. The controller mathematical forms and design process is discussed in detail with a frequency domain evaluation using Nichols plots, gain and phase margins.

Chapter 5 is concerned with the evaluation of the different active vehicles and the two sets of controllers. It presents the results of comparing the active vehicles with a passive vehicle and against each other on different track profiles. The track profiles contain a variety of low and high frequency disturbances which are explained in detail.

This comparison is used to present a logical case for the choice of active vehicle and controller used for the track switch simulations in chapter 6. The track switch simulations include two switches with different speed curvature radii and consequently different speed restrictions.

Chapter 7 draws conclusions on the main findings of the thesis with some suggestions for further work.

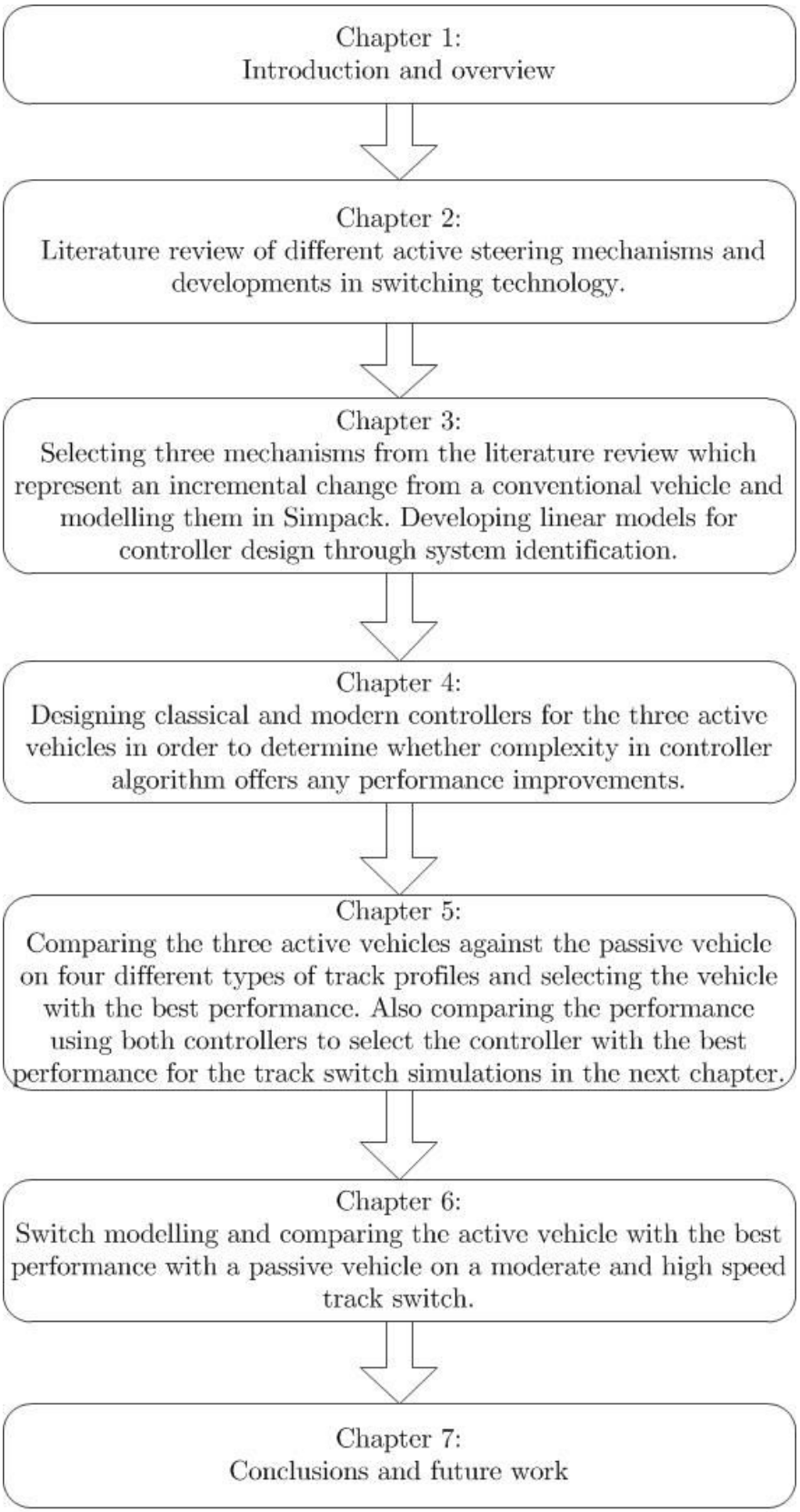

Figure 1.3: Thesis outline

1.5 Thesis contributions

This thesis analyses the performance of a vehicle with an active suspension on a conventional railway track switch. The approach here is to first establish the ideal performance benefits rather than focusing on the practicalities of sensing and actuation.

- The initial contribution is to analyse the performance of high-fidelity models of actively-controlled vehicles against that of a conventional vehicle on different track profiles. Previous studies on such comparisons used simplified models whereas the models used in this work are a better representation of a 'real' rail vehicle. Simpack is used to develop models of conventional and actively-controlled vehicles, which takes into account the non-linearities in the wheel-rail profile, contact forces and suspension components. The performance of the active vehicles is compared to that of the conventional vehicle and against each other to establish the vehicle that showed the best performance.

- This vehicle is then simulated on the through and diverging routes of two track switches with different speed restrictions to demonstrate the performance of active steering on conventional track switches. The main contribution of this thesis is to show the performance improvements of an actively controlled vehicle compared to a conventional vehicle on moderate and high speed track switches.

The work presented in this thesis has been published in the following journal papers:

- N. Farhat, C.P. Ward, R.M. Goodall, R. Dixon, "The benefits of mechatronically-guided railway vehicles: A multi-body physics simulation study", IFAC Journal of Mechatronics, Vol. 51, May 2018, pg 115-126.

- N. Farhat, C.P. Ward, R. Dixon, R.M. Goodall, "Benefits of mechatronically-guided vehicles on railway track switches", IMechE Part F Journal of Rail and Rapid Transit, Accepted Aug 2018.

- P.D. Hubbard, N. Farhat, C.P. Ward, G.A. Amarantidis, "Contact force estimation in the wheel/ rail interface for curving scenarios through regions of reduced adhesion", IFAC Journal of Mechatronics, Aug 2017.

Chapter 2

Developments in railway vehicle and track switch technology

2.1 A typical rail vehicle

A conventional rail vehicle illustrated in Figure 2.1, consists of a car body, two bogies and four wheelsets (two per bogie). The wheelsets, as shown in Figure 2.2 have a solid axle between the wheels which have a conical tread. Each body has six degrees of freedom in the longitudinal, lateral, vertical, roll, yaw and pitch directions. There are a two stages of suspension in a typical passenger rail vehicle. The primary suspension consists of springs and dampers connecting the wheelsets to the bogie. The primary suspension is usually very stiff and deals with the guidance and stability of the vehicle along the track. The secondary suspension connects the bogie to the vehicle body and consists of a softer set of airsprings and dampers to isolate the high frequency track disturbances whilst following the track. This two stage suspension therefore allows a good ride quality where the passengers don't experience vibrations from the track irregularities. Improving ride comfort by having a two stage suspension is one of the main reasons for using bogies.

Bogies also reduce wheel-rail wear by reducing the yaw angle of the wheels with respect to the track, which is also known as the angle of attack. Wheel-rail wear depends on the angle of attack of the wheels which in turn depends on the angle between two wheelsets that are constrained in yaw. Without bogies, this angle would be governed by the length of the vehicle body, whereas with bogies, the angle can be reduced to get acceptable wear due to the shorter length.

A typical rail wheel, illustrated in Figure 2.2, has a flange and a conical tread. The conicity is a non-linear function of the lateral displacement of the wheelset, where conicity

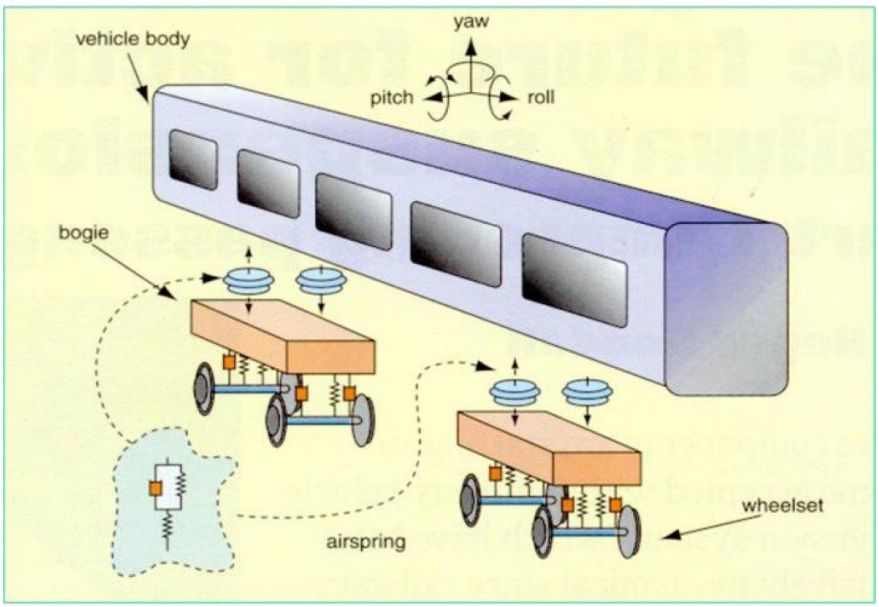

Figure 2.1: Components of a railway vehicle [17]

increases as the wheel-rail contact region approaches the flange. Figure 2.3 shows the conicity changes with the wheelset lateral displacement. The conical tread of a conventional railway wheelset provides the vehicle guidance mechanism that has been accepted best practice for nearly two centuries. Contrary to popular belief, the flange does not provide the majority of the guidance but is there as a safety measure to prevent derailment. Normally the wheel-rail contact region would not approach the flanges, however it is possible in tight curves, especially during transitions from straight to curved tracks and vice versa or due to large lateral track irregularities.

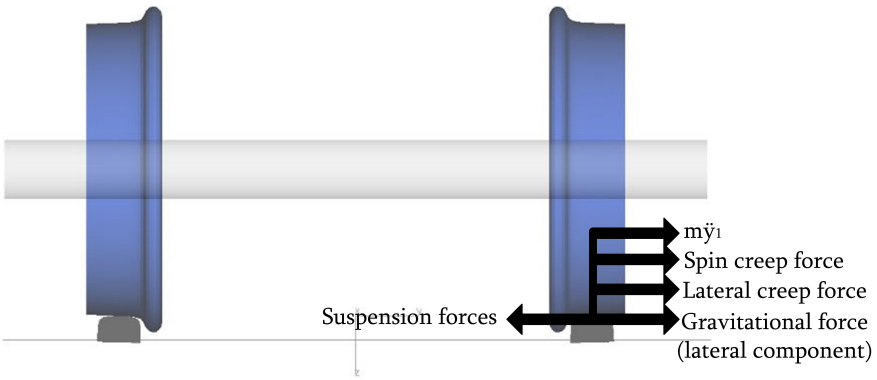

Figure 2.2: A conventional solid-axle wheelset

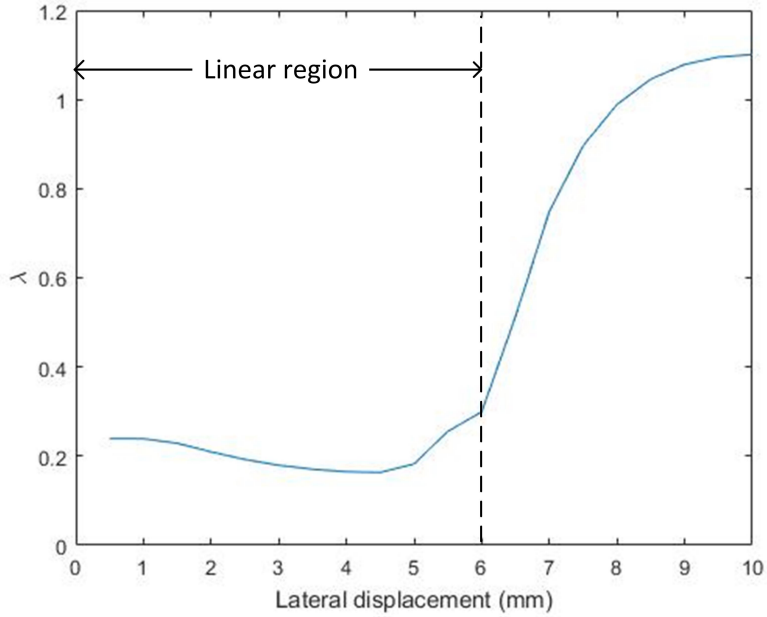

Figure 2.3: Conicity as a function of wheelset lateral displacement

2.2 Conventional guidance mechanism

Although each body has six degrees of freedom, they can be separated into two sets which can be considered independently. The plan view mode consists of the lateral, yaw and roll modes while the side view mode considers the vertical, longitudinal and pitch modes. These two modes are only very weakly coupled and are often viewed separately to reduce the complexity of the vehicle dynamics. To understand the main forces involved in wheelset guidance, it is essential to discuss the lateral dynamics of a wheelset. The lateral acceleration $\ddot{y}_1$ of the front wheelset of the front bogie of a rail vehicle can be described by the following simplified linearised equation [18],

$$\ddot{y}_1 = \frac{1}{m}\left\{-\frac{2f_{22}}{v}(\dot{y}_1 + \frac{r_0\lambda}{l}\dot{y}_1 - v\psi_1) - \frac{2f_{23}}{v}\dot{\psi}_1 - \frac{W\lambda}{l}(y_1 - d) + k_y(y_{bf} - y_1) + f_y(\dot{y}_{bf} - \dot{y}_1)\right\} \tag{2.1}$$

where, m is the mass of the wheelset in kg, f_{22} is the lateral creep coefficient in N, f_{23} is the spin creep coefficient in N, v is the vehicle velocity in m/s, r_0 is the nominal wheel radius in m, λ is the equivalent wheel conicity, l is half of the gauge width in m, ψ_1 is the wheelset yaw angle in radians, W is the weight on each wheelset in N, d is the lateral track irregularities in m, y_{bf} is the lateral displacement of the front bogie in m, k_y is the primary lateral spring stiffness in N/m and f_y is the primary lateral damping coefficient in Ns/m. In this equation,

the conicity is assumed to be linear, although in practice significant non-linearities exist as the wheel-rail contact moves towards the flange. This simplification is justified because the active guidance helps to maintain minimal flange contact.

It can be deduced from the equation that the main forces contributing to the lateral acceleration are the lateral creep force, spin creep force, gravitational stiffness and the suspension forces. Likewise, the yaw dynamics are concerned with the longitudinal creep force, spin creep force, inertia force due to the roll motion, yaw gravitational stiffness and suspension forces. The wheelset yaw acceleration $\ddot{\psi}_1$ can be described using the equation,

$$\ddot{\psi}_1 = \frac{1}{I}\Big\{-2f_{11}(\frac{l\lambda}{r_0}(y_1-d)+\frac{l^2}{v}\dot{\psi}_1)-\frac{2f_{33}}{v}\dot{\psi}_1-\frac{I_{wy}v\lambda}{lr_0}\dot{y}_1+\frac{f_{23}}{v}(\dot{y}_1+\frac{r_0\lambda}{l}\dot{y}_1-v\psi_1) \\ +W\lambda l\psi_1-k_\psi\psi_1-f_\psi\dot{\psi}_1\Big\} \tag{2.2}$$

where, I is the wheelset yaw inertia in kgm^2, I_{wy} is the wheelset lateral inertia in kgm^2, f_{11} is the longitudinal creep coefficient in N, f_{33} is the spin creep coefficient in N, k_ψ is the primary yaw spring stiffness in N/rad and f_ψ is the primary yaw damping coefficient in Ns/rad. Each wheel experiences longitudinal, lateral and spin creepages. Creepage or creep forces are generated when the wheel does not have a purely rolling motion and instead slides against the rail. The longitudinal (ε_x), lateral (ε_y) and spin (ε_{sp}) creepages are defined by Carter [19] as

$$\varepsilon_x = \frac{v_{wx}-v_{rx}}{v_{rx}} \tag{2.3}$$

$$\varepsilon_y = \frac{v_{wy}-v_{ry}}{v_{ry}} \tag{2.4}$$

$$\varepsilon_{sp} = \frac{v_{wsp}-v_{rsp}}{v_{rsp}} \tag{2.5}$$

where v_{wx} is longitudinal velocity of the wheel in m/s, v_{rx} is longitudinal velocity of rail at contact point in m/s, v_{wy} is lateral velocity of wheel in m/s, v_{ry} is lateral velocity of rail at contact point in m/s, v_{wsp} is angular velocity of wheel in rad/s and v_{rsp} is angular velocity of rail at contact point in rad/s.

Gravitational stiffness is the component of the normal force in the lateral or yaw directions and depends on the conicity of the wheels. It provides a small self-centering force in a conventional solid-axle wheelset. The majority of the self-centering force comes from the creep forces.

If a wheelset is unconstrained, the conical tread of the wheels make it marginally stable and oscillate along the track in a sinusoidal motion known as 'hunting' [20], [21]. To avoid this problem, the yaw motion of the wheelsets is constrained by a stiff suspension, stabilizing the wheelsets but interfering with the natural curving action of the wheelset which enables them to negotiate curved track profiles. This is a well-known problem and suspensions have to be designed to meet the contradictory requirements of curving and stability at high speeds, with vehicles optimised for a particular operating regime.

Although there have been a number of innovations in bogie design, many authors suggest that passive suspensions have reached a performance limit which is determined principally by the spring stiffnesses, damper coefficients and their masses [22]. Active control has been suggested for some time now as an alternative way forward. The performance of an active suspension depends on sensors, actuators and the controller design in addition to the mechanical components.

2.3 Ideal guidance and curving

Conventional vehicles produce large unnecessary creep forces which are generated due to the relative velocity of the wheel and the rail when the wheels 'slip' on the rails [23]. A certain level of creep forces is necessary to balance the centripetal forces. However, conventional vehicles generate large unnecessary creep forces, particularly in the longitudinal direction due to the stiffness of the yaw suspension. These large creep forces lead to excessive wear, of both the wheel tread and the rail head, and unwanted noise.

Mechatronically-guided vehicles consist of actuators that are used in conjunction with the passive suspension components to provide the additional stiffness or damping forces that are required to optimise the vehicle for a variety of track disturbances. The expectation is that active suspensions can provide the optimal suspension forces to reduce wheel-rail wear. The wear due to traction, braking and balancing the centripetal forces is unavoidable, however the wear that is caused by the sub-optimal steering performance of the suspensions can be reduced dramatically by using active suspension concepts.

Active steering could also be used to control the angle of attack to reduce the level of creep forces produced. Currently, the angle of attack of the wheels is maintained at acceptable values by bogies which shorten the distance between two wheelsets constrained in yaw. Active steering would make this functionality of bogies redundant, leading to the possibility of bogie-less vehicles which would be mechanically simpler [24]. Although this is beyond the scope of this thesis, in the longer term active steering presents a range of possibilities from simply retrofitting actuators to current bogies through to completely

redesigning vehicles to remove bogies. Without a bogie, train floors could be lowered to create more internal space in the same loading gauge to accommodate double-deck trains in the UK.

In order to understand the different steering strategies discussed in literature, it is necessary to first establish the 'ideal' curving scenario for a wheelset. Curved tracks are raised at an angle from the horizontal plane which is known as cant (θ_c in Figure 2.4). During curving, centripetal force cancels the component of gravitational force along the track at balancing speed. At speeds greater than the balancing speed, the centripetal force will be larger which means that there will be a net lateral acceleration to the outside of the curve. This creates a cant deficiency, that is, the amount of superelevation or banking is lesser than that required to balance the centripetal forces. There are several benefits of operating at cant deficiency. It permits higher speed on curves as the lateral acceleration felt by passengers is reduced by the acceleration due to gravity in the plane of the track. This reduces the need to decelerate when entering a curve or accelerate when exiting a curve. However, at cant deficiency, the unbalanced centripetal forces need to be balanced by lateral creep forces.

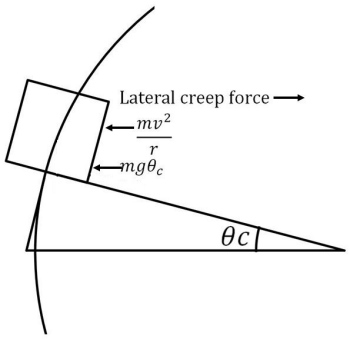

Figure 2.4: Contact forces on a curve

In the absence of cant deficiency, an unrestrained wheelset will adopt a radial position [25]. However, high yaw stiffnesses are needed to overcome the kinematic instability of the solid-axle wheelset. This causes wheels to lose their natural guidance, produce large unnecessary creep forces and generate wear on wheels and rails. It follows from this that for ideal curving, the wheelsets must be radially aligned with the curve, provided of-course that there is no cant deficiency. In the presence of cant deficiency, which is the normal operating condition, the angle of attack has to be sufficient to generate lateral creep forces to balance the centripetal forces. This means that ideally, all the wheelsets should have equal lateral creep forces or equal angles of attack. This has an important implication in terms of safety where large lateral forces on the rail could pose a risk of derailment. If the front wheelset of a bogie has large lateral creep force, which is the case for passive vehicles, it sets the limiting

speed for the safe running of the vehicle. The second condition is that the longitudinal creep forces produced by the wheelsets should ideally be zero, which is indicative of minimal wheel slip. This means that the wheelset lateral displacement should be sufficient to give the required difference in the rolling radii of the two wheels such that the yaw torque from the creep forces is zero. This is usually not possible and large creep forces are generated.

2.4 Active steering strategies

The active steering strategies discussed in this section involve both solid-axle and independently-rotating wheelsets (IRWs). IRWs produce negligible longitudinal creep forces as the wheels are able to roll at different speeds on the same axle to reduce slip [26]. This is the reason why the actuation requirement of an IRW mechanism is lower than that of a solid-axle wheelset. The disadvantage is that IRWs require a guidance mechanism which needs to be provided through a differential wheel torque [27]. This is conflicting to traction and braking control which require that the left and right wheel longitudinal forces are balanced. For this reason, guidance and traction are often combined for IRWs.

Active steering can be applied either directly through the primary suspension or indirectly through the secondary suspension. The direct approach involves providing the steering torque to a wheelset with a solid axle or independently-rotating wheels to influence the plan view modes, mainly lateral and yaw dynamics. Some examples of this are the Actuated Solid-axle Wheelset (ASW), Actuated Independently-Rotating Wheelset (AIRW), Driven Independently-Rotating Wheelset (DIRW), Directly Steered Wheelset (DSW) strategies. The ASW configuration involves applying a yaw torque directly to the wheelset, usually using longitudinal actuators on either side of the wheelset centre, which act in opposition. The AIRW configuration also uses the same mechanism, but with IRWs. In the DIRW configuration, each wheel on the IRWs has its own drive-train so that they can be individually controlled. The DSW concept, inspired by motor vehicles, involves actively steering the independent wheels which are mounted on a carrying frame using stub-axles. Indirect control involves applying the steering from the secondary suspension level to affect the running dynamics of the vehicle as in the Secondary Yaw Control (SYC) configuration. The additional moment cannot affect wheelsets individually but can compensate for the unequal lateral forces on the front and rear wheelsets of a bogie. The indirect approach means that it has lesser implications to the safety of the vehicle but will have relatively less impact than the direct mechanisms on the running dynamics.

The exact mechanical configuration and a literature survey of these five different active steering configurations is given in this section.

2.4.1 Secondary yaw control

In the secondary yaw control (SYC) scheme an actuator is placed between the bogie and the vehicle body as shown in Figure 2.5. The actuator is placed in the same position as a traditional yaw damper. The control is at the secondary suspension level instead of primary because the basic idea is to balance the lateral creep forces on the two axles of the same bogie by applying a steering action.

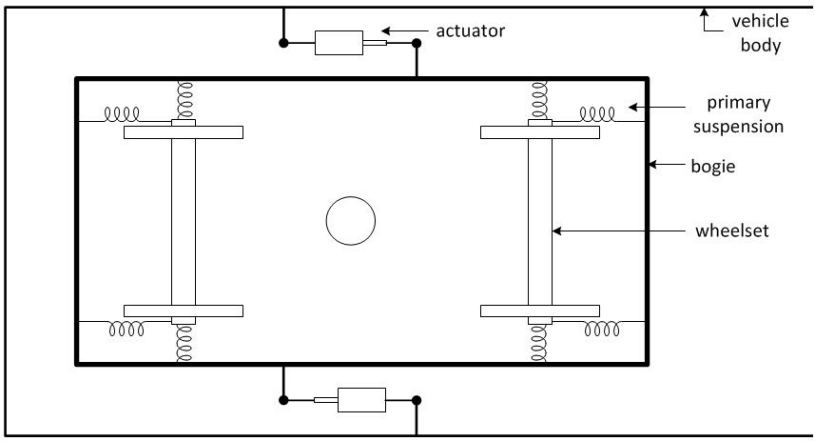

Figure 2.5: Configuration for secondary yaw control

This configuration was studied by Diana et al. [28] where on a straight track, the actuator force is proportional to the bogie/vehicle-body relative speed and opposite to it, much like a passive yaw damper to control the problem of 'hunting'. During curve negotiation, an additional force has to be provided which is obtained from a look-up table based on the curve radius, bogie yaw speed and vehicle speed. The control aims to reduce the lateral force on the front and rear axles of the same bogie. A limitation of this approach is that there are several look-up tables for different bogies, different friction coefficient values and wear levels, all of which are not easily accessible parameters in practice.

The same mechanical concept was also studied by Braghin et al. [29] where the active yaw damper was implemented in two different configurations, longitudinally and transversely. The latter configuration gave better improvements in performance, at the cost of deteriorating ride quality and a more radical change in the conventional bogie configuration. This configuration could perhaps be integrated with active control of vertical modes of the vehicle to improve ride comfort.

In a passive vehicle, if the primary yaw stiffness (PYS) is reduced, the curving performance improves but stability is compromised. SYC can also be used [30] to overcome the instability. The active control therefore does not improve curving, but allows the use of a soft

PYS improving guidance whilst maintaining stability. A soft PYS has shown very significant decrease in wear and derailment coefficient, for the track conditions studied.

2.4.2 Actuated solid-axle wheelset

An obvious strategy of implementing active steering is to apply a yaw torque directly to the wheelset. This can be done by either using a yaw actuator on each wheelset or a pair of longitudinal actuators working in opposition from the bogie to each axlebox to generate a yaw torque. This configuration is illustrated in Figure 2.6.

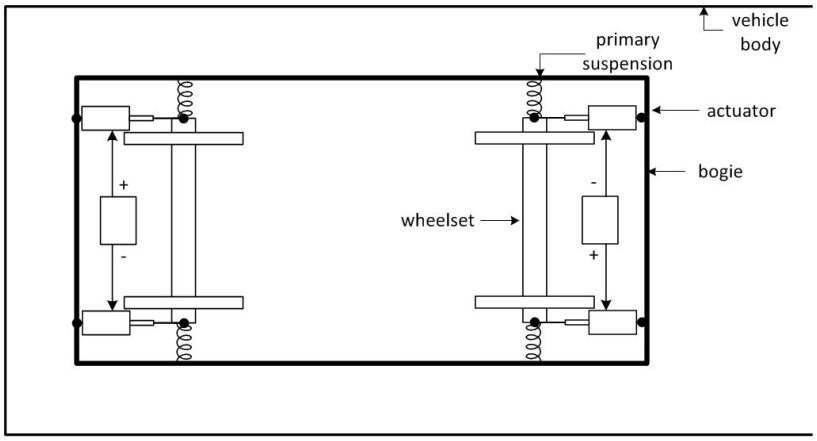

Figure 2.6: Configuration for an actuated solid-axle wheelset

This configuration was introduced by Shen and Goodall [31] who proposed using active traction rods incorporating actuators so that their length can be varied on curves. The actuators are placed in series with longitudinal springs so that higher frequency oscillations of the wheelset are stabilised by the springs and low bandwidth active control is provided by the actuators. This is called active yaw relaxation and it allows the wheelsets to take up their natural curving position. Simulation studies show an improved curving performance using a very simple control strategy where the steady-state wheelset yaw moment is controlled to zero. This minimises the longitudinal creep forces which is a condition for ideal curving. Mei et al. [27] implemented the ASW configuration by controlling the wheelset yaw angles directly using measurements of suspension deflections. Simulation studies have shown that the conditions for ideal curving are achieved by applying a wheelset torque to control the suspension forces. This has the disadvantage of requiring very accurate measurements as the deflections are typically less than 10 mm. Three different control strategies have been studied by Perez et al. [32] - control of the wheelset lateral position for pure rolling, control of wheelset yaw moment for pure rolling (pure rolling implies that no yaw moments are

transmitted from the bogie to the wheelset), control of the relative angle between wheelsets. All three strategies are shown to give significantly better performance than the passive vehicle.

The ASW configuration has also been studied on two-axled bogie-less vehicles [33]. Lateral and yaw actuation schemes have been proposed which involve applying the control either using a lateral force or a yaw couple produced by two longitudinal actuators. Both schemes have similar performances, however the yaw actuation requires a lower control force and provides better ride quality.

A physical implementation of the ASW configuration was undertaken by a Bombardier project [34] where an integrated active control approach was used to apply a torque for both stability and steering. Stability and steering control have different needs because wheelset kinematic modes occur at high frequencies (2 Hz and higher), whereas steering control torques typically have low frequencies (less than 1 Hz). A soft secondary yaw suspension improves curving but degrades stability which is achieved using stability controllers. The vehicle was successfully stabilised at high speeds but controller robustness degrades.

The Bombardier FLEXX Tronic WAKO technology is a practical implementation of the ASW control strategy on a full-scale bogie [35]. It has been tested on a roller rig at speeds up to 400 km/h and on real tracks up to 282 km/h and shown a significant reduction in wheel and rail wear [36].

2.4.3 Actuated independently-rotating wheelset

A logical progression from the ASW configuration is to apply the same concept to independently rotating wheels, as shown in Figure 2.7. IRWs have no solid connection between the wheels and therefore have significantly less longitudinal creep forces than solid-axle wheelsets. The actuation effort required for steering is consequently less [33]. However, IRWs suffer from kinematic instability similar to a conventional wheelset, but the stability can be provided by damper rather than a stiffness, which does not affect curving [37].

Unlike solid-axle wheelsets, IRWs need a guidance mechanism that enables the wheelset to follow the track. In the design of active guidance strategies for independently rotating wheelsets, a key issue is that of feedback signals. Angle of attack of the wheelsets and lateral wheel-rail displacement seem logical choices for feedback signals. However, in practice, they are difficult to measure as inertial sensors mounted on wheelsets are extremely undesirable due to the severe vibration environment and consequent expense required to provide accurate sensors in this environment. Observers have been used to estimate the signals from bogie-based or vehicle-based sensors but their robustness drops in the presence of large parameter variations at high speeds [34]. Two guidance strategies have been studied by Perez et al. [38]. These involve control of the lateral position of the wheelset or control of the differential

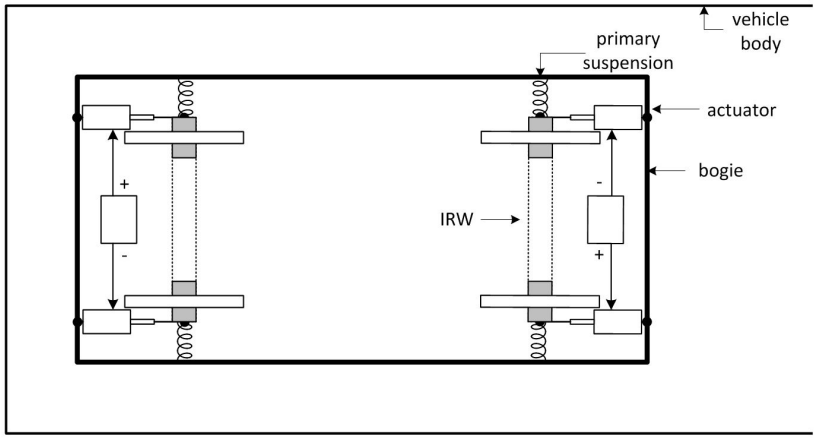

Figure 2.7: Configuration for an actuated independently rotating wheelset

rotational speed of the wheels. In the first control strategy an observer estimates the values of the lateral displacements of the wheelsets from speed-sensors, accelerometers and gyros. This method uses a lot of sensors, and is hence not the preferred method. The second strategy uses four differential rotational speed sensors. The simulation results show that the active vehicle is able to avoid flange contact during curve negotiation. Lateral contact forces are moderately reduced, but still higher than that required to compensate the cant deficiency.

Practical strategies for implementing guidance and steering control on IRWs have been proposed by Mei and Goodall [27, 39]. To reduce the order of the system and model complexity a modal approach is used to de-couple the model into independent sub-systems. Yaw velocity of the wheelset is used as feedback for the wheelset stabilization as it offers flexibility for active or passive implementation. The active implementation allows adequate damping at different vehicle speeds and the passive damper gives extra safety in case of actuator failure. For guidance control, the relative wheel speeds are used as feedback which is readily available because they are measured for controlling wheel-slide during braking. This is done by using an actuator to achieve zero relative speed between the two wheels, which does not cause them to have the same angular position as in solid-axle wheelsets.

2.4.4 Driven independently-rotating wheelset

Each wheel in the bogie is independently driven by its own drive-train as illustrated in Figure 2.8. The basic concept is to maintain a difference in rotational speed of the wheels on curves and to drive the wheels on a straight track at the same speed (assuming there are no stochastic irregularities).

The DIRW configuration was investigated by Gretzschel et al. [40, 41] on a 1:5 scaled two-axled bogie on a roller rig. Controlling the speed of the motors creates an electronic

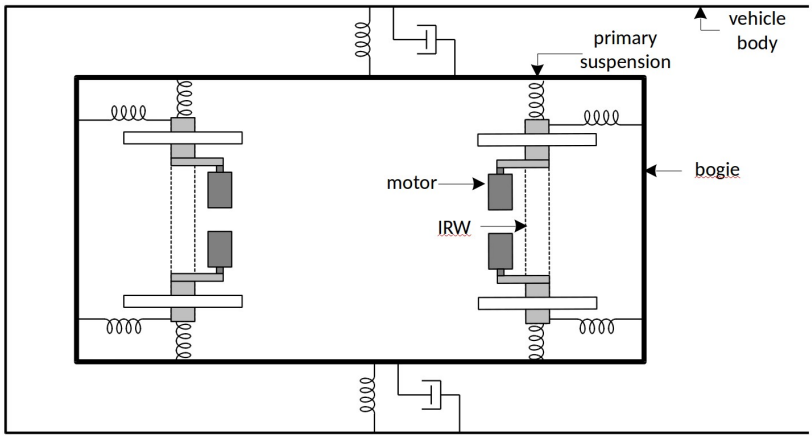

Figure 2.8: Configuration for a driven independently rotating wheelset

axle and makes the wheelsets suffer from all the problems of a solid-axle wheelset including kinematic instability. Torque controlled motors however affect the rotational acceleration of the wheels, which causes them to have different angular positions and therefore not behave like solid-axle wheelsets. The motor torques are calculated using a Proportional Integral plus Derivative (PID) controller which uses wheelset lateral displacement and yaw velocity as feedback signals. Tests conducted on the scaled roller rig show improved curving and stability even at speeds greater than the critical speed where hunting would be observed on a conventional vehicle [42].

The DIRW configuration was studied on a conventional vehicle architecture with bogies by Perez et al. [43]. The feedback for guidance/ steering is the relative speed of the wheels, which is easily available and can be used to implement a combined strategy for traction and steering. Supplying traction separately to each wheel of a wheelset can produce a yaw torque which can be exploited to provide steering/ guidance control. The feedback for the traction control is the sum of the left and right wheel motor torques. This combined control can be used for enhancing fault tolerance which is a critical issue for actively steered vehicles. The mechanical integration of the wheel and the traction motor has been developed by SET Ltd. and a prototype “wheelmotor" was retrofitted to a Blackpool tram [44], [45]. Simulation studies of the wheelmotor on a tram show high stability on a straight track with irregularities [46]. The feedback signal used is the position of the track relative to the front of the vehicle which is obtained from an array of inductive metal detectors. Simulation studies on trams have also been conducted on curved tracks of varying radii [47].

Practical implementation of the DIRW concept using wheelmotors has been undertaken on a full-scale tram by SET Ltd. The DLR Next Generation Train project is implementing

the concept on a full-scale rail vehicle [42], [48]. They are being used on freight trains as a first step and can achieve speeds up to 200 km/h on existing track infrastructure [49].

2.4.5 Directly steered wheelset

If wheels are mounted onto a stiff frame using stub axles as shown in Figure 2.9 such that their pivots are joined by an active linkage, then the wheels can be directly steered by the lateral displacement of the track rod. This is similar to rack-and-pinion steering mechanism in automobiles where the lateral displacement of the rack steers the wheels by an angle. The wheels rotate freely on the bearings of the stub-axles which are allowed to rotate in yaw relative to the carrying frame. Figure 2.10 shows the overall configuration of a vehicle with the DSW mechanism.

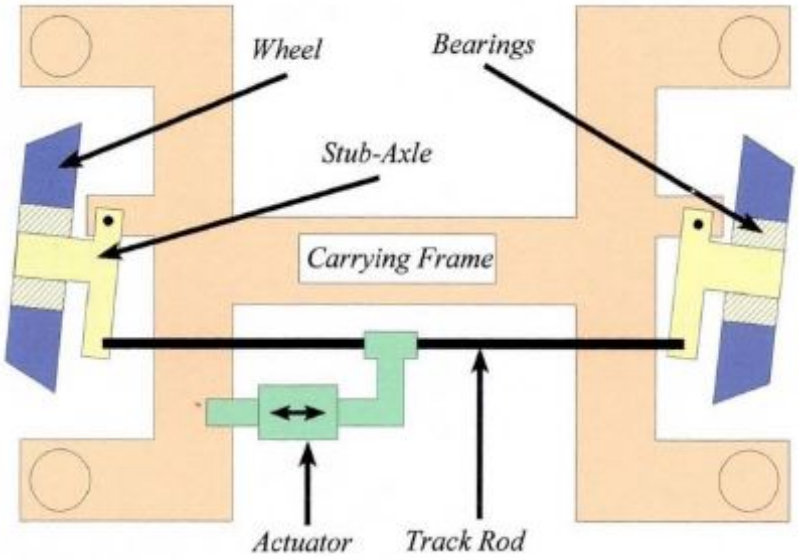

Figure 2.9: Plan view of the active wheelset [50]

Directly steered wheels was first studied by Wickens [51] and the feedback signal was the displacement of the wheel with respect to a reference line fixed to the track. This measurement is not easily accessible but in theory the model shows improved stability and curving performance. DSW was also studied by numerical simulations and tests on a 1/10 scaled roller rig by Michitsuji and Suda [52], where the bogie is designed such that the self-curving ability of a passive wheelset is allowed and an additional steering action is provided on transition curves. In the experiment, the steering action is provided by a DC motor which also provides yaw damping. The DSW configuration was studied with varied positions of the stub axle pivots [50]. The pivots could be on the wheel axis or displaced

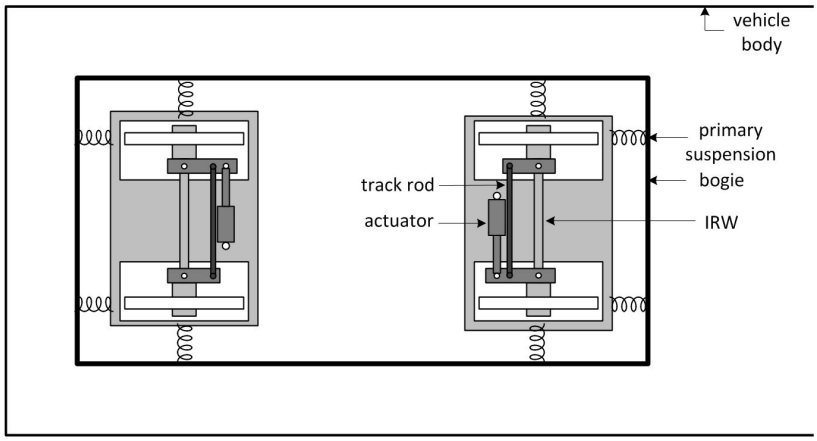

Figure 2.10: Configuration for directly steered wheelset

inwards, outwards, before or after the wheels. The different positions significantly affect the guidance and stability of the vehicle.

2.5 Control methods

A key part of implementing any active steering mechanism is the controller. A vast number of control methods exist which can be broadly categorised into single-input single-output (SISO) controllers and state-feedback controllers. SISO controllers can be implemented in multiple loops if a strong coupling exists between certain states. For example, the lateral displacements of different wheelsets, especially those on the same bogie of a railway vehicle can interact with each other and therefore multiple loops are usually necessary to steer each of the wheelsets [32]. State-feedback controllers allow multiple variables to be used as feedback signals which usually provide a better performance because most systems are multi-variable. However, measuring all the states of the system can be impractical. Because of this reason, multi-variable controllers are only used if the performance using SISO controllers is unsatisfactory.

The majority of controllers for active vehicles are standard SISO controllers [53], [54]. For example in the case of steering a rail vehicle, the input is an actuator force/ torque to a wheelset and the output is the lateral displacement of the same wheelset. The effectiveness of such controllers relies on weak coupling between unpaired inputs and outputs. If the cross coupling is strong, then using multiple independent SISO loops may not be effective. A modal control approach was studied by Mei and Goodall [55] to overcome the effects of strong coupling between the vehicle lateral and yaw motions. By adding or subtracting the lateral

acceleration equations of two wheelsets on the same bogie, it was possible to effectively decouple the lateral mode from the yaw mode and design the controllers separately.

Multi-variable controllers usually work by optimising a cost function. The Linear Quadratic Regulator (LQR) is a common optimal controller where the gains are calculated by minimising a cost function [56]. The minimisation algorithm relies on state feedback and requires a weighting to be allocated to each state and input. The LQR controller has been applied to linear state space models of both two-axled and bogie-based vehicles [57]. Satisfactory performance was achieved with different curve radii and creep coefficients. However, the use of an optimal controller is limited in practice due to the difficulty of measuring all the states. H_∞ control techniques allow the optimisation algorithm to be applied to specific states instead of minimizing all the states [58]. Mei and Goodall [39] developed a H_∞ controller for active steering of IRWs on a two-axled vehicle using practical sensors (accelerometers and gyros). The controller was shown to be robust even in the presence of parametric variations. An assessment of optimal and SISO controllers was undertaken on a two-axled vehicle with solid-axle wheelsets by Mei and Li [59]. A well-tuned SISO controller was shown to give a better performance on straight tracks and high speed curves.

The control methodology that has been adopted in this thesis is to disregard the multi-variable nature of a rail vehicle. Multiple SISO loops that consider the different loops to be effectively decoupled are initially designed. Classical PID controllers are used because they are widely understood and accepted. More complex controllers are not designed because the results obtained using classical SISO control loops meet the requirements. The use of the classical controllers provides a benchmark improvement in performance that can be expected when using active steering. However, modern optimal control methods such as LQR should theoretically give a better performance. In order to determine the improvement in performance that can be achieved with a more complex control algorithm, without the requirement of measuring multiple states, proportional-integral-plus (PIP) controllers are also designed. The PIP controller can be designed on the basis of a single input and a single output signal. This is explained in more detail in Chapter 4.

2.6 Implementation status of active steering

The use of active control to improve the running dynamics of a rail vehicle has mostly been confined to prototype testing. There are several practical limitations of implementing active primary suspensions for guidance and steering. A key issue is that of sensors and actuators. The appropriate sensing technology must be accurate, reliable and cost efficient which means

that the cost of the sensors is marginal with respect to the cost of the bogies. Most active guidance and steering strategies require the lateral displacement of the wheel with respect to the rail or the wheelset angle of attack as feedback signals. However, measuring these signals require sensors to be placed on the axlebox which is highly undesirable as it is a high vibration environment. Consequently, extremely accurate/ expensive sensors will need to be used. Therefore, bogie-based or vehicle-based inertial sensors have been used and the required feedback signals are estimated using Kalman filters [60, 61]. More recently, wheelset lateral displacement has been measured using non-contacting sensors or estimated from bogie-mounted inertial sensors or a combination of both. However, estimators can cause a reduction in the robustness of the controller [34] and in general estimates can be biased or divergent [62]. Other strategies which use the measurement of forces or deflections in the primary suspension have also been studied [63]. In this thesis, ideal sensing and actuation is assumed with the idea that further work is needed to consider the practical implementation of these active steering strategies.

Actuator technology has to be chosen carefully and must have a good response time (to avoid bandwidth issues). Actuator dynamics can affect the robustness and stability of controllers. Controllers have to be implemented such that they are robust in the presence of large parameter variations or significant increase in non-linearities, and also in the presence of dynamic uncertainty resulting from actuator dynamics. The control effort required for active steering is usually high (in the order of kN) but the power requirement of actuators is low in general due to low actuator velocity [39]. IRWs require far less control effort than solid-axle wheelsets as the longitudinal creep forces are almost zero because they are not restrained by a solid-axle.

The biggest challenge in implementing active steering is providing the required level of safety and reliability. This involves condition monitoring and fault detection and isolation (FDI), on which there are some published papers [64, 65]. Active primary control directly affects ride safety and this is the principal reason they are confined to prototype testing. Meeting required safety standards means that redundancies and condition monitoring techniques have to be implemented on the vehicle which would increase its cost. The increase in manufacturing cost must be justifiable by improved performance or significant reduction in maintenance costs. The challenges posed by active suspensions have already been overcome at the secondary suspension level through the adoption of tilting trains for high speed curves [54]. In the aerospace sector, fly-by-wire concepts are widely accepted by commercial airliners [66]. Steer-by-wire technology is receiving increasing attention in the automotive sector and has been implemented in production vehicles such as the Infiniti Q50 [67].

In literature, active steering has always been envisioned as an approach to improve guidance and steering in conventional vehicles or in vehicles with IRWs. Active steering could also be used on track switches to provide an additional steering force. This is a new area of research which does not have any published works yet apart from those published as a result of the work presented in this thesis. Broadly speaking, there are two possibilities. The additional steering force could reduce some of the impact forces at S&Cs to reduce wear and increase their lifetime. A longer term ambition, which is not explored in this thesis, is to perform the switching mechanism entirely from on-board the vehicle to enable a redesigned track switch where both routes are enabled at the same time. This would mean that there would be no moving parts on track switches potentially leading to a substantial decrease switch failures and associated maintenance costs.

2.7 Current practice at S&Cs

Track switches come in many different layouts and dimensions, however the basic mechanism has not changed since their invention more than 200 years ago [68]. A typical S&C, illustrated in Figure 1.1 in Chapter 1, has two stock rails, two switch rails and a crossing fastened to wooden sleepers by bolts or clips. The sleepers are attached to a concrete slab or ballast. The stock rails have a permanent fixed position while the ends of the switch rails can displace laterally to close the gap between itself and the adjacent rail on one side while maintaining a gap on the opposite side for the flange to pass through. The check rails guide the wheelsets into the correct lateral position and constrain them. The distance between the two switch rails is maintained by the stretcher bars between them. Points operating equipment (POE) positions the switch rails accurately, holds them in position while a train passes and reports their position status to the signalling system. Recently, high-performance switch systems (HPSS) [69] have been used to measure switch blade positions accurately and immediately identify if the safe limits of positions are breached. Although there are several types of POEs, this 'lock and detection' mechanism is the fundamental working principle of all POEs. High-speed switches have longer switch blades and require multiple actuation points. This is because the planar nature of switches means that track cant cannot be provided to compensate for lateral acceleration. This also results in very shallow divergence angles of high speed switches.

The variation in rail profiles at switches gives rise to large impact forces on the rails. At switch toes, the width of the switch rail is very small in order to facilitate a smooth transition from stock to switch rail. The small width of the switch blade combined with the high impact

forces it needs to endure as a result of the rapid change in contact profiles make it a weak structure.

At crossings, wheels have to travel across the gap designed to provide flange clearance for both the through and diverging routes. On low to moderate speed switches, the gap is small enough that it can be traversed safely. However, the crossing nose endures high impact forces as a result of the discontinuity in the running rail. In comparison to an arbitrary rail head, the crossing suffers two to four times higher impact forces [70]. On high speed turnouts, the shallow divergence angle means that the crossing gap is significantly bigger. This necessitates a movable crossing nose which displaces laterally to close the gap so that it forms a continuous rail in the desired route of travel [12].

Due to the high impact forces at S&Cs they need regular inspection and maintenance during which all services using it have to be completely stopped. The inability to operate at a lower operational capacity makes switch problems very critical to the running of railways, especially where a wider diversionary route is not possible.

2.8 Developments in track switching technology

There has been a considerable effort in industry and academia to make the load transition from stock rail to switch rail smoother. Optimisation studies have been undertaken in simulation to improve the load transition to reduce the energy dissipation or wear [71]. One of the main problems at the switch toes is flange contact on the switch blade arising from the varying rail profiles. Kinematic gauge widening in the through-route has been proposed to reduce the adverse effects of wheel and switch blade wear at the switch toe. This mechanism, called FAKOP is developed by an Austrian company VAE GmbH [72] and induces a lateral displacement in the wheelset by changing the gauge width at the toe as shown in Figure 2.11a.

The purpose is to allow higher speeds on the through-route by removing the shift from stock to switch rail as in a conventional turnout. In simulation studies, FAKOP shows a reduction in wheel-rail wear and impact forces compared to a conventional switch [73]. However, it does not improve the wear on divergent routes and requires complex designing tools which make its production difficult. Another mechanism which works by introducing a lateral displacement at the toe is CATFERSAN, which involves machining the stock rail to reduce its height on the side where the wheel flange travels [74], as illustrated in Figure 2.11b. Unlike FAKOP, it involves machining of standard stock rail and is therefore fairly inexpensive to produce.

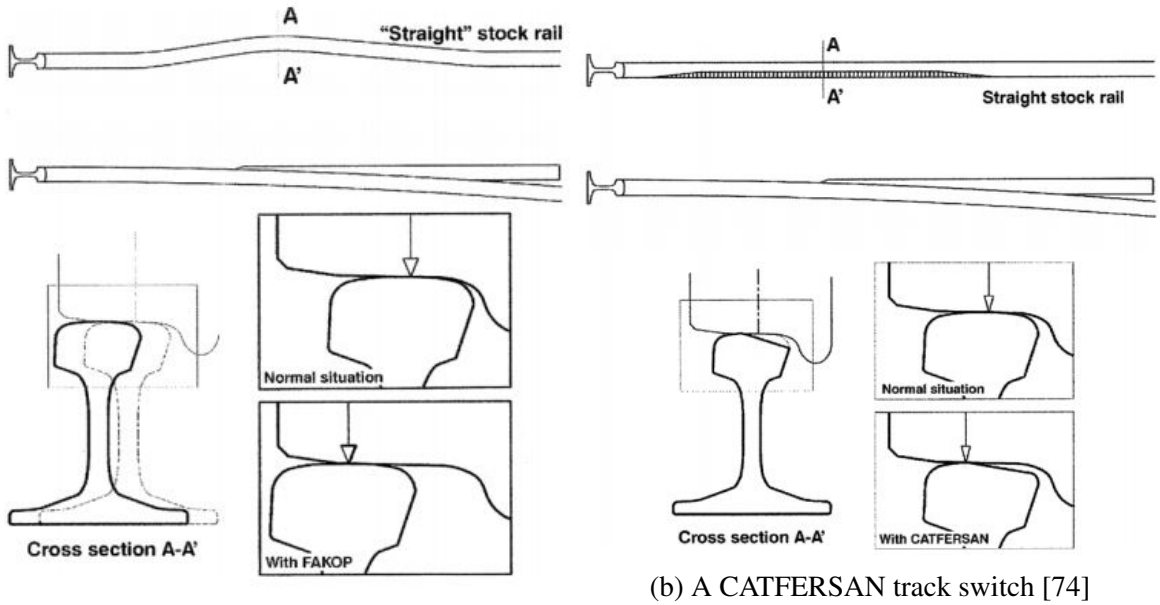

(a) A FAKOP track switch [73]

(b) A CATFERSAN track switch [74]

Figure 2.11: Different track switching mechanisms

To address the lack of operational redundancy of a conventional track switch in the event of a failure, a novel track switching mechanism called Redundantly-Engineered POINTs, abbreviated as REPOINT, has been proposed [75]. It uses multiple actuators for redundancy and the mechanism involves using stub switches which lift and drop into the desired location as shown by the arrows in Figure 2.12. According to current practice, the distance between consecutive trains has to be sufficient to safely stop in the event of a failure, however a fault-tolerant and redundant switch like REPOINT allows the distance to be reduced which can potentially increase the capacity of railways as a transport system.

The reduction of impact forces at crossings is also a key issue for which a few different mechanisms have been proposed. This includes the introduction of moveable crossing nose for high speed turnouts. Other efforts include flange bearing crossings which support a wheel from under the flange to allow rail vehicles to ride on their wheel flange [13]. This minimises the vertical disturbances to reduce impact on the crossing nose and the wheels. Figure 2.13 illustrates a flange bearing crossing nose. On-going work on novel track switching concepts is being undertaken in several European projects such as In2track [76], Shift2rail [4] and S-code [5].

Despite these improvements in technology, track switches still remain a largely mechanical concept that rely on the switch rails moving laterally. Consequently, there is a rapid change in contact profiles leading to the associated problems of disproportionately high impact forces and wear. The concept of VBS is to fundamentally change the switching mechanism from the track to the vehicle.

Figure 2.12: Laboratory demonstrator of a RE-POINT track switch [75]

Figure 2.13: Flange bearing crossing nose [13]

2.9 Current status of VBS

Vehicle-based switching proposes to perform switching from on-board the vehicle. The motivation is to have a purely passive track switch, which does not rely on any moving parts and the switching is done entirely from the vehicle instead. Vehicle-based switching has probably been conceptualised since the invention of railways with 'Rivington's self-acting railway switches' being one of the earliest appearances in literature [77]. The underside of the vehicle has an inclined plane which pushes a bell crank which moves the switch blades into position, as illustrated in Figure 2.14. Although it is largely a mechanical concept, it represents a shift in controlling the switching from track to vehicle, although the switch action itself remains part of the track. Another such application of controlling a track switch from the vehicle is done in trams the driver chooses the switch position from the dashboard. However, these mechanisms are inherently different than having a track switch with no moving parts, which is the more recent motivation behind VBS.

With developments in electronics, vehicle-based switching has been envisioned as a control application where the wheels can be individually controlled with torque-controlled motors relying on sensors. One such proposition is that of Koseki et al. [78], where the wheels on a wheelset can be individually-driven to generate the required creep forces to

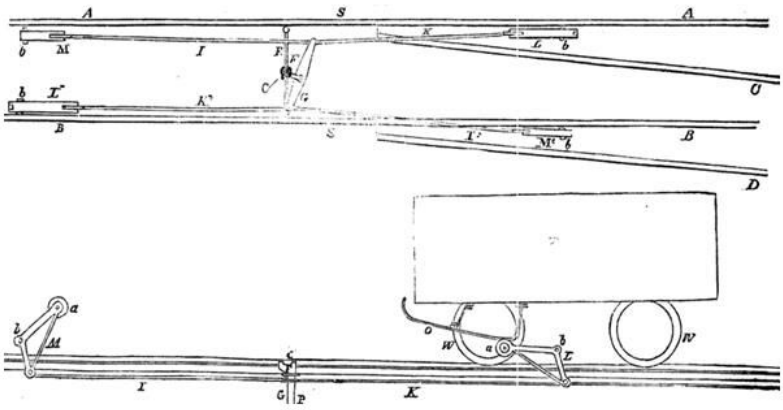

Figure 2.14: Rivington's self-acting switches [77]

produce the necessary yaw angle. This is similar to the mechanism used in this study, a conceptual illustration of which is shown in Figure 2.15. Another idea is to have a permanent magnet on the underside of the vehicle and electromagnetic rails for both through and diverging routes [79]. When the vehicle goes over the switch it is attracted to either the rails for the through or the diverging route depending on which of the electromagnets is turned on. This mechanism is shown in Figure 2.16.

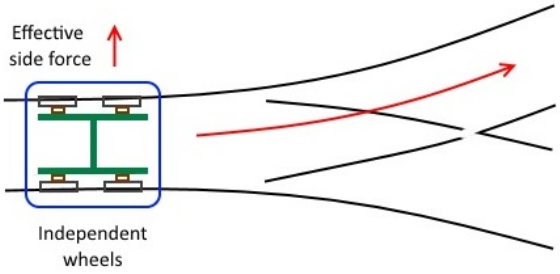

Figure 2.15: On-board turnout using controlled steering force [78]

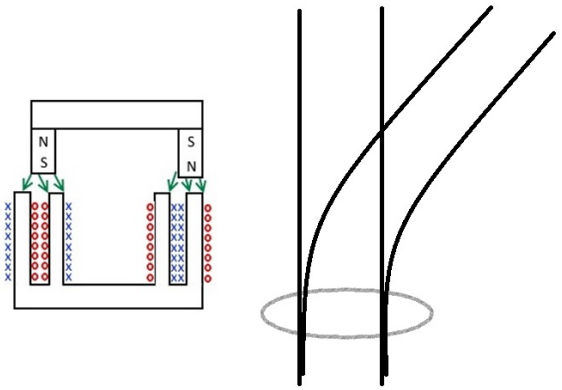

Figure 2.16: Vehicle switching using magnetic forces [79]

There has been considerable research into using active elements to influence the running dynamics of rail vehicles on straight and curved sections of track, most of which is theoretical but provides a strong understanding of its possibilities and limitations. Applying such mechanisms on track switches has only been hypothesised and not studied scientifically. The nature of VBS as is envisioned in the technology route-map in Chapter 1 is novel and radical.

This study shows the improvements of applying an active vehicle on a conventional switch and gives an idea of the control requirements in terms of sensing and actuation. The longer term vision of VBS presents numerous research challenges but can potentially revolutionise the way trains operate. VBS could be combined with electronically-coupled trains which are long on premier-routes but allow individual vehicles to de-couple to serve at intermediate stations. They could also be combined with intelligent systems on-board which allow them to negotiate with each other at junctions to allow timetable-less running.

2.10 Conclusions

This chapter provided background information on conventional guidance and steering before reviewing relevant literature of different active steering mechanisms and the status of their implementation till date. It also provided details on the state-of-the-art in track switching technology which are mostly a purely mechanical arrangement from the track with no influence from the vehicle.

The ASW, AIRW and SYC configurations were chosen from the five configurations discussed in this chapter to present an incremental implementation of active steering where both the SYC and ASW configurations can be achieved by retrofitting actuators onto a current bogie through to completely redesigning a conventional vehicle to have individually driven wheels as in the DIRW mechanism. The SYC mechanism has lesser safety implications than the ASW due to being in the secondary suspension but also offers fewer potential improvements to the running dynamics.

Applications of actively steered vehicles on track switches are yet to be explored and is the motivation for this research. This gap in literature is addressed in this thesis by:

1. Studying actively steered vehicles on different track profiles to assess their performance against a conventional passive vehicle.

2. Comparing the performance of controller algorithms with varying complexity on the different active vehicles considered.

3. Selecting the active vehicle and the controller with the best performance and comparing it against a passive vehicle on conventional track switches.

The next chapter explains the modelling of the three active vehicle described in this chapter and of a conventional passive vehicle. Chapter 5 discusses the results from simulations of the vehicles on a variety of track profiles.

Chapter 3

Vehicle modelling

A rail vehicle is a very complex dynamic system with a high level of cross coupling between different degrees of freedom. Dynamic vehicle modelling is usually undertaken as a mathematical representation of this complex system. A vehicle model attempts to serve two main purposes. Firstly, it allows frequency and time domain analysis of the system which can be used for various controller design methods. Secondly, several parameters can be changed to view the corresponding effect on performance without any safety implications. Vehicle models in general are used for other purposes as well, such as for designing vehicles and gauging. This chapter discusses the modelling of a full rail vehicle developed in a software called Simpack [80], which is used by researchers and railway engineers in industry to model vehicle dynamics to an acceptable accuracy [81, 38]. A review and comparison of the state-of-the-art of MBS software was undertaken as part of the “Manchester benchmark" project [82] indicating good correlation to reality.

Vehicle modelling is usually achieved by identifying the relevant degrees of freedom to form the differential equations describing the modes of interest. If guidance is the only consideration, a simplified modelling approach would only consider the plan view modes (mainly lateral and yaw) and ignore coupling with other modes. However, a multi-body simulation software like Simpack considers all degrees of freedom and their coupling which increases its fidelity and therefore its correlation to the dynamics of a real rail vehicle. Simpack also models the non-linearities in the rail-wheel profile and certain suspension components. The interacting forces between bodies are defined through joint and force elements so that the equations of motion don’t have to be formulated directly by the user. The dynamics of these individual components and their interaction are discussed in this chapter.

Two sets of models are developed and discussed in this chapter. One set consists of non-linear Simpack models of a conventional passive vehicle and the Actuated Solid-axle Wheelset (ASW), Secondary Yaw Control (SYC) and Driven Independently-Rotating

Wheelsets (DIRW) vehicles. These are called the ‘simulation’ models. The other set consists of simplified linearised models obtained from applying system identification methods to selected inputs and outputs of the Simpack models. The linear models allow the systems to be analysed in the frequency domain which is useful for designing controllers and are therefore called the ‘design’ models. The ‘simulation’ models are a level up in complexity from the ‘design’ models and provide an additional level of proof that the algorithms will cope with parametric and structural uncertainty, as will be the case in application.

3.1 Passive vehicle modelling in Simpack

The vehicle has six degrees of freedom, of which three are translational (longitudinal, lateral and vertical movements) and three are rotational (roll, pitch and yaw movements). The Simpack model takes into account all of the vehicle degrees of freedom and allows movements between bodies that are considered to be effectively rigid. The x axis is in the forward direction of motion of the vehicle. The vertical z-axis is relative to the rails and is positive in the downward direction. The lateral y position is measured relative to the track centreline. Figure 3.1 shows the axis system relative to a track. Each body has its own axis system which is especially useful when the vehicle is on a curved section of track. All the bodies are rigid which means that they do not change their geometry or mass during simulation.

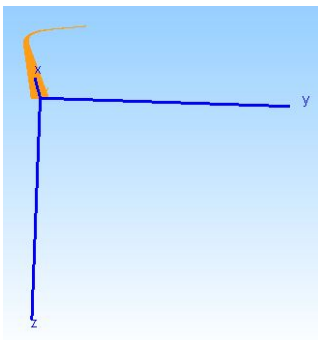

Figure 3.1: Axis system in Simpack, track is highlighted in yellow.

The Simpack models are developed on the basis of a standard vehicle model in the rail module of version 9.10.2. It is considered representative of the dynamics of a modern rail vehicle and can be easily adapted to a specific vehicle by changing the model parameters. The conventional vehicle model consists of a car body suspended on top of two bogies. The car body and bogies are defined using their mass, centre of gravity and their roll, pitch and

yaw inertial moments. Each bogie consists of a frame, a bolster and four radius arms as shown in Figure 3.2.

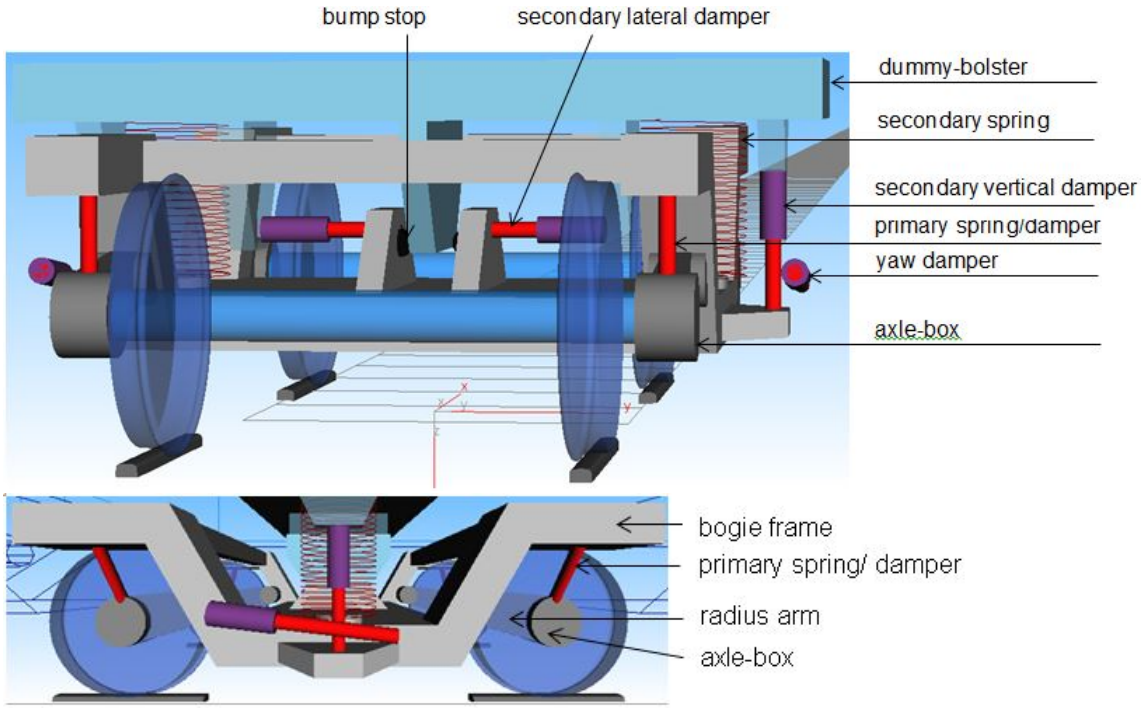

Figure 3.2: 3D Simpack model of bogie

The bolster connects the bogie to the car body through the secondary suspension which consists of three force elements on each side, two spring/damper elements and one shear spring. The shear spring elements in the secondary suspension model the airsprings in most passenger vehicles by coupling the shear forces and bending torques. A simplified model would usually separate it into lateral and vertical springs. The two spring/damper elements provide stiffness and damping in the vertical and lateral directions. The secondary suspension also has a yaw stiffness and damping which influences the critical speed above which hunting occurs. The lateral and yaw damping in the secondary suspensions are non-linear functions of relative velocity as illustrated in Figures 3.3 and 3.4. The bumpstop provides a progressive stiffness rate to absorb energy and prevent the suspension from reaching the end of its deflection limit so it doesn't get damaged. It has a dead-band region and high stiffness when the relative position is over a threshold value as shown in Figure 3.5.

The radius arm connects the wheel axlebox to the bogie chassis. The end that is connected to the bogie has a bushing component which is modelled as stiffness and damping between the bogie and the radius arm in multiple axis directions - three translations as well as three rotations. The primary suspension between each wheelset and bogie consists of lateral, longitudinal and vertical springs. A damper is also connected in parallel to the lateral spring,

the damping of which varies non-linearly with relative lateral displacement of the wheelsets to the bogie as shown in Figure 3.6. The longitudinal forces are transmitted through a traction rod which is modelled as a spring and a damper in parallel.

The mass and inertia of different bodies and the stiffness and damping of the suspension components in the model are chosen to represent a typical modern rail vehicle [83]. The main vehicle parameters are listed in Table 3.1. It should be noted that the primary longitudinal stiffness value given in the table is that of a conventional passive vehicle operating at maximum speeds of ≈45 m/s. At higher speeds, the stiffness needs to be increased to prevent hunting. The stiffness is reduced for the active vehicle configurations to minimise the control action opposing a stiff suspension and is instead provided actively. This is discussed in more detail in Section 3.2. More detailed drawings on the passive vehicle model and a detailed table of parameter values is in Appendix A.

Table 3.1: Simpack vehicle parameters for a passive vehicle

Primary suspension element	Value	Units
longitudinal parallel stiffness	3.14×10^7	N/m
lateral parallel stiffness	6.5×10^5	N/m
lateral parallel damping	6×10^5	Ns/m
vertical parallel stiffness	1.22×10^6	N/m
stiffness of vertical damper	6×10^5	N/m
Secondary suspension element	**Value**	**Units**
longitudinal shear stiffness	1.6×10^5	N/m
lateral shear stiffness	1.6×10^5	N/m
vertical stiffness	4.3×10^5	N/m
roll bending stiffness	1.05×10^4	Nm/rad
pitch bending stiffness	1.05×10^4	Nm/rad
stiffness of vertical damper	6×10^6	N/m
vertical damping	2.5×10^4	Ns/m
lateral stiffness	1×10^6	N/m
yaw stiffness	3.75×10^5	N/m
Key vehicle parameters	**Value**	**Units**
Vehicle body mass	20000	kg
Bogie mass	2615	kg
Wheelset mass	1200	kg
Half vehicle body length	11.2	m
Bogie semi-wheelbase	1.28	m
Half gauge width	0.75	m
Axlebox lateral semi-spacing	1	m
Wheel rolling radius	0.46	m

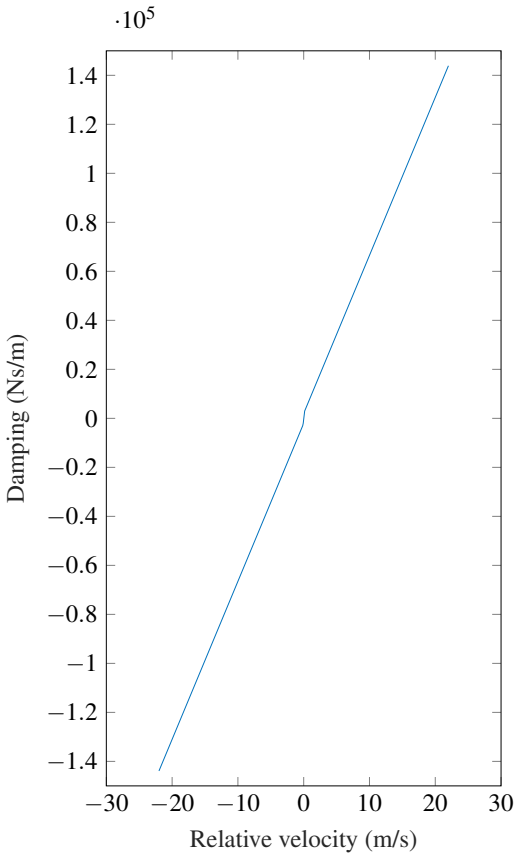

Figure 3.3: Secondary lateral damper

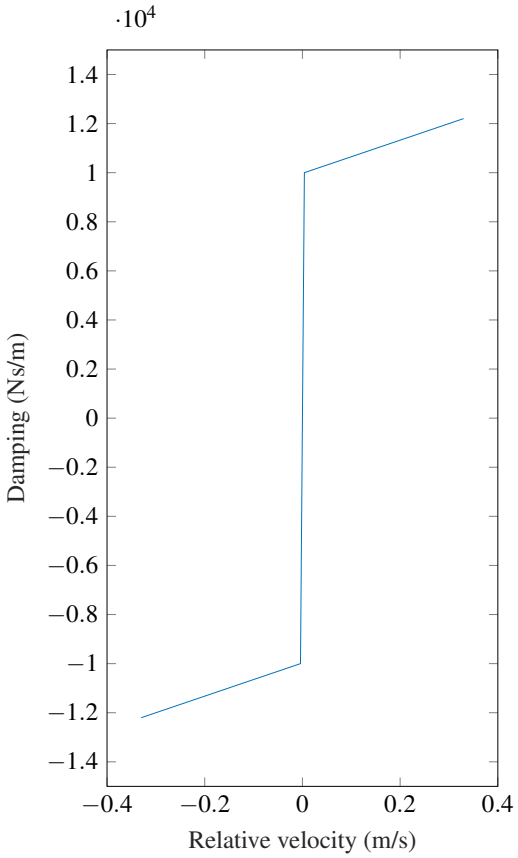

Figure 3.4: Secondary yaw damper

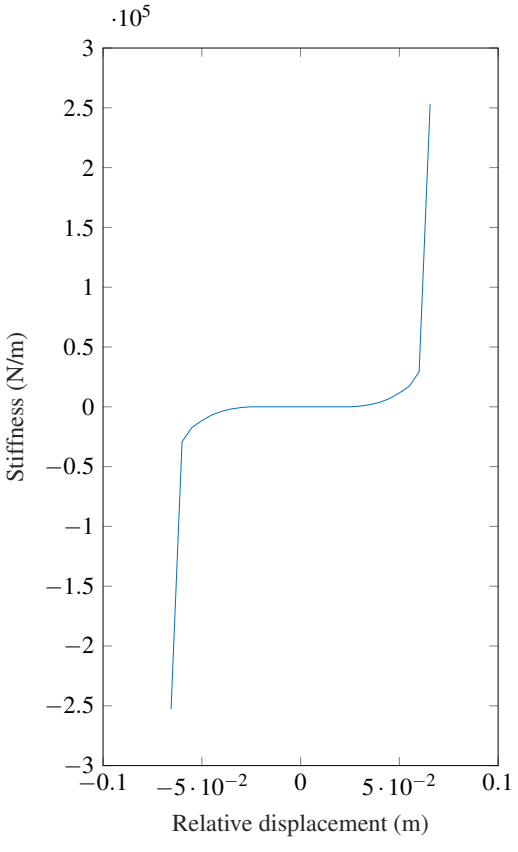

Figure 3.5: Bump stop

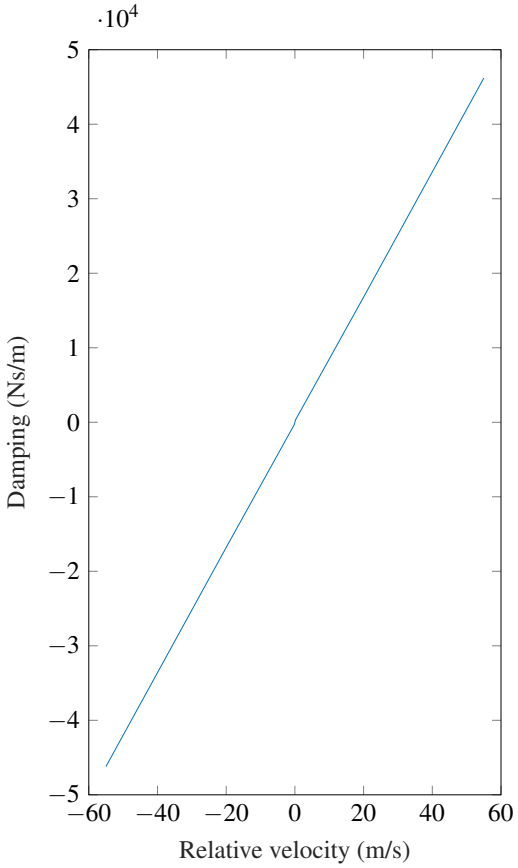

Figure 3.6: Primary vertical damper

The contact forces at the wheel-rail interface are calculated by first identifying the contact patch sizes and locations and then determining the normal and tangential contact forces. Multiple points of contact are possible especially when the wheel flanges approach the rails [84]. A contact patch is the area where the rail profile and the wheel outline intersect and is modelled as an ellipse. Each contact patch has a local coordinate system which adjusts accordingly as the wheelset yaw angle changes. Figure 3.7 shows the contact patch orientation for different yaw ψ positions or angles of attack. The contact transitions from the centre of the track (left figure) to flange contact at a higher angle of attack (right figure).

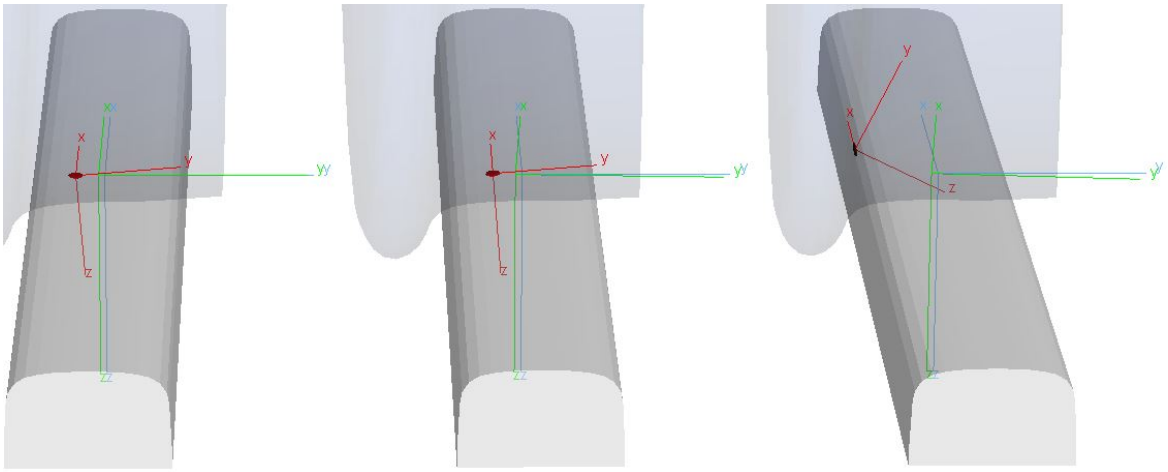

Figure 3.7: Contact patch orientation when $\psi = 0°$ (left), $3°$ (centre) and $6°$ (right). The rail marker is blue, the wheel marker is green and the contact patch marker is red.

The normal forces are based on the rail-wheel contact area. The Hertzian method is used for normal force calculation which is a function of the semi-axes of the elliptical contact patch, Young's modulus and Poisson ratio. The wheel-rail material properties are a function of the latter two parameters. The tangential forces are calculated using the FASTSIM (Fast Algorithm for the Simplified non-linear theory of contact) algorithm which is based on Kalker's "simplified" theory, explained in detail in [85]. The contact is modelled by a series of three-spring systems such that each point on the wheel-rail surface can elastically displace in any direction, independently of the neighbouring contact points. FASTSIM provides a very good approximation and has a quick computation time making it the accepted standard method [86].

The wheel and rail profiles used are S1002 [87] and UIC60 [88] respectively. The S1002 profile is used on high speed vehicles and on most passenger vehicles. The UIC60 profile is used across the British rail network. The simulation results of creep forces generated will be higher with worn wheel profiles as they have a higher conicity than the S1002. However the overall trends across the different active vehicles will still be the same with different wheel

and rail profiles. The rails are inclined towards the track centreline by 1 in 40 on all track profiles except on switches where they are inclined by 1 in 20. 1:40 inclination is widely used across Europe whereas in Britain, a rail inclination of 1:20 is common practice [89]. Simpack allows the user to change different rail inclinations and wheelset properties such as parameters defining the wheel-rail material properties, adhesion coefficients, normal force and creep force calculation methods.

Creep forces are a function of adhesion and will therefore vary with changes in adhesion. All the simulations in this study assume normal adhesion conditions at which the adhesion coefficient has negligible effect on the guidance mechanism, which is mainly dependent on creep forces. Very low adhesion which is indicative of poor weather and foliage on track is not considered here [90]. Figures 3.8 to 3.11 show the lateral creep forces of the four wheelsets at varying values of the adhesion coefficient μ on a curved track profile. The curvature and cant variation of the track profile used is shown in Figure 3.12. From the graphs it can be seen that at different μ values, the change in the lateral creep forces at the four wheelsets of a rail vehicle is not very significant [1]. The controllers are designed to be able to cope with such parametric variations as will be the case in practice.

3.2 Active vehicle modelling in Simpack

Three active vehicle models are developed in Simpack based on the SYC, ASW and DIRW configurations. The SYC and ASW vehicles have solid-axle wheelsets while the DIRW vehicle has independently-rotating wheelsets. The Simpack modelling for a vehicle with independently-rotating wheelsets is similar to that of a vehicle with solid-axle wheelsets. The only difference is at the wheelset level and this is illustrated in Figure 3.13. The solid-axle wheelset, shown on the right is modelled as a single body with six dofs with respect to the track and force elements to model the creep forces. The independently-rotating wheelset is modelled as three bodies - two wheels and an axle. The wheels are free to rotate along the y-axis wrt the axle which has 6 dofs wrt the track.

Both the SYC and the ASW vehicles are able to guide without the active elements due to having solid-axle wheelsets. The purpose of the active elements is to provide an additional steering torque. The SYC vehicle uses actuators in the same place as a conventional anti-yaw damper which would normally influence the hunting modes of the vehicle. Figure 3.14a shows the position of the SYC actuators. The actuators provide a steering torque to the bogie which is determined using controllers designed using frequency-domain design methods which is discussed in more detail in Chapter 4. The difference between the lateral creep

[1] The R^2 correlation in lateral creep force responses with a μ variation of 0.1 is $\approx$95%. Correlation is calculated using Equation 3.20

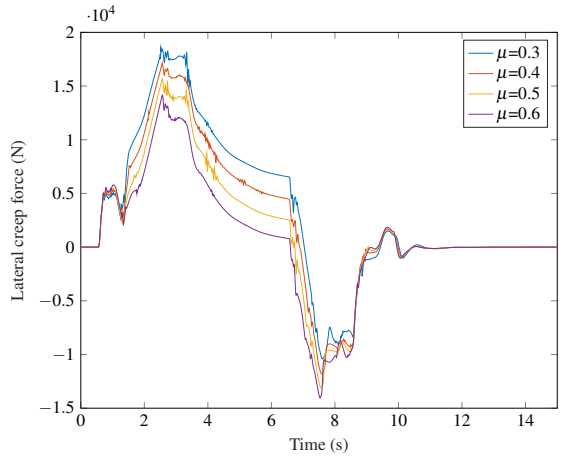

Figure 3.8: Front bogie front wheelset

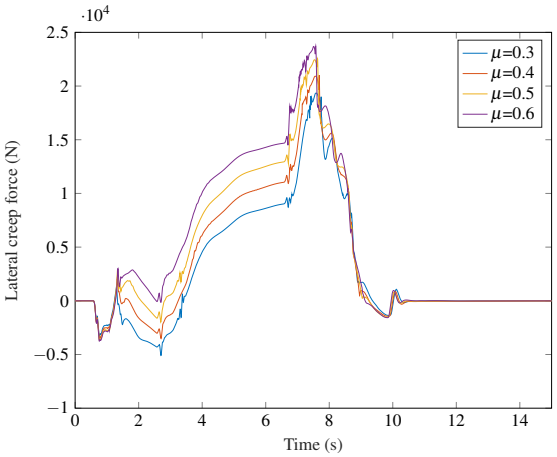

Figure 3.9: Front bogie rear wheelset

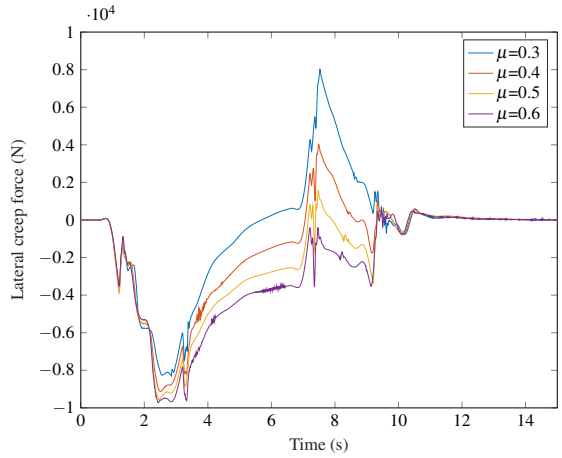

Figure 3.10: Rear bogie front wheelset

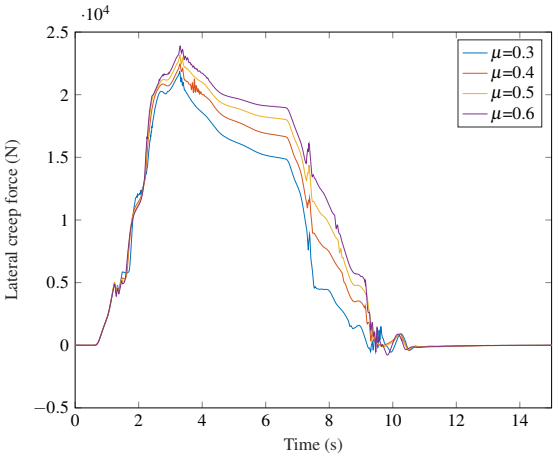

Figure 3.11: Rear bogie rear wheelset

forces at the wheel-rail contact of the front and rear wheelsets in each bogie is used as the feedback signal to calculate the control torque. This is the mechanism of the SYC control as explained in Section 2.4.1. The control torque is purely for the purpose of stabilisation as guidance is provided by the solid-axle wheelsets. The controller aims to equalise the lateral creep forces generated by the front and rear wheelsets of a bogie. This would therefore require estimation in practice using a model based filter, such as a Kalman-Bucy filter to estimate creep forces at the wheel-rail contact [91], [92].

In the ASW vehicle, the steering yaw torque is applied directly to the wheelset using a pair of longitudinal actuators as shown in Figure 3.14b. The actuators are in parallel with the longitudinal springs to maintain a conventional suspension configuration. The idea is to apply a yaw torque to the wheelsets to reduce the relative longitudinal forces between the contact points on the wheels and rails as explained in Section 2.4.2. The controller aims to achieve ‘pure rolling’ by controlling the longitudinal creep forces to zero. Similar to the SYC

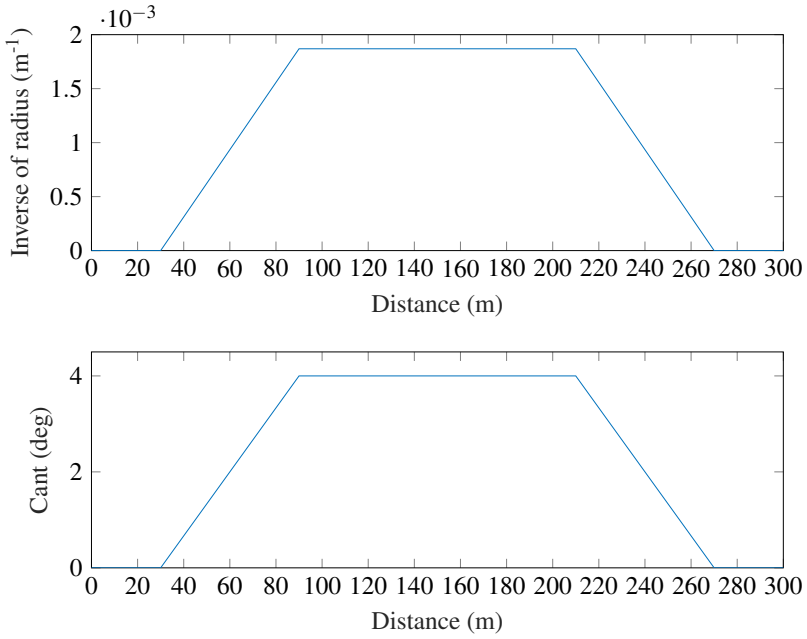

Figure 3.12: Curved track profile with radius = 535 m, cant = 4°

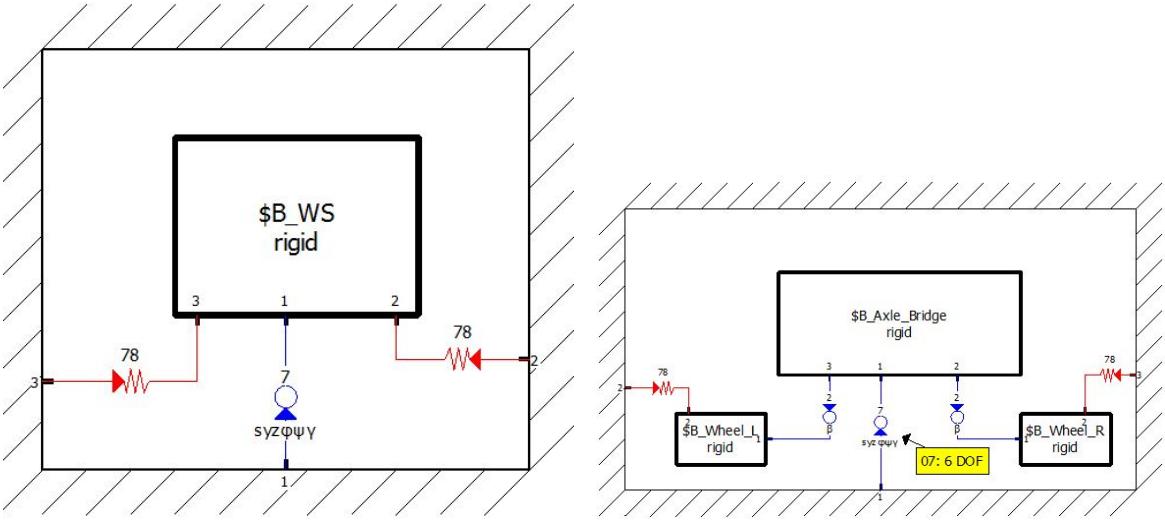

(a) Solid axle wheelset (b) IRW

Figure 3.13: 2D diagrams of IRW and solid-axle wheelsets

configuration, an estimator will be needed to estimate the longitudinal creep forces which are used as feedback signals. Also, as in the case of the SYC configuration, the control torque aims to provide the steering while the guidance is provided by the solid-axle wheelsets.

The DIRW vehicle uses wheel motors as illustrated in Figure 3.14c to provide an overall wheelset steering torque to minimise the longitudinal creep forces. In this study, traction control is not integrated with the steering control, however in practice a combined strategy

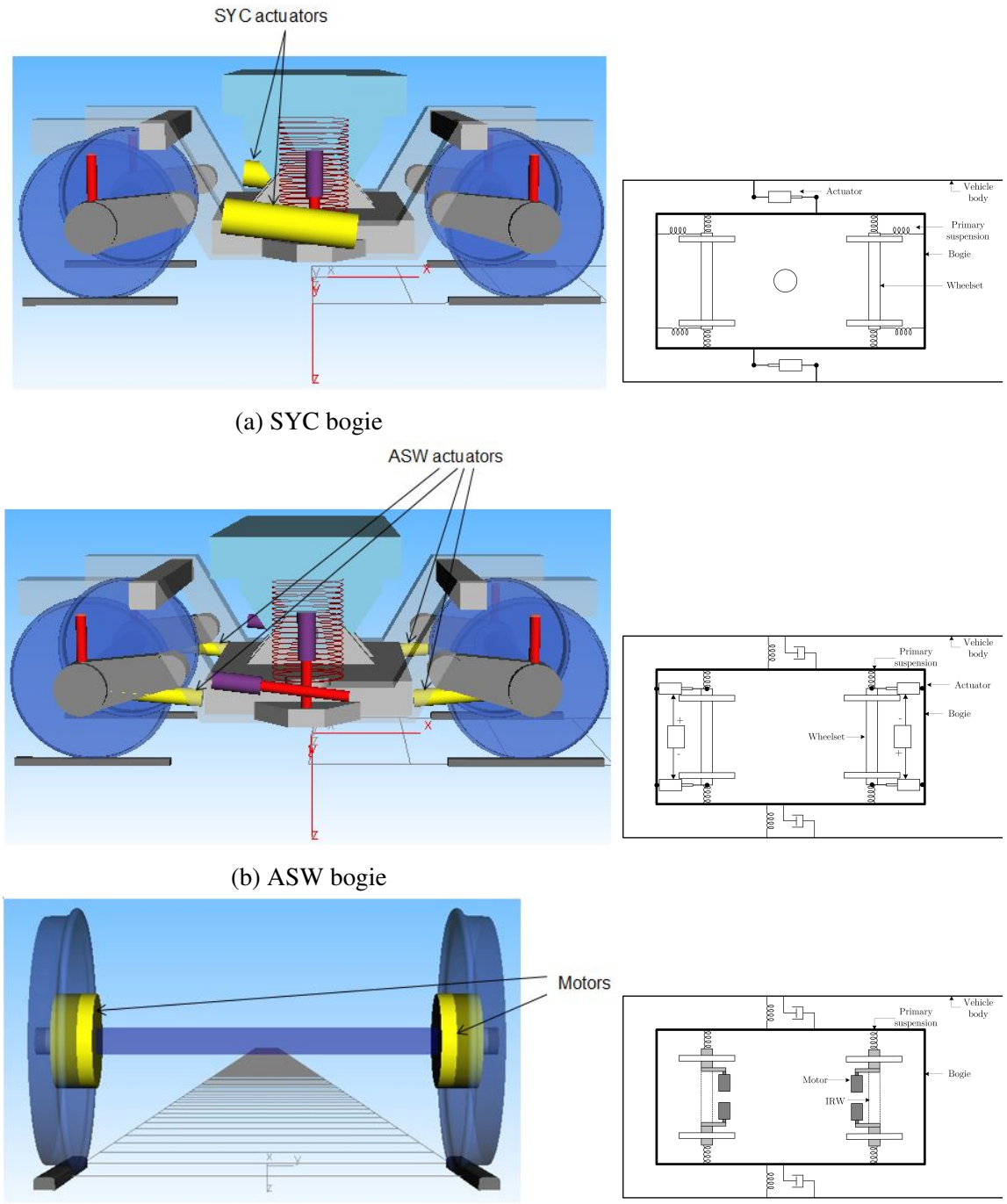

(a) SYC bogie

(b) ASW bogie

(c) DIRW wheelset

Figure 3.14: Actuator positions for the SYC, ASW and DIRW vehicles

would need to be considered. The motor torques are calculated using wheelset lateral

displacement as the feedback signal. Perfect sensing is assumed because the aim is to quantify the benefits for an ideal scenario.

All three active vehicle simulations are undertaken at moderate (30 m/s) and high (45 m/s) speeds to analyse performance in a variety of scenarios. Typical primary longitudinal stiffness for a high speed train is in the 30-60 MN/m range [93]. The stiffness of the longitudinal springs in the primary suspension of the active vehicle models is reduced to 3.14 MN/m to lower the actuation torque required. The reduction in longitudinal stiffness does not compromise stability because it allows the control mechanism to provide the stability without needing to overcome high stiffnesses.

3.3 Developing linear models

The Simpack model has non-linear rail-wheel profile and suspension components and is considered to be a good representation of a real rail vehicle short of full-scale testing. However, in order to design controllers, it is necessary to analyse the frequency response of the system to understand how it may respond to different harmonic excitations. The vast majority of frequency analysis methods discussed in literature and applied in industry is performed on linear systems. Designing controllers based on the linear models can be justified on the basis that the control action would minimise flange contact to operate in the linear region of the wheel-rail contact. Most controllers are designed on the basis of linear systems but are able to cope with non-linearities due to having a level of robustness.

The linear models can be developed by selecting the relevant inputs and output signals from the Simpack model and applying system identification methods. This process produces a "slice" of the complete model that relates the input signal to the output signal and is not a linear representation of the entire vehicle model. An advantage of this method is that it can be implemented practically from a measurable input to an output signal.

A full vehicle linear model can also be developed using equations such as 2.1 for the wheelset lateral acceleration and Newtonian mechanics to describe the equations of motion for the plan view modes. This means that internal states can be measured unlike system identification where they are not accessible. However, developing the equations of motion requires detailed knowledge of the dynamics of the system, which can be especially complex for non-linear systems. The next subsection describes the equations of motion for the lateral and yaw modes of a rail vehicle.

3.3.1 Equations of motion

The plan view schematic of a passive rail vehicle is shown in Figure 3.15. Only the plan view modes (lateral and yaw) is considered here. The following notation is used in the schematic and in the equations of motion describing the lateral and yaw dynamics of a vehicle with two bogies and two wheelsets on each bogie.

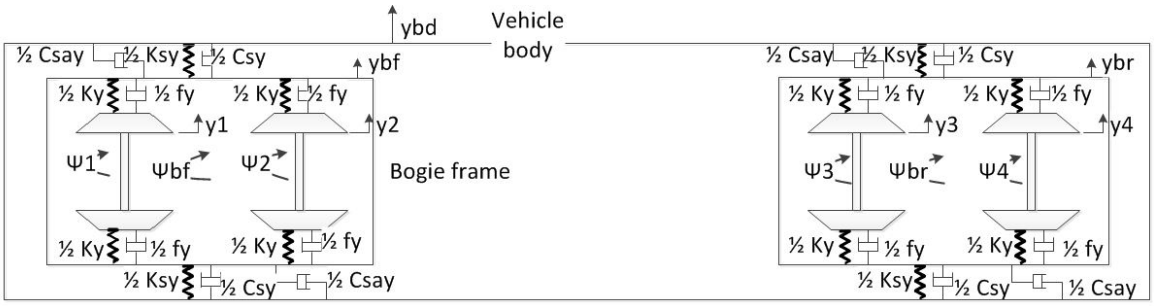

Figure 3.15: Plan view schematic of a railway vehicle

where,

$y_1 \rightarrow$ front bogie, front wheelset lateral position

$y_2 \rightarrow$ front bogie, rear wheelset lateral position

$y_3 \rightarrow$ rear bogie, front wheelset lateral position

$y_4 \rightarrow$ rear bogie, rear wheelset lateral position

$y_{bf} \rightarrow$ front bogie lateral position

$y_{br} \rightarrow$ rear bogie lateral position

$y_{bd} \rightarrow$ vehicle body lateral position

$\psi_1 \rightarrow$ front bogie, front wheelset yaw angle

$\psi_2 \rightarrow$ front bogie, rear wheelset yaw angle

$\psi_3 \rightarrow$ rear bogie, front wheelset yaw angle

$\psi_4 \rightarrow$ rear bogie, rear wheelset yaw angle

$\psi_{bf} \rightarrow$ front bogie yaw angle

$\psi_{br} \rightarrow$ rear bogie yaw angle

$\psi_{bd} \rightarrow$ vehicle body yaw angle

$K_y \rightarrow$ primary lateral stiffness

$f_y \rightarrow$ primary lateral damping

$K_{sy} \rightarrow$ secondary lateral stiffness

$C_{sy} \rightarrow$ secondary lateral damping

$C_{say} \rightarrow$ secondary anti-yaw damping

The lateral acceleration of the wheelsets can be described using the following equations:

$$\ddot{y_1} = \frac{1}{m}\left\{-\frac{2f_{22}}{v}(\dot{y_1} + \frac{r_0\lambda}{l}\dot{y_1} - v\psi_1) - \frac{2f_{23}}{v}\dot{\psi_1} - \frac{W\lambda}{l}(y_1 - d) + k_y(y_{bf} - y_1) + f_y(\dot{y_{bf}} - \dot{y_1})\right\} \tag{3.1}$$

$$\ddot{y_2} = \frac{1}{m}\left\{-\frac{2f_{22}}{v}(\dot{y_2} + \frac{r_0\lambda}{l}\dot{y_2} - v\psi_1) - \frac{2f_{23}}{v}\dot{\psi_2} - \frac{W\lambda}{l}(y_2 - d) + k_y(y_{bf} - y_2) + f_y(\dot{y_{bf}} - \dot{y_2})\right\} \tag{3.2}$$

$$\ddot{y_3} = \frac{1}{m}\left\{-\frac{2f_{22}}{v}(\dot{y_3} + \frac{r_0\lambda}{l}\dot{y_3} - v\psi_1) - \frac{2f_{23}}{v}\dot{\psi_3} - \frac{W\lambda}{l}(y_3 - d) + k_y(y_{bf} - y_3) + f_y(\dot{y_{bf}} - \dot{y_3})\right\} \tag{3.3}$$

$$\ddot{y_4} = \frac{1}{m}\left\{-\frac{2f_{22}}{v}(\dot{y_4} + \frac{r_0\lambda}{l}\dot{y_4} - v\psi_1) - \frac{2f_{23}}{v}\dot{\psi_4} - \frac{W\lambda}{l}(y_4 - d) + k_y(y_{bf} - y_4) + f_y(\dot{y_{bf}} - \dot{y_4})\right\} \tag{3.4}$$

The yaw dynamics of the wheelsets are described by the following equations:

$$\begin{aligned}\ddot{\psi_1} = \frac{1}{I}\Big\{&-2f_{11}(\frac{l\lambda}{r_0}(y_1 - d) + \frac{l^2}{v}\dot{\psi_1}) - \frac{2f_{33}}{v}\dot{\psi_1} - \frac{I_{wy}v\lambda}{lr_0}\dot{y_1} + \frac{f_{23}}{v}(\dot{y_1} + \frac{r_0\lambda}{l}\dot{y_1} - v\psi_1)\\ &+W\lambda l\psi_1 - k_\psi\psi_1 - f_\psi\dot{\psi_1}\Big\}\end{aligned} \tag{3.5}$$

$$\begin{aligned}\ddot{\psi_2} = \frac{1}{I}\Big\{&-2f_{11}(\frac{l\lambda}{r_0}(y_2 - d) + \frac{l^2}{v}\dot{\psi_2}) - \frac{2f_{33}}{v}\dot{\psi_2} - \frac{I_{wy}v\lambda}{lr_0}\dot{y_2} + \frac{f_{23}}{v}(\dot{y_2} + \frac{r_0\lambda}{l}\dot{y_2} - v\psi_2)\\ &+W\lambda l\psi_2 - k_\psi\psi_2 - f_\psi\dot{\psi_2}\Big\}\end{aligned} \tag{3.6}$$

$$\begin{aligned}\ddot{\psi_3} = \frac{1}{I}\Big\{&-2f_{11}(\frac{l\lambda}{r_0}(y_3 - d) + \frac{l^2}{v}\dot{\psi_3}) - \frac{2f_{33}}{v}\dot{\psi_3} - \frac{I_{wy}v\lambda}{lr_0}\dot{y_3} + \frac{f_{23}}{v}(\dot{y_3} + \frac{r_0\lambda}{l}\dot{y_3} - v\psi_3)\\ &+W\lambda l\psi_3 - k_\psi\psi_3 - f_\psi\dot{\psi_3}\Big\}\end{aligned} \tag{3.7}$$

$$\begin{aligned}\ddot{\psi_4} = \frac{1}{I}\Big\{&-2f_{11}(\frac{l\lambda}{r_0}(y_4 - d) + \frac{l^2}{v}\dot{\psi_4}) - \frac{2f_{33}}{v}\dot{\psi_4} - \frac{I_{wy}v\lambda}{lr_0}\dot{y_4} + \frac{f_{23}}{v}(\dot{y_4} + \frac{r_0\lambda}{l}\dot{y_4} - v\psi_4)\\ &+W\lambda l\psi_4 - k_\psi\psi_4 - f_\psi\dot{\psi_4}\Big\}\end{aligned} \tag{3.8}$$

The lateral position of the bogies is given by the following equations:

$$m_b\ddot{y}_{bf} = F_{ky_1} + F_{cy_1} + F_{ky_2} + F_{cy_2} - F_{kbd} - F_{cbd} \tag{3.9}$$

where, F_{ky_1} is the spring force from the front wheelset,

F_{cy_1} is the damping force from the front wheelset,

F_{ky_2} is the spring force from the rear wheelset,

F_{cy_2} is the damping force from the front wheelset,
F_{kbd} is the spring force from the vehicle body,
F_{cbd} is the damping force from the vehicle body

$$\begin{aligned} m_b\ddot{y}_{bf} &= -k_y(y_{bf}-y_1)-f_y(\dot{y}_{bf}-\dot{y}_1)-k_y(y_{bf}-y_2)-f_y(\dot{y}_{bf}-\dot{y}_2)+k_{sy}(y_{bd}-y_{bf}) \\ &\quad + c_{sy}(\dot{y}_{bd}-\dot{y}_{bf}) \\ &\quad k_y y_1 + k_y y_2 - (2k_y+k_{sy})y_{bf} + f_y\dot{y}_1 + f_y\dot{y}_2 - (2f_y+C_{sy})\dot{y}_{bf} + k_{sy}y_{bd} - C_{sy}\dot{y}_{bd} \end{aligned} \tag{3.10}$$

Similarly, for the rear bogie,

$$m_b\ddot{y}_{br} = k_y y_3 + k_y y_4 - (2k_y+k_{sy})y_{br} + f_y\dot{y}_3 + f_y\dot{y}_4 - (2f_y+C_{sy})\dot{y}_{br} + k_{sy}y_{bd} - C_{sy}\dot{y}_{bd} \tag{3.11}$$

The yaw dynamics of the bogies is given by the following equation:

$$I_b\ddot{\psi}_{bf} = F_{ky_1}(-a) + F_{ky_2}(a) + F_{c_1} + F_{c_2} \tag{3.12}$$

where, F_{c_1} and F_{c_2} are the secondary yaw damping forces.

$$\begin{aligned} I_b\ddot{\psi}_{bf} &= -k_y(y_{bf}-a\psi_{bf}-y_1)(-a)-k_y(y_{bf}+a\psi_{bf}-y_2)(a)-C_{say}(\dot{\psi}_{bf}-\dot{\psi}_1) \\ &\quad - C_{say}(\dot{\psi}_{bf}-\dot{\psi}_2) \\ &= 2k_y a^2\psi_{bf} - k_y a y_1 + k_y a y_2 - 2C_{say}\dot{\psi}_{bf} + C_{say}\dot{\psi}_1 - C_{say}\dot{\psi}_2 \end{aligned} \tag{3.13}$$

Similarly, for the rear bogie,

$$I_b\ddot{\psi}_{br} = 2k_y a^2\psi_{br} - k_y a y_3 + k_y a y_4 - 2C_{say}\dot{\psi}_{br} + C_{say}\dot{\psi}_3 - C_{say}\dot{\psi}_4 \tag{3.14}$$

The vehicle body lateral dynamics equation is

$$m_{bd}\ddot{y}_{bd} = F_{kbf} + F_{kbr} + F_{cbf} + F_{cbr} \tag{3.15}$$

$$\begin{aligned} m_{bd}\ddot{y}_{bd} &= -K_{sy}(y_{bd}-y_{bf})-K_{sy}(y_{bd}-y_{br})-C_{sy}(\dot{y}_{bd}-\dot{y}_{bf})-C_{sy}(\dot{y}_{bd}-\dot{y}_{br}) \\ &= -2K_{sy}y_{bd} + K_{sy}y_{bf} + K_{sy}y_{br} - 2C_{sy}\dot{y}_{bd} + C_{sy}\dot{y}_{bf} + C_{sy}\dot{y}_{br} \end{aligned} \tag{3.16}$$

The vehicle body yaw motion equation is

$$I_{bd}\psi_{bd} = F_{kbf}(-L) + F_{kbr}(L) + F_{cbf}(-L) + F_{cbr}(L) \tag{3.17}$$

$$\begin{aligned} I_{bd}\psi_{bd} &= -K_{sy}(y_{bd}-L\psi_{bd}-y_{bf})(-L)-K_{sy}(y_{bd}+L\psi_{bd}-y_{br})(L) \\ &\quad - C_{sy}(\dot{y}_{bd}-L\dot{\psi}_{bd}-\dot{y}_{bf})(-L)-C_{sy}(\dot{y}_{bd}+L\dot{\psi}_{bd}-\dot{y}_{br})(L) \\ &= -2K_{sy}L^2\psi_{bd} - K_{sy}y_{bf}L + K_{sy}Ly_{br} - 2C_{sy}L^2\dot{\psi}_{bd} - C_{sy}\dot{y}_{bf}L + C_{sy}L\dot{y}_{br} \end{aligned} \tag{3.18}$$

The linear model derived above from first principles was simulated in a curved track profile and compared to the responses from the non-linear Simpack model. The curve has a radius of 535 m, cant of 4° and the vehicle speed is 30 m/s. The profile transitions from straight to curved between 1 s and 3 s then back to straight between 7 s and 9 s as shown in Figure 3.12. Figures 3.16 and 3.17 show the lateral and yaw dynamics of a vehicle negotiating the curved track profile.

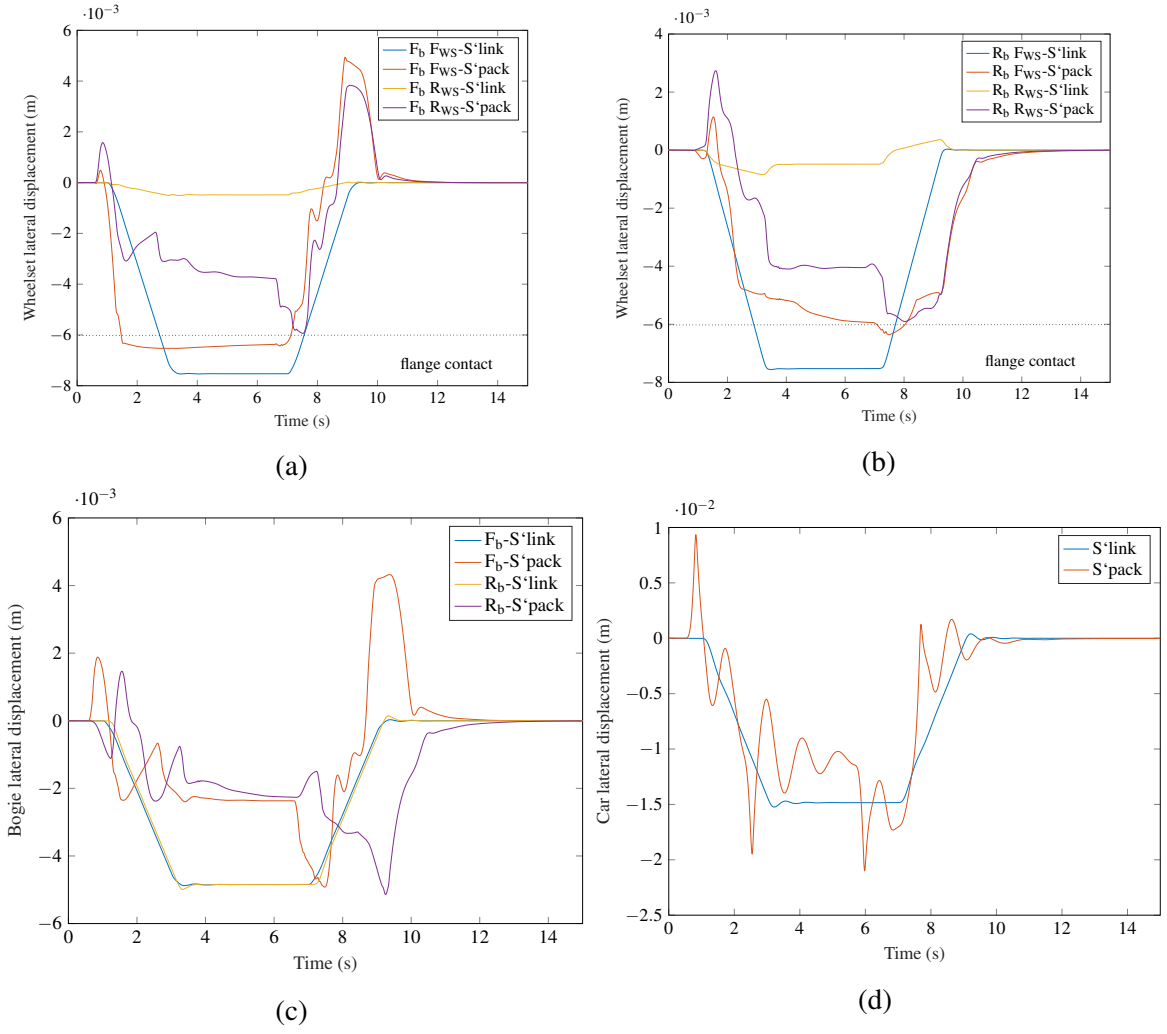

Figure 3.16: Wheelset, bogie and car body lateral displacements on a curved track with radius = 535 m, cant = 4° and vehicle speed = 30 m/s. The notations F_{WS}, R_{WS}, F_b and R_b used in the graph labels mean ‘front wheelset’, ‘rear wheelset’, ‘front bogie’ and ‘rear bogie’ respectively. ‘S’link’ and ‘S’pack’ denote the Simulink and Simpack models respectively, where the Simulink vehicle is a linear model developed from formulating equations of motion and the Simpack vehicle is non-linear.

As can be seen from the figures, there are significant differences in the responses during the transitions and the steady states. The poor correlation between the models is mainly due to the fact that the the wheel-rail contact region approaches the flange. There are also differences in the modelling of the suspension elements in the two models. For these reasons, system identification is used to develop the linear models which is discussed in the next section.

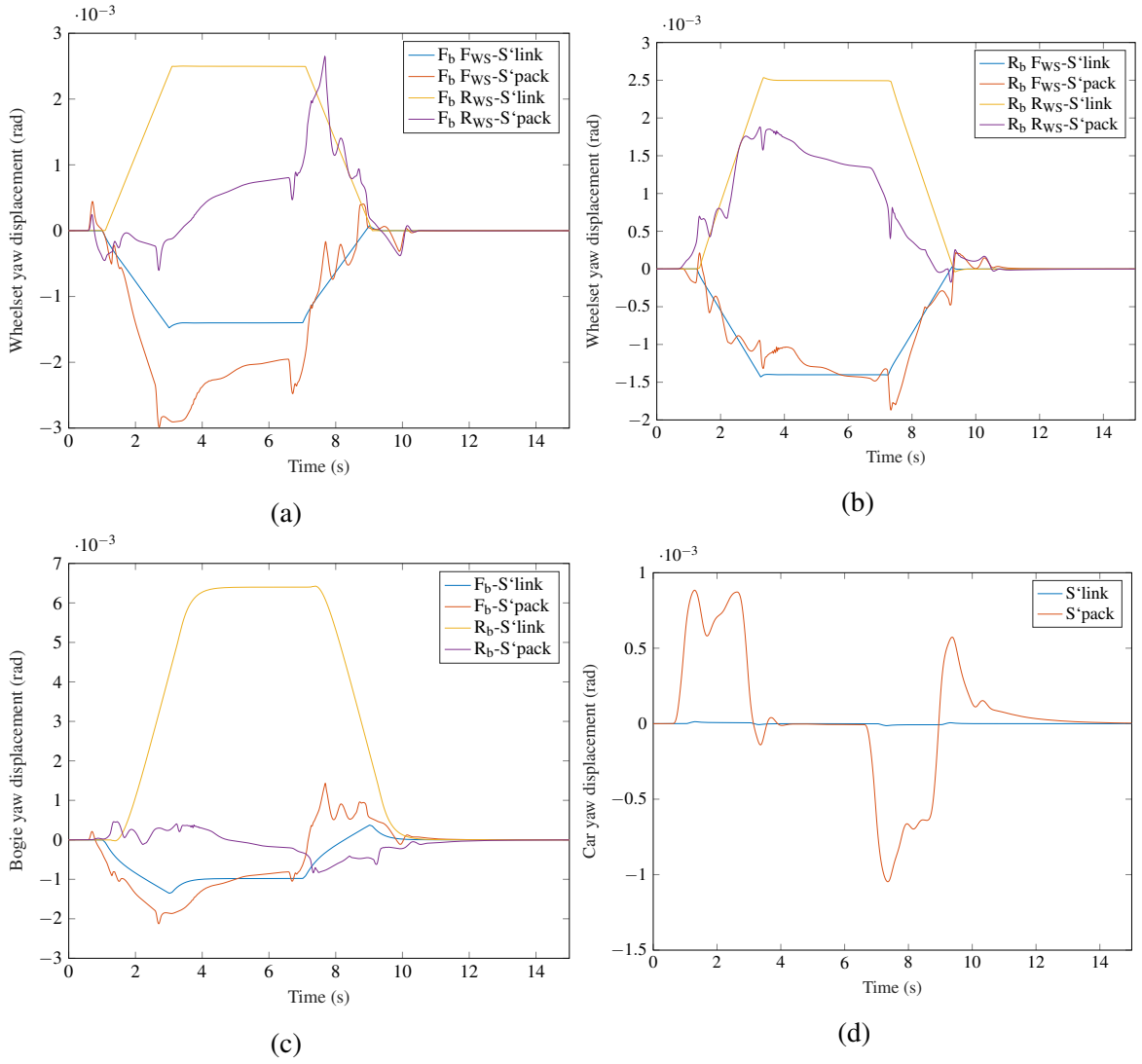

Figure 3.17: Wheelset, bogie and car body yaw angular positions on a curved track with radius = 535 m, cant = 4° and vehicle speed = 30 m/s. The notations F_{WS}, R_{WS}, F_b and R_b used in the graph labels mean ‘front wheelset’, ‘rear wheelset’, ‘front bogie’ and ‘rear bogie’ respectively. ‘S’link’ and ‘S’pack’ denote the Simulink and Simpack models respectively, where the Simulink vehicle is a linear model developed from formulating equations of motion and the Simpack vehicle is non-linear.

3.3.2 System identification

System identification gives a model based on input and output signals and is preferred for its ease of applicability where the signals can be easily measured. All of the estimated models are linear AutoRegressive eXogenous (ARX) models which means that the model relates the output to past values of the output and present and past values of the input. This is a black-box approach where the system dynamics are unknown. Other black-box model structures could be used which are usually more complex than the ARX model and useful for noisy data. However, in this case the data is not noisy and a simple ARX model was sufficient to give a good linear model. The ARX models are generated using MATLAB/ Simulink and have the following general form

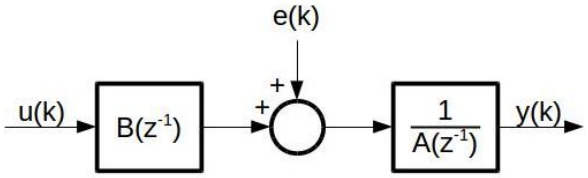

Figure 3.18: General ARX model

$$A(z)y(k) = B(z)u(k-n) + e(k) \tag{3.19}$$

where u(k) is the system inputs, y(k) is the outputs, e(k) is the disturbance at the k^{th} sample point. n is the delay, A(z), B(z) are the polynomials as a function of the delay operator z^{-1}.

$$A(z^{-1}) = 1 + a_1 z^{-1} + ... + a_n z^{-n}$$

$$B(z^{-1}) = b_1 z^{-1} + b_2 z^{-2} + ... + b_m z^{-m}$$

For applying system identification the rail vehicle is run in Simpack on a straight track with no stochastic disturbances and a small input force/ torque is applied to excite the system dynamics. The input force/ torque is a pulse signal, the amplitude of which is chosen to be high enough to excite the system while maintaining the wheel-rail contact non-linearities to a minimum. The pulse is applied in both directions in order that the model does not settle on the flanges to keep non-linearities to a minimum. A small pulse width of 0.25 s is chosen to accentuate the higher frequencies to get a better estimated system. The output signal is the resulting creep force or wheelset lateral displacement.

Once the model is identified, the correlation of the linear model response to the non-linear model is assessed by calculating the coefficient of determination or R^2, which is calculated as

$$R^2 = 1 - \frac{\sum_{i=1}^{n}(y_i - \hat{y}_i)^2}{\sum_{i=1}^{n}(y_i - \bar{y})^2} \tag{3.20}$$

where y_i is the observed data with n values $y_1, y_2, ..., y_n$, $\hat{y}_i$ are the estimated values, and $\bar{y}$ is the mean of the observed data. The R^2 values tend to unity as the fit of the estimated values to the observed data improves. The R^2 values are converted to a % and a value of 90 % is set as the threshold above which the dominant dynamics are captured to give a linear estimated model that behaves similarly to the Simpack model. The linear models are then used to design controllers which are implemented on the nonlinear Simpack 'simulation' models. Figure 3.19 illustrates this system identification process.

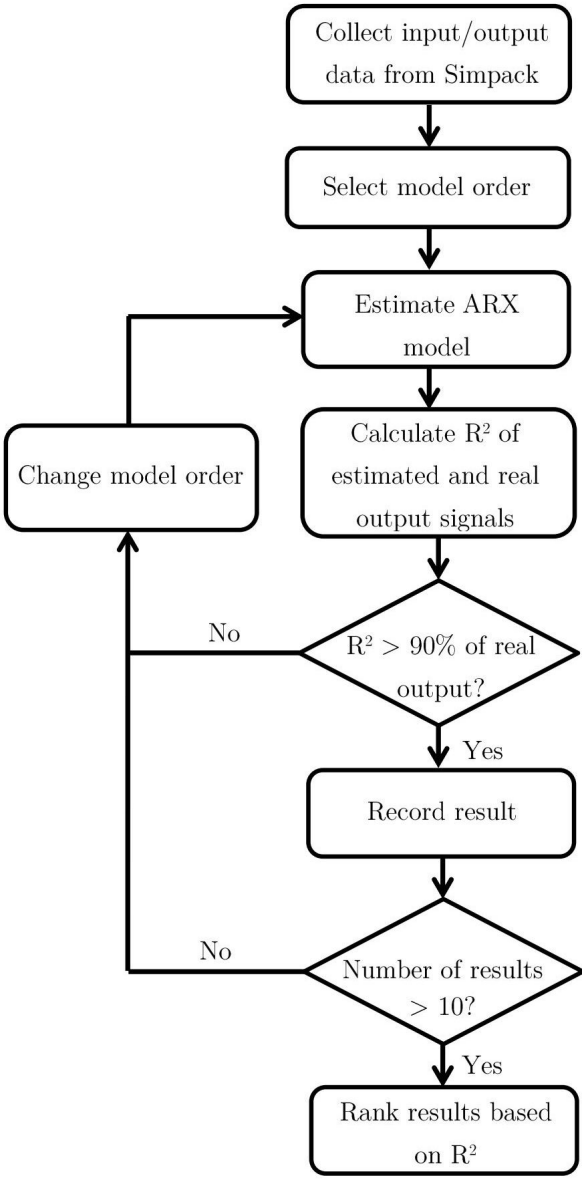

Figure 3.19: The system identification process

SYC

For the SYC configuration the input is a torque pulse of amplitude 10 kNm from the vehicle body to the front bogie. The output is the difference between the lateral creep forces at the front and rear wheelsets of the front bogie. Table 3.2 shows the R^2 metric of identified models with different orders, na and nb are the number of denominator and numerator coefficients respectively of the estimated transfer functions, nc is the delay from the input to the output.

Table 3.2: Candidate SYC linear models from system identification

na	nb	nc	$R^2\%$
8	8	2	93.84
8	8	1	93.86
10	8	2	94.07
9	8	2	94.09
10	8	1	94.45
10	9	0	94.46
10	9	1	95.23
9	9	1	95.25
9	9	2	95.42
10	9	2	95.44

The estimated model chosen is a tenth order system with na=10, nb=9 and nc=1. This was chosen because it was the model which showed the highest R^2 metric with a strictly proper transfer function and delay of one sample time. With more delay the increase in R^2 is marginal. The transfer function of the estimated model is

$$G(z) = \frac{0.04616z^{-1} + 0.03352z^{-2} - 0.0111z^{-3} - 0.07599z^{-4} + 0.01116z^{-5} - 0.0454z^{-6}}{1 - 2.004z^{-1} + 1.332z^{-2} - 0.3859z^{-3} + 0.05019z^{-4} - 0.05362z^{-5} + 0.03737z^{-6}} \cdots \\ \frac{0.009797z^{-7} + 0.001171z^{-8} + 0.03093z^{-9}}{0.2132z^{-7} - 0.3653z^{-8} + 0.2593z^{-9} - 0.06283z^{-10}} \tag{3.21}$$

The estimated response has an R^2 metric of 95.23 %. Figure 3.20 shows the input torque and the resulting responses from the 'observed' Simpack model and the 'estimated' ARX model. The error is calculated as the difference in the two model responses and has a peak of 2kN which is very small compared to a peak of 10 kN in the model response. The correlation is considered to be good enough for the purpose of controller design. The frequency response of the system is shown in the Bode plot in Figure 3.21. The response is that of a non-minimal phase system. There are two positive zeros outside the unit circle, both of which are at 78.6 Hz.

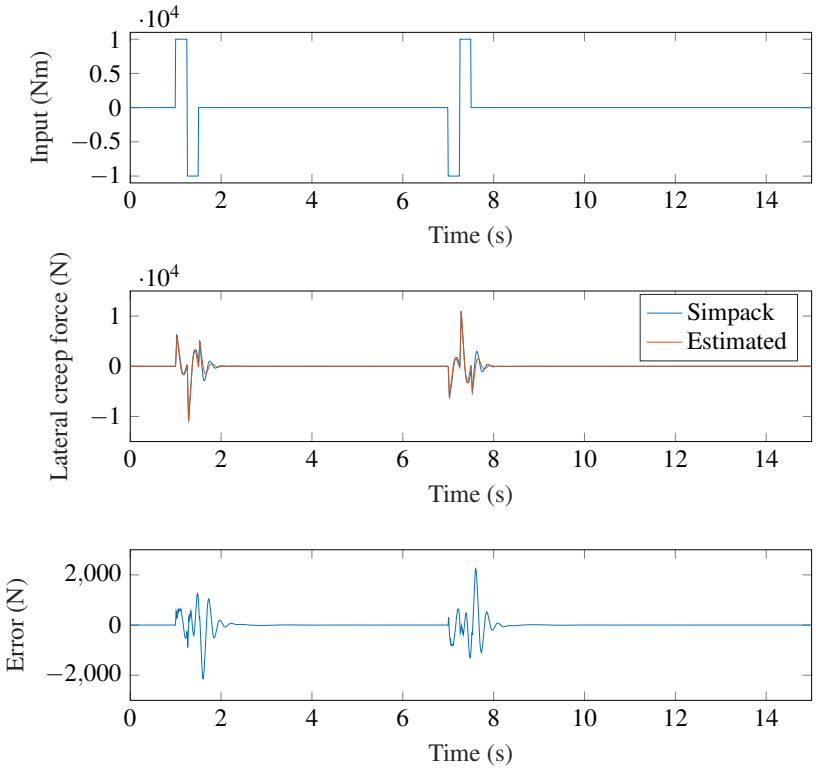

Figure 3.20: System identification applied to the SYC model

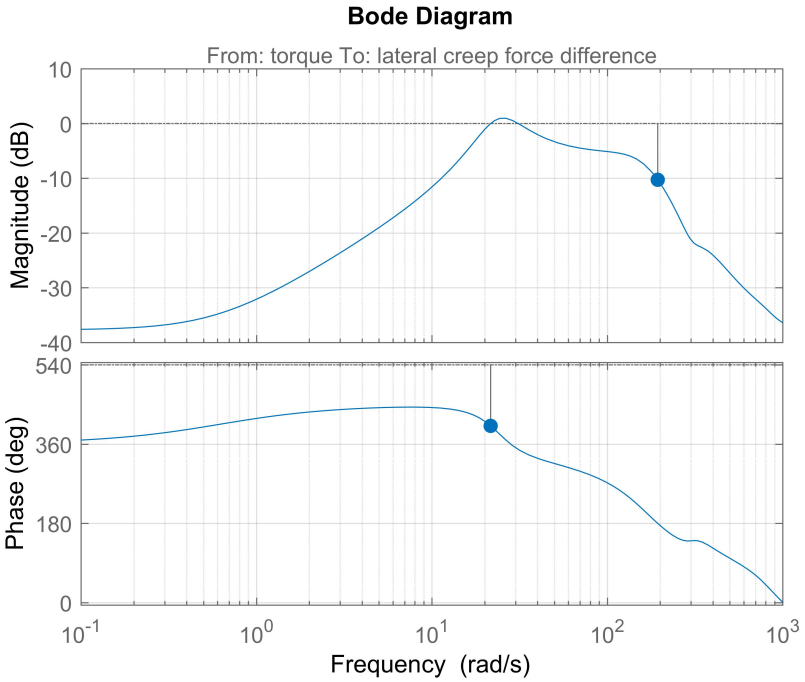

Figure 3.21: Frequency response of the linear SYC model

ASW

To apply system identification in the ASW configuration, the input is a longitudinal force pulse of amplitude 10 kN applied from the left actuator of the front wheelset to the front bogie. The output is the longitudinal creep force of the front wheelset. Table 3.3 shows the R^2 metric of identified models with different orders where na and nb are the number of denominator and numerator coefficients respectively. nc is the delay from the input to the output.

Table 3.3: Candidate ASW linear models from system identification

na	nb	nc	$R^2\%$
1	1	1	90.43
1	1	0	90.82
4	1	0	92.56
3	1	0	92.67
4	2	0	92.91
3	2	0	93.04
3	3	1	95.31
4	4	0	95.55
4	3	1	95.75
4	4	1	95.83

The estimated system is fourth order with na=4, nb=3, nc=1. This was chosen because it was the model showing the highest R^2 value with a strictly proper transfer function and a delay of one sample time. Most real systems have some delay and therefore an nc value of 0 is not realistic.

The identified model has the following transfer function

$$G(z) = \frac{0.742z^{-1} - 1.331z^{-2} + 0.636z^{-3}}{1 - 1.635z^{-1} + 1.032z^{-2} - 0.3843z^{-3} - 0.0441z^{-4}} \tag{3.22}$$

The estimated response has an R^2 metric of 95.75%. The input force, observed and estimated system responses and the error between them are shown in Figure 3.22. As can be seen, the error is small compared to the amplitude of the observed response. The frequency response of the system is shown in the Bode plot in Figure 3.23.

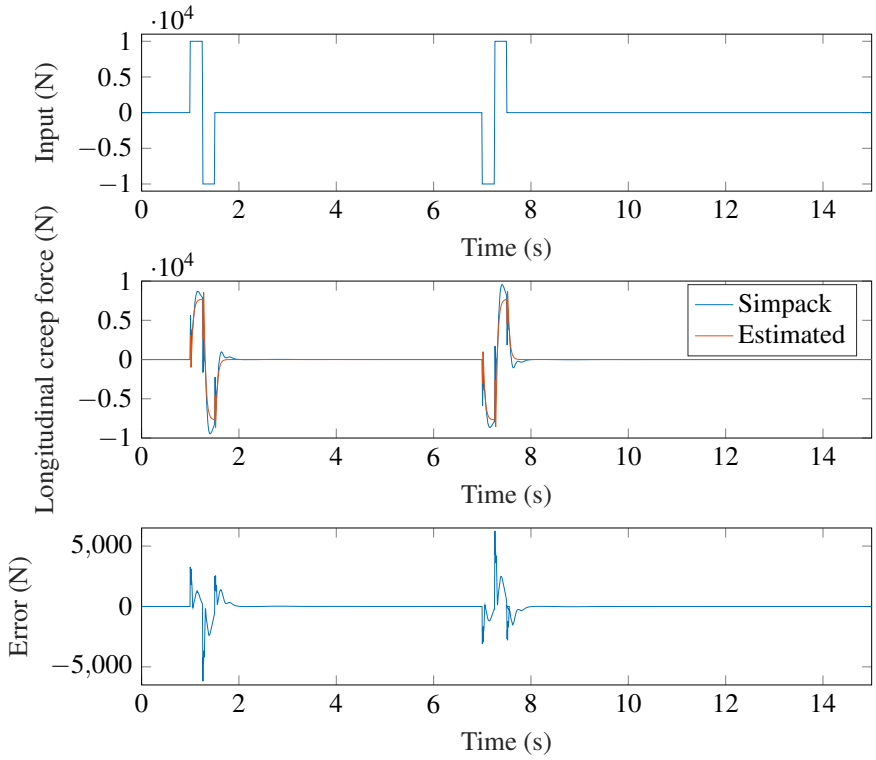

Figure 3.22: System identification applied to the ASW model

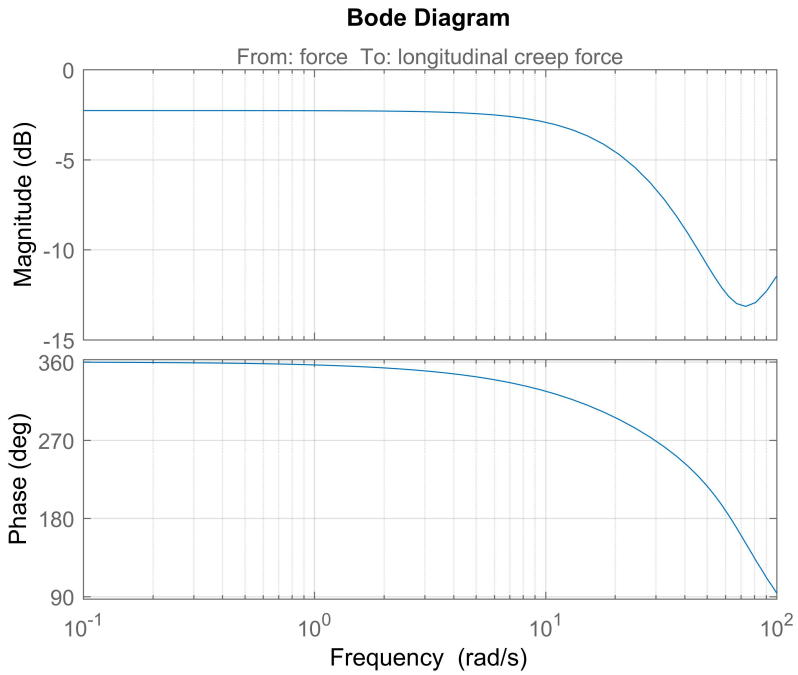

Figure 3.23: Frequency response of the linear ASW model

DIRW

For the DIRW configuration, the input is a motor torque pulse of amplitude 200 Nm applied to the right wheel of the front wheelset of the front bogie. The output is the lateral displacement of the front wheelset. If the input torque is applied to both wheels, the amplitude of the output displacement is doubled but is the same otherwise. So only a single-input single output (SISO) system with a single wheel torque is estimated for simplicity. However, such a SISO system identification also assumes that each wheelset is decoupled from the others, which is not strictly true. In reality, the cross-coupling means that it is a multiple-input multiple output (MIMO) system which can be expressed in matrix form as

$$\begin{bmatrix} y_1 \\ y_2 \\ y_3 \\ y_4 \end{bmatrix} = \begin{bmatrix} T_{y1F1} & T_{y1F2} & T_{y1F3} & T_{y1F4} \\ T_{y2F1} & T_{y2F2} & T_{y2F3} & T_{y2F4} \\ T_{y3F1} & T_{y3F2} & T_{y3F3} & T_{y3F4} \\ T_{y4F1} & T_{y4F2} & T_{y4F3} & T_{y4F4} \end{bmatrix} \begin{bmatrix} F_1 \\ F_2 \\ F_3 \\ F_4 \end{bmatrix}$$

where the y terms denote the lateral displacement outputs, F denotes the torque inputs and T is a transfer function describing the relationship between a particular input and output. So for example the front wheelset lateral displacement can be expressed as

$$y_1 = T_{y1F1}F_1 + T_{y1F2}F_2 + T_{y1F3}F_3 + T_{y1F4}F_4 \tag{3.23}$$

In order to establish the cross-coupling between the lateral displacements of different wheelsets, a motor torque excitation was applied to each wheelset in the Simpack model and the resultant corresponding wheelset lateral displacements were observed. Figure 3.24 shows the lateral displacement of the front wheelset when a torque is applied to each wheelset individually. The 'true' value of y_1 according to equation 3.23 is shown in green and the 'assumed' value from assuming no cross-coupling is shown in blue. The 'error' graph is plotting the difference between the 'true' and 'assumed' values. The red, yellow and purple lines show the y_1 response when torques are applied to the rear wheelset of the front bogie, and front and rear wheelsets of the rear bogie respectively. As can be seen from the figure, the coupling is particularly high between two wheelsets on the same bogie as may be expected. However, considering only the diagonal terms to design a controller works because the lateral dynamics of both wheelsets on a bogie are largely similar. So a controller designed considering only one wheelset is able to cope with the addition of the off-diagonal terms because the additional coupling terms don't oppose the control action.

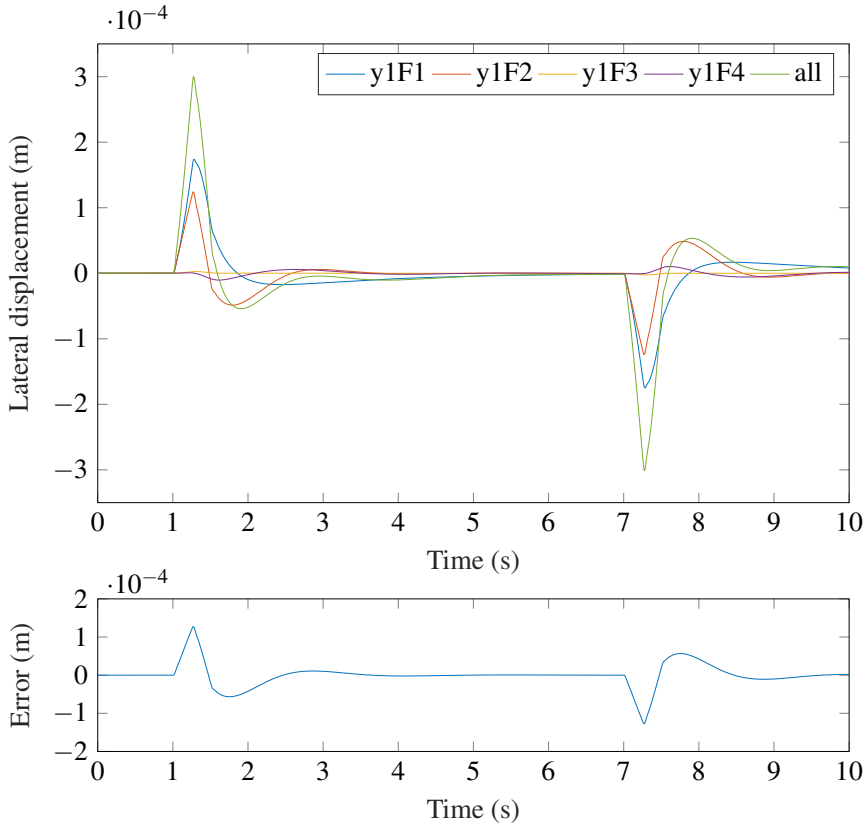

Figure 3.24: The notations ‘y1F1’, ‘y1F2’, ‘y1F3’ and ‘y1F4’ used in the graph labels are used to denote the lateral displacement of the front wheelset y_1 when a torque is applied to the each wheelset of the rail vehicle individually. So ‘F1’ for example denotes a torque applied to the front wheelset of the front bogie. The label ‘all’ is the response of y_1 calculated according to equation 3.23. The error signal is the difference between the green and blue lines.

For this reason, only a SISO model is identified. Table 3.4 shows the R^2 metric of identified models with different orders where na and nb are the number of denominator and numerator coefficients respectively. nc is the delay from the input to the output.

The estimated system selected is a sixth order model with na=6, nb=5 and nc=1. This model was chosen because it is strictly proper and has a delay of one sample time. The transfer function of the model is

$$G(z) = \frac{1.489e-10z^{-1} - 1.416e-09z^{-2} + 4.432e-10z^{-3} - 1.237e-09z^{-4}}{1 - 2.621z^{-1} + 2.016z^{-2} - 0.1192z^{-3} - 0.065z^{-4} - 0.4573z^{-5}} \cdots \\ \frac{+1.785e-09z^{-5}}{-0.2472z^{-6}} \tag{3.24}$$

Table 3.4: Candidate DIRW linear models from system identification

na	nb	nc	$R^2\%$
6	6	1	92.94
7	4	2	92.96
6	5	1	92.97
6	4	2	93.03
6	5	2	93.09
7	5	2	93.41
7	7	2	93.53
7	7	1	93.60
6	6	2	93.83
7	6	2	93.90

The estimated response has an R^2 metric of 92.97%. The estimated model response is considered to have a good enough correlation to the observed model response for the purpose of controller design. The input torque, model responses and resulting error is illustrated in Figure 3.25. The frequency response of the system is shown in the Bode plot in Figure 3.26.

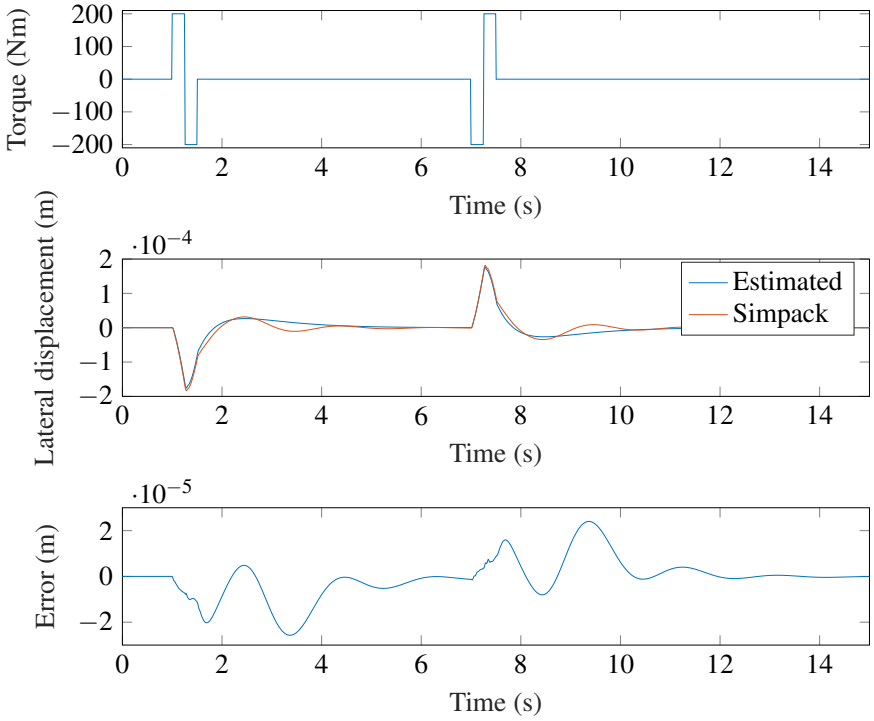

Figure 3.25: System identification applied to the DIRW model

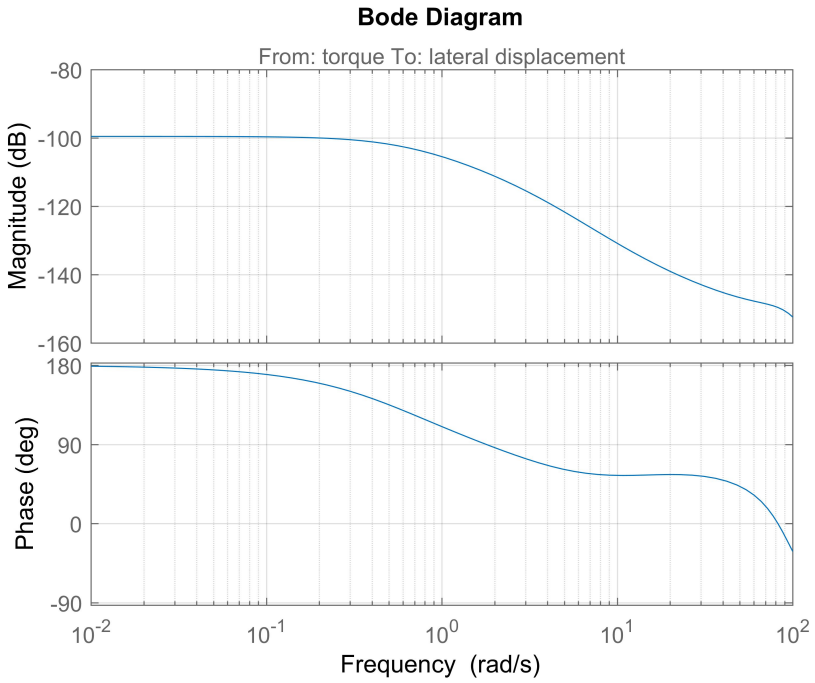

Figure 3.26: Frequency response of the linear DIRW model

3.4 Conclusions

This chapter explained the vehicle modelling process of the conventional passive vehicle and the SYC, ASW and DIRW active vehicles in Simpack. These vehicles are non-linear and while they are a good representation of a real rail vehicle, they cannot be used to analyse the frequency response of the system because of their non-linearity. Almost all model-based control design methods are applicable mainly to linear models. For this reason, linear models were developed first using first principles in Simulink. However, the model didn't have a good fit to the Simpack model, almost certainly due to the non-linearities becoming more significant as the wheel-rail contact region approaches flanges. System identification was used to develop linear models for each of the three active vehicles and this process is discussed in this chapter. These models show a good correlation to the non-linear Simpack model. The next chapter uses the frequency analysis of these linear models to design controllers. The controller design process is also covered in detail in the next chapter.

Chapter 4

Controller design

This chapter explains the design methodology for the controllers in the Secondary Yaw Control (SYC), Actuated Solid-axle Wheelset (ASW) and Driven Independently-Rotating Wheelset (DIRW) mechanisms. The controllers are designed in Simulink using time and frequency-based methods on the linear models developed in the previous chapter. The controllers in Simulink are then run in co-simulation with the non-linear Simpack models to analyse the time responses.

Two sets of controllers are developed for each active steering mechanism in order to present a logical case for the choice of controller used finally in the track switch simulations in Chapter 6. One set is that of classical controllers such as proportional integral (PI) or phase advance (PA) which deal with linear time invariant single-input single-output systems. Classical controllers are chosen for their simplicity and practicability. The other set is a more advanced proportional integral plus (PIP) control. A PIP controller is chosen as it allows state variable feedback where all the states depend only on the present and past inputs and outputs of the system. Therefore they are directly measurable unlike a state-space form which may require observers for unmeasurable states. A PIP controller should theoretically give a better performance than the classical controller because it uses state-feedback [94]. So although both controllers are constrained by only the input and output signals and no internal states, they differ in the complexity of the control algorithms.

4.1 Design requirements

In order to design controllers, it is first necessary to establish the requirements. In the frequency domain, gain and phase margins are used to assess the system stability. The gain margin (GM) is a measure of how much the gain can be increased before the system reaches the point of critical stability. Likewise, the phase margin (PM) is the additional phase lag that

the system can tolerate before it becomes unstable. These margins are an indication of the robustness of the controller against parametric variations, system non-linearities or external disturbances as will be the case in application. They also indicate whether the controller gains can be increased to improve the system performance. Small margins mean that the controller is fragile and could easily become unstable. The GM and PM can be easily measured from a Bode, Nichols or Nyquist plot. The GM is calculated as the value in dB by which the system magnitude must be increased to reach 0 dB when the phase is 180°. PM is calculated as the phase lag required to make the system phase 180° when the gain is 0 dB.

There are few references in the literature for acceptable values of gain and phase margins, however typical examples use a GM greater than 6 dB and a PM greater than 60° [95]. These margins are used as the design requirements in the frequency domain for all the controllers designed in this chapter. The use of these margins is justified on the basis that changes in parameters such as vehicle speed do not alter the frequency response significantly. The margins can usually cope with such variations. In order to establish how the frequency response of the models change at different vehicle speeds, the Simpack model was run at four different speeds of 20 m/s, 30 m/s, 40 m/s and 50 m/s. Linear ARX models were identified through system identification for each case. The transfer functions of the models can be found in Appendix A. Figures 4.1, 4.2 and 4.3 show the variation in the Nichols plot of the linear SYC, ASW and DIRW models respectively at the different vehicle speeds.

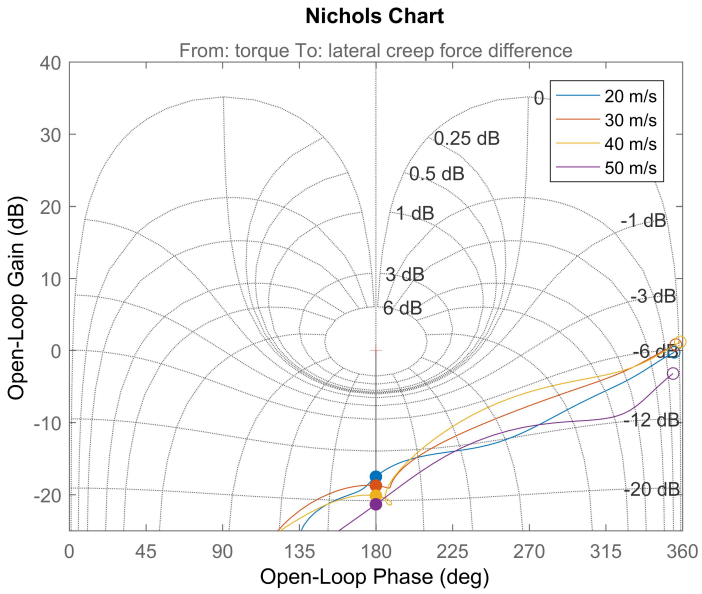

Figure 4.1: Nichols plot of the linear SYC model at different vehicle speeds.

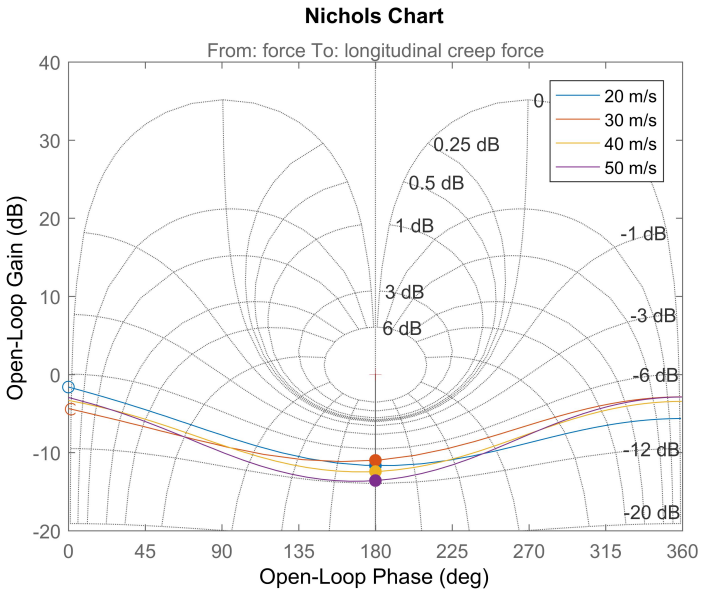

Figure 4.2: Nichols plot of the linear ASW model at different vehicle speeds.

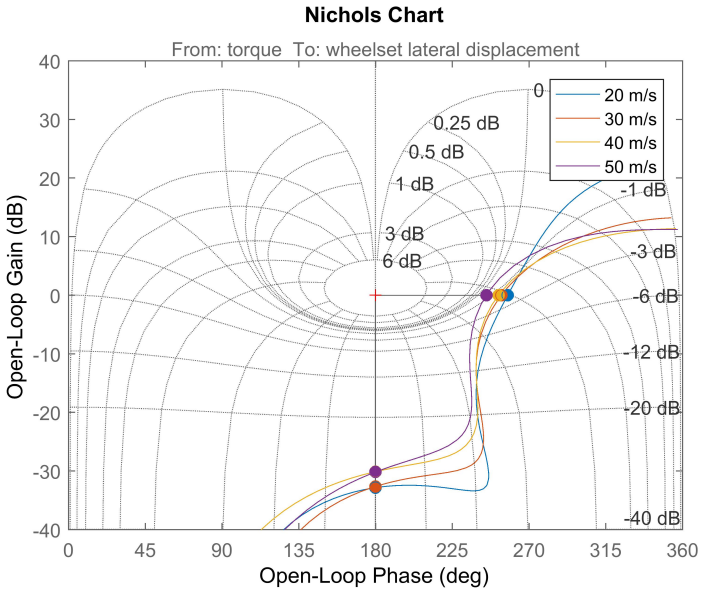

Figure 4.3: Nichols plot of the linear DIRW model at different vehicle speeds

From the figures it can be seen that the GM of the uncompensated open loop response of the SYC model varies from 17.5 dB at 20 m/s to 21.3 at 50 m/s which is a variation of 3.8 dB while the PM is infinity. For the ASW vehicle, the GM variation is 2.6 dB from 11 dB at 20 m/s to 13.6 dB at 50 m/s while the PM is infinity. The uncompensated open loop response of the DIRW model is from the motor torque in kNm to the wheelset lateral displacement in

millimeters. The DIRW model frequency response varies from a GM of 32.6 dB and a PM of 77.5 degrees at 20 m/s to a GM of 30.1 dB and a PM of 64.9 degrees at 50 m/s. So it can be seen that these variations are less than the 6 dB GM and 60 degrees PM design requirements, which suggests that these requirements are sufficient to cope with some changes in the model.

In the time domain, there should be minimal steady state error. The overshoot requirement is less than 10 % of the final value. The rise time is calculated as the time taken to go from 10 % to 90 % of the final value. The settling time is calculated as the time taken to reach within 2 % of the final value from the instant the step input occurs. From the system bandwidths in Tables 4.1 and 4.3, it can be seen that the SYC vehicle bandwidth is ≈ 0.1 Hz and that of the ASW and DIRW vehicles are ≈ 1 Hz, which are indicative of slow reacting systems. Therefore a rise time and a settling time of 1 s and 5 s are set as the requirements.

4.2 Classical controller design

Classical controllers typically have a combination of proportional, integral or derivative action. The simplest form is having only a proportional gain which vertically shifts the frequency response of the system on a Nichols plot. However, an integral action is usually needed to remove steady-state errors which works by increasing the gain at low frequencies. A proportional integral (PI) controller has two tunable parameters, a gain K and an integrator time constant τ to influence the integral action. $\tau = 1/\omega$ where omega is the break frequency below which the gain is higher than K and above which it is equal to K. This means that when the system is at a steady state at low frequencies the high gain removes any errors. The PI controller has the following transfer function.

$$K(s) = \frac{K(1+\tau s)}{\tau s} \tag{4.1}$$

Integral action has the problem of introducing phase lag into the system which makes the system response much slower and in extreme situations makes the system unstable. Adding a simple derivative term increases the phase but also introduces high gain at high frequencies and therefore amplifies sensor noise in the feedback signals. A phase advance (PA) controller however, introduces the derivative action only at the desired frequency to change the phase margin whilst constraining the gain at higher frequencies. The PA controller has the following transfer function where K_{pa} is the proportional gain, K_{ratio} is the phase advance ratio and τ_l is the phase lag time constant.

$$K(s) = \frac{K_{pa}(1+K_{ratio}\tau_l s)}{1+\tau_l s} \tag{4.2}$$

For the SYC steering, a PI controller is chosen to remove any low frequency error signals. The feedback is the difference between the lateral creep forces of the front and rear wheelsets in each bogie. A schematic of the SYC control mechanism is shown in Figure 4.5.

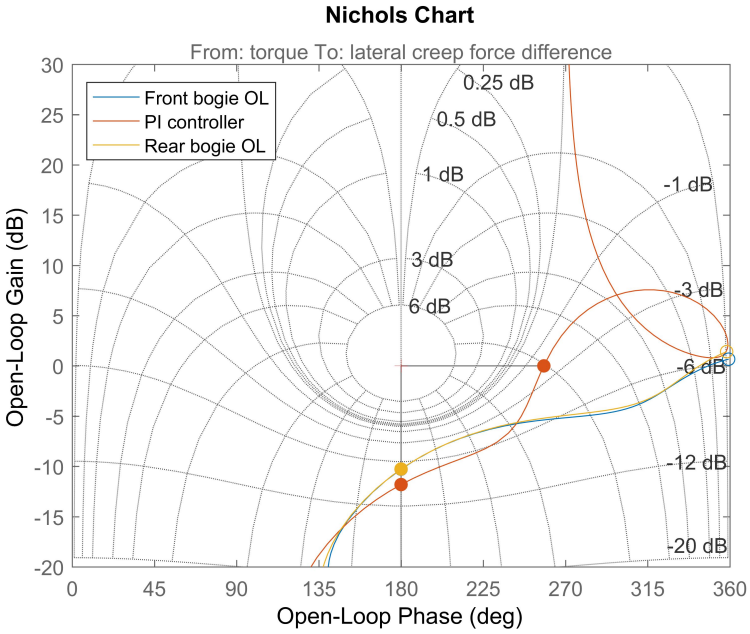

Figure 4.4: Nichols plot for PI controller design for SYC configuration

Figure 4.4 shows the open loop frequency response of both the front and rear bogies. The system identification process explained in the previous chapter was used again to identify a model of the lateral creep force difference of the front and rear wheelsets of the rear bogie from a torque applied to the rear bogie. It can be seen clearly from the figure that the frequency responses of both bogies are very similar. For this reason, only one PI controller is designed. The open loop frequency response with the PI controller is also shown in the figure. The controller is given a zero demand signal, to equalise the lateral creep forces at the front and rear wheelsets of each bogie. As can be seen from the figure, the PI controller adds integral action at low frequencies to remove steady-state errors.

A proportional gain K of 0.5 Nm/N and integrator time constant τ value of 0.01 s changes the GM to 11.8 dB and the PM to 78.1° as listed in Table 4.1. Theoretically, the gain could be increased more. However, doing so increases the control force required to levels of over 200 kN per actuator which are difficult to realise in practice.

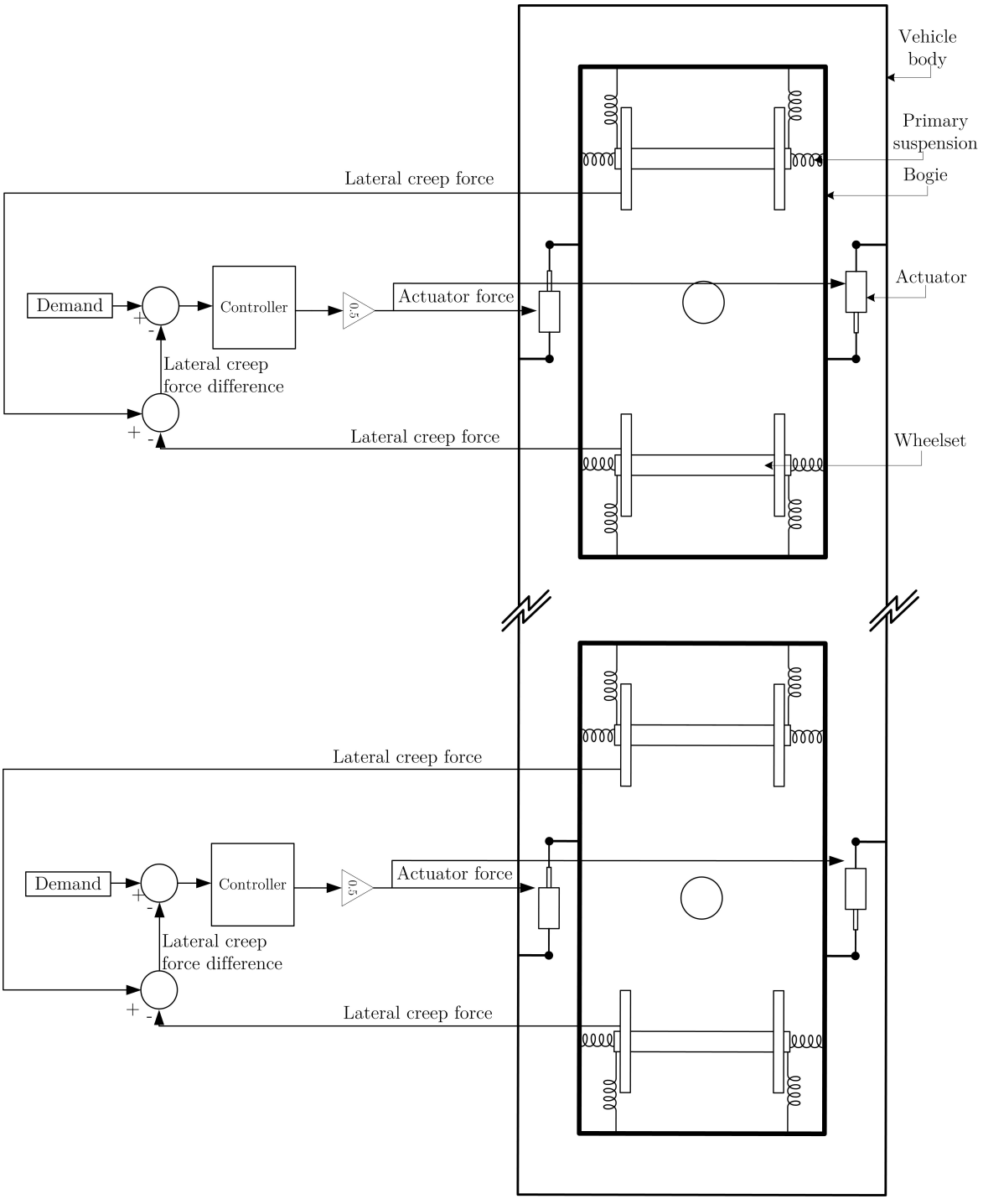

Figure 4.5: Schematic of the SYC control mechanism

The controller for the ASW vehicle is also a PI controller with a K value of 0.7 N/N and a τ value of 0.1 s. The wheelset longitudinal creep forces are used as the feedback signal. The aim is to reduce them to zero. A schematic of the ASW control mechanism is shown in Figure 4.7. Figure 4.6 shows the open loop frequency response of all the four wheelsets of the vehicle. The model for each wheelset was identified using system identification from input force to the output longitudinal creep force. This is explained in detail in the previous chapter. From the figure it can be seen that the frequency response of all the wheelsets are very similar. So only one PI controller is designed and applied to all the wheelsets.

The open loop frequency response with the PI controller is also shown in Figure 4.6. From the figure it can be seen that the PI controller increases the gain at low frequencies. The controller gains are not increased further so that the demand force does not exceed ≈80 kN per actuator.

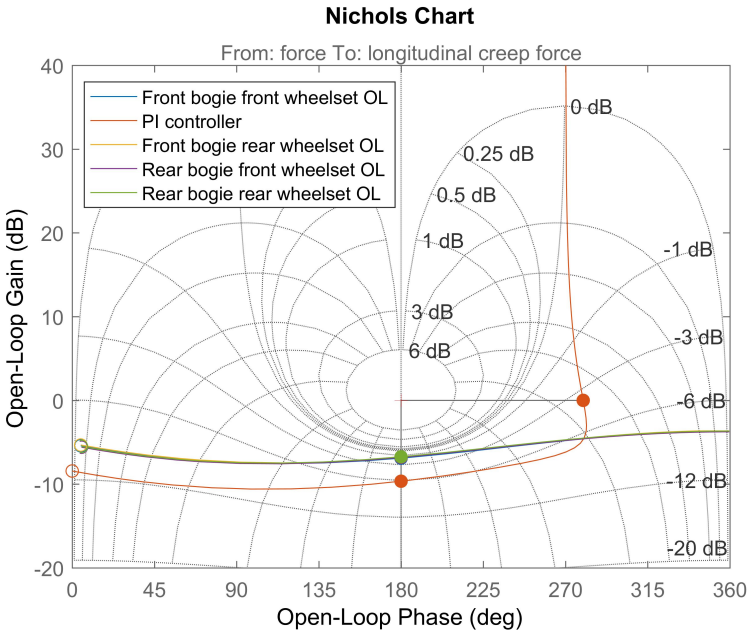

Figure 4.6: Nichols plot for PI controller design for ASW configuration

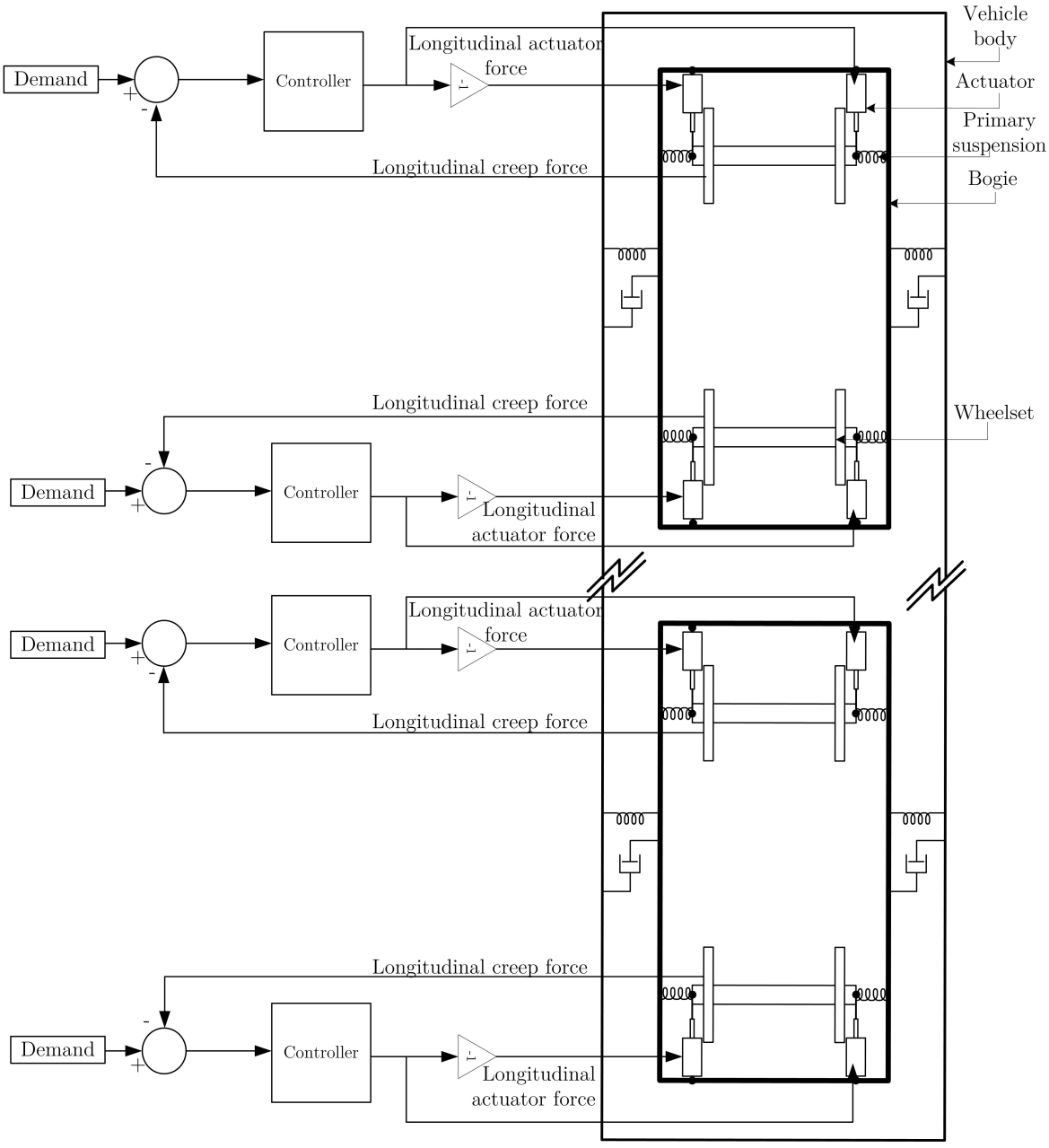

Figure 4.7: Schematic of the ASW control mechanism

For the DIRW configuration, a phase advance plus integral controller was chosen to overcome phase lag in the system and introduce more proportional gain without compromising stability. The integrator removes steady-state errors. The feedback signal is the wheelset lateral displacement and the control effort aims to reduce this to zero. A schematic of the DIRW control mechanism is shown in Figure 4.9.

Figure 4.8 shows the open loop frequency response of the four wheelsets of the DIRW vehicle. The uncompensated open loop is plotted from the motor torque in kNm to the wheelset lateral displacement in millimeters. The model for each wheelset was developed by identifying a system from an input torque to the relevant wheelset to the corresponding output wheelset lateral displacement. The frequency response of both wheelsets on the same bogie are very similar. However, the response of wheelsets on the front and rear bogies are slightly different. The uncompensated open loop gain margin is the same for all wheelsets at ≈ 29.6 dB. The phase margin of the front bogie wheelsets is ≈ 66.1 degrees and that of the rear bogie wheelsets is ≈ 86.8 degrees. This difference is not considered to be significant and therefore only one controller is designed for all four wheelsets.

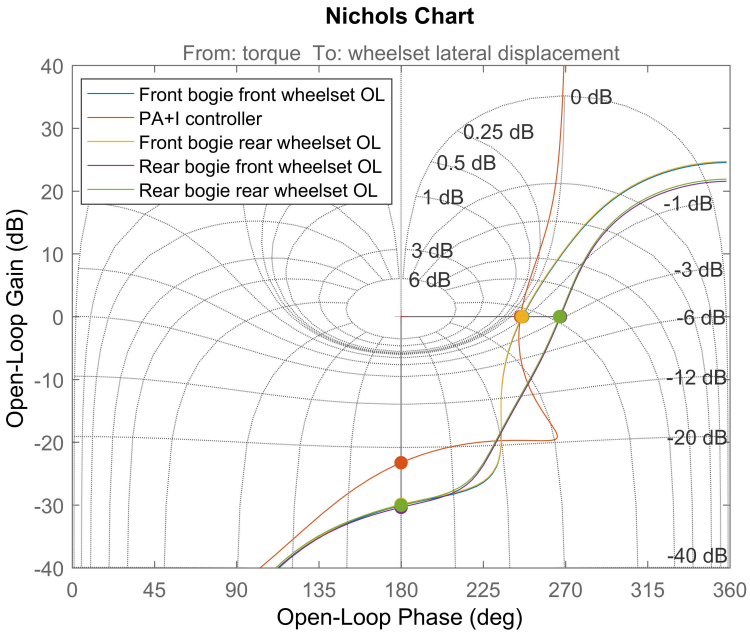

Figure 4.8: Nichols plot for PA+I controller design for DIRW configuration.

The K_{pa}, K_{ratio}, τ_l and τ values were selected to be $1.2 \times 10^6 N/m, 6$, $2.5 \times 10^{-3} s$ and 3 s respectively. Figure 4.8 shows the open loop Nichols plot with the controller in the DIRW configuration. The PM of the DIRW configuration with the PA+I controller is 65.4 deg which is relatively low compared to the other two models, however it is still well within the PM design requirement of 60 degrees. Changing the controller gains to increase the PM worsens the creep force response of the model.

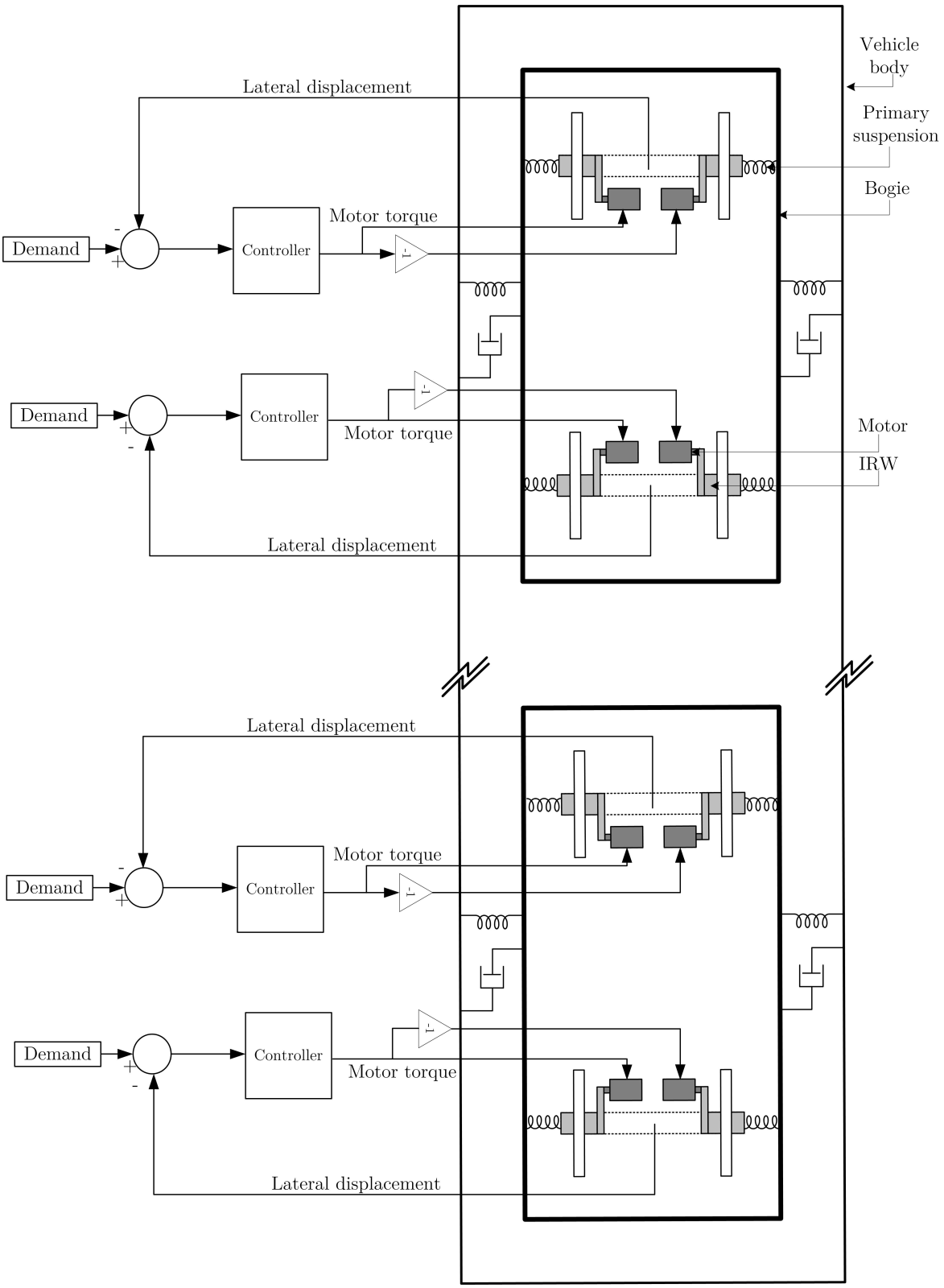

Figure 4.9: Schematic of the DIRW control mechanism

Table 4.1 lists the stability margin and closed loop system bandwidth values for each of the active steering methodologies. As can be seen, all the vehicles satisfy the GM and PM design requirements.

Table 4.1: System bandwidth and stability margins

	GM (dB)	PM (deg)	Bandwidth (Hz)
SYC	11.8	78.1	0.07
ASW	9.65	101	1.07
DIRW	22.4	65.4	1.16

Figures 4.10 and 4.11 show the closed loop step response obtained from applying the PI controllers on the SYC and ASW linear models in Simulink. The PA+I controller implemented on the linear DIRW model in Simulink gives the step response shown in Figure 4.12.

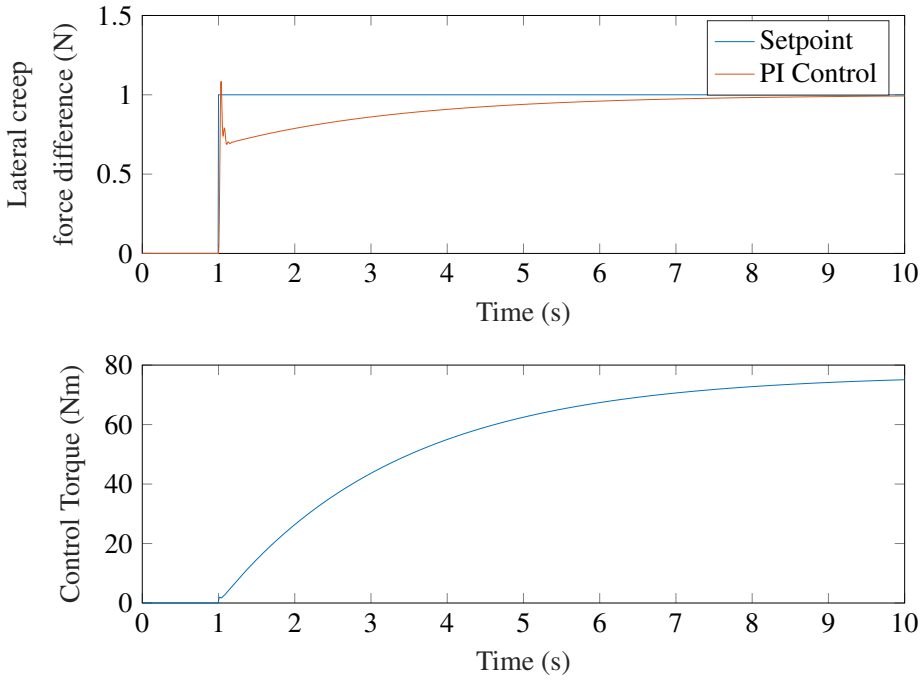

Figure 4.10: Closed loop response of PI control applied to the SYC model

The key performance metrics from the closed loop step responses using the classical controllers are listed in Table 4.2. There was no steady state error in any of the responses. From the table it can be seen that the overshoot and rise time requirements are satisfied for all the three vehicle controllers. The SYC settling time however is higher than the requirement of 5 s while the ASW and DIRW settling times are well within the requirement.

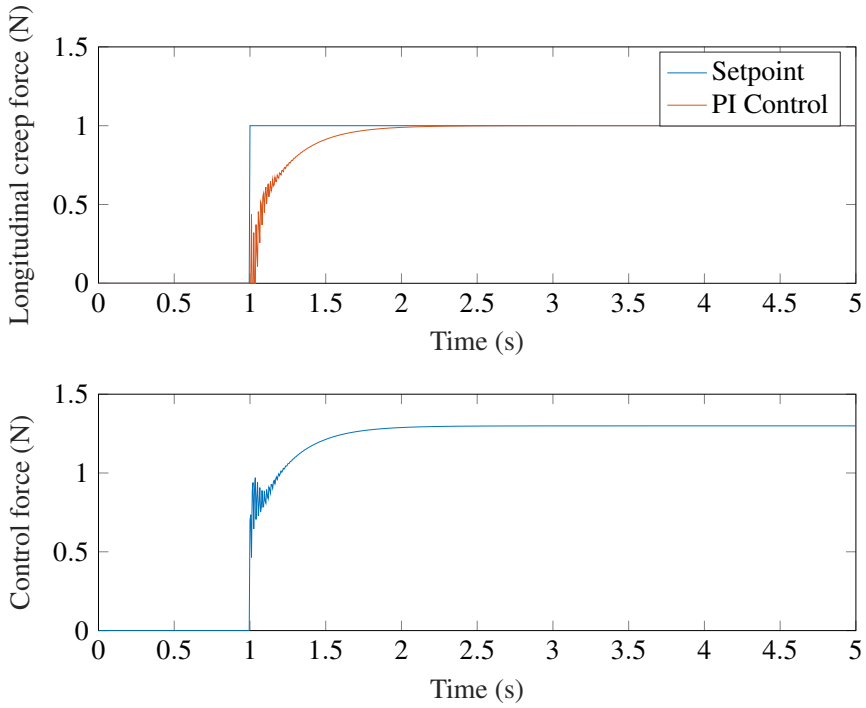

Figure 4.11: Closed loop response of PI control applied to the ASW model

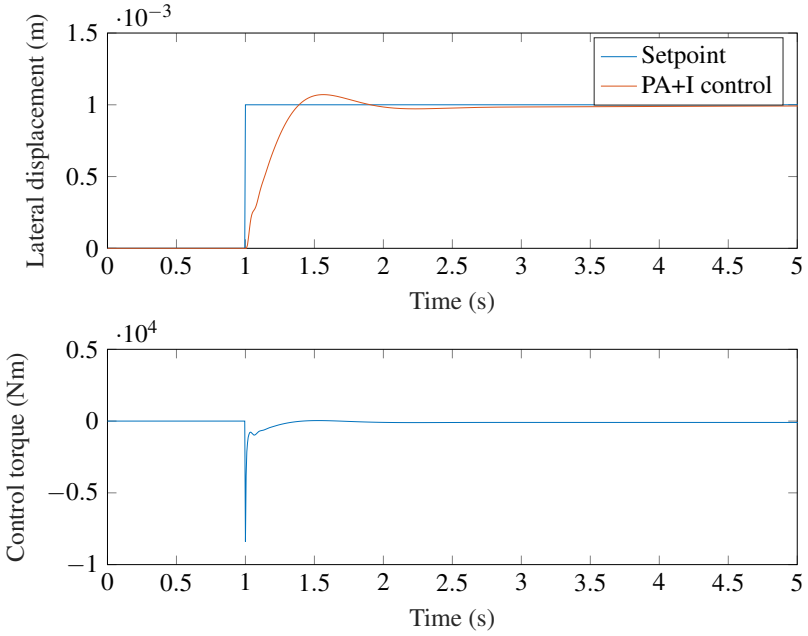

Figure 4.12: Closed loop response of PA+I control applied to the DIRW model

Table 4.2: Time domain performance from applying classical controllers.

	Rise time (s)	Settling time (s)	Overshoot (%)
SYC	0.01	6.64	8.5
ASW	0.42	1	0
DIRW	0.305	1.035	7.2

4.3 PIP controller design

The PIP control system was introduced by Young et al [94]. It requires a non-minimal state space (NMSS) representation of a linear, discrete-time transfer function. In the NMSS form, all the states depend on the present and past inputs and outputs of the system. An n^{th} order single-input single-output (SISO) system in discrete-time can be expressed as

$$y(k) = \frac{B(z^{-1})}{A(z^{-1})}u(k) \tag{4.3}$$

where z^{-1} is the delay operator and B and A denote the numerator and denominator of the transfer function such that

$$A(z^{-1}) = 1 + a_1 z^{-1} + ... + a_n z^{-n}$$

$$B(z^{-1}) = b_1 z^{-1} + b_2 z^{-2} + ... + b_m z^{-m}$$

The NMSS form is expressed using the following equations

$$x(k) = Fx(k-1) + gu(k-1) + dy_d(k) \tag{4.4}$$

$$y(k) = Hx(k) \tag{4.5}$$

where k is the discrete-time variable, y_d is the command input and,

$$F = \begin{bmatrix} -a_1 & ... & -a_{n-1} & -a_n & b_2 & ... & b_{m-1} & b_m & 0 \\ 1 & ... & 0 & 0 & 0 & ... & 0 & 0 & 0 \\ \vdots & & \vdots & \vdots & \vdots & & \vdots & \vdots & \vdots \\ 0 & ... & 1 & 0 & 0 & ... & 0 & 0 & 0 \\ 0 & ... & 0 & 0 & 0 & ... & 0 & 0 & 0 \\ 0 & ... & 0 & 0 & 1 & ... & 0 & 0 & 0 \\ \vdots & & \vdots & \vdots & \vdots & & \vdots & \vdots & \vdots \\ 0 & ... & 0 & 0 & 0 & ... & 1 & 0 & 0 \\ a_1 & ... & a_{n-1} & a_n & -b_2 & ... & -b_{m-1} & -b_m & 1 \end{bmatrix}$$

$$g = \begin{bmatrix} b_1 \\ 0 \\ \vdots \\ 0 \\ 1 \\ 0 \\ \vdots \\ 0 \\ -b_1 \end{bmatrix} \quad d = \begin{bmatrix} 0 \\ 0 \\ \vdots \\ 0 \\ 0 \\ 0 \\ \vdots \\ 0 \\ 1 \end{bmatrix}$$

$$H = \begin{bmatrix} 1 & \dots & 0 & 0 & 0 & \dots & 0 & 0 & 0 \end{bmatrix}$$

The F, g, d, H matrices depend only on the past inputs and outputs and not on any internal states. The PIP control law resulting from the NMSS model is of the usual state-variable feedback form $u(k) = -kx(k)$. If the state vector is of the form

$$x(k) = \begin{bmatrix} y(k) & y(k-1) & \dots & y(k-n+1) & u(k-1) & \dots & u(k-m+1) & z(k) \end{bmatrix}$$

where the integral or error term, $z(k) = z(k-1) + y_d(k) - y(k)$ and the gain vector is

$$k = \begin{bmatrix} f_0 & f_1 & \dots & f_{n-1} & g_1 & \dots & g_{m-1} & -k_1 \end{bmatrix}$$

then the PIP control law is

$$u(k) = -f_0 y(k) - f_1 y(k-1) \dots - f_{n-1} y(k-n+1) - g_1 u(k-1) \dots - g_{m-1} u(k-m+1) + k_1 z(k) \tag{4.6}$$

If the previous input $u(k-1)$ is subtracted from the current input $u(k)$, then the PIP control law can be rewritten as

$$\begin{aligned} u(k) - u(k-1) = & - f_0\{y(k) - y(k-1)\} - f_1\{y(k-1) - y(k-2)\} \dots \\ & - f_{n-1} y\{(k-n+1) - y(k-n)\} - g_1\{u(k-1) - u(k-2)\} \dots \\ & - g_{m-1} u\{(k-m+1) - u(k-m)\} + k_1\{y_d(k) - y(k)\} \end{aligned} \tag{4.7}$$

If the input signal is saturated due to the physical limitations of the system, then the controller can have an integral windup problem where the integral error accumulates and prevents the controller from responding quickly to a decrease in the input signal. For this

reason, u(k) is limited where if u(k)$\geq u_{max}$, u(k)= u_{max} or if u(k)$\leq u_{min}$, u(k)= u_{min}. Then it can be seen from equation 4.7 that the integral error term can be constrained.

For a first order system with one sample time delay and one parameter in the numerator polynomial, the PIP controller takes the form of a classical PI controller. For more complex systems, the PI element is retained and additional derivative action is provided through feedback from the higher order terms, which explains the name 'proportional integral plus'. This effect can be seen from the block diagram representation of the PIP controller in Figure 4.13.

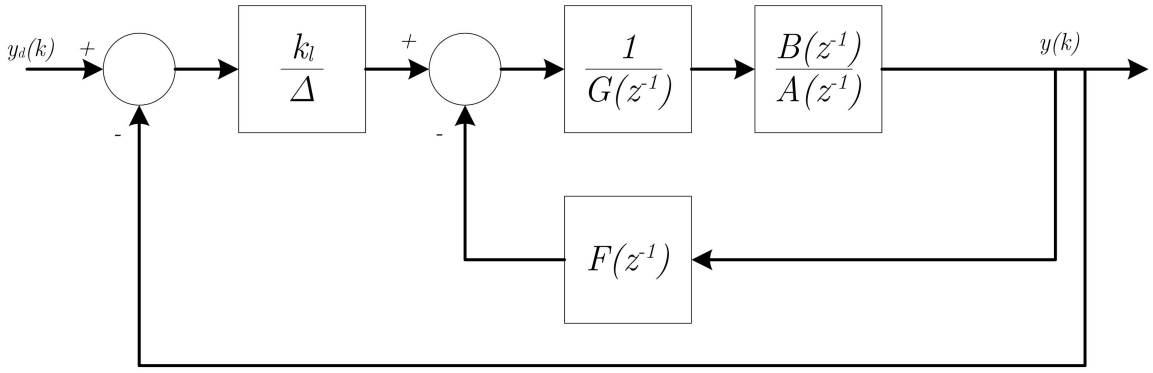

Where:-

k_I/Δ	- Integral Control	$= k_I/(1\text{-}z^{-1})$
$F(z^{-1})$	- Feedback Filter	$= f_0 + f_1z^{-1} + f_2z^{-2} + \ldots + f_{n-1}z^{-(n-1)}$
$G(z^{-1})$	- Input Filter	$= 1 + g_1z^{-1} + g_2z^{-2} + \ldots + g_{m-1}z^{-(m-1)}$

Figure 4.13: PIP controller block diagram representation [94]

The gain matrix k can be calculated using any state variable feedback method. Here it is calculated using the linear quadratic (LQ) algorithm where the cost function J represented in the equation below is minimised subject to some weighting factors.

$$J(u) = \sum_{n=1}^{\infty} x(n)^T Qx(n) + u(n)^T Ru(n) \tag{4.8}$$

This minimisation is performed using the 'dlqr' function in MATLAB where the weightings on the input, output and integral-of-error terms need to be specified. Q is a diagonal matrix with weighting factors W_y, W_u and W_z which are tuned to achieve the desired frequency response and closed loop performance. W_y affects the response to the disturbance, W_u applies a weighting to the control torque and W_z governs the speed of the response.

The design process is similar for all the three controllers, so only the DIRW controller is explained in detail. From the DIRW linear model transfer function expressing the relationship

between the input wheel torque and the wheelset lateral displacement in equation 3.24, the F,g,d,H matrices for expressing the NMSS form are given below

$$g = \begin{bmatrix} 2\times10^{-10} \\ 0 \\ 0 \\ 0 \\ 0 \\ 0 \\ 0 \\ 1 \\ 0 \\ 0 \\ 0 \\ 0 \\ 0 \\ -2\times10^{-10} \end{bmatrix} \quad d = \begin{bmatrix} 0 \\ 0 \\ 0 \\ 0 \\ 0 \\ 0 \\ 0 \\ 0 \\ 0 \\ 0 \\ 0 \\ 0 \\ 0 \\ 1 \end{bmatrix}$$

H=[1 0 0 0 0 0 0 0 0 0 0 0 0 0]

$$
F = \left[\begin{array}{cccccccccc|c}
2.5 & -2 & 0.3 & 0.1 & -0.1 & 0.3 & -0.1 & -1.6e^{-9} & 6.9e^{-10} & -1.9e^{-9} & 2.1e^{-9} & -5.2e^{-10} & 6.2e^{-10} & 0 \\
1 & 0 & 0 & 0 & 0 & 0 & 0 & 0 & 0 & 0 & 0 & 0 & 0 & 0 \\
0 & 1 & 0 & 0 & 0 & 0 & 0 & 0 & 0 & 0 & 0 & 0 & 0 & 0 \\
0 & 0 & 1 & 0 & 0 & 0 & 0 & 0 & 0 & 0 & 0 & 0 & 0 & 0 \\
0 & 0 & 0 & 1 & 0 & 0 & 0 & 0 & 0 & 0 & 0 & 0 & 0 & 0 \\
0 & 0 & 0 & 0 & 1 & 0 & 0 & 0 & 0 & 0 & 0 & 0 & 0 & 0 \\
0 & 0 & 0 & 0 & 0 & 1 & 0 & 0 & 0 & 0 & 0 & 0 & 0 & 0 \\
0 & 0 & 0 & 0 & 0 & 0 & 0 & 1 & 0 & 0 & 0 & 0 & 0 & 0 \\
0 & 0 & 0 & 0 & 0 & 0 & 0 & 0 & 1 & 0 & 0 & 0 & 0 & 0 \\
0 & 0 & 0 & 0 & 0 & 0 & 0 & 0 & 0 & 1 & 0 & 0 & 0 & 0 \\
0 & 0 & 0 & 0 & 0 & 0 & 0 & 0 & 0 & 0 & 1 & 0 & 0 & 0 \\
0 & 0 & 0 & 0 & 0 & 0 & 0 & 0 & 0 & 0 & 0 & 1 & 0 & 0 \\
-2.5 & 2 & -0.3 & -0.1 & 0.1 & -0.3 & 0.1 & 1.6e^{-9} & -6.9e^{-10} & 1.9e^{-9} & -2.1e^{-9} & 5.2e^{-10} & -6.2e^{-10} & 1
\end{array}\right]
$$

The k matrix is calculated from minimising the cost function with the weightings $W_y = 0.1$, $W_u = 1 \times 10^{-4}$ and $W_z = 1 \times 10^{6}$.

$k = 1 \times 10^{8}$ [-0.98 1.50 -0.42 -0.12 -0.03 -0.14 0.17 0.00 ... 0.00]

The weightings for each of the PIP controllers for the SYC, ASW and DIRW were selected heuristically to achieve the same GM and PM requirements established for the classical controllers. Figures 4.14, 4.15 and 4.16 show the open loop frequency response with and without the PIP controller applied in the SYC, ASW and DIRW configurations respectively. The weightings selected and the corresponding margins and bandwidth for each of the controllers is given in Table 4.3. From the table it can be seen that the GM and PM requirements are satisfied for each controller. As with the classical controller design, the margins are not pushed excessively so as to keep the control force/ torque required to practically realisable levels. From the Nichols plots it can be seen that the gain is increased at lower frequencies to remove any steady state errors.

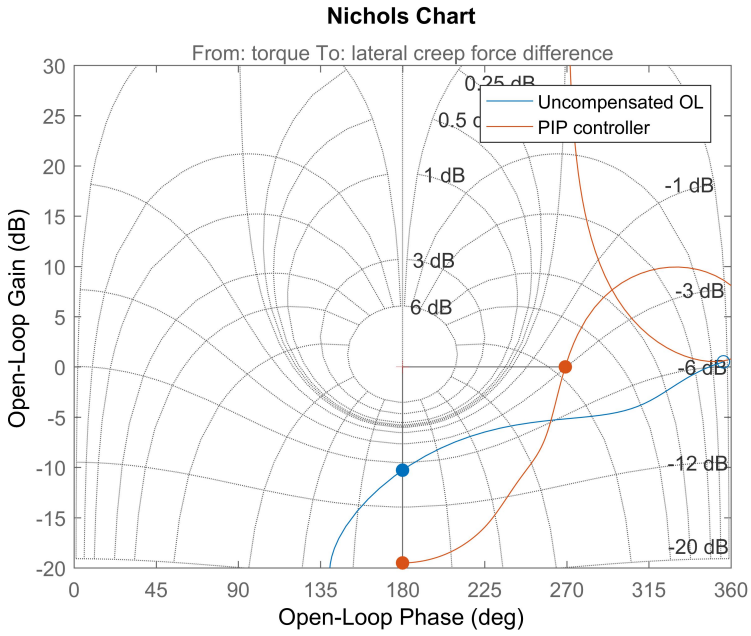

Figure 4.14: Nichols plot for PIP controller design for SYC configuration

Table 4.3: System bandwidth and stability margins

	controller weightings	GM (dB)	PM (deg)	Bandwidth (Hz)
SYC	W_y=0.1, W_u=1, W_z=2	19.5	85.6	0.12
ASW	W_y=1, W_u=1, W_z=0.01	7.92	79.8	1.17
DIRW	W_y=0.1, $W_u = 1 \times 10^{-4}$, $W_z = 1 \times 10^{6}$	34.1	61.9	1.92

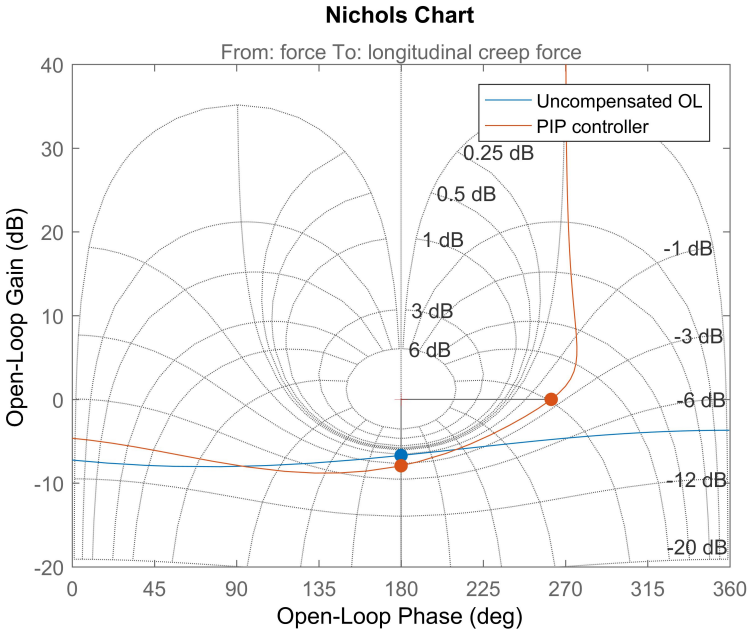

Figure 4.15: Nichols plot for PIP controller design for ASW configuration

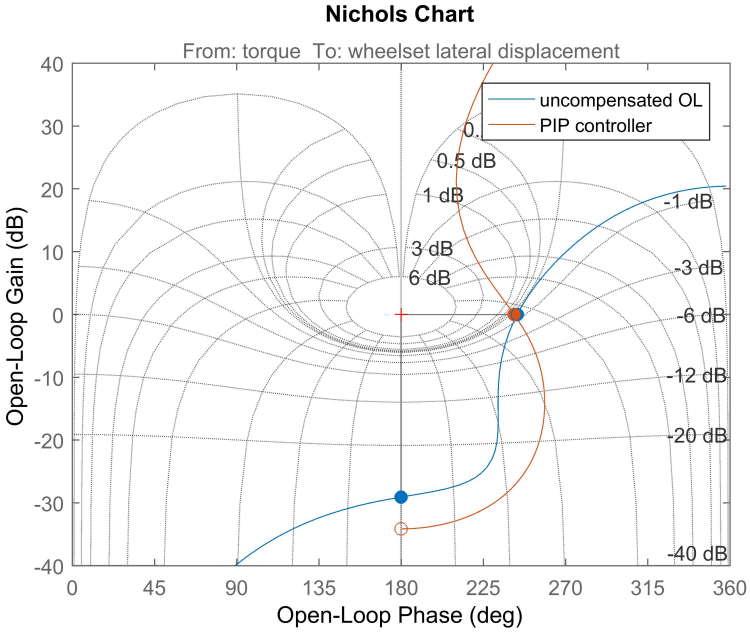

Figure 4.16: Nichols plot for PIP controller design for DIRW configuration

The closed loop step response obtained with the PIP controller implemented on the linear SYC, ASW and DIRW models in Simulink is shown in Figures 4.17, 4.18 and 4.19 respectively.

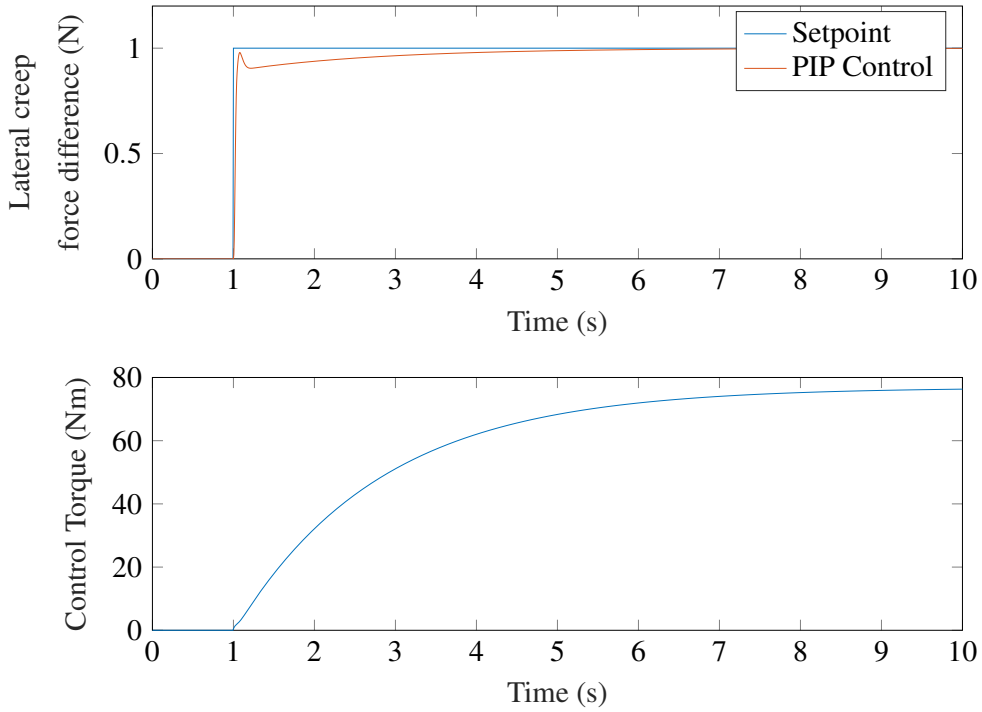

Figure 4.17: Closed loop response of PIP control applied to the SYC model

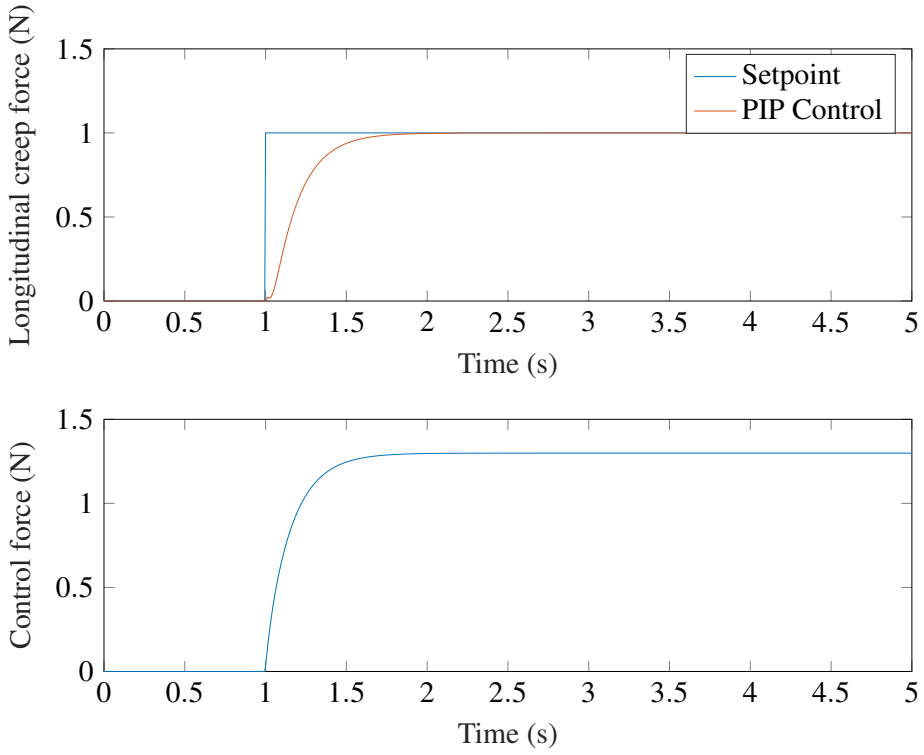

Figure 4.18: Closed loop response of PIP control applied to the ASW model

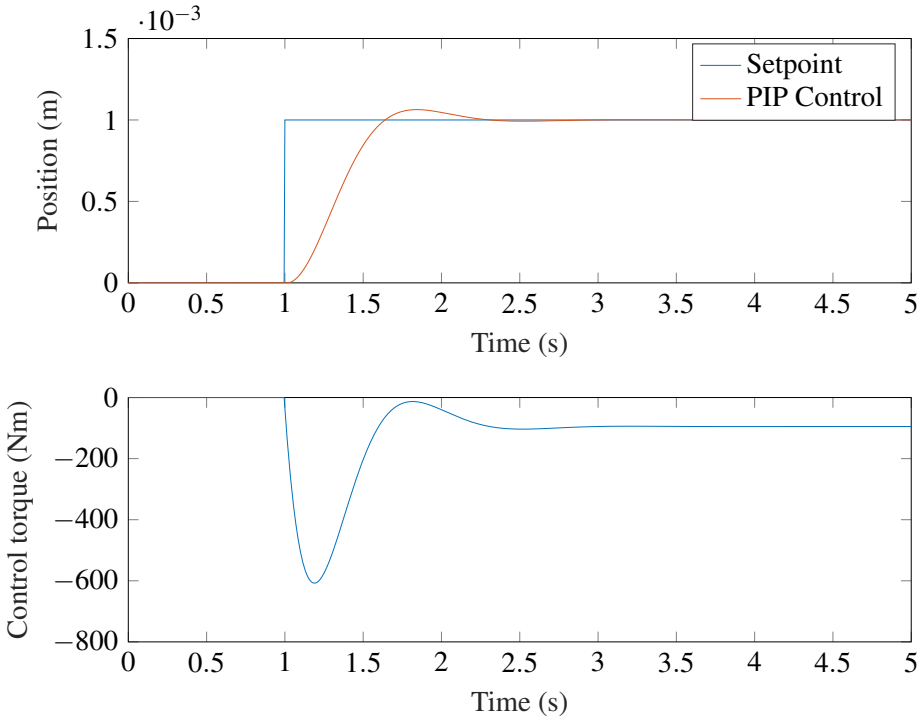

Figure 4.19: Closed loop response of PIP control applied to the DIRW model

There was no steady state error in any of the step responses. The key performance metrics from the closed loop step responses using the PIP controllers are listed in Table 4.4. The PIP controllers satisfy the rise time, settling time and overshoot requirements for each controller. For the SYC case, the settling time is reduced using the PIP controller, but the rise time is higher. In the ASW case, the both the rise and settling times are reduced using the PIP controller. For the DIRW configuration, there is a marginal increase in the rise and settling times, but the overshoot is reduced using the PIP controller designed.

Table 4.4: Time domain performance from applying PIP controllers.

	Rise time (s)	Settling time (s)	Overshoot (%)
SYC	0.085	3.055	0
ASW	0.365	0.685	0
DIRW	0.41	1.155	6.4

4.4 Conclusions

In this chapter a classical controller and a PIP controller are developed for each of the active steering configurations. The classical controllers show the performance using simple algorithms which could theoretically be further improved using the state-feedback control with the PIP controllers. The following key conclusions can be drawn from applying the controllers on the linear models obtained from system identification.

- For the SYC model, the PIP controller nearly doubles the system bandwidth compared to the classical PI controller. As a consequence, the rise and settling times is significantly reduced. The PIP controller also eliminates overshoot which is 8.5 % of the steady state value using the PI controller. The torque requirements using both controllers are very similar. The reduction in settling time and overshoot clearly demonstrate a better performance using the PIP controller.
- The bandwidth of the ASW model is also marginally higher using the PIP controller. The rise and settling times are reduced indicating that the PIP controller shows a better performance the classical PI control. The torque requirements using both controllers are similar.
- The DIRW model shows a very similar response using both the PIP and the classical PA+I controllers. There is a marginal increase in the rise and settling times using the PIP controller. The overshoot is marginally lower using the PIP controller.

Both types of controllers are applied to the three active vehicle non-linear models in the next chapter. Applying the controllers developed in this chapter will provide a level of proof of robustness that the algorithms will cope with the model non-linearities. The Simpack 'simulation models' are more complex than the linear ARX 'design models'. The next chapter also compares the performance of the two controllers for each steering mechanism to present a logical reasoning for the controller selected for the track switch simulations.

Chapter 5

Active vehicle non-linear model simulations

This chapter discusses the simulation results of the different active vehicle models Secondary Yaw Control (SYC), Actuated Solid-axle Wheelset (ASW) and Driven Independently-Rotating Wheelset (DIRW), developed in Chapter 3 in a variety of scenarios. Both sets of controllers developed in the Chapter 4 are used. There are two main objectives of this chapter. Firstly, the different active steering mechanisms are compared to each other and to the passive vehicle model. This comparison allows a performance analysis of the different schemes in terms of wheel-rail wear, guidance and steering. The improvement in performance is demonstrated by quantifying their benefits with respect to a conventional vehicle model on some common track profiles. This includes straight track profiles, moderate and high speed curves with lateral, vertical and gauge width irregularities. Simple classical controllers are used initially in these simulations. A more complex proportional integral plus (PIP) controller is also applied to each active vehicle model. This is used to achieve the second objective of this chapter which is to compare the relative performance of the classical and PIP controllers. The controller that gives a better performance is then used with the active vehicle configuration that promises the best performance for the track switch simulations in the next chapter.

5.1 Co-simulation using MATLAB and Simpack

The controllers are run in MATLAB/ Simulink in parallel with Simpack using the SIMAT co-simulation interface [96]. It enables the non-linear Simpack models to run in parallel with the control mechanisms designed in Simulink for exchanging signals to close the control loop. Both the classical and PIP controllers designed in the previous chapter are applied to the active vehicle simulation models developed in Chapter 3 through co-simulation between MATLAB and Simpack. An overview of the SIMAT co-simulation interface is illustrated in Figure 5.1. The sampling frequency is set to 200 Hz for all the models which is sufficiently

high to prevent any sampling delays because the highest system bandwidth is 2 Hz as can be seen from Tables 4.1 and 4.3.

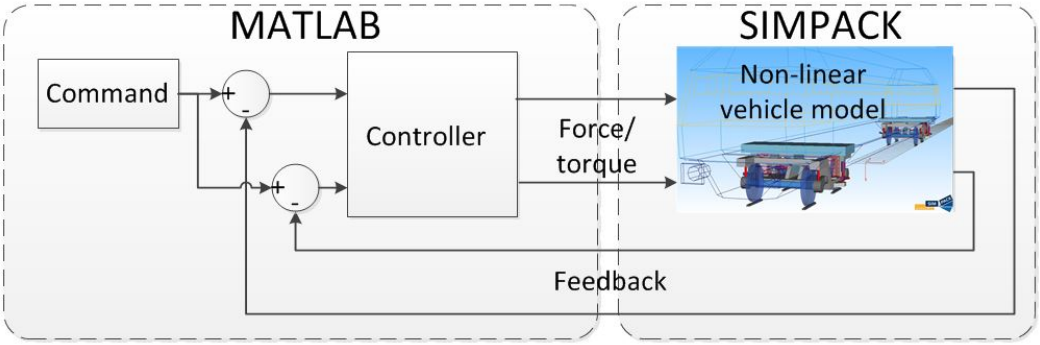

Figure 5.1: Co-simulation overview

The inputs and outputs to each of the Simpack models are different and are listed in Table 5.1. In the ASW configuration for example, the input to the Simpack model is the actuator forces and the output is the wheelset longitudinal creep forces. The actuator force is the controller output that is calculated in Simulink using the feedback signal which is the output of the Simpack model.

Table 5.1: Inputs and outputs of Simpack SYC, ASW, DIRW models

	Input signal	Output/feedback signal
SYC	Actuator force from vehicle body to bogie	Difference in lateral creep forces at front and rear wheelsets
ASW	Actuator force from bogie to wheelset	Wheelset longitudinal creep force
DIRW	Motor torque on each wheel	Wheelset lateral displacement wrt track

5.2 Description of track profiles

The vehicles are run on a variety of track profiles, both straight and curved with deterministic and stochastic excitations. The deterministic inputs are an intended feature of the track such as curve, cant or gradient variation on hills. Although gradients do not usually vary significantly due to the consequent decrease in adhesion in the wheel-rail contact, curve and cant variation is more common as tracks are rarely ever perfectly straight. The stochastic inputs represent the track irregularities which are an unintended feature but are a result of misalignment and wear.

The DynoTRAIN project developed a Virtual Test Track (VTT) toolkit which generates a series of test tracks based on the specified vehicle speed [97]. The test tracks fall into four zones - zone 1: straight and very large radii, zone 2: large radius curves and high cant

deficiency, zone 3: small radius curve, zone 4: very small radius curve. The track profiles chosen in this section are representative of sections of track as specified in the VTT. Profile 1 described below fits the zone 1 of the VTT requirements, profile 2 falls into zone 3 and profiles 3 and 4 into zone 2. Zone 4 specifies curves between 250 m and 400 m which are not considered here because they have very low speed restrictions. The four different track profiles under consideration are specified below:

1. **Straight track with lateral, vertical, gauge width, radius and cant stochastic disturbances**

   The straight track profile is based on recording car data from the Paddington to Bristol Great Western main line in the UK. It contains track irregularities in the form of curvature and cant variation, lateral/ vertical excitation and gauge width variation.

   Figure 5.2 shows the frequency distribution of the lateral disturbances of a section of track. It can be seen that most of the stochastic disturbances are have low frequencies. Figure 5.3 shows the vertical, gauge width, curvature and cant variation of the corresponding section of track. From the figure, it can be seen that the lateral disturbances are not centred about 0 mm, but instead by $\approx$ 2.5 to 3 mm.

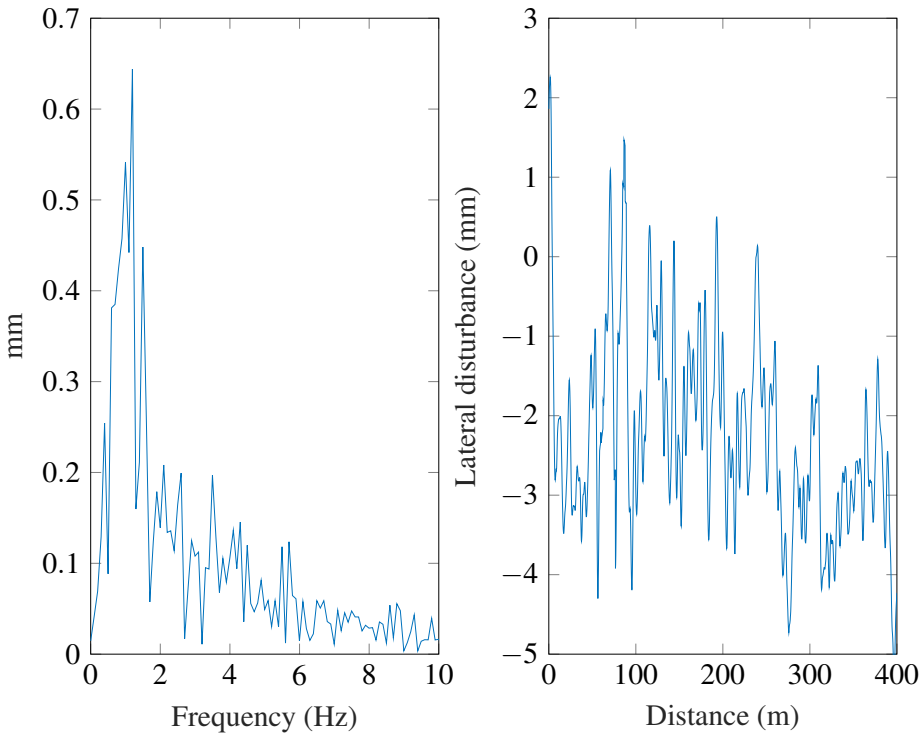

Figure 5.2: Frequency distribution of lateral disturbance

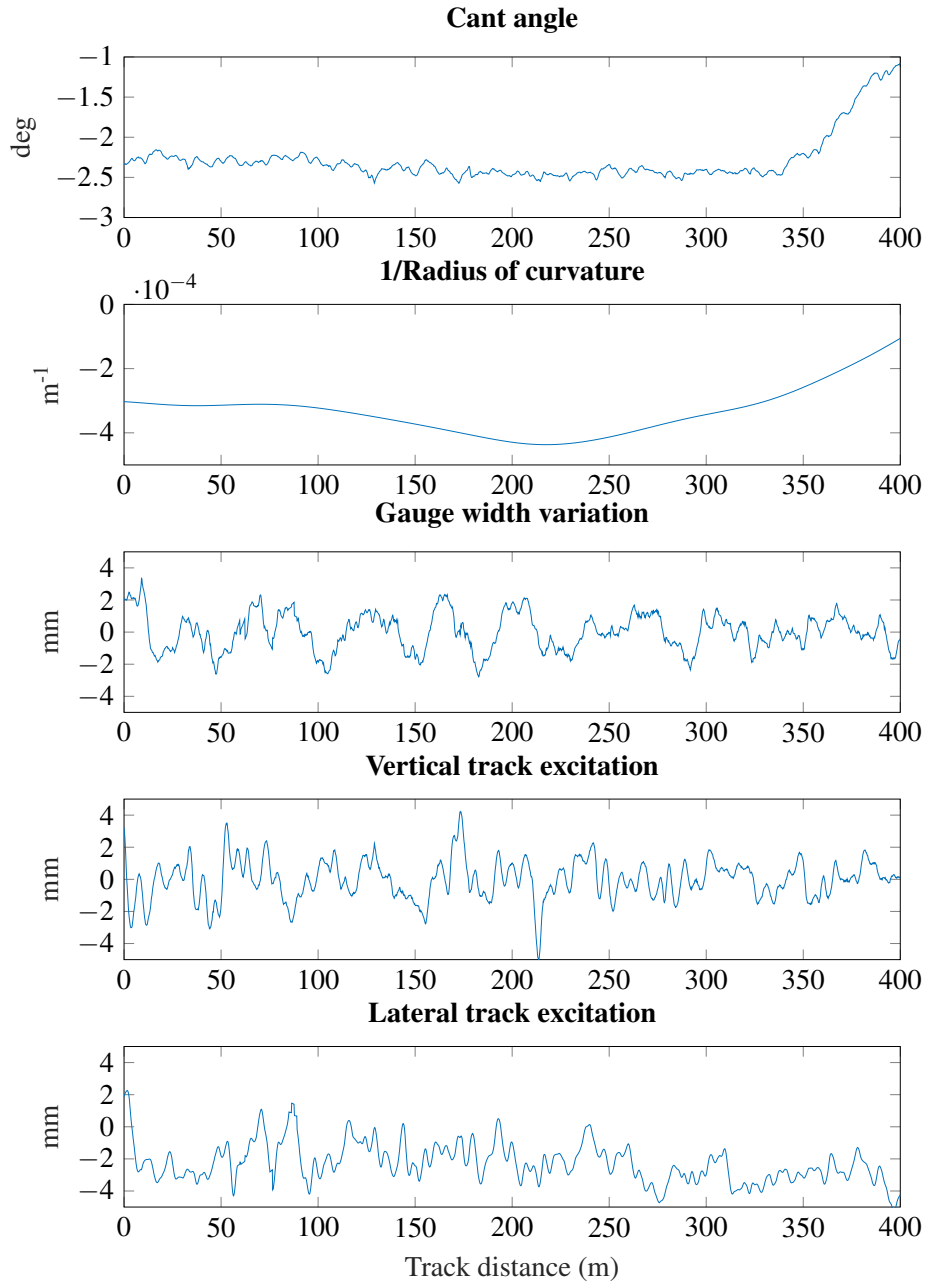

Figure 5.3: Straight track profile with stochastics

2. **Curved track with radius = 535 m, cant = 4° and vehicle speed = 30 m/s**

   All of the curved track profiles are selected to have a cant deficiency of 1 m/s^2 (10% g) which is an accepted industry standard [89]. The cant deficiency or net lateral acceleration experienced by the vehicle is calculated using the equation

$$a = \frac{v^2}{R} - g\theta_c \tag{5.1}$$

   where a is the lateral acceleration, R is the curve radius, v is the vehicle speed, g is acceleration due to gravity and θ_c is the cant angle. At a moderate vehicle speed of 30 m/s and a cant angle of 4°, the curve radius required to give a $1 m/s^2$ cant deficiency was calculated to be $\approx$ 535 m. This radius and cant is the steady state value between 90 m to 210 m from the start of the track as shown in Figure 5.4. The track profile transitions from a straight track to the constant radius curve. The transition occurs between 30 m and 90 m after the start of the track. This would mean that as a time-variant profile, the transition occurs from 1 s to 3 s and the constant curve from 3 s to 7 s. The profile transitions back into straight from 7 s to 9 s. The track cant also transitions accordingly.

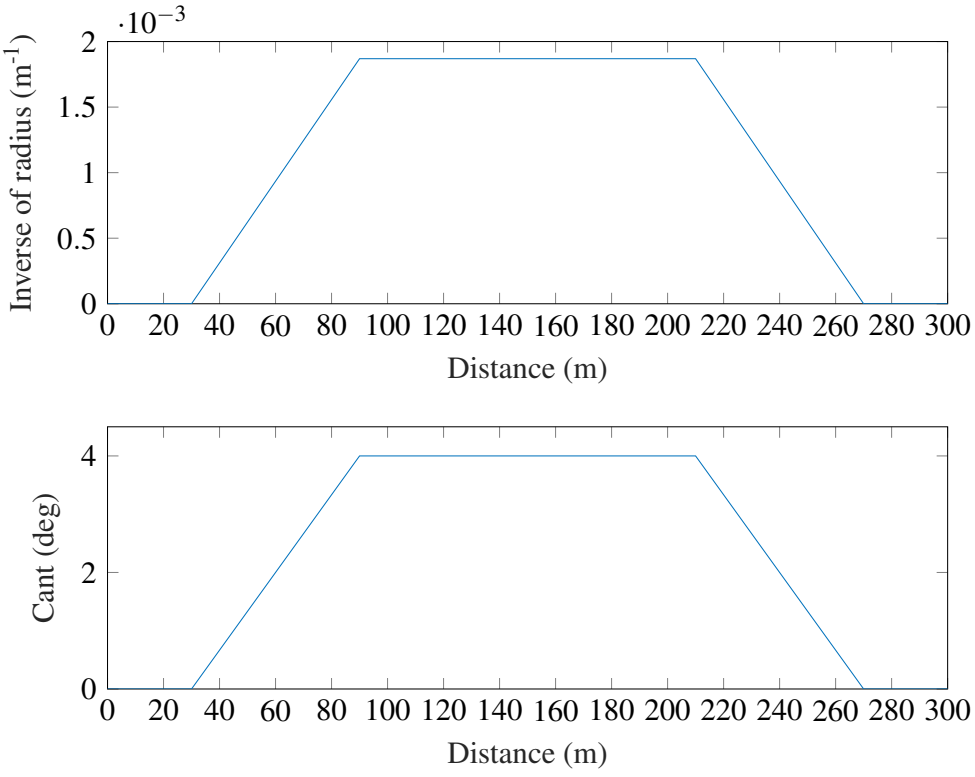

Figure 5.4: Curved track profile with radius = 535 m, cant = 4°

3. **Curved track with radius = 1200 m, cant = 4° and vehicle speed = 45 m/s**

   A vehicle speed of 45 m/s was chosen to analyse the performance on high speed curves. With the same calculations as in the previous profile, the curve radius is determined to be 1200 m. As before the there are transitions from straight to curve and back to straight. The distances at which the profiles change from the start of the track are changed so that the transition occurs from 1 s to 3 s and the constant curve from 3 s to 7 s as shown in Figure 5.5.

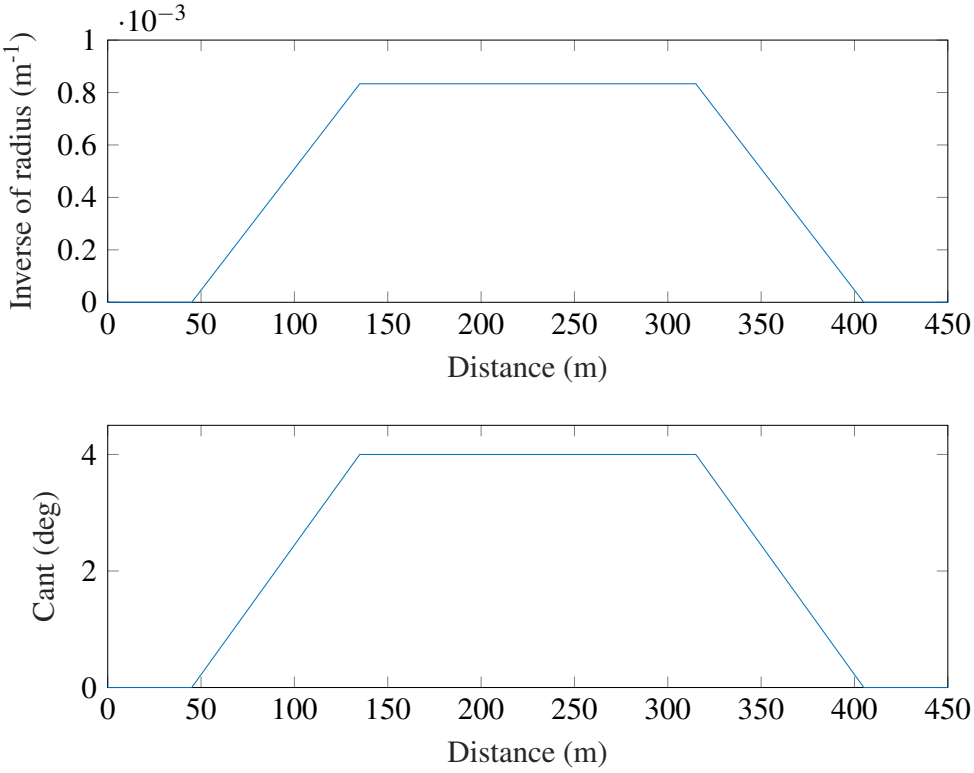

Figure 5.5: Curved track profile with radius = 1200 m, cant = 4°

4. **Curved track with radius = 1200 m, cant = 4° and vehicle speed = 45 m/s with lateral, vertical and gauge width stochastic disturbances**

   This track profile has the same curve and cant variation as the previous one, however it also has lateral, vertical and gauge width stochastic disturbances as shown in Figure 5.6. The ideal curving scenario is explained in more detail in section 2.3.The disturbances are the same as that described in the straight track profile with stochastics. This track profile is used to determine whether the appropriate steering torques are generated even in the presence of disturbances on a curved track.

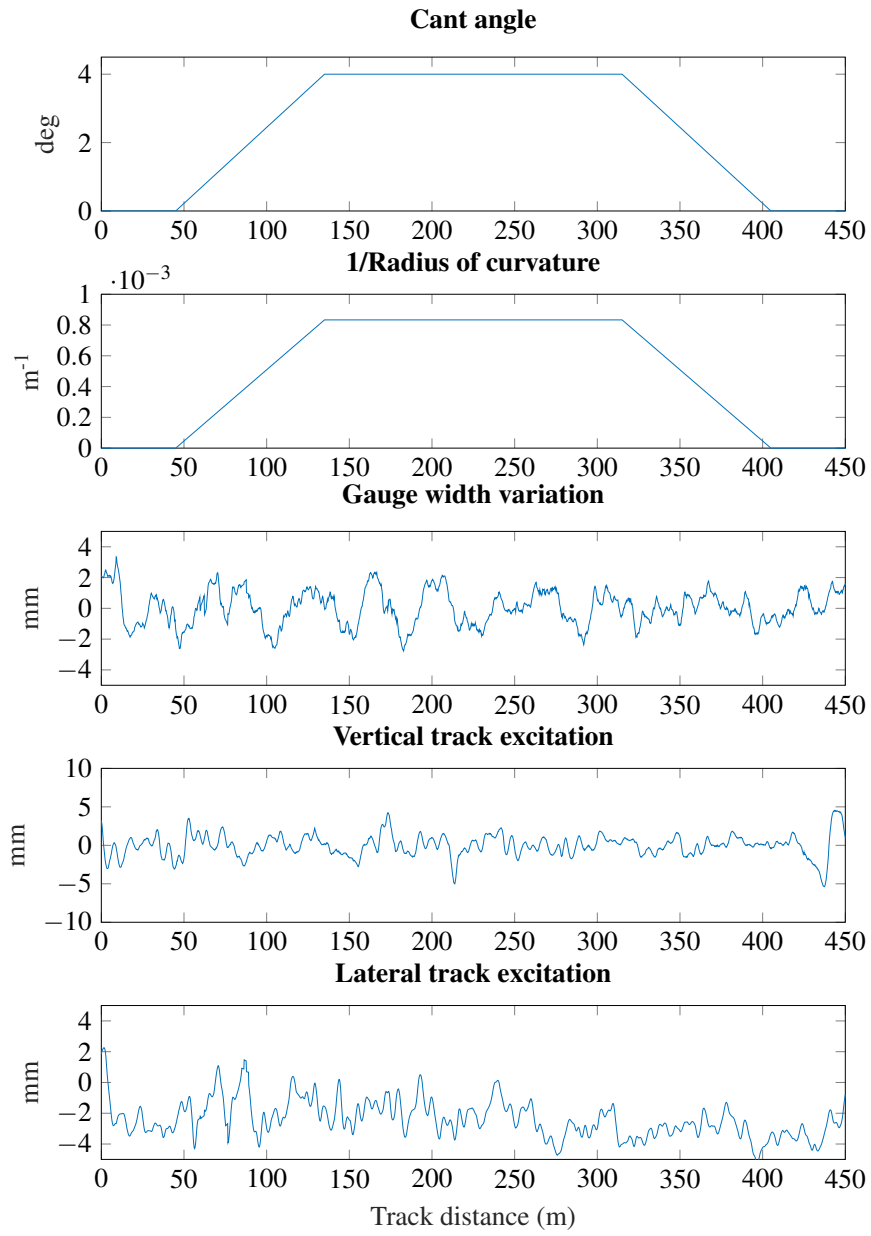

Figure 5.6: Curved track profile with stochastics

5.3 Performance indicators

Control strategies for active steering are concerned with better guidance which eliminates all unnecessary creep forces and associated wheel-rail wear to achieve near-optimal performance of the running gear. For this reason, the longitudinal/ lateral creep forces and a wear index ($T\gamma$) are used as key performance indicators. In addition the wheelset lateral displacement indicates distance from the flange and provides a geometric understanding of wheel-rail wear.

The actuation power is calculated to realise the practical requirements of the three control strategies. These different indicators are described in this section in more detail.

1. **Lateral creep forces**

   The lateral creep forces generated by the front and rear wheelsets of each bogie should ideally be similar in order that the maximum allowable speed of a vehicle can be increased on curves. Conventionally, the front wheelset of a bogie generates most of the lateral creep forces which limits the safe running speed of the vehicle. If the creep forces at the two wheelsets are equalised, the maximum vehicle speed can be higher.

2. **Longitudinal creep forces**

   Ideally the longitudinal creep force generated by each wheelset should be zero. This would mean that the wheels are in 'pure rolling' motion where the relative longitudinal speeds of the contact points on the wheel and rail are zero. In the case of a conventional solid-axle wheelset, this is rarely the case on curves where the relative speed of the wheels on the same axle are limited by the difference in their rolling radii. In independently-rotating wheelsets, the wheels are able to move freely resulting in negligible longitudinal creep forces.

3. **Wheelset lateral displacement**

   The wheelset lateral displacement with respect to the rails should be less than 6 mm as shown in Figure 5.7 to minimise flange contact and resultant non-linearities. Conventional wheel profiles have been optimised for passive solid-axle wheelsets which could be modified in the future for active vehicles.

4. **Contact patch frictional energy**

   The energy dissipated in the wheel-rail contact patch is used to give an indication of wear. It is denoted as $T\gamma$ and is calculated for each wheelset as

   $$T\gamma = F_x\varepsilon_x + F_y\varepsilon_y \tag{5.2}$$

   where F_x, F_y are the longitudinal and lateral creep forces and $\varepsilon_x, \varepsilon_y$ are the longitudinal and lateral creepages respectively [98]. $T\gamma$ can be used to model rolling contact fatigue (RCF) initiation. Rail life is dominated by RCF which can be caused by a wide variety of reasons associated with material properties and rail wear [99]. Cracks that are initiated due to traffic intensity and axle load can be reduced significantly by having the appropriate $T\gamma$ values [1]. Figure 5.8 shows RCF as a function of $T\gamma$. Below the fatigue threshold of 15 J/m, the energy generated in the contact patch is not sufficient to cause RCF. At very high

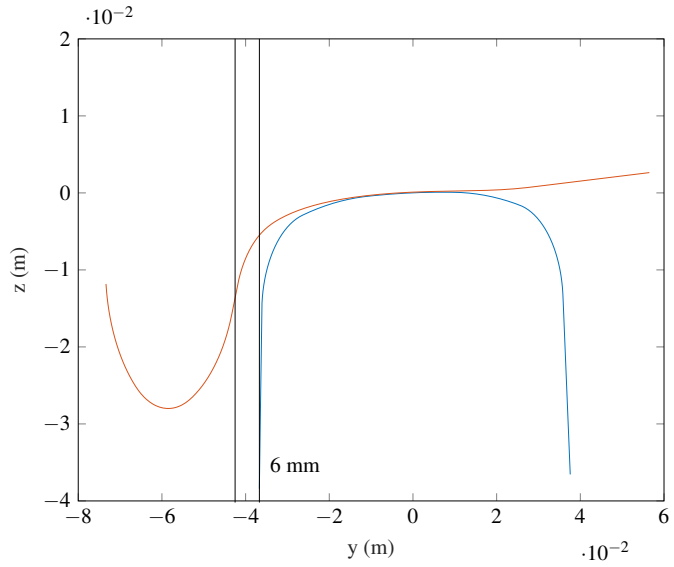

Figure 5.7: Overview of wheel and rail profile.

values of $T\gamma$ above 175 J/m, the rails get worn out due to the excessive energy and the wear is the dominant form of damage instead of RCF.

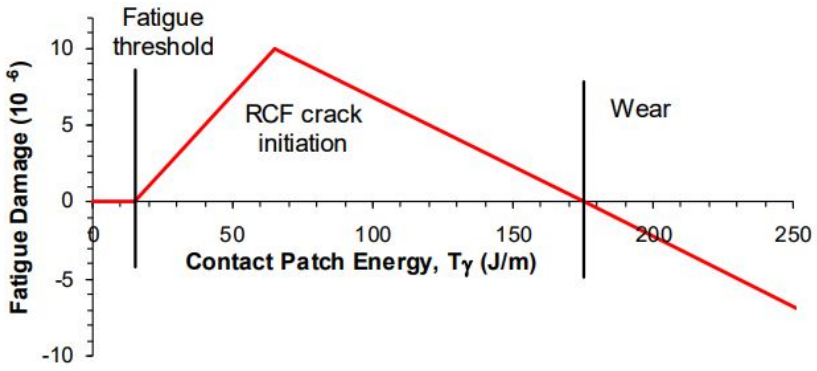

Figure 5.8: RCF crack initiation function [1]

It should be noted however that this model of RCF prediction based on $T\gamma$ values is only valid for a conventional solid-axle wheelset. Such models have not yet been validated for IRWs.

5. **Actuation power**

The actuation power must be achievable using an actuator physically small enough to fit in the desired space. For example, for the SYC configuration, the actuators are fit into the same position as a traditional secondary yaw damper. The ASW actuators need to be similar in size to the primary longitudinal springs with which they are connected in

parallel. Similarly, the DIRW motors need to be appropriately sized so that they can be fit onto wheels. For all the actuators, simple indicators such as maximum force and actuation power are used to ensure that the system is practically realisable with real actuators. Actuator dynamics are not taken into account, which would need to be considered in future work.

5.4 Active vehicle simulations using classical controllers

In this section the different actively steered vehicles are compared to the passive vehicle and to each other. Only the simple classical controllers are used for these simulations. The PIP controller simulations are in the next section. The front bogie graphs are discussed here. The rear bogie behaves similar to the front bogie and all the graphs from the rear bogie are in Appendix B.

5.4.1 SYC

Figures 5.9 to 5.12 show the wheelset lateral displacement, lateral creep forces, longitudinal creep forces of the SYC vehicle compared to the passive vehicle in all the track scenarios under consideration. The total torque applied to each bogie is also shown.

On the curved track with radius = 535 m, cant = 4° and vehicle speed = 30 m/s, the lateral creep forces of the front and rear wheelsets of the front bogie on the SYC vehicle are equalised as shown in Figure 5.9a. However, in order to achieve this, the front wheelset is laterally displaced by ≈6 mm as shown in Figure 5.9c which means that it approaches the flanges on the curve. The longitudinal creep forces of both the front and rear wheelsets are very similar to that of the passive vehicle as shown in Figure 5.9b. The results indicate that the controller successfully works to drive the difference in the lateral creep forces of the front and rear wheelsets to zero, but results in flange contact by doing so which gives an overall poor performance.

Figure 5.10 shows the response of the SYC vehicle on the high speed curve. The difference between the front and rear wheelset lateral creep forces are driven to zero again as shown in Figure 5.10a. The resultant high wheelset lateral displacement and longitudinal creep forces can also be seen in Figures 5.10c and 5.10b respectively. The SYC vehicle hits the flange on the front wheelset and has a residual lateral displacement after the transition to straight track. This is contributing to the undesirably high longitudinal creep forces. The control torque is higher than in the previous track profile as can be seen from Figures 5.9d and 5.10d. This is because of a bigger difference in the lateral creep forces of the front and rear wheelsets. Logically however, the torque should be lower on a curve with a shallower radius. This further shows that the SYC mechanism generates unnecessary creep forces.

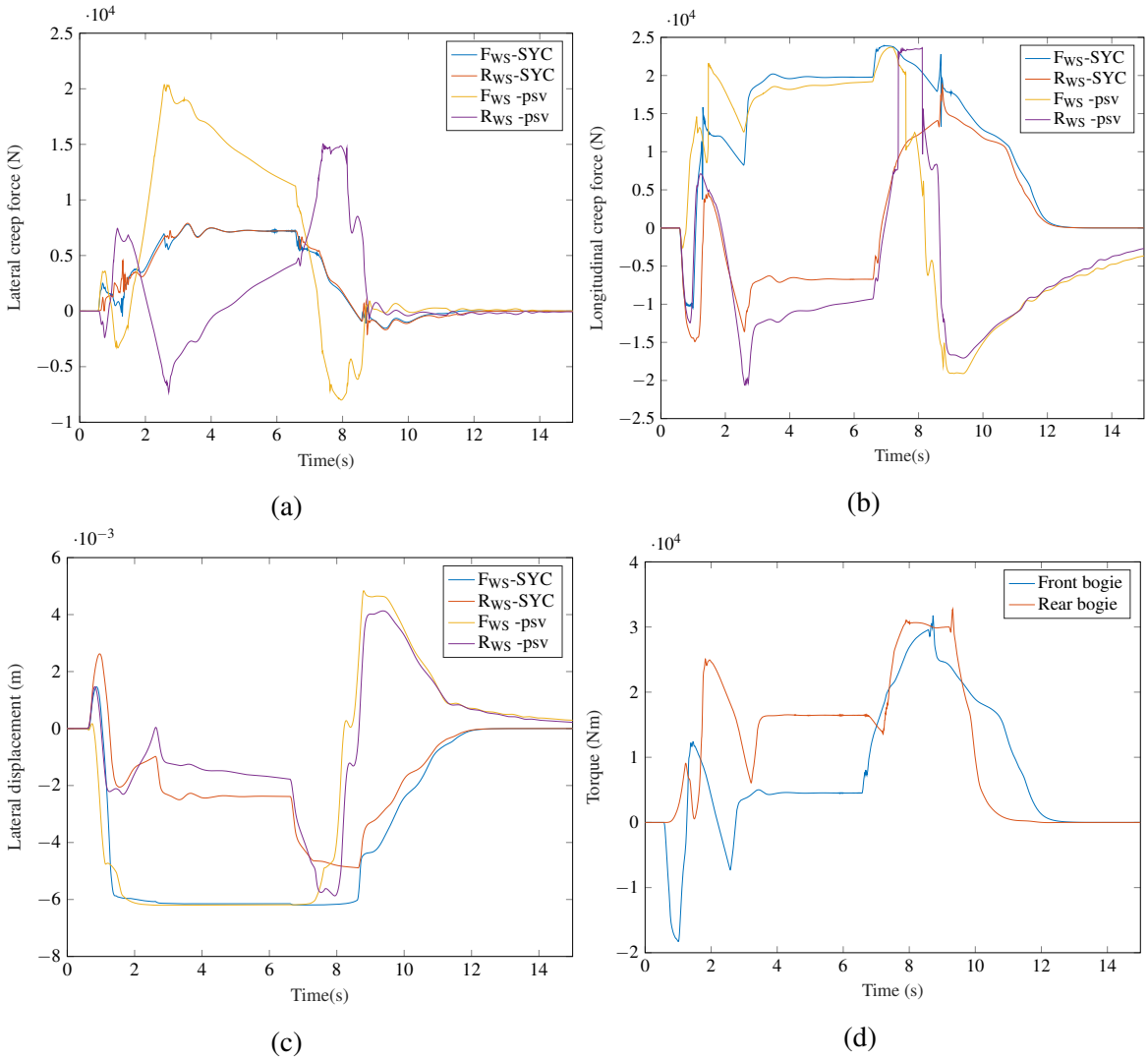

Figure 5.9: Lateral creep force, longitudinal creep force and lateral displacement response of the SYC vehicle compared to the passive vehicle on **curved track with radius = 535 m, cant = 4° and vehicle speed = 30 m/s**. The notations F_{WS}, R_{WS} and psv used in the graph labels mean 'front wheelset', 'rear wheelset' and 'passive' respectively. Figure 5.9d shows the total yaw torque acting on each bogie of the SYC vehicle.

Figure 5.11 shows the response of the SYC vehicle on the high speed curve with stochastics. For this track case in all the different vehicle simulations, the start of the track profile is defined as a straight track without any stochastics to allow the vehicle some transition length. Therefore although the simulation starts at 0 s, the figures are zoomed in to lend more visual clarity to the graphs. It can be seen from Figure 5.11a that the controller reduces the difference between the lateral creep forces of the front and rear wheelsets even in the presence of disturbances. The longitudinal creep forces and the wheelset lateral displacements are

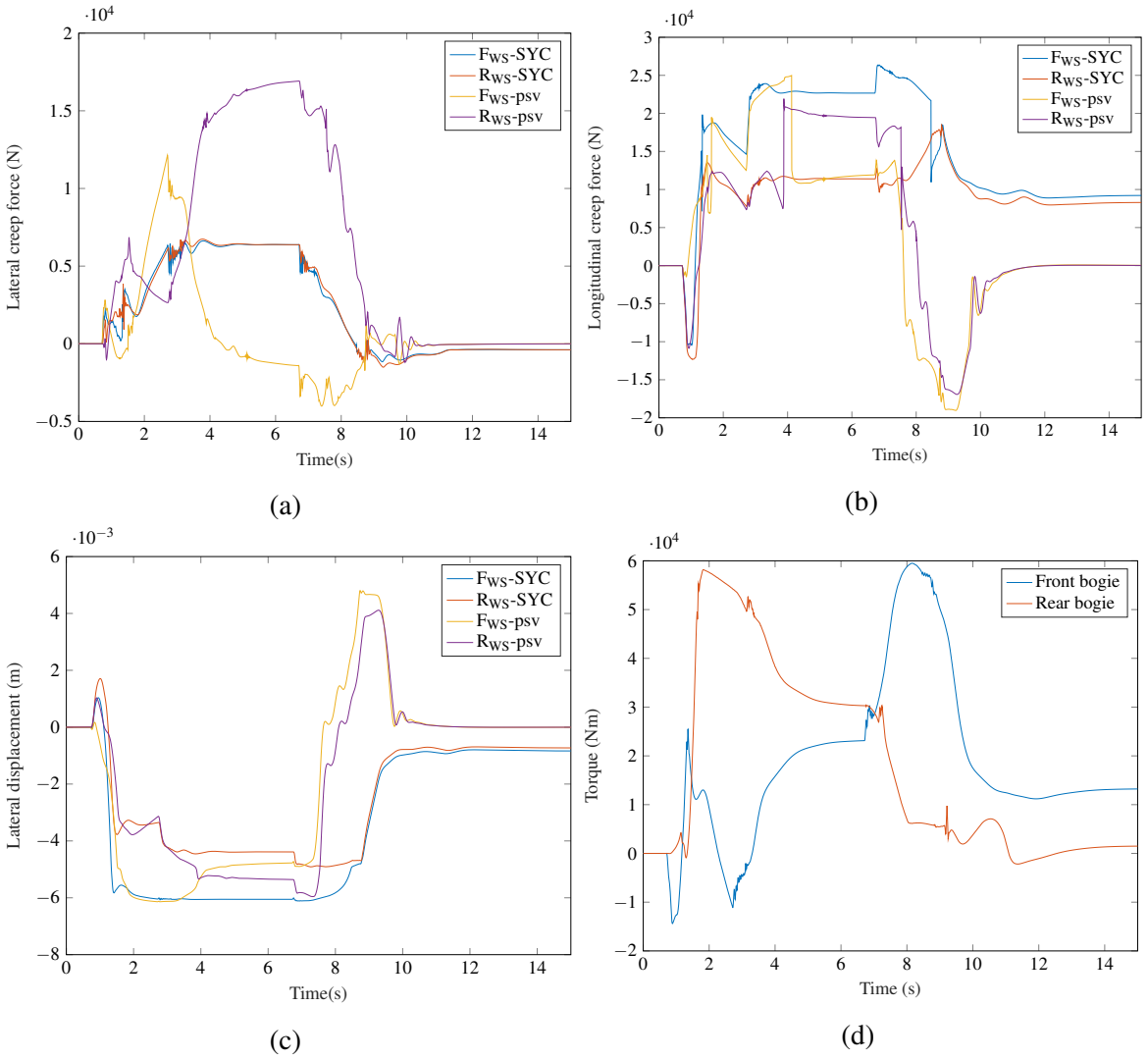

Figure 5.10: Lateral creep force, longitudinal creep force and lateral displacement response of the SYC vehicle compared to the passive vehicle on **curved track with radius = 1200 m, cant = 4° and vehicle speed = 45 m/s**. The notations F_{WS}, R_{WS} and psv used in the graph labels mean 'front wheelset', 'rear wheelset' and 'passive' respectively. Figure 5.10d shows the total yaw torque acting on each bogie of the SYC vehicle.

largely similar to the passive vehicle as shown in Figures 5.11b and 5.11c. The wheelsets on both vehicles are approaching flange contact. Comparing the torque requirement in the previous case with this case as shown in Figures 5.10d and 5.11d respectively, it can be seen that the maximum torque required on a curved track without any stochastics is higher than that on a curved track with stochastics. This is an interesting result as the latter is a more realistic track scenario.

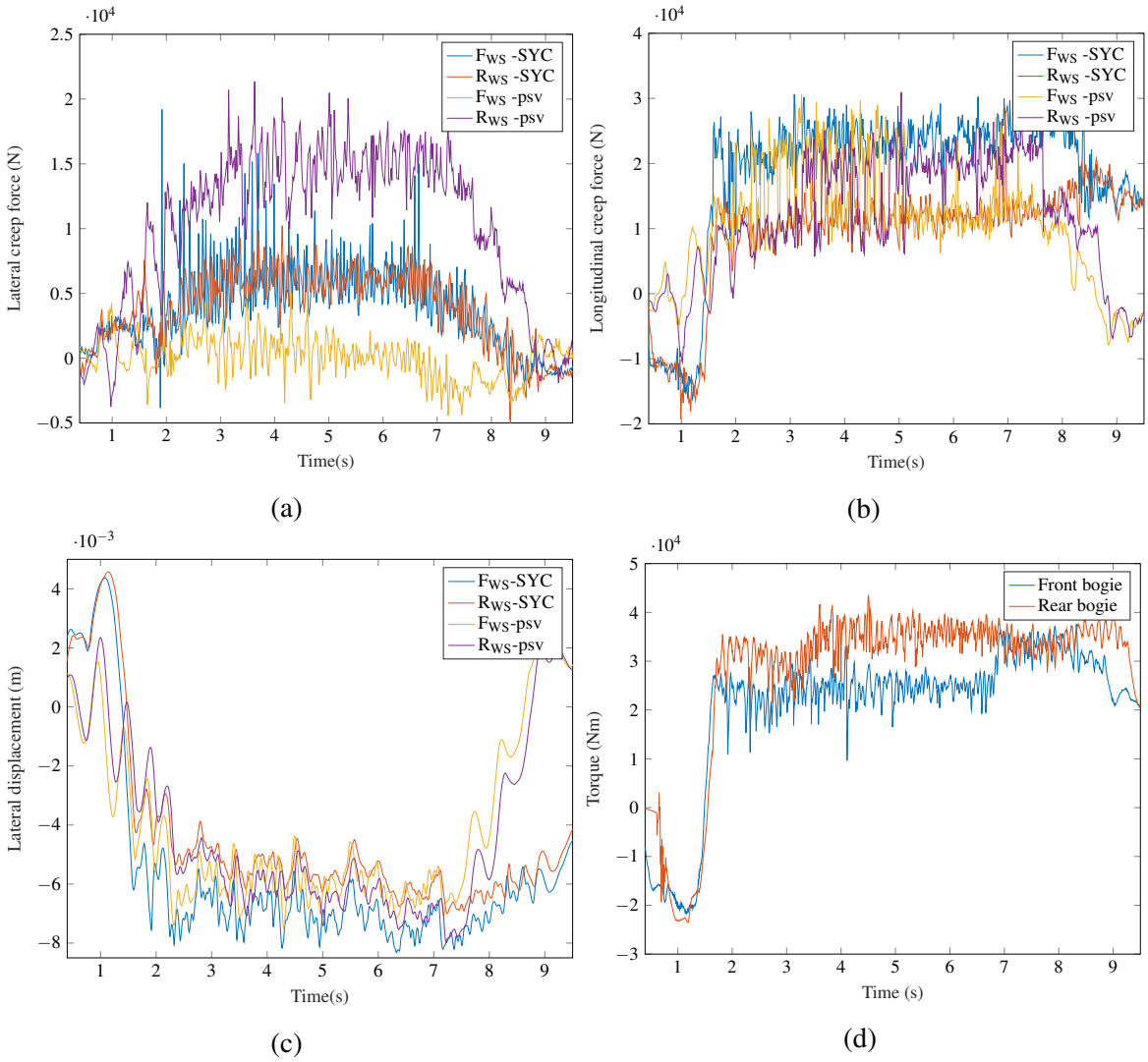

Figure 5.11: Lateral creep force, longitudinal creep force and lateral displacement response of the SYC vehicle compared to the passive vehicle on **curved track with radius = 1200 m, cant = 4° and vehicle speed = 45 m/s, with lateral, vertical and gauge width stochastics**. The notations F_{WS}, R_{WS} and psv used in the graph labels mean 'front wheelset', 'rear wheelset' and 'passive' respectively. Figure 5.11d shows the total yaw torque acting on each bogie of the SYC vehicle.

Figure 5.12 shows the response of the SYC vehicle on the straight track profile with stochastics. Here again as in the previous case, a length of track at the beginning is used for all the vehicle simulations to transition from a perfectly smooth track to one with stochastics. The figures have been zoomed in for visual clarity. The difference in the lateral creep forces of the front and rear wheelsets is shown in Figure 5.12a instead of the individual forces to show the clear decrease in the SYC vehicle compared to the passive vehicle.

This is achieved at the cost of higher longitudinal creep forces and wheelset lateral displacement as shown in Figures 5.12b and 5.12c. The lateral displacement is not centred about 0 mm because the lateral excitation in this particular section of track is not centred about 0 mm as can be seen clearly from Figure 5.3.

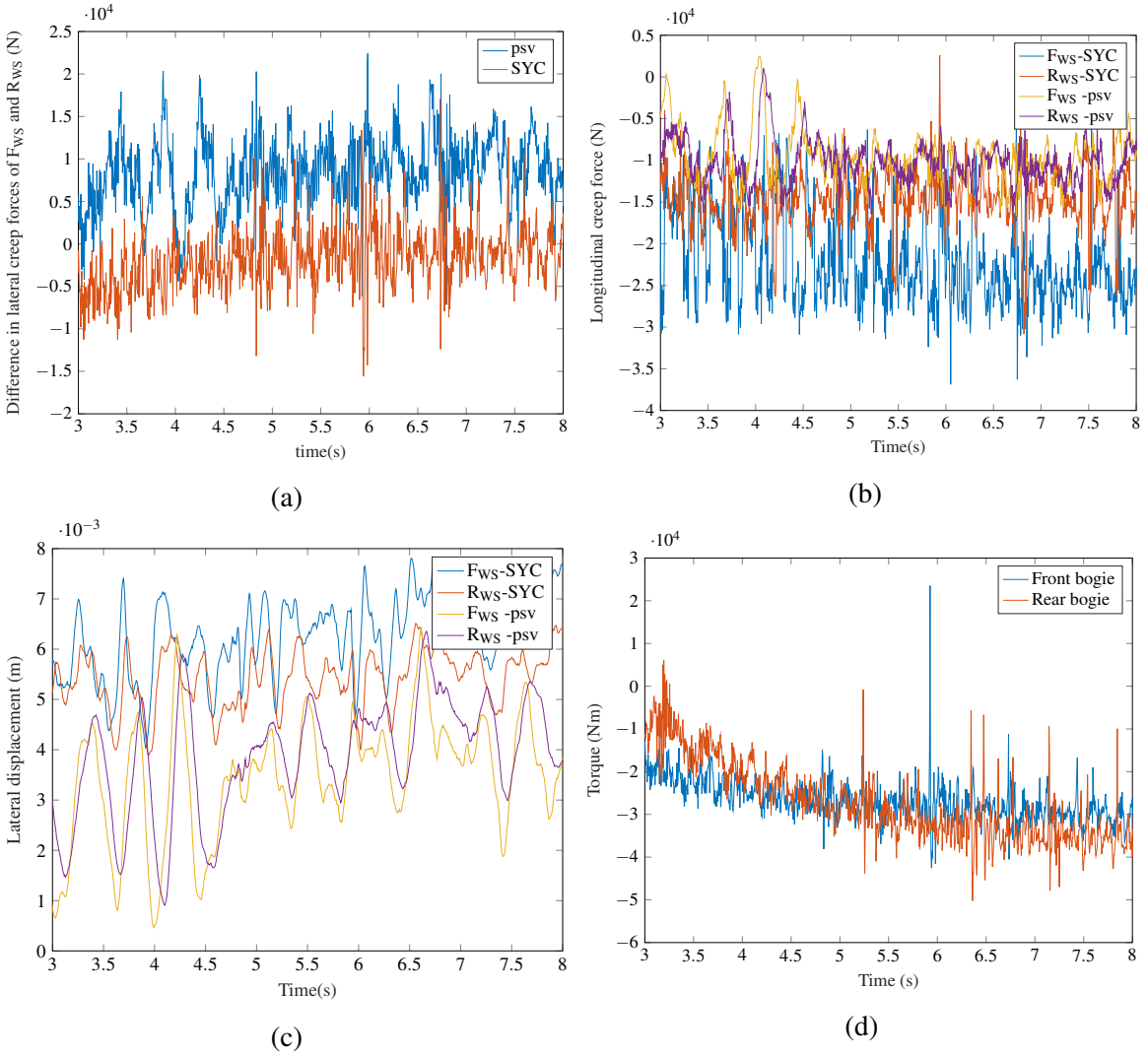

Figure 5.12: Longitudinal creep force and lateral displacement response of the SYC vehicle compared to the passive vehicle on the **straight track with stochastic disturbances**. The notations F_{WS}, R_{WS} and psv used in the graph labels mean 'front wheelset', 'rear wheelset' and 'passive' respectively. Figure 5.12a compares the difference in the lateral creep forces of the front and rear wheelsets of the SYC and passive vehicles. Figure 5.12d shows the total yaw torque acting on each bogie of the SYC vehicle.

5.4.2 ASW

Figure 5.13d compares the response of the ASW vehicle to the passive vehicle on a curve with radius = 535 m, cant = 4° and vehicle speed = 30 m/s. The controller in the ASW mechanism aims to reduce the longitudinal creep forces which are significantly lower than the passive vehicle as shown in Figure 5.13b. The difference in the lateral creep forces at the front and rear wheelsets is marginally higher in the steady states than the passive vehicle, but lower in the transition periods as can be seen in Figure 5.13a. Both wheelsets maintain minimum flange contact as shown by the wheelset lateral displacement in Figure 5.13c. The actuator force is quite high due to the small curve radius as shown in Figure 5.13d.

Figure 5.14 shows the response of the ASW vehicle on the curve with radius = 1200 m, cant = 4° and vehicle speed = 45 m/s. Figure 5.14b shows that the longitudinal creep forces are successfully reduced to zero in the steady states and are significantly lower than the passive vehicle during transitions. The difference in the lateral creep forces at the front and rear wheelsets is also lower than that of a passive vehicle as shown in Figure 5.14a. The wheelset lateral displacement is significantly reduced and both wheelsets avoid flange contact as shown in Figure 5.14c. Comparing Figures 5.14d and 5.13d shows that the actuator forces are still quite high but lower than the previous track scenario, peaking at about 50 kNm for the front wheelset. The actuator forces can be reduced further by placing the actuator in series with the longitudinal springs [31].

Figure 5.15 shows the ASW vehicle on the high speed curve with stochastics. The figures are zoomed in to show only the transition periods and the constant curved track profile response. A similar trend to the previous track profile is observed in Figures 5.15a, 5.15b and 5.15c where an overall improvement is seen in terms of reduction in the difference in lateral creep forces between the front and rear wheelsets, reduction in longitudinal creep forces and wheelset lateral displacements. From Figure 5.15d it is interesting to note that the actuator forces are lower than in the previous track scenario indicating that the ASW actuation power may be lower on a real track scenario than on an ideal curve without any stochastics.

Figure 5.16 shows the response of the ASW vehicle on the straight track profile with stochastics. The ASW vehicle has a significantly lower longitudinal creep forces and wheelset lateral displacements than the passive vehicle as shown in Figures 5.16b and 5.16c. Figure 5.16a shows the lateral creep force difference of the front and rear wheelsets instead of the individual graphs to show the clear decrease in the ASW vehicle compared to the passive vehicle.

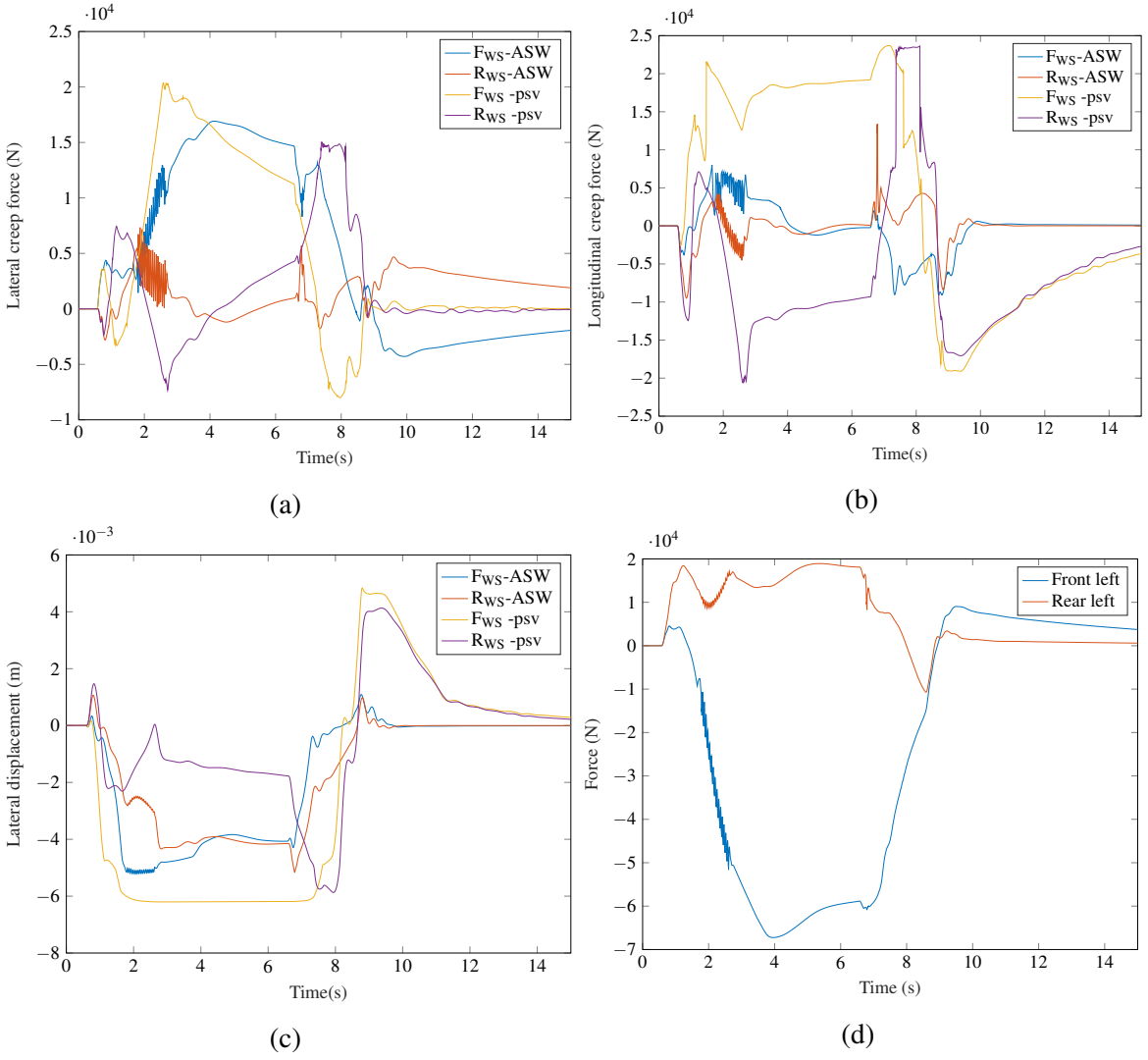

Figure 5.13: Lateral creep force, longitudinal creep force and lateral displacement response of the ASW vehicle compared to the passive vehicle on **curved track with radius = 535 m, cant = 4° and vehicle speed = 30 m/s**. The notations F_{WS}, R_{WS} and psv used in the graph labels mean 'front wheelset', 'rear wheelset' and 'passive' respectively. Figure 5.13d shows the left ASW actuator forces on the front and rear wheelsets of the front bogie.

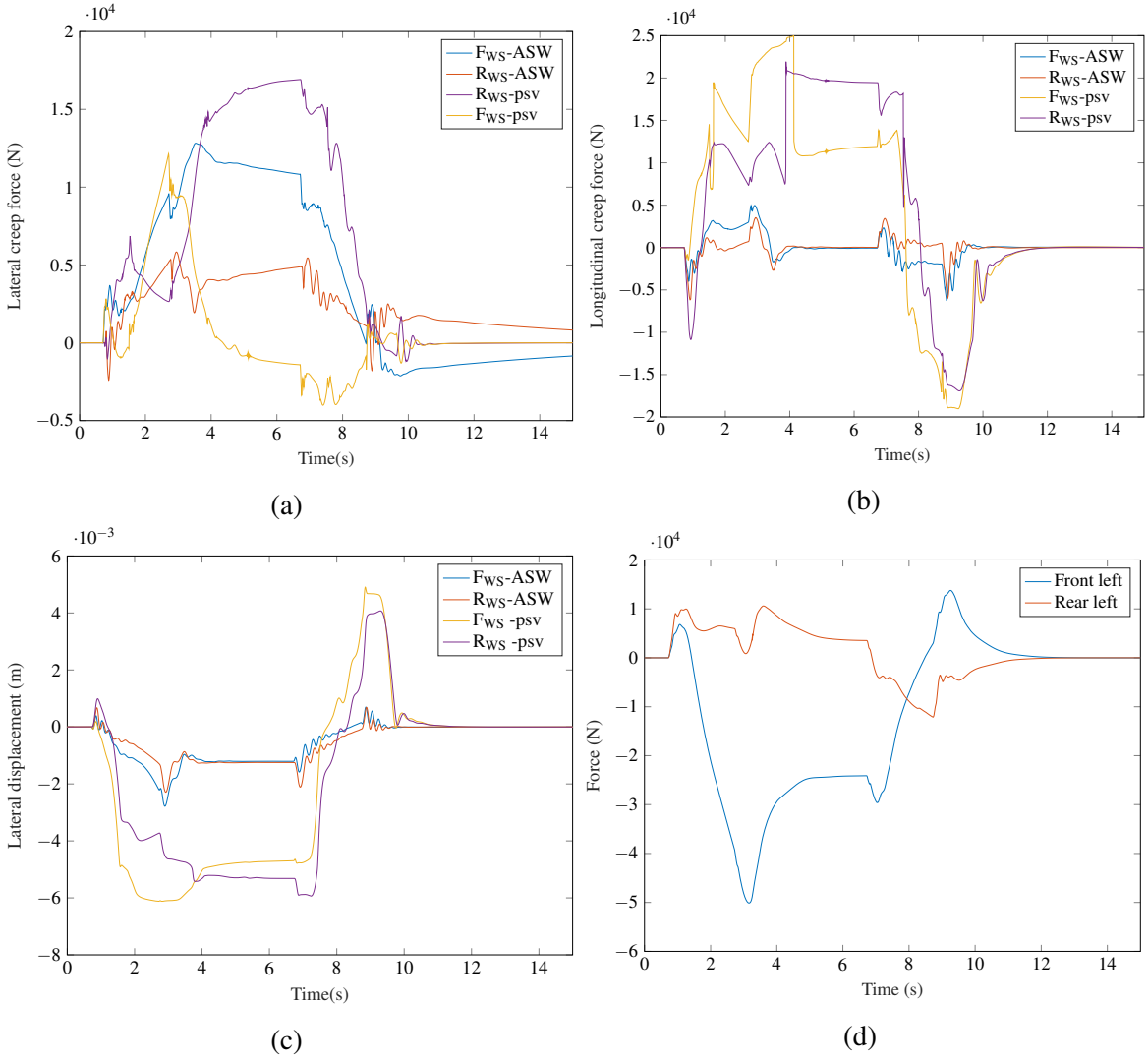

Figure 5.14: Lateral creep force, longitudinal creep force and lateral displacement response of the ASW vehicle compared to the passive vehicle on **curved track with radius = 1200 m, cant = 4° and vehicle speed = 45 m/s**. The notations F_{WS}, R_{WS} and psv used in the graph labels mean 'front wheelset', 'rear wheelset' and 'passive' respectively. Figure 5.14d shows the left ASW actuator forces on the front and rear wheelsets of the front bogie.

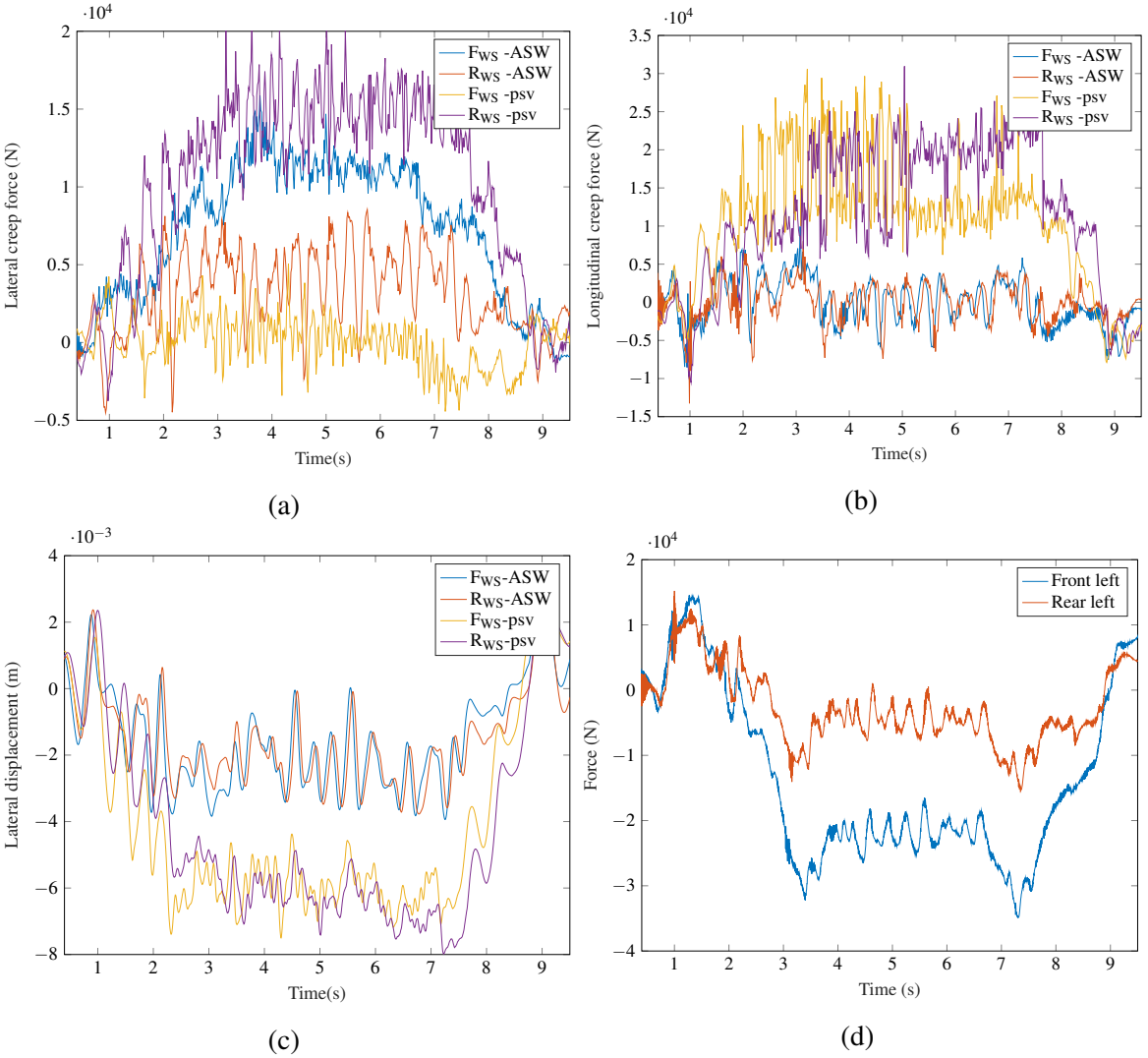

Figure 5.15: Lateral creep force, longitudinal creep force and lateral displacement response of the ASW vehicle compared to the passive vehicle on **curved track with radius = 1200 m, cant = 4° and vehicle speed = 45 m/s, with lateral, vertical and gauge width stochastics**. The notations F_{WS}, R_{WS} and psv used in the graph labels mean 'front wheelset', 'rear wheelset' and 'passive' respectively. Figure 5.15d shows the left ASW actuator forces on the front and rear wheelsets of the front bogie.

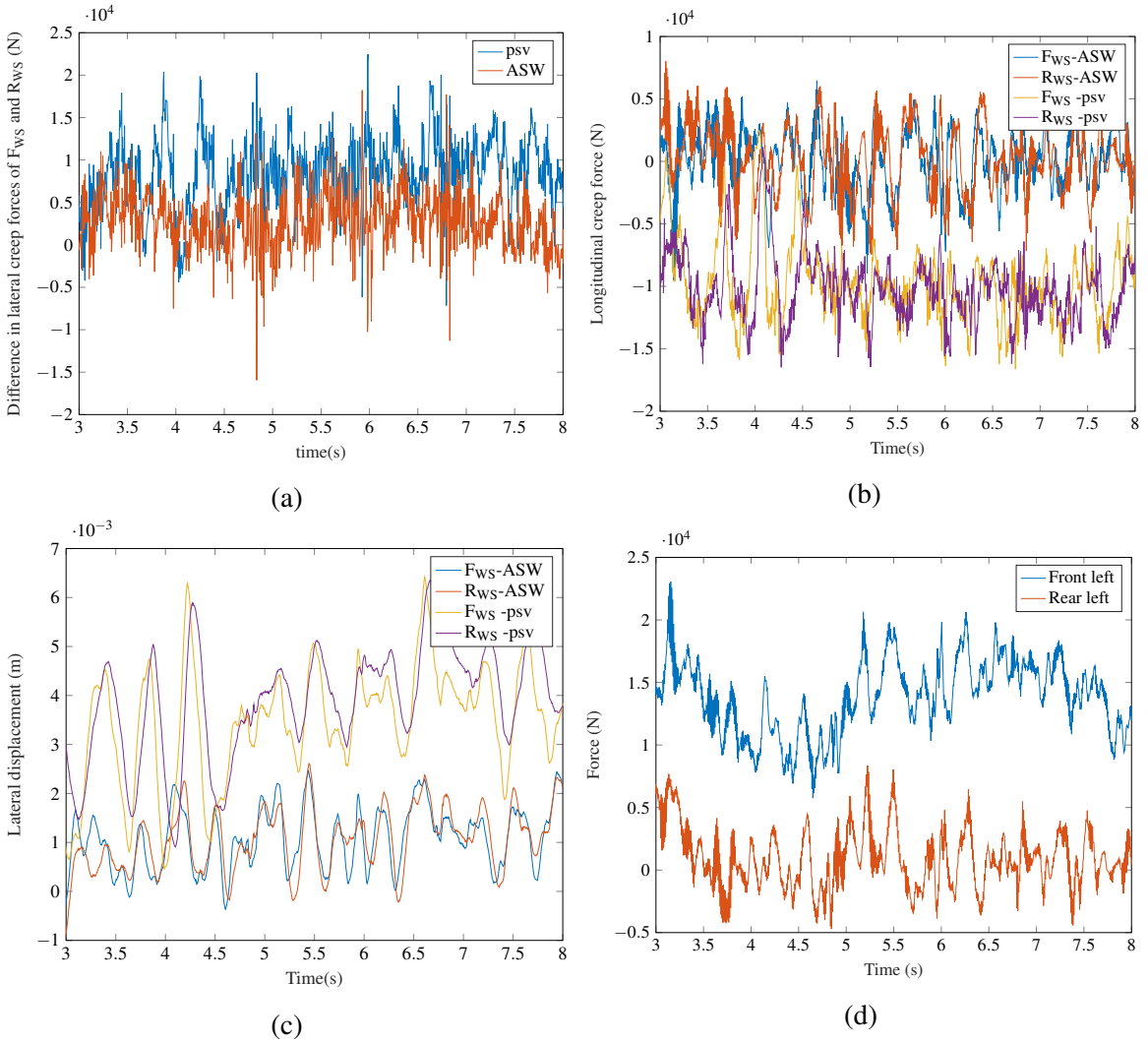

Figure 5.16: Longitudinal creep force and lateral displacement response of the ASW vehicle compared to the passive vehicle on the **straight track with stochastic disturbances**. The notations F_{WS}, R_{WS} and psv used in the graph labels mean 'front wheelset', 'rear wheelset' and 'passive' respectively. Figure 5.16a compares the difference in the lateral creep forces of the front and rear wheelsets of the ASW and passive vehicles. Figure 5.16d shows the left ASW actuator forces on the front and rear wheelsets of the front bogie.

5.4.3 DIRW

Figure 5.17 shows the response of the DIRW vehicle on a curve with radius = 535 m, cant = 4° and vehicle speed = 30 m/s. The controller in the DIRW mechanism aims to reduce the wheelset lateral displacement to zero. Figure 5.17c shows that the lateral displacement is significantly reduced compared to the passive vehicle on the steady states. The DIRW vehicle also shows lower longitudinal creep forces on the steady states as can be seen in Figure 5.17b. The DIRW concept relies on motor torques generating longitudinal creep forces to provide a yawing action to the wheelset. The longitudinal creep forces are lower than that of a conventional vehicle because only the forces necessary for steering are generated and not those compensating for the kinematic steering effects. Conventionally, large unnecessary longitudinal creep forces are generated due to the sub-optimal performance of the suspension. If the wheelset lateral displacement is not controlled to go to zero, the longitudinal creep forces can be reduced further. The difference in the lateral creep forces of front and rear wheelsets is also reduced as shown in Figure 5.17a. The motor torques peak at about 6 kNm for each wheelmotor as shown in Figure 5.17d. The low actuation requirement is due to the fact that the wheels are able to rotate independently of each other and therefore have very low slip compared to a solid-axle wheelset. The lower longitudinal creep forces are also indicative of this low slip.

Figure 5.18 shows the response of the DIRW vehicle on the high speed curve with radius = 1200 m, cant = 4° and vehicle speed = 45 m/s. An overall improvement is seen in the DIRW vehicle response compared to the passive vehicle in terms of reduced lateral creep force difference of the front and rear wheelsets and lower longitudinal creep forces and wheelset lateral displacements in Figures 5.18a, 5.18b and 5.18c. The torque requirement in this scenario is lower than in the previous track profile as can be seen by comparing Figures 5.18d and 5.17d which is expected due to the shallower curve radius.

Figure 5.19 shows the response of the DIRW vehicle on the high speed curve with stochastic disturbances. The graphs have been zoomed in to show only the constant curve and the transitions for visual clarity. It can be seen from Figure 5.19c the controller successfully reduces the wheelset lateral displacement even in the presence of track disturbances. The longitudinal creep forces are reduced as shown in Figure 5.19b. The difference in lateral creep forces at the front and rear wheelsets is lower than in the passive vehicle as shown in Figure 5.19a. The torque requirement is marginally higher as shown in Figure 5.19d than on the curve without any stochastics.

Figure 5.20 shows the response of the DIRW vehicle on the straight track profile with stochastic disturbances. The lateral wheelset displacement is significantly lower than the passive vehicle as shown in Figure 5.20c. The longitudinal creep forces and the lateral creep

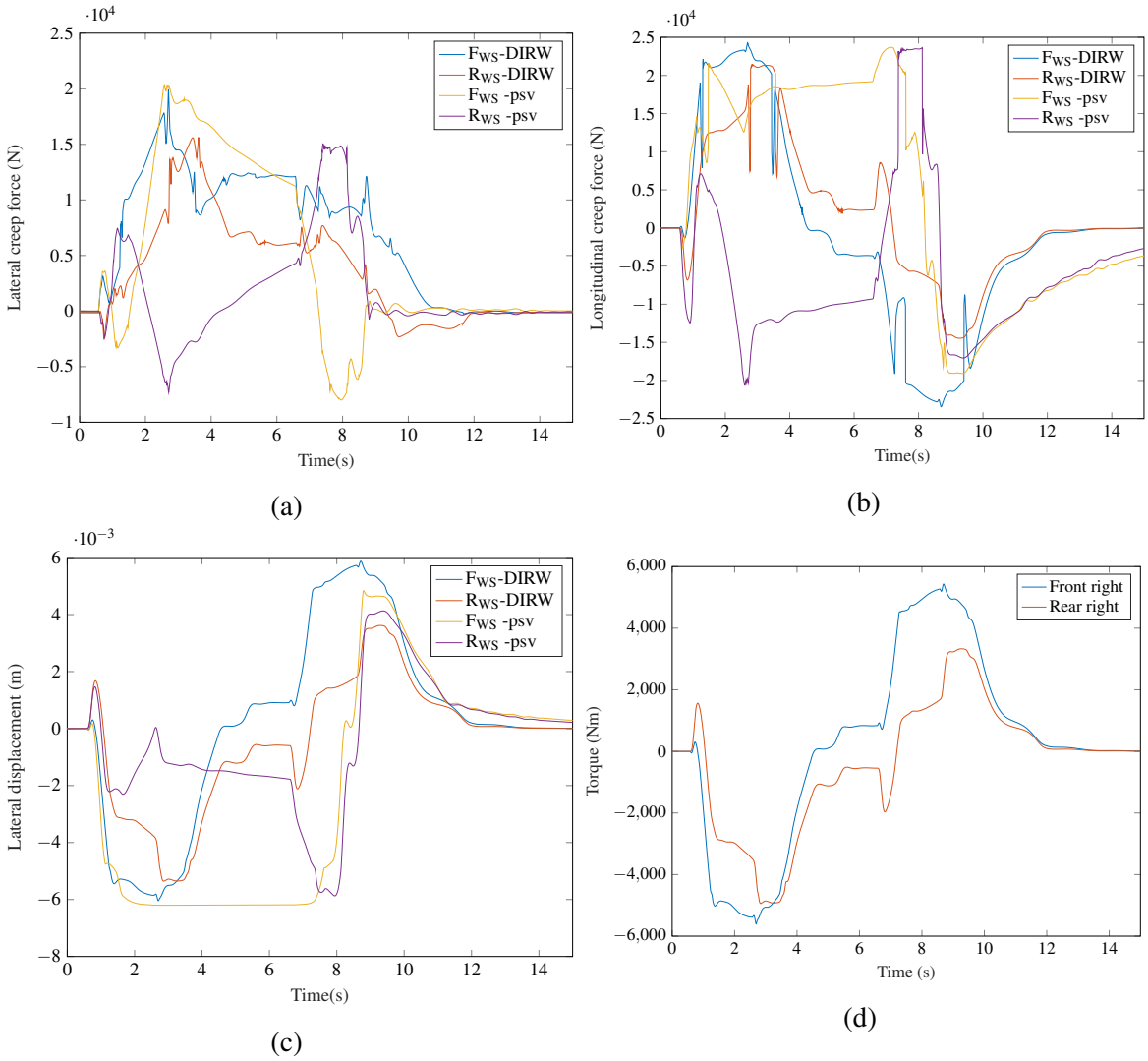

Figure 5.17: Lateral creep force, longitudinal creep force and lateral displacement response of the DIRW vehicle compared to the passive vehicle on **curved track with radius = 535 m, cant = 4° and vehicle speed = 30 m/s**. The notations F_{WS}, R_{WS} and psv used in the graph labels mean 'front wheelset', 'rear wheelset' and 'passive' respectively. Figure 5.17d shows the right DIRW motor forces on the front and rear wheelsets of the front bogie.

force difference between the front and rear wheelsets is also lower as can be seen from Figures 5.20b and 5.20a respectively.

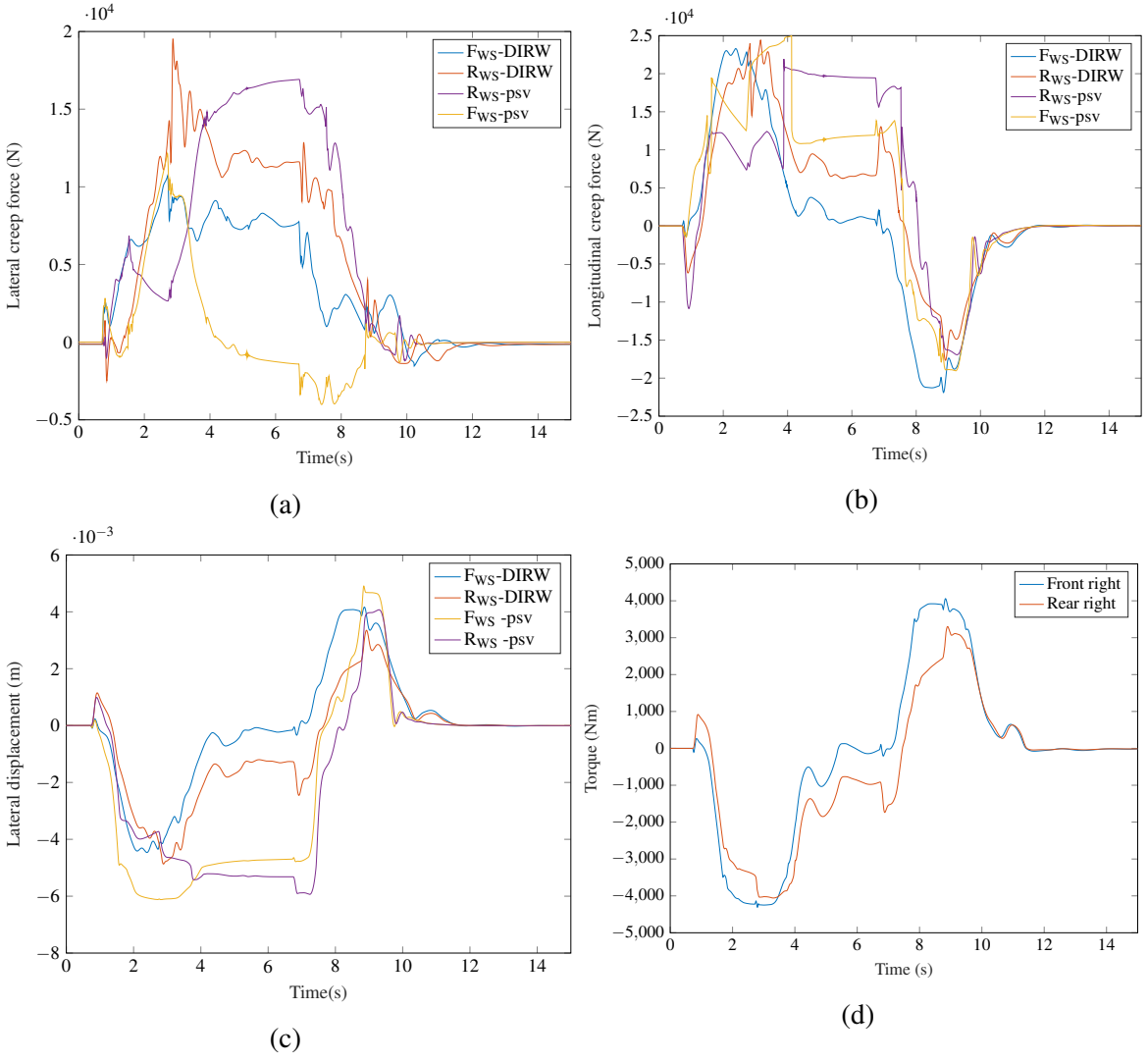

Figure 5.18: Lateral creep force, longitudinal creep force and lateral displacement response of the DIRW vehicle compared to the passive vehicle on **curved track with radius = 1200 m, cant = 4° and vehicle speed = 45 m/s**. The notations F_{WS}, R_{WS} and psv used in the graph labels mean 'front wheelset', 'rear wheelset' and 'passive' respectively. Figure 5.18d shows the right DIRW motor forces on the front and rear wheelsets of the front bogie.

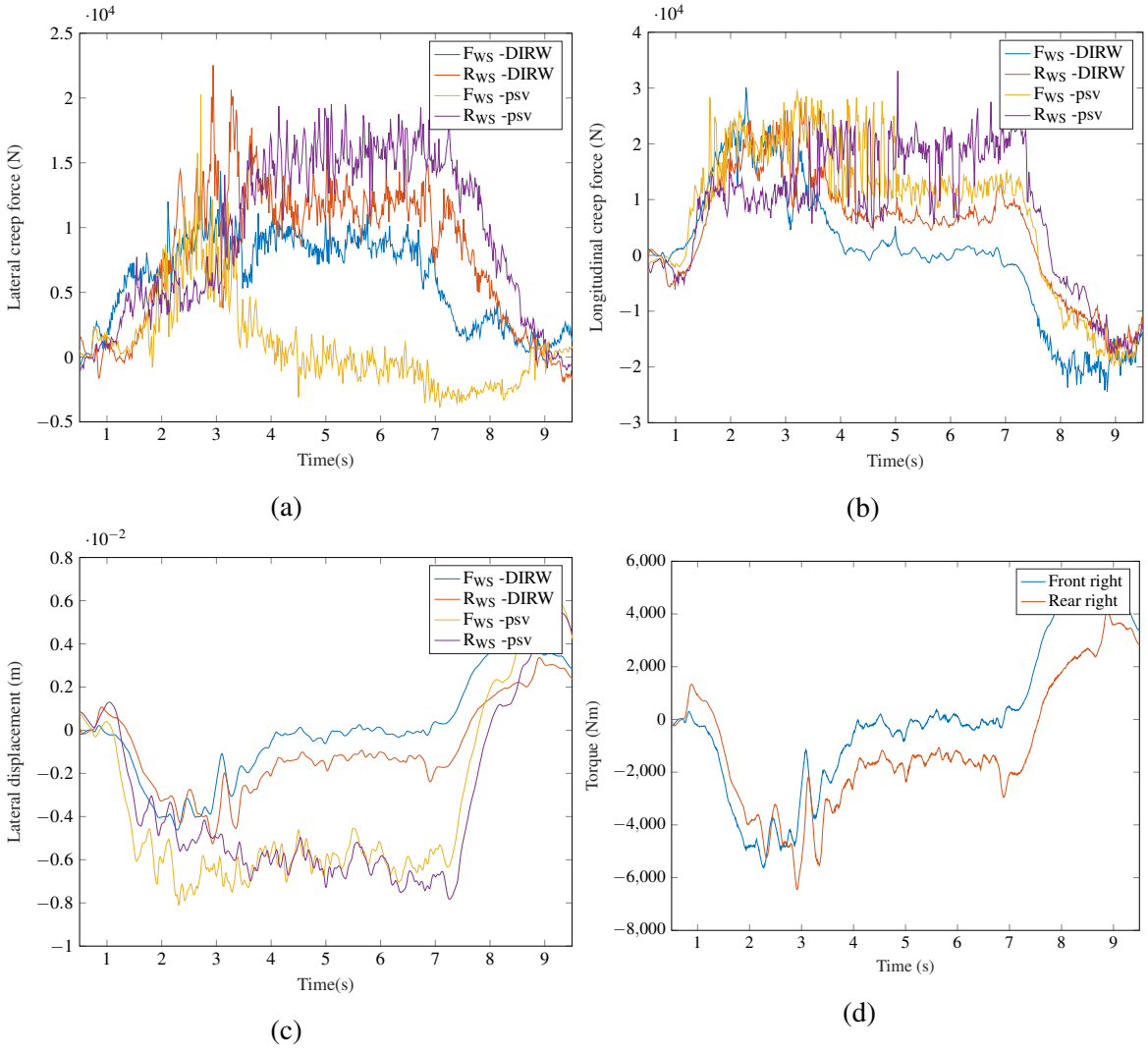

Figure 5.19: Lateral creep force, longitudinal creep force and lateral displacement response of the DIRW vehicle compared to the passive vehicle on **curved track with radius = 1200 m, cant = 4° and vehicle speed = 45 m/s, with lateral, vertical and gauge width stochastics**. The notations F_{WS}, R_{WS} and psv used in the graph labels mean 'front wheelset', 'rear wheelset' and 'passive' respectively. Figure 5.19d shows the right DIRW motor forces on the front and rear wheelsets of the front bogie.

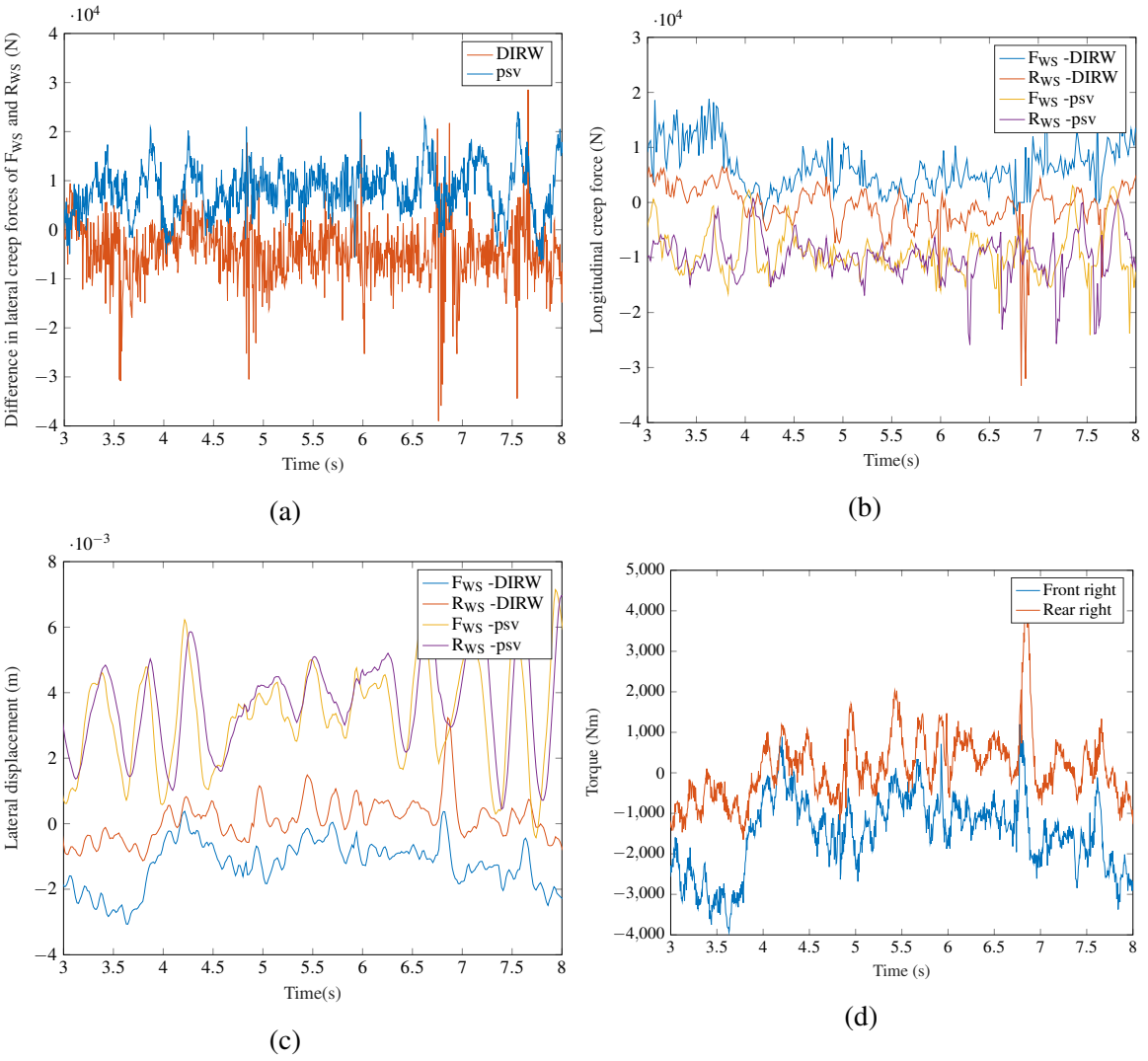

Figure 5.20: Longitudinal creep force and lateral displacement response of the DIRW vehicle compared to the passive vehicle on the **straight track with stochastic disturbances**. The notations F_{WS}, R_{WS} and psv used in the graph labels mean 'front wheelset', 'rear wheelset' and 'passive' respectively. Figure 5.20a compares the difference in the lateral creep forces of the front and rear wheelsets of the DIRW and passive vehicles. Figure 5.20d shows the right DIRW motor forces on the front and rear wheelsets of the front bogie.

5.4.4 Wheel-rail wear

The wheel-rail wear is assessed in terms of the energy dissipated in the contact patch which is denoted as $T\gamma$. Graphical $T\gamma$ results are in Appendix B. Average $T\gamma$ values of each wheelset in the four different vehicles on the track profiles under consideration are given in Table 5.2. The total $T\gamma$ values are also expressed as a percentage of the passive vehicle in each scenario.

The SYC vehicle has very high values of $T\gamma$, higher in several track profiles than the passive vehicle. This is due to the high longitudinal creep forces generated when the wheelsets make flange contact by displacing laterally to reduce the lateral creep force difference between the front and rear wheelsets to zero. Although it controls the lateral creep force difference as expected, it does not provide the best overall performance.

From the graphs in section 5.4.2, it was deduced that the ASW vehicle has lower longitudinal creep forces, lateral creep force difference and wheelset lateral displacement. This contributes to the lower $T\gamma$ values than the passive vehicle in all the track scenarios under consideration as can be seen in Table 5.2.

The DIRW vehicle has even lower values of $T\gamma$. This can be attributed to the fact that IRWs generate low longitudinal creep forces due to the absence of a rigid connection between the two wheels on the same axle. If the wheelset lateral displacement is not controlled to zero, the longitudinal creep forces can be further reduced which would contribute to a lower wear index value. However, from all the graphical results it can be seen that the DIRW vehicle has lower wheelset lateral displacement, longitudinal creep forces and a reduced difference in the lateral creep forces between the front and rear wheelsets than the passive vehicle. The torque requirement of the DIRW mechanism is also lower than that of the other active vehicles due to the absence of the constraints from a solid-axle wheelset.

In terms of RCF initiation due to wear, the values in bold in Table 5.2 are above the RCF threshold. It can be seen that most of the values that exceed the threshold are those of the passive and SYC vehicles.

The SYC vehicle has less implications in terms of safety than the ASW vehicle due to being in the secondary suspension but does not offer a significant improvement in performance. It is interesting to note that the DIRW vehicle requires the most radical change but promises the best performance.

Table 5.2: Average $T\gamma$ values on the different track profiles considered using classical controllers. Note that the units for the $T\gamma$ values is J/m. Values in bold are those above the RCF threshold.

Curved track at R=1200 m, v=45 m/s				
	Passive	SYC	ASW	DIRW
Front bogie front WS	**30.03**	**21.55**	9.92	0.15
Front bogie rear WS	10.25	0.64	1.77	0.08
Rear bogie front WS	1.72	**59.92**	1.22	1.49
Rear bogie rear WS	3.62	15.82	12.37	5.89
Total $T\gamma$ on all WSs	45.62	97.94	25.29	7.61
Percentage of passive	100	222.24	57.38	17.27
Curved track at R=534.52 m, v=30 m/s				
	Passive	SYC	ASW	DIRW
Front bogie front WS	**84.47**	**16.85**	15.44	1.13
Front bogie rear WS	4.99	2.10	0.24	0.84
Rear bogie front WS	**26.16**	**48.94**	1.56	10.23
Rear bogie rear WS	**39.38**	6.62	**27.78**	10.48
Total $T\gamma$ on all WSs	155.00	74.52	45.02	22.67
Percentage of passive	100	48.08	29.05	14.63
Curved track with stochastics at R=1200 m, v=45 m/s				
	Passive	SYC	ASW	DIRW
Front bogie front WS	13.59	**22.42**	10.45	1.39
Front bogie rear WS	12.31	1.19	2.18	0.63
Rear bogie front WS	0.57	**59.42**	1.23	2.20
Rear bogie rear WS	**17.08**	15.50	13.39	4.86
Total $T\gamma$ on all WSs	43.55	98.52	27.25	9.08
Percentage of passive	100	226.25	62.57	20.86
Straight track with stochastics				
	Passive	SYC	ASW	DIRW
Front bogie front WS	0.81	15.22	3.89	1.21
Front bogie rear WS	**18.99**	13.52	3.04	2.89
Rear bogie front WS	0.34	**24.19**	2.05	7.70
Rear bogie rear WS	**17.39**	**47.83**	6.79	3.63
Total $T\gamma$ on all WSs	37.53	100.76	15.77	15.43
Percentage of passive	100	268.48	42.02	41.11

5.4.5 Actuation requirements

The maximum force/ torque output from the actuators in each of the active vehicles is given in Table 5.3. The 'straight track' values are those obtained from the straight track profile with stochastics and the 'curved track' is the track profile with radius = 1200 m, cant = 4° and vehicle speed = 45 m/s. Some examples of actuators that could be used in each application are also listed which shows that the required control force is achievable using readily available actuators of reasonable power consumption.

Power requirement is lowest for SYC vehicle on straight track due to the natural guidance mechanism of wheelsets as on a conventional vehicle. The DIRW mechanism power requirement is also much lower on straight track compared to the ASW mechanism as the control is not acting against the natural guidance of the wheelsets. In the curved track scenario, the transition period is fairly slow, leading to a low maximum velocity of the actuator for the SYC and ASW vehicles. The power consumption for the DIRW mechanism is still high because power is still required to drive one of the wheels faster and the other slower to follow the track centre line. The velocities of the two wheels on a single wheelset are not equal and opposite about the nominal velocity due to a net lateral displacement when the vehicle is negotiating a curve. This lateral displacement is necessary to provide the appropriate lateral creep forces. The power from the decelerating wheel is considered to be used to drive the accelerating wheel. It is important to note that although the maximum per wheel power consumption in the DIRW mechanism is 1.55 kW, this is only for a very short period during the transition from straight to curved track. On steady state it is approximately 200 W which is fractional compared to the power consumption of each wheel to drive the vehicle which is $\approx$ 100 kW [1].

In spite of the higher power requirement of the DIRW vehicle on a curved track, it appears to give the best solution. It shows the most significant improvement compared to a conventional vehicle in terms of reduced wear and minimal flange contact with much less actuation effort than the ASW mechanism which offers the next best performance.

[1] This is calculated based on an acceleration of 0.5 m/s^2 from $P = mass \times acceleration \times velocity$ where the vehicle velocity is 45 m/s and the mass on each wheel is $\approx$ 4300 kg.

Table 5.3: Actuation requirements on straight and curved track

Straight track requirements	SYC	ASW	DIRW
Average force/ torque	9.76/ 19.52 kN	9.6/ 22.93 kN	0.46/ 1.39 kNm
Maximum force/ torque	195/ 390 kN	79.4/ 518 kN	5.2/ 18.57 kNm
Average power	51.73/ 103.46 W	200/ 676.3 W	121/ 600 W
Maximum power	34/ 68 kW	69.4/ 169.3 kW	19/ 3.88 kW
Maximum displacement	5.37 mm	9.1 mm	continuous
Maximum velocity	1.54×10^{-1} m/s	2.05 m/s	104.4 rad/s
Curved track requirements	**SYC**	**ASW**	**DIRW**
Maximum force/ torque	16.39/ 32.78 kN	50.12/ 86.6 kN	5.37/ 21.76 kNm
Maximum power	79.22/ 158.44 W	198.59/ 448 W	1.55/ 2.31 kW
Maximum displacement	5 mm	3.6 mm	continuous
Maximum velocity	7.8×10^{-3} m/s	4.3×10^{-3} m/s	97.9 rad/s
Example actuator	MTS Series 244.12 [100]	Moog A085 [101]	Alstom 4 FXA 4553 [102]
Dimensions	height= 625 mm diameter=141 mm	height= 137.9 mm width= 101.6 mm	width x height x length = 190 x 190 x 242 mm

Note:

1. Where there are two values separated by a '/', the first value indicates that for each actuator and the second is that per bogie. The force/ power values for each actuator for a particular mechanism are different and the 'per bogie' values are the sum of those on the front bogie.

2. For the curved track situation, average force and power values are not calculated as maximum values are more relevant when the rail vehicle is transitioning from straight to curved track and vice versa.

3. Maximum displacement for the DIRW mechanism is indicated as 'continuous' because the motors are in motion due to the forward running of the vehicle.

4. Maximum velocity for the DIRW mechanism can be misleading as it includes the nominal wheel rotational velocity which is 45/0.46 rad/s based on the vehicle running velocity and the nominal wheel radius.

5. The force and power requirements for the DIRW mechanism are calculated by isolating that required for the running of the vehicle to give a common platform to compare all three mechanisms.

5.5 Active vehicle simulations using PIP controllers

In this section, the SYC, ASW and DIRW vehicles are compared to the passive vehicle and to each other using the PIP controller designed in Chapter 4. As with the classical controllers, only the front bogie plots are presented and discussed here. The rear bogie dynamics were found to be largely similar to the dynamics of the front bogie in the classical case and therefore and the graphs from the rear bogie are not included for the PIP simulations.

5.5.1 SYC

On the curved track profile with radius = 535 m, cant = 4° and vehicle speed = 30 m/s, the PIP controller in the SYC vehicle reduces the difference in lateral creep forces at the front and rear wheelsets to zero effectively as shown in Figure 5.21a. The longitudinal creep forces are similar to the passive vehicle as shown in Figure 5.21b. The wheelset lateral displacement graphs in Figure 5.21c show that the front wheelset makes flange contact.

Figure 5.22 shows the response of the SYC vehicle on a curve with radius = 1200 m, cant = 4° and vehicle speed = 45 m/s. The wheelset lateral displacement graphs in Figure 5.22c show that the wheelsets on the SYC vehicle sit against the flanges resulting in high longitudinal creep forces as shown in Figure 5.22b. Comparing Figures 5.21d and 5.22d which show the actuation torques on the 30 m/s and 45 m/s curves respectively, it can be seen that the requirement for the latter scenario is higher. This is unusual as the torque should be lower for a curve of larger radius, indicating that the SYC mechanism is inefficient in terms of using much of the torque to “fight" against the natural guidance of the solid-axle wheelsets and therefore generating unnecessary longitudinal creep forces.

Figure 5.23 shows the response of the SYC vehicle on the high speed curve with stochastics. The figures have been zoomed in to show only the curve transitions and steady state. From Figure 5.23a it can be seen that the PIP controller successfully reduces the difference in the lateral creep forces at the front and rear wheelset. Figure 5.23c shows that the wheelsets on both the SYC and passive vehicles make flange contact. The longitudinal creep forces of both vehicles are in a similar range as can be seen in Figure 5.23b. The torque requirement is marginally higher as shown in Figure 5.23d than the previous case which is expected due to the addition of stochastics.

Figure 5.24 shows the response of the SYC vehicle on the straight track profile with stochastics. The figures have been zoomed in for visual clarity. From Figure 5.24a it can be seen that the PIP controller successfully reduces the difference in the lateral creep forces at the front and rear wheelset. Figures 5.24c and 5.24b show that the SYC vehicle has a larger wheelset lateral displacement and longitudinal creep forces than the passive vehicle.

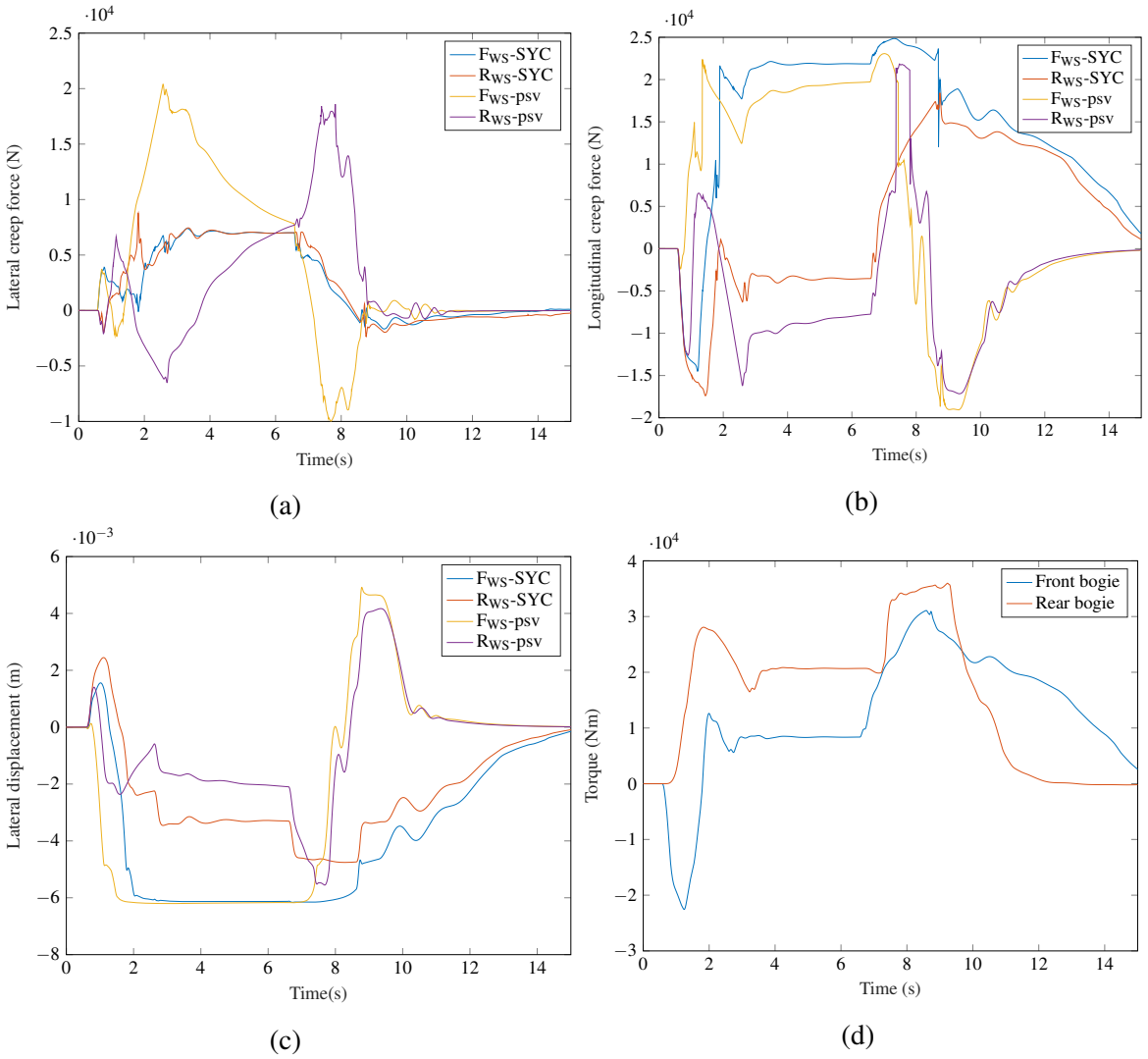

Figure 5.21: Lateral creep force, longitudinal creep force and lateral displacement response of the SYC vehicle compared to the passive vehicle on **curved track with radius = 535 m, cant = 4° and vehicle speed = 30 m/s**. The notations F_{WS}, R_{WS} and psv used in the graph labels mean 'front wheelset', 'rear wheelset' and 'passive' respectively. Figure 5.21d shows the total yaw torque acting on each bogie of the SYC vehicle.

The lateral displacement is not centred about 0 mm because the lateral track excitation is not centred about 0 mm.

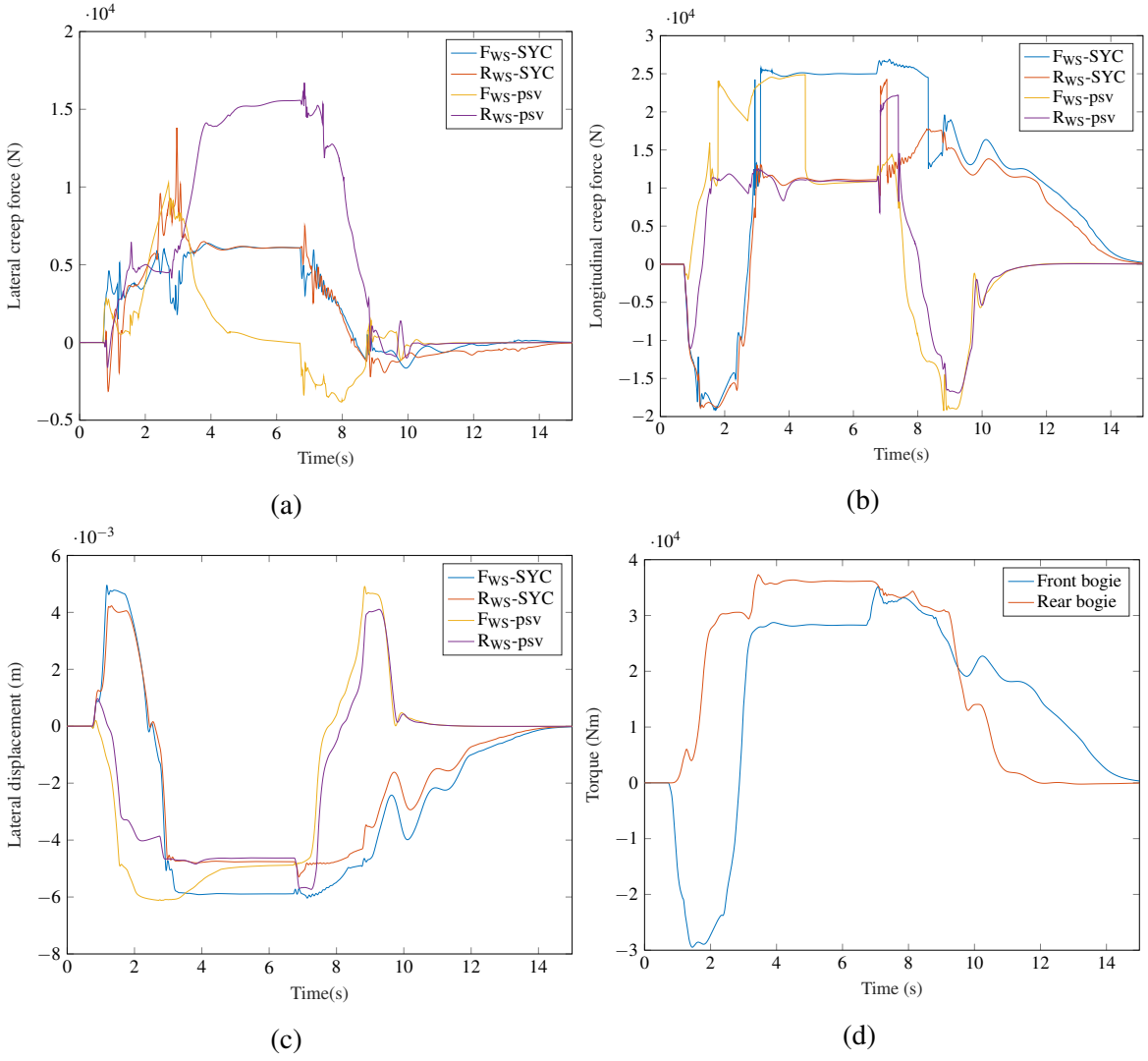

Figure 5.22: Lateral creep force, longitudinal creep force and lateral displacement response of the SYC vehicle compared to the passive vehicle on **curved track with radius = 1200 m, cant = 4° and vehicle speed = 45 m/s**. The notations F_{WS}, R_{WS} and psv used in the graph labels mean 'front wheelset', 'rear wheelset' and 'passive' respectively. Figure 5.22d shows the total yaw torque acting on each bogie of the SYC vehicle.

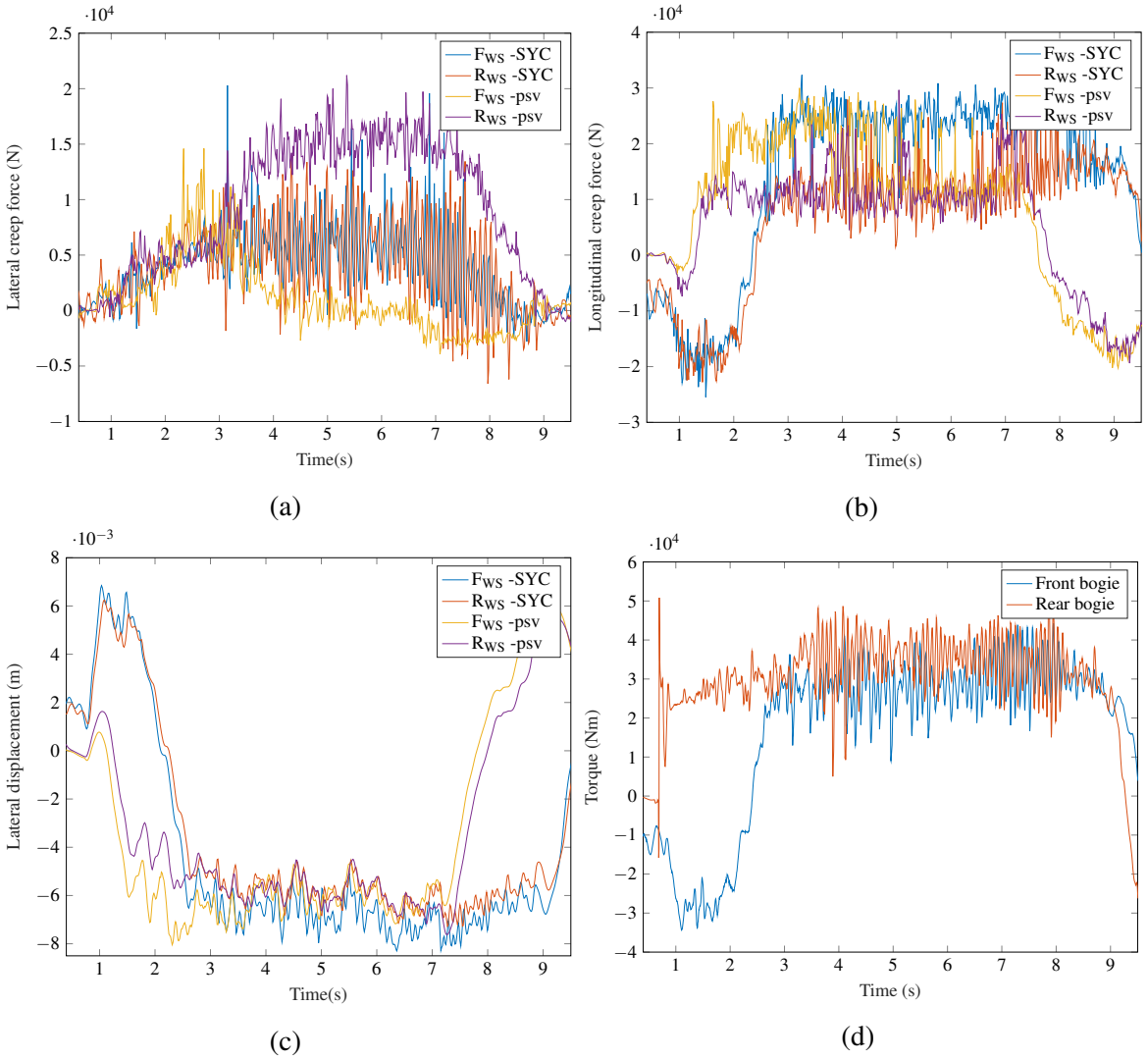

Figure 5.23: Lateral creep force, longitudinal creep force and lateral displacement response of the SYC vehicle compared to the passive vehicle on **curved track with radius = 1200 m, cant = 4° and vehicle speed = 45 m/s, with lateral, vertical and gauge width stochastics**. The notations F_{WS}, R_{WS} and psv used in the graph labels mean 'front wheelset', 'rear wheelset' and 'passive' respectively. Figure 5.23d shows the total yaw torque acting on each bogie of the SYC vehicle.

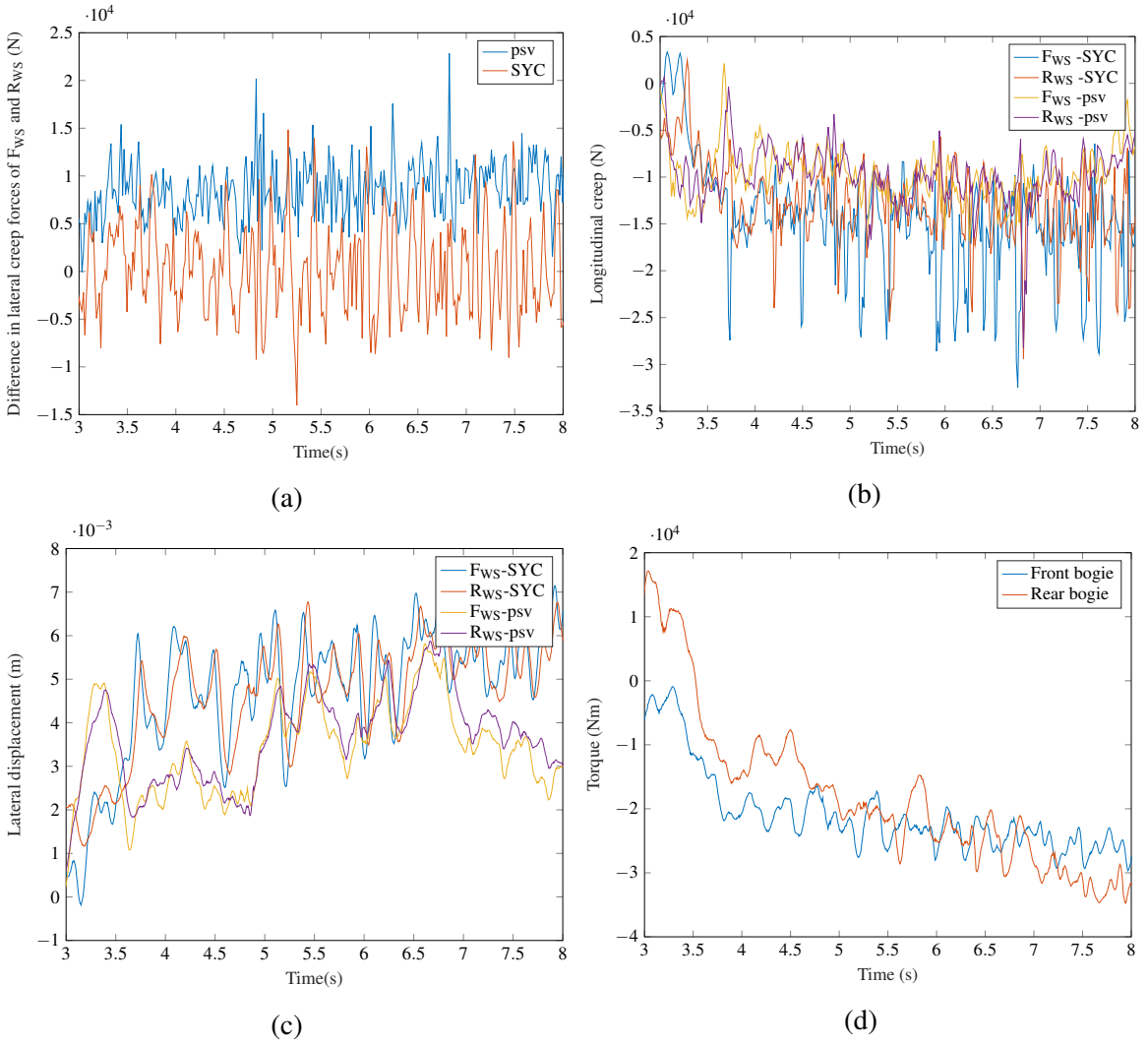

Figure 5.24: Longitudinal creep force and lateral displacement response of the SYC vehicle compared to the passive vehicle on the **straight track with stochastic disturbances**. The notations F_{WS}, R_{WS} and psv used in the graph labels mean 'front wheelset', 'rear wheelset' and 'passive' respectively. Figure 5.24a compares the difference in the lateral creep forces of the front and rear wheelsets of the SYC and passive vehicles. Figure 5.24d shows the total yaw torque acting on each bogie of the SYC vehicle.

5.5.2 ASW

Figure 5.25 shows the response of the ASW vehicle on the curved track with radius = 535 m, cant = 4° and vehicle speed = 30 m/s. The PIP controller in the ASW vehicle successfully reduces the longitudinal creep forces to zero as can be seen from Figure 5.25b. The difference between the lateral creep forces at the front and rear wheelsets is lesser than that of the passive vehicle during curve transitions but slightly higher on the steady states as shown in Figure 5.25a. The wheelset lateral displacements graphs in Figure 5.25c show that both wheelsets stay clear of the flange although the rear wheelset has a higher lateral displacement than in the passive vehicle.

On the high speed curve, the longitudinal creep forces are significantly lower than the passive vehicle during curve transitions and successfully reduced to zero on the steady states as shown in Figure 5.26b. Figure 5.26c shows that the wheelset lateral displacement on the DIRW vehicle is significantly lower than that of the passive vehicle. The difference in lateral creep forces at the front and rear wheelsets are also reduced as shown in Figure 5.26a. Comparing Figures 5.25d and 5.26d shows that the force requirement for the shallower curve is lower, which is logically expected.

Figure 5.27 shows the response of the ASW vehicle on the high speed curve with stochastics using a PIP controller. As can be seen from Figure 5.27b the longitudinal creep forces are significantly lower than the passive vehicle. The wheelset lateral displacement and the difference in lateral creep forces between the front and rear wheelsets are also lower than the passive vehicle as can be seen from Figures 5.27c and 5.27a respectively.

On the straight track profile with stochastics, the longitudinal creep forces are lower than the passive vehicle as shown in Figure 5.28b. Figures 5.28a and 5.28c show that the difference in lateral creep forces at the front and rear wheelsets and the wheelset lateral displacement is lower than the passive vehicle.

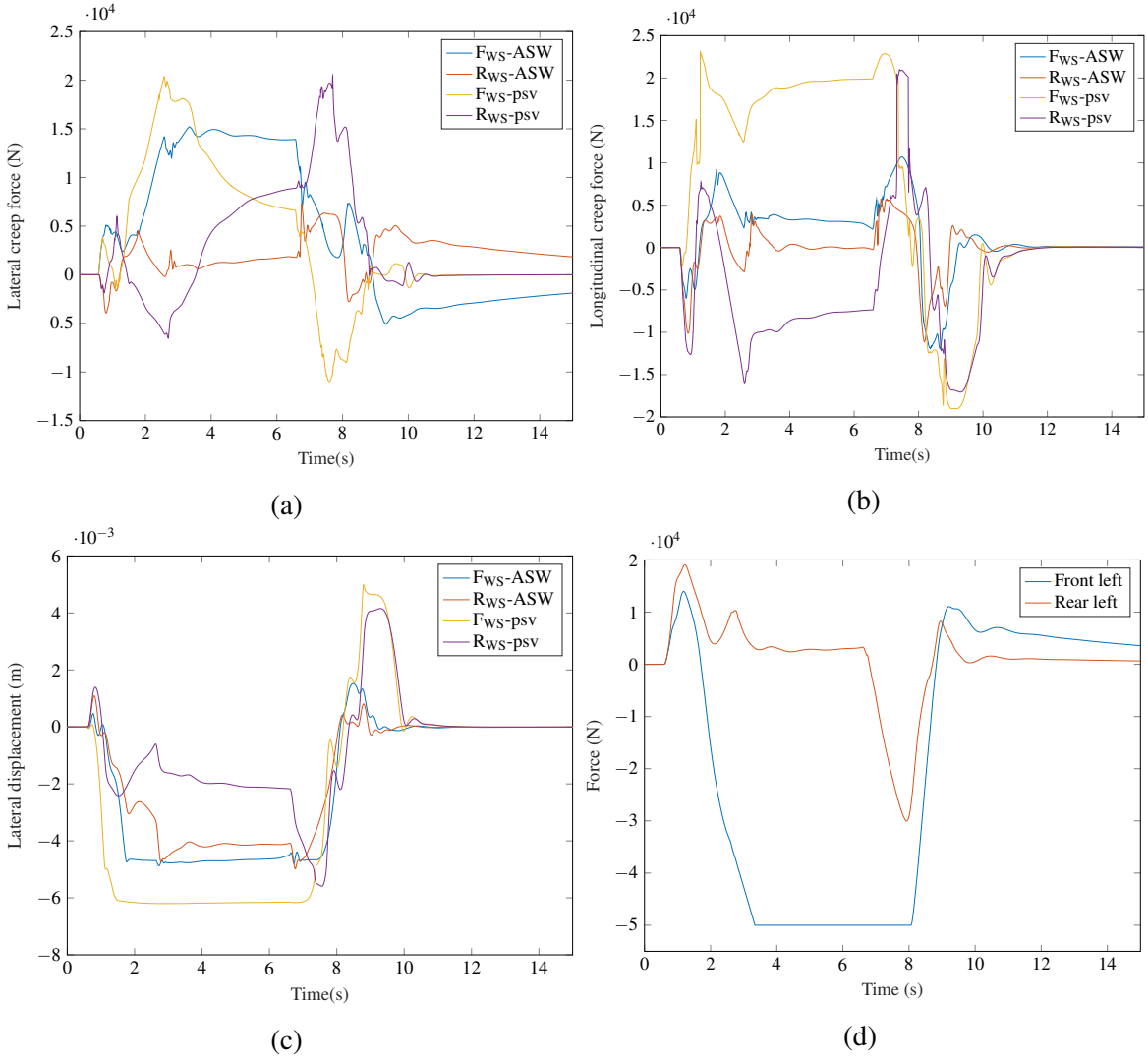

Figure 5.25: Lateral creep force, longitudinal creep force and lateral displacement response of the ASW vehicle compared to the passive vehicle on **curved track with radius = 535 m, cant = 4° and vehicle speed = 30 m/s**. The notations F_{WS}, R_{WS} and psv used in the graph labels mean 'front wheelset', 'rear wheelset' and 'passive' respectively. Figure 5.25d shows the left ASW actuator forces on the front and rear wheelsets of the front bogie.

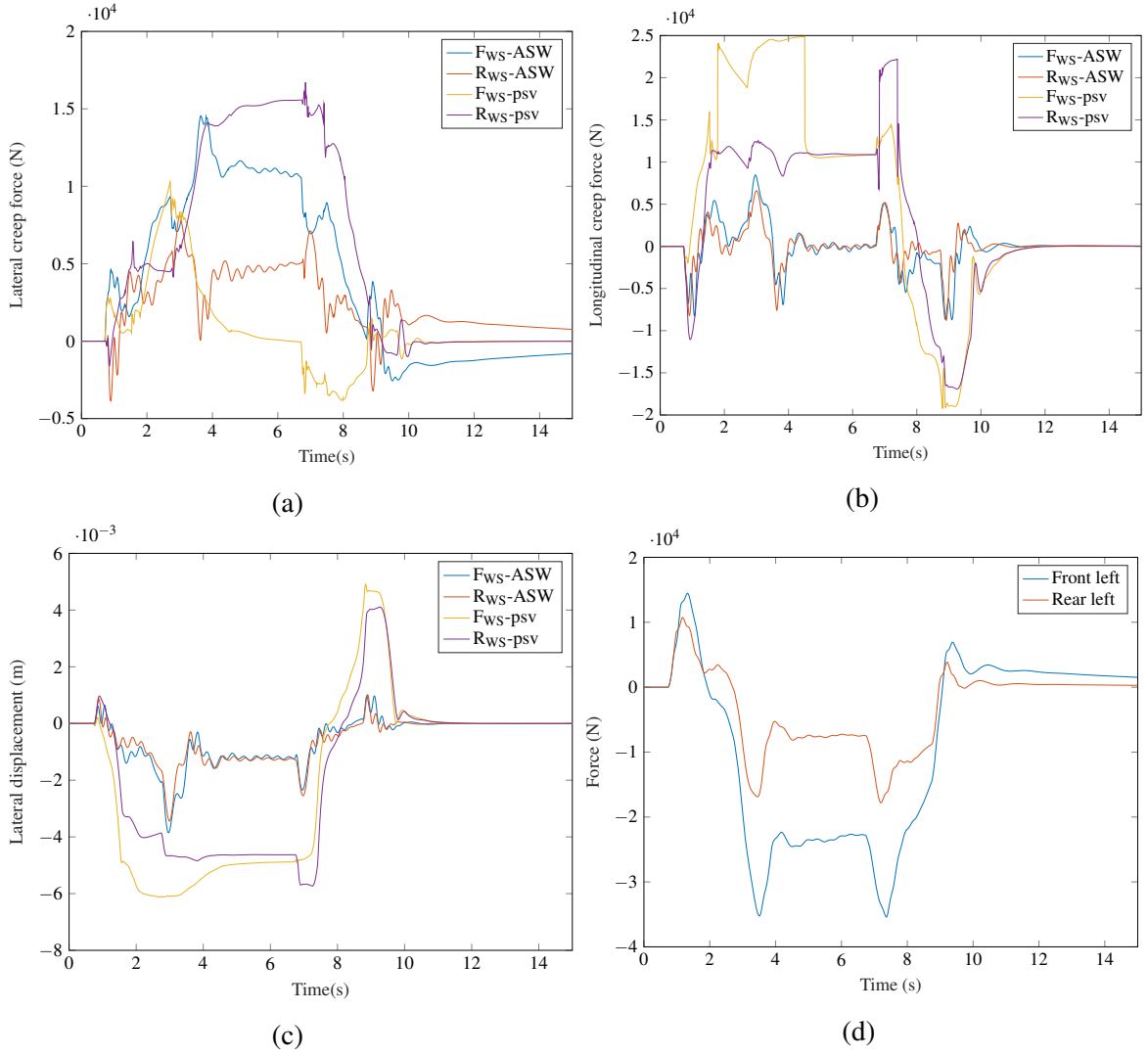

Figure 5.26: Lateral creep force, longitudinal creep force and lateral displacement response of the ASW vehicle compared to the passive vehicle on **curved track with radius = 1200 m, cant = 4° and vehicle speed = 45 m/s**. The notations F_{WS}, R_{WS} and psv used in the graph labels mean 'front wheelset', 'rear wheelset' and 'passive' respectively. Figure 5.26d shows the left ASW actuator forces on the front and rear wheelsets of the front bogie.

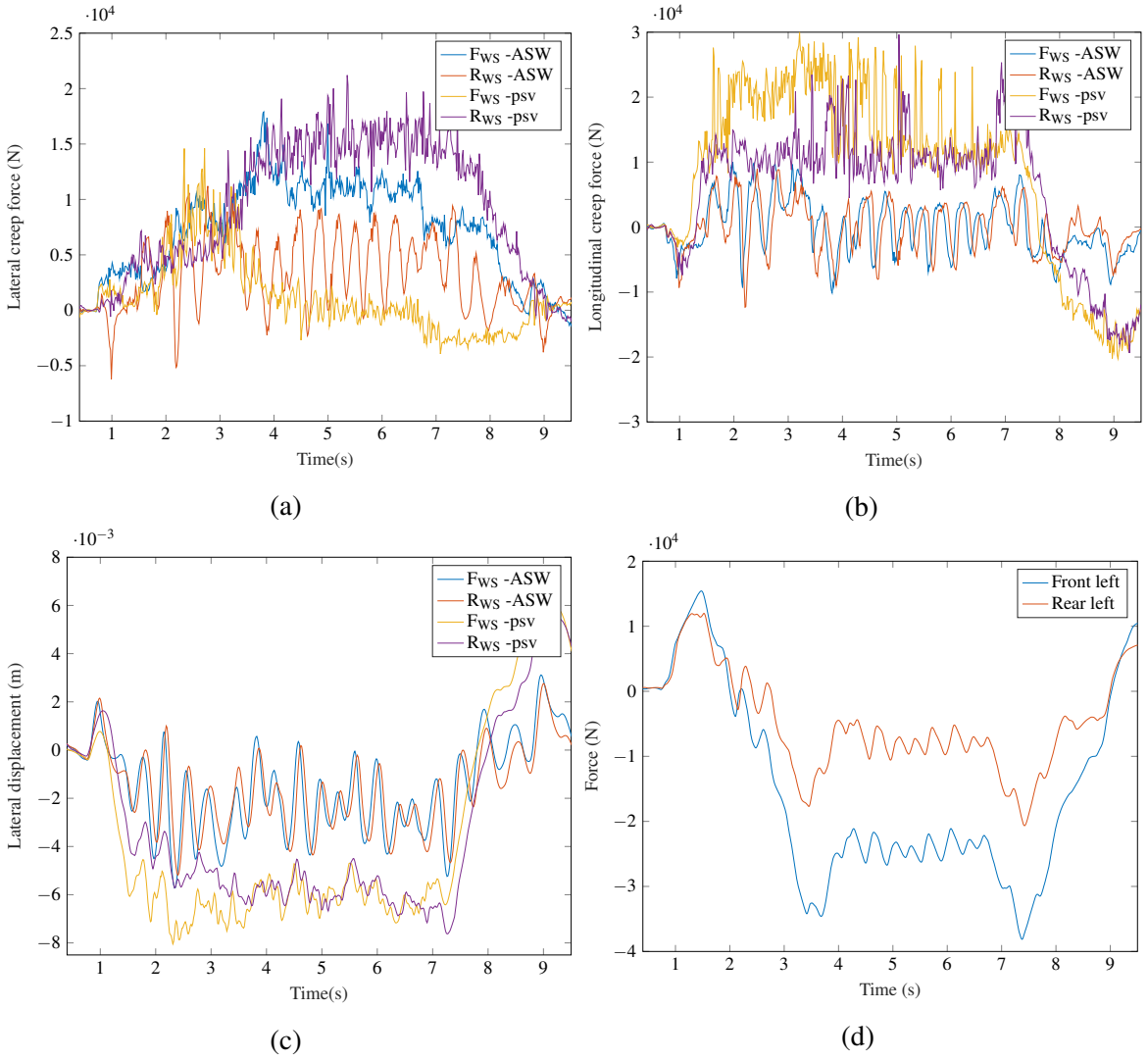

Figure 5.27: Lateral creep force, longitudinal creep force and lateral displacement response of the ASW vehicle compared to the passive vehicle on **curved track with radius = 1200 m, cant = 4° and vehicle speed = 45 m/s, with lateral, vertical and gauge width stochastics**. The notations F_{WS}, R_{WS} and psv used in the graph labels mean 'front wheelset', 'rear wheelset' and 'passive' respectively. Figure 5.27d shows the left ASW actuator forces on the front and rear wheelsets of the front bogie.

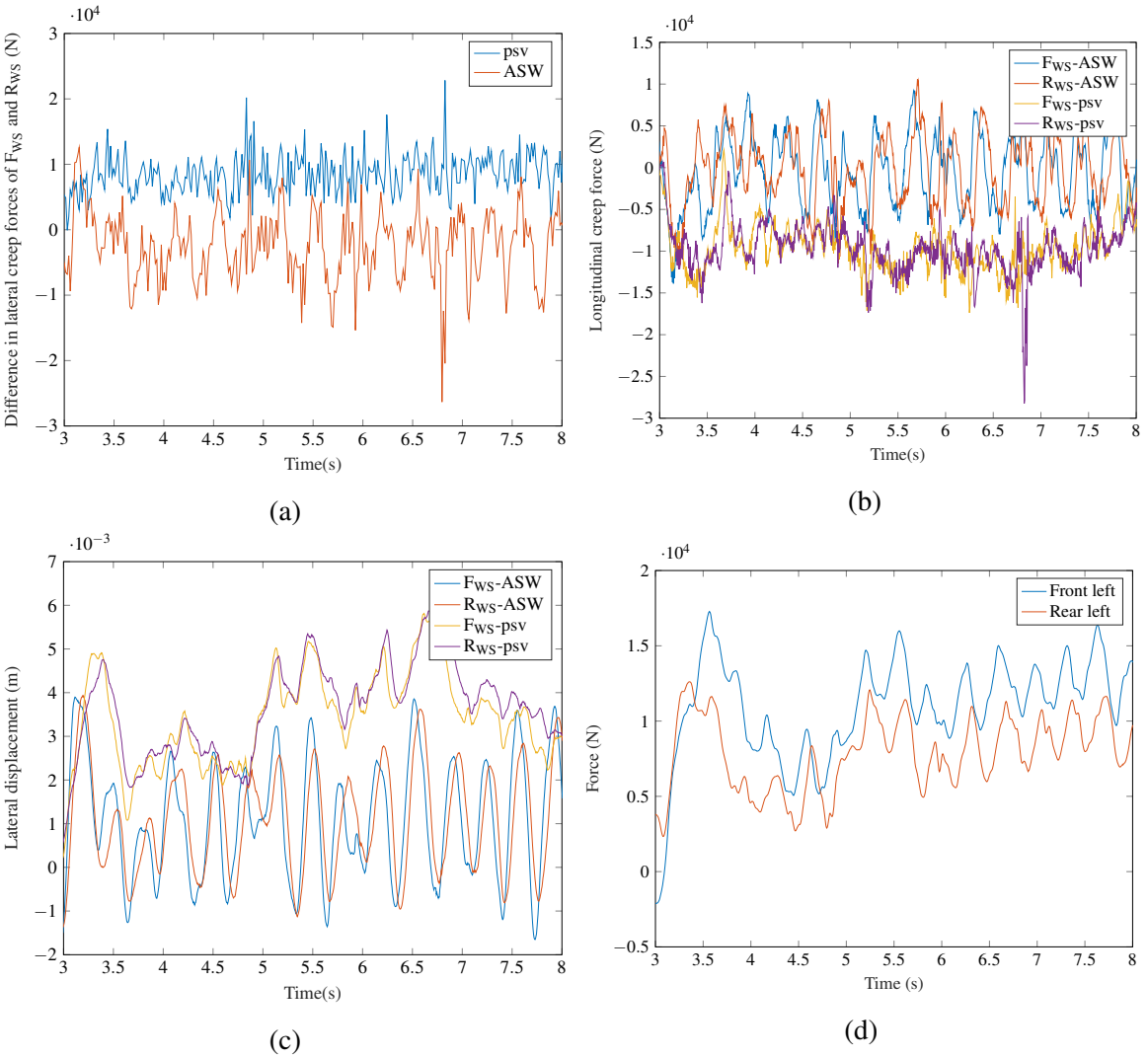

Figure 5.28: Longitudinal creep force and lateral displacement response of the ASW vehicle compared to the passive vehicle on the **straight track with stochastic disturbances**. The notations F_{WS}, R_{WS} and psv used in the graph labels mean 'front wheelset', 'rear wheelset' and 'passive' respectively. Figure 5.28a compares the difference in the lateral creep forces of the front and rear wheelsets of the ASW and passive vehicles. Figure 5.28d shows the left ASW actuator forces on the front and rear wheelsets of the front bogie.

5.5.3 DIRW

The PIP controller was applied to the DIRW vehicle on the four different track profiles under consideration. Figure 5.29 shows the response of the DIRW vehicle on the curved track with radius = 535 m, cant = 4° and vehicle speed = 30 m/s. Figure 5.29c shows that wheelset lateral displacements are reduced with both wheelsets maintaining minimum flange contact. The longitudinal creep forces are lower than the passive vehicle on the curve steady state and marginally higher on curve transitions as shown in Figure 5.29b. The lateral creep force difference between the front and rear wheelset is significantly reduced in the transitions while the reduction is less in the steady states as shown in Figure 5.29a.

On the high speed curve, the longitudinal creep forces of the DIRW vehicle are lower than that of the passive vehicle as shown in Figure 5.30b. The lateral creep force difference between the front and rear wheelsets is lower than the passive vehicle in the steady state but marginally higher in the transitions as shown in Figure 5.30a. The wheelset lateral displacement is also lower than the passive vehicle and both wheelsets maintain minimal flange contact as shown in Figure 5.30c. The torque requirement is fairly similar on both curved track profiles as shown in Figures 5.29d and 5.30d with a slightly lower requirement on the steady state of the high speed curve which is expected due to the shallow radius.

On the curved track with stochastics, it can be seen from Figure 5.31c that the PIP controller successfully reduces the wheelset lateral displacement. The lateral creep force difference between the front and rear wheelsets and the longitudinal creep forces are also reduced as shown in Figures 5.31a and 5.31b.

Figure 5.32 shows the response of the DIRW vehicle using a PIP controller on the straight track profile with stochastics. There is a clear decrease in the wheelset lateral displacement as shown in Figure 5.32c. A reduction in the lateral creep force difference between the front and rear wheelsets can also be seen in Figure 5.32a. There is a decrease in the longitudinal creep force of the front wheelset compared to that of the passive vehicle, however the front wheelset longitudinal creep forces are similar as shown in Figure 5.32b.

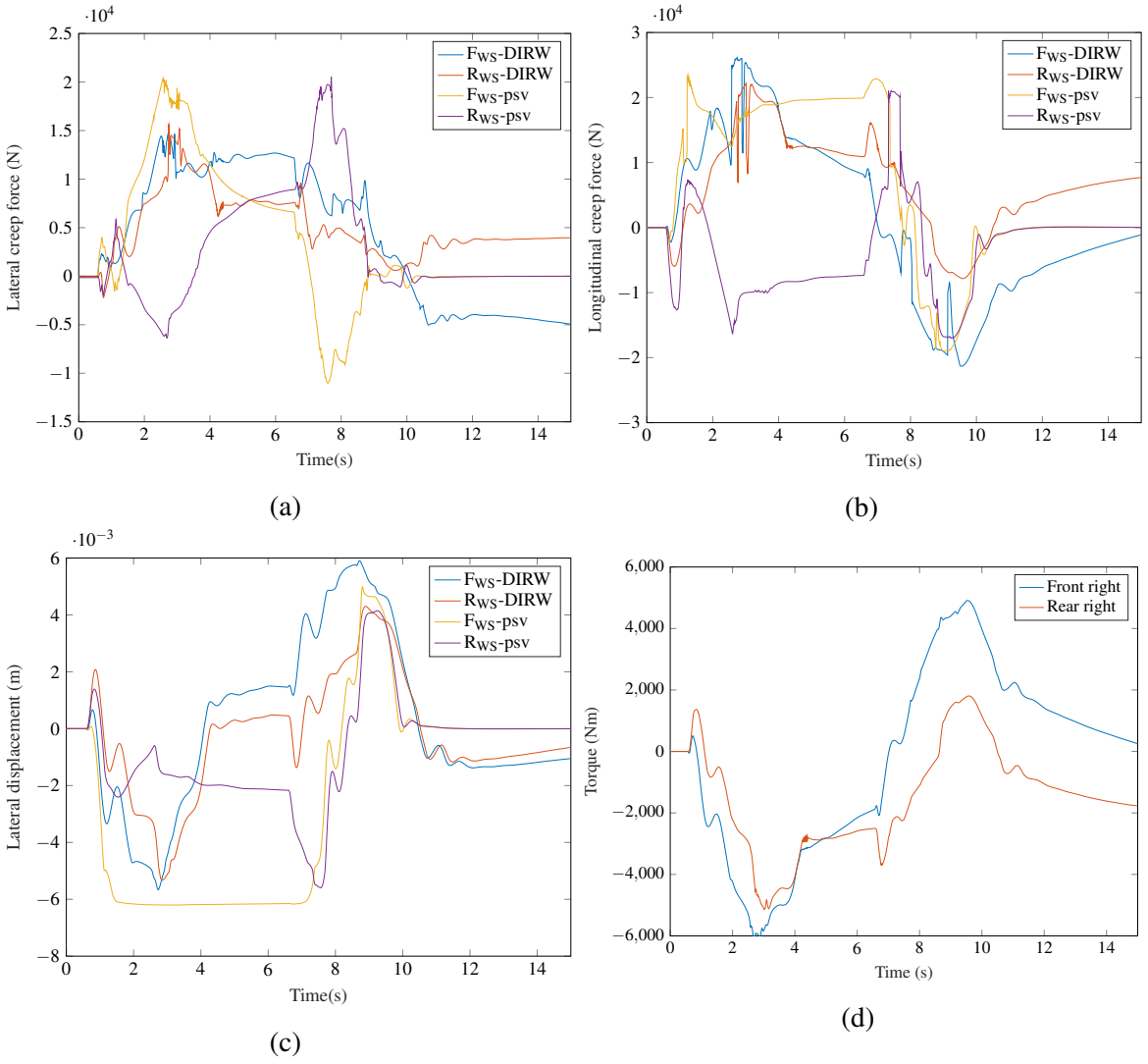

Figure 5.29: Lateral creep force, longitudinal creep force and lateral displacement response of the DIRW vehicle compared to the passive vehicle on **curved track with radius = 535 m, cant = 4° and vehicle speed = 30 m/s**. The notations F_{WS}, R_{WS} and psv used in the graph labels mean 'front wheelset', 'rear wheelset' and 'passive' respectively. Figure 5.29d shows the right DIRW motor forces on the front and rear wheelsets of the front bogie.

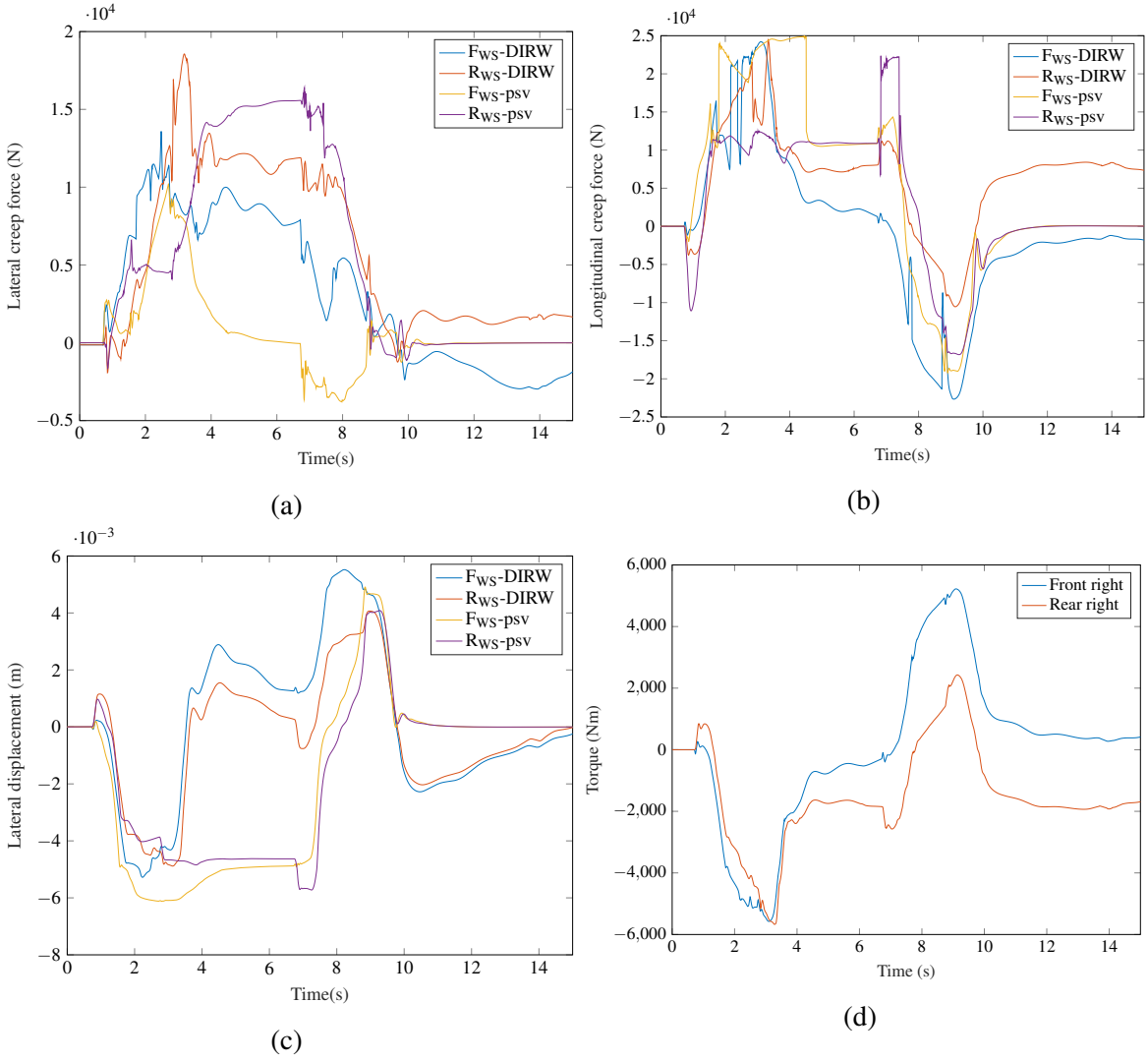

Figure 5.30: Lateral creep force, longitudinal creep force and lateral displacement response of the DIRW vehicle compared to the passive vehicle on **curved track with radius = 1200 m, cant = 4° and vehicle speed = 45 m/s**. The notations F_{WS}, R_{WS} and psv used in the graph labels mean 'front wheelset', 'rear wheelset' and 'passive' respectively. Figure 5.30d shows the right DIRW motor forces on the front and rear wheelsets of the front bogie.

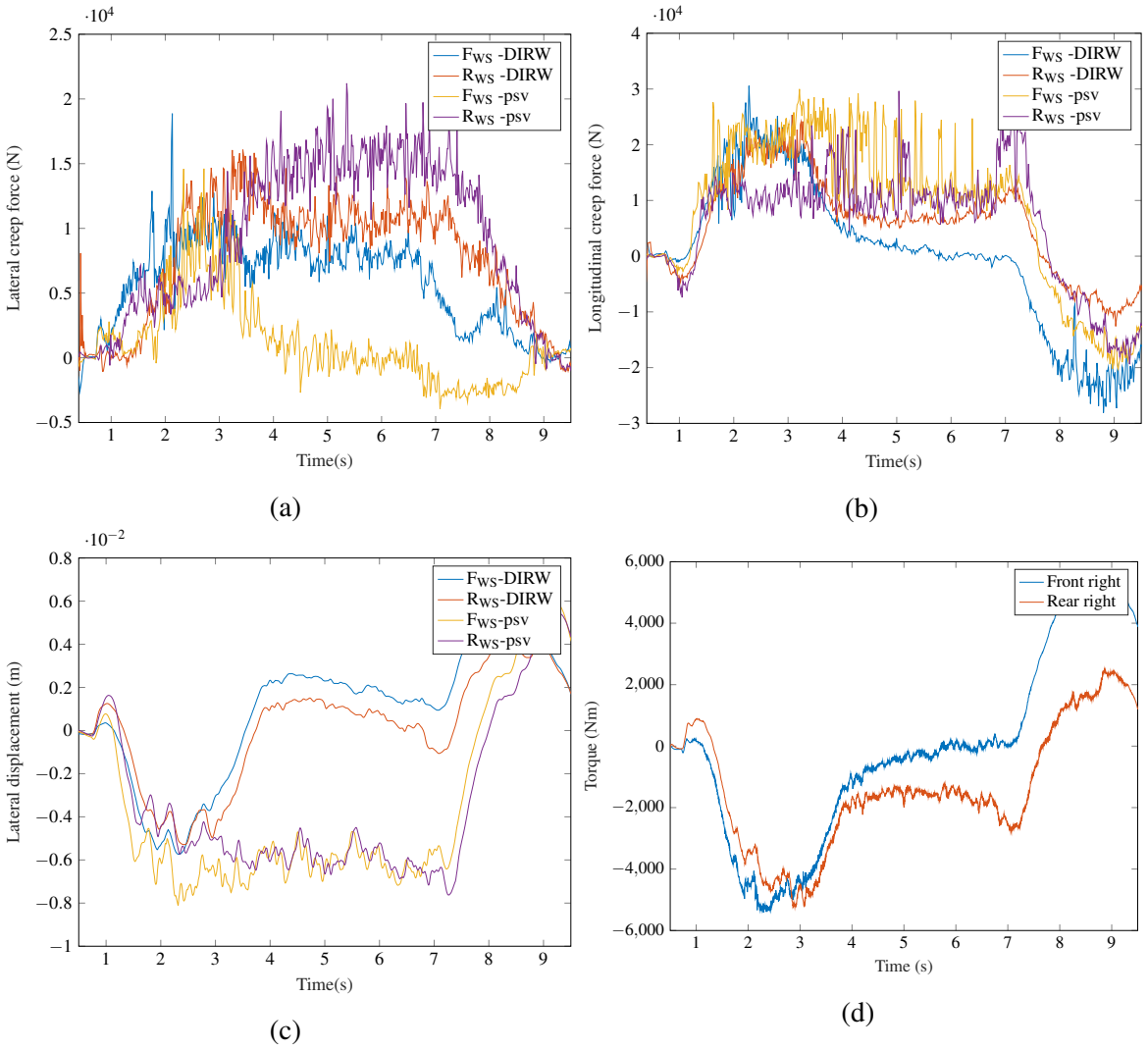

Figure 5.31: Lateral creep force, longitudinal creep force and lateral displacement response of the DIRW vehicle compared to the passive vehicle on **curved track with radius = 1200 m, cant = 4° and vehicle speed = 45 m/s, with lateral, vertical and gauge width stochastics**. The notations F_{WS}, R_{WS} and psv used in the graph labels mean 'front wheelset', 'rear wheelset' and 'passive' respectively. Figure 5.31d shows the right DIRW motor forces on the front and rear wheelsets of the front bogie.

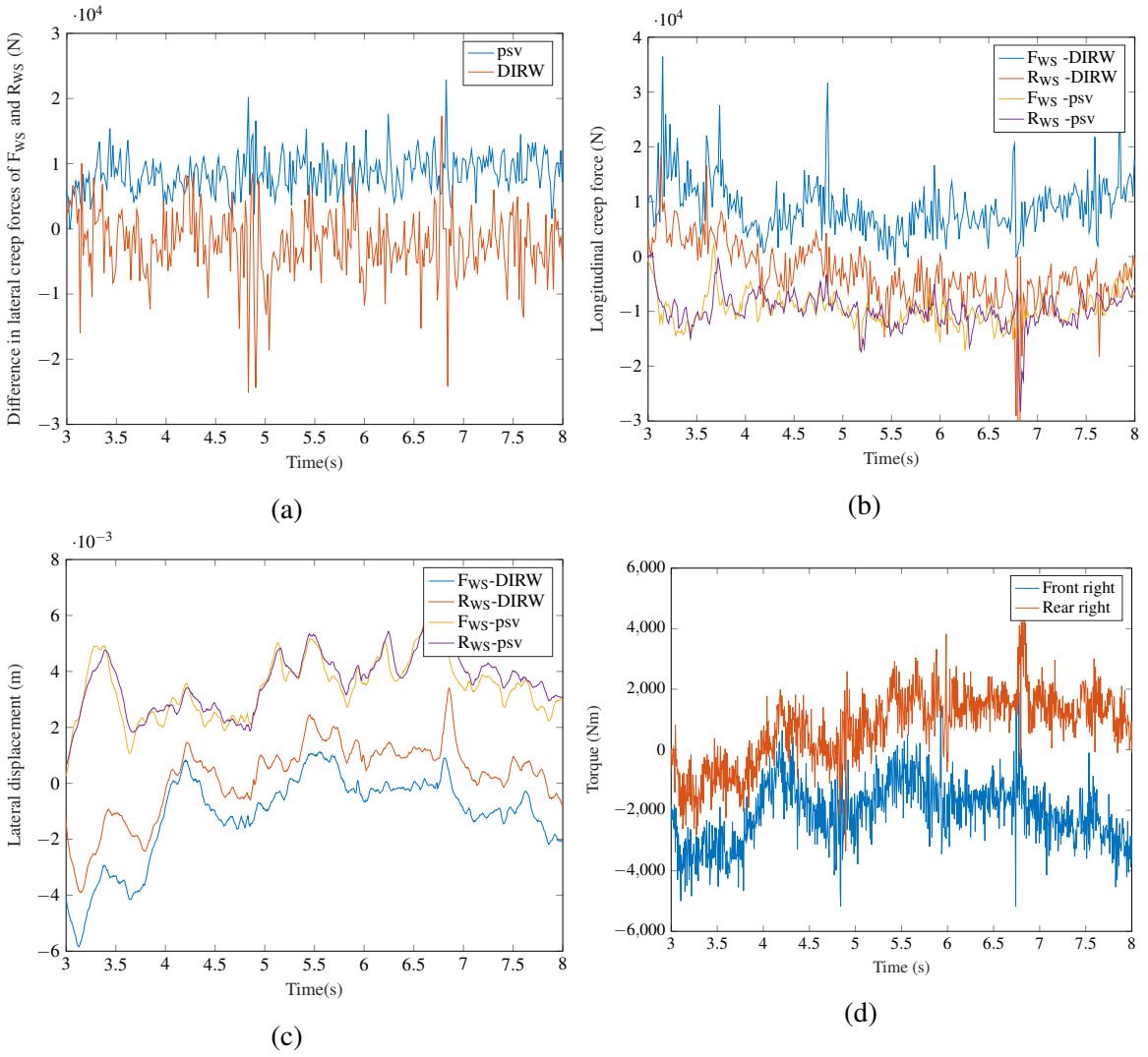

Figure 5.32: Longitudinal creep force and lateral displacement response of the DIRW vehicle compared to the passive vehicle on the **straight track with stochastic disturbances**. The notations F_{WS}, R_{WS} and psv used in the graph labels mean 'front wheelset', 'rear wheelset' and 'passive' respectively. Figure 5.32a compares the difference in the lateral creep forces of the front and rear wheelsets of the DIRW and passive vehicles. Figure 5.32d shows the right DIRW motor forces on the front and rear wheelsets of the front bogie.

5.5.4 Wheel-rail wear

From the average $T\gamma$ values using the PIP controllers listed in Table 5.4 it can be seen that the trends are similar to those observed from using the classical controllers. The DIRW vehicle generally has the lowest wear levels, followed by the ASW vehicle. The SYC vehicle generally has a worse wear than the passive vehicle, except perhaps on moderate speed

curves. The values in bold in the table are indicative of those above the RCF threshold. It can be seen that most of these undesirable values are for the passive and SYC vehicles.

Table 5.4: Average $T\gamma$ values using the PIP controllers on the different track profiles considered. Note that the units for the $T\gamma$ values is J/m. Values in bold are those above the RCF threshold.

Curved track at R=1200 m, v=45 m/s				
	Passive	SYC	ASW	DIRW
Front bogie front WS	**30.03**	6.49	6.12	0.05
Front bogie rear WS	10.25	4.34	1.41	3.07
Rear bogie front WS	1.72	**35.17**	0.86	2.06
Rear bogie rear WS	3.62	**31.99**	8.27	5.05
Total $T\gamma$ on all WSs	45.62	77.98	16.65	10.23
Percentage of passive	100	176.94	37.77	23.22
Curved track at R=534.52 m, v=30 m/s				
	Passive	SYC	ASW	DIRW
Front bogie front WS	**84.47**	7.22	10.17	1.68
Front bogie rear WS	4.99	2.65	0.78	1.07
Rear bogie front WS	**26.16**	**28.86**	1.58	2.68
Rear bogie rear WS	**39.38**	6.62	**18.22**	10.72
Total $T\gamma$ on all WSs	155.00	45.35	30.76	16.14
Percentage of passive	100	29.26	19.84	10.41
Curved track with stochastics at R=1200 m, v=45 m/s				
	Passive	SYC	ASW	DIRW
Front bogie front WS	13.59	8.58	6.37	1.17
Front bogie rear WS	12.31	5.62	1.88	3.61
Rear bogie front WS	0.57	**31.46**	0.54	2.58
Rear bogie rear WS	**17.08**	**27.43**	10.15	4.93
Total $T\gamma$ on all WSs	43.55	73.09	18.95	12.29
Percentage of passive	100	167.85	43.52	28.22
Straight track with stochastics				
	Passive	SYC	ASW	DIRW
Front bogie front WS	0.81	6.68	0.59	7.22
Front bogie rear WS	**18.99**	11.69	4.73	2.57
Rear bogie front WS	0.34	12.47	1.41	5.84
Rear bogie rear WS	**17.39**	**25.73**	6.44	1.87
Total $T\gamma$ on all WSs	37.53	56.57	13.17	17.51
Percentage of passive	100	150.73	35.09	46.66

5.6 Comparison of controllers

In this section the classical and PIP controller performances are compared on each of the four track profiles under consideration.

5.6.1 SYC

Figures 5.33 to 5.36 compare the lateral creep force, longitudinal creep force, wheelset lateral displacement and actuation forces using the two controllers on the SYC vehicle simulated on the four track scenarios.

The lateral creep force, longitudinal creep force and wheelset lateral displacement responses using the two controllers are largely similar on the 30 m/s curve as can be seen from Figures 5.33a, 5.33b and 5.33c. The torque using the PIP controller is marginally higher than with the classical controller as shown in Figure 5.33d

On the 45 m/s curve, there is an increase in the lateral creep forces using the PIP controllers during curve transitions as can be seen in Figure 5.34a, which is due to a lower actuation torque as shown in Figure 5.34d. The wheelset lateral displacements and the longitudinal creep forces achieved using both controllers are similar as shown in Figures 5.34c and 5.34b. On the straight track profile, the longitudinal creep forces on the front wheelset using the PIP controller are considerably lower than using the classical PI controller.

The graphical results from using both controllers on the curved track with stochastics are very similar as shown in Figure 5.35.

On the straight track with stochastics, the PIP controller removes some of the big lateral displacements (occurring between 3.5 s and 5 s) as shown in Figure 5.36c. The longitudinal creep force of the front wheelset is significantly reduced using the PIP controller as shown in Figure 5.36b. Figure 5.36d shows that the torque requirement using the PIP controller is also marginally lower.

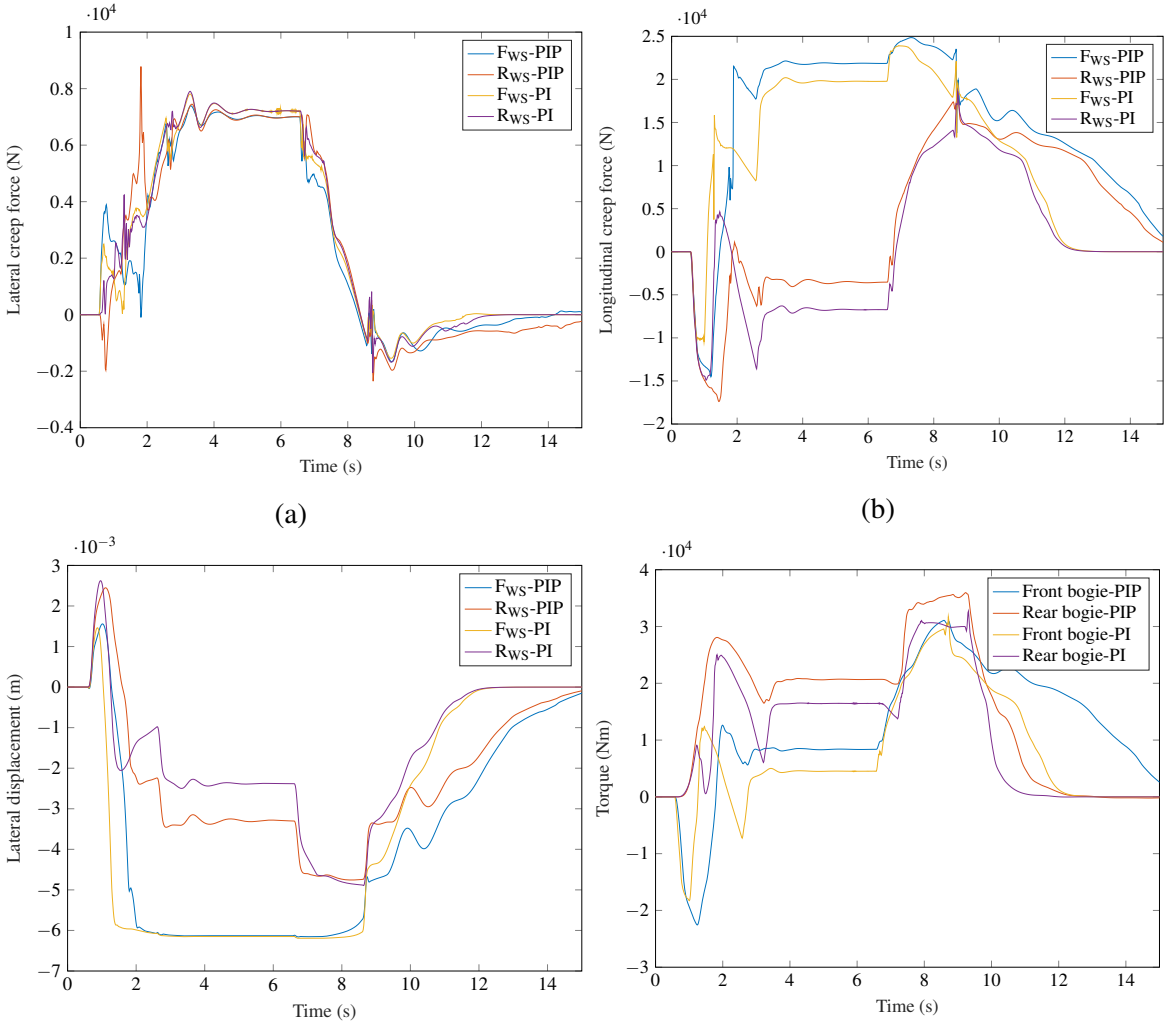

Figure 5.33: Lateral creep force, longitudinal creep force and lateral displacement response of the SYC vehicle using classical and PIP controllers on the **curved track with radius = 535 m, cant = 4° and vehicle speed = 30 m/s**. The notations F_{WS}, R_{WS} and psv used in the graph labels mean 'front wheelset', 'rear wheelset' and 'passive' respectively. Figure 5.33d shows the total yaw torque acting on each bogie of the SYC vehicle.

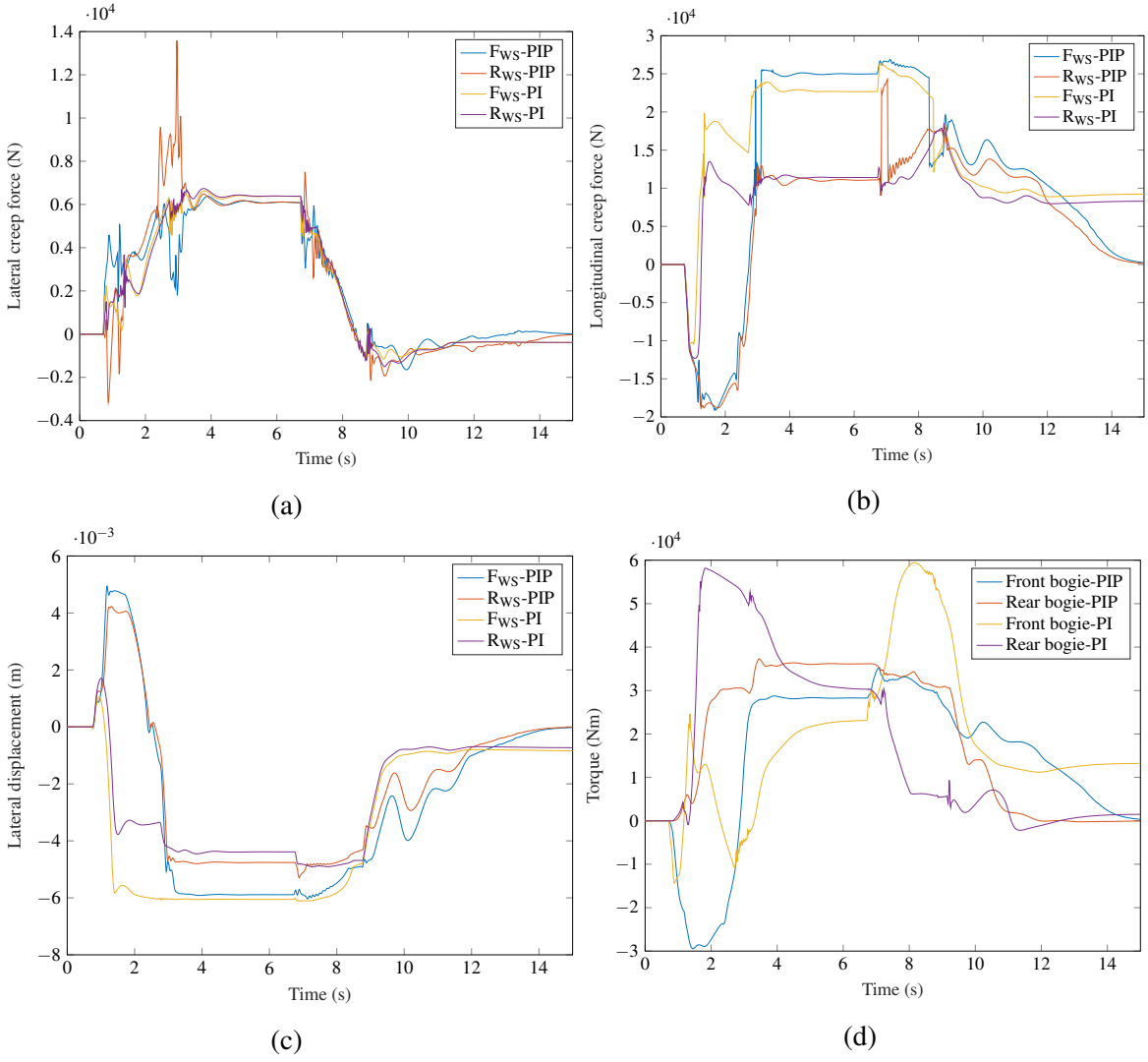

Figure 5.34: Lateral creep force, longitudinal creep force and lateral displacement response of the SYC vehicle using classical and PIP controllers on the **curved track with radius = 1200 m, cant = 4° and vehicle speed = 45 m/s**. The notations F_{WS}, R_{WS} and psv used in the graph labels mean 'front wheelset', 'rear wheelset' and 'passive' respectively. Figure 5.34d shows the total yaw torque acting on each bogie of the SYC vehicle.

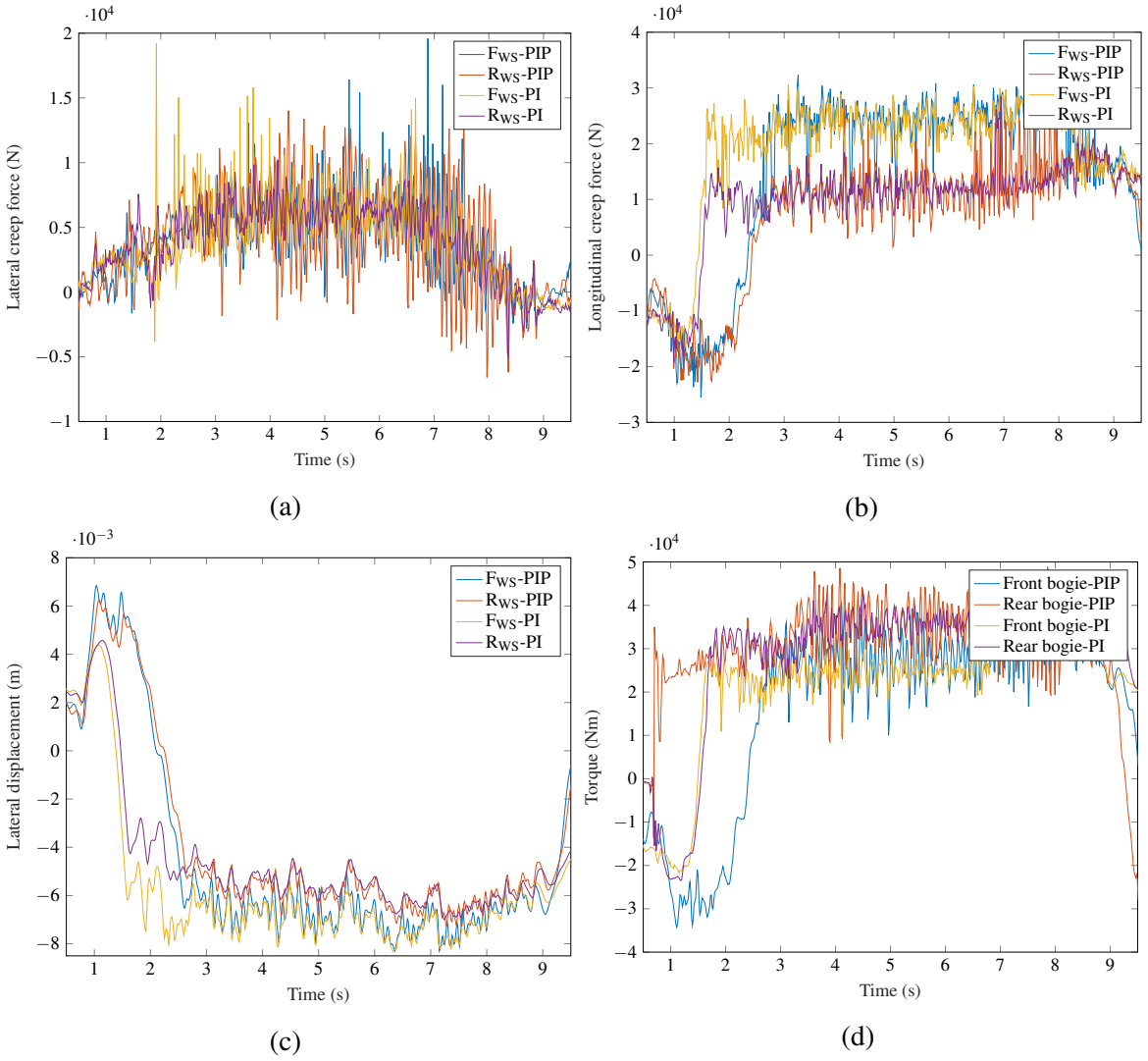

Figure 5.35: Lateral creep force, longitudinal creep force and lateral displacement response of the SYC vehicle using classical and PIP controllers on the **curved track with radius = 1200 m, cant = 4° and vehicle speed = 45 m/s, with lateral, vertical and gauge width stochastics**. The notations F_{WS}, R_{WS} and psv used in the graph labels mean 'front wheelset', 'rear wheelset' and 'passive' respectively. Figure 5.35d shows the total yaw torque acting on each bogie of the SYC vehicle.

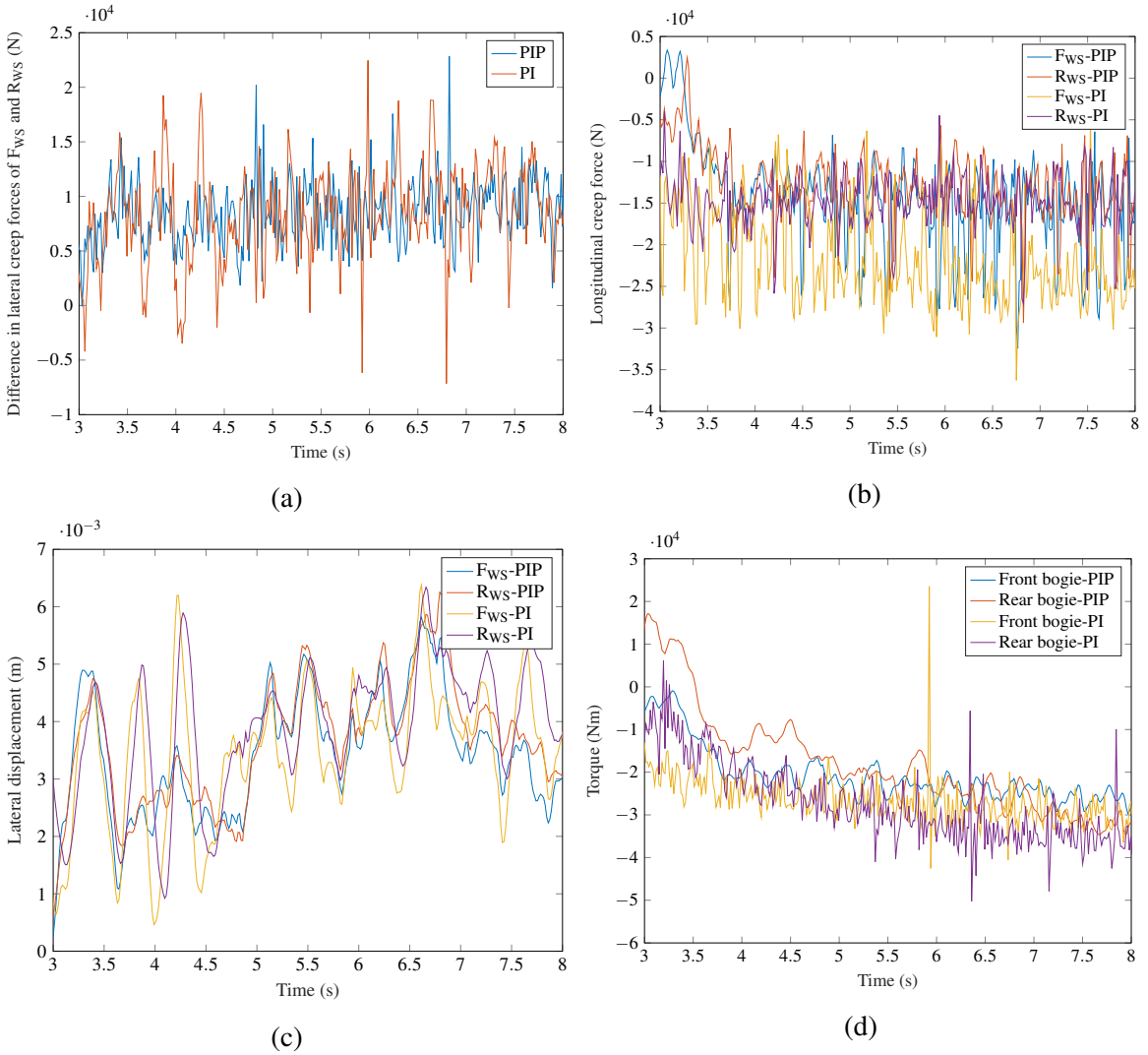

Figure 5.36: Longitudinal creep force and lateral displacement response of the SYC vehicle using classical and PIP controllers on the **straight track with stochastic disturbances**. The notations F_{WS}, R_{WS} and psv used in the graph labels mean 'front wheelset', 'rear wheelset' and 'passive' respectively. Figure 5.36a compares the difference in the lateral creep forces of the front and rear wheelsets of the SYC and passive vehicles. Figure 5.36d shows the total yaw torque acting on each bogie of the SYC vehicle.

5.6.2 ASW

Figures 5.37 to 5.40 show the creep forces, wheelset lateral displacement and actuation forces from applying the PIP and classical PI controllers on the ASW vehicle simulated on the four different track profiles under consideration. On the 30 m/s curve, the PIP controller gives a smoother response during curve transitions than the PI controller. The lateral creep force, longitudinal creep force and wheelset lateral displacement using both controllers are largely similar as shown in Figures 5.37a, 5.37b and 5.37c. The force requirement using the PIP controller is less than when using the classical controllers as shown in Figure 5.37d.

On the high speed curve, the PIP controller gives marginally higher lateral and longitudinal creep forces on the curve transitions as shown in Figures 5.38a and 5.38b respectively. Both controllers give similar wheelset lateral displacement as shown in Figure 5.38c. Figure 5.38d shows that the force requirement of the front wheelset using the PIP controller is lower than with the PI controller, however that of the rear wheelset is slightly higher using the PIP controller than with the PI controller.

Figures 5.39 and 5.40 show the response of the ASW vehicle using both controllers on the curved track with stochastics and the straight track with stochastics respectively. There is no significant difference in the graphical results. From Figure 5.40d it can be seen that the force requirement of the front wheelset is lower using the PIP controller but that of the rear wheelset is higher.

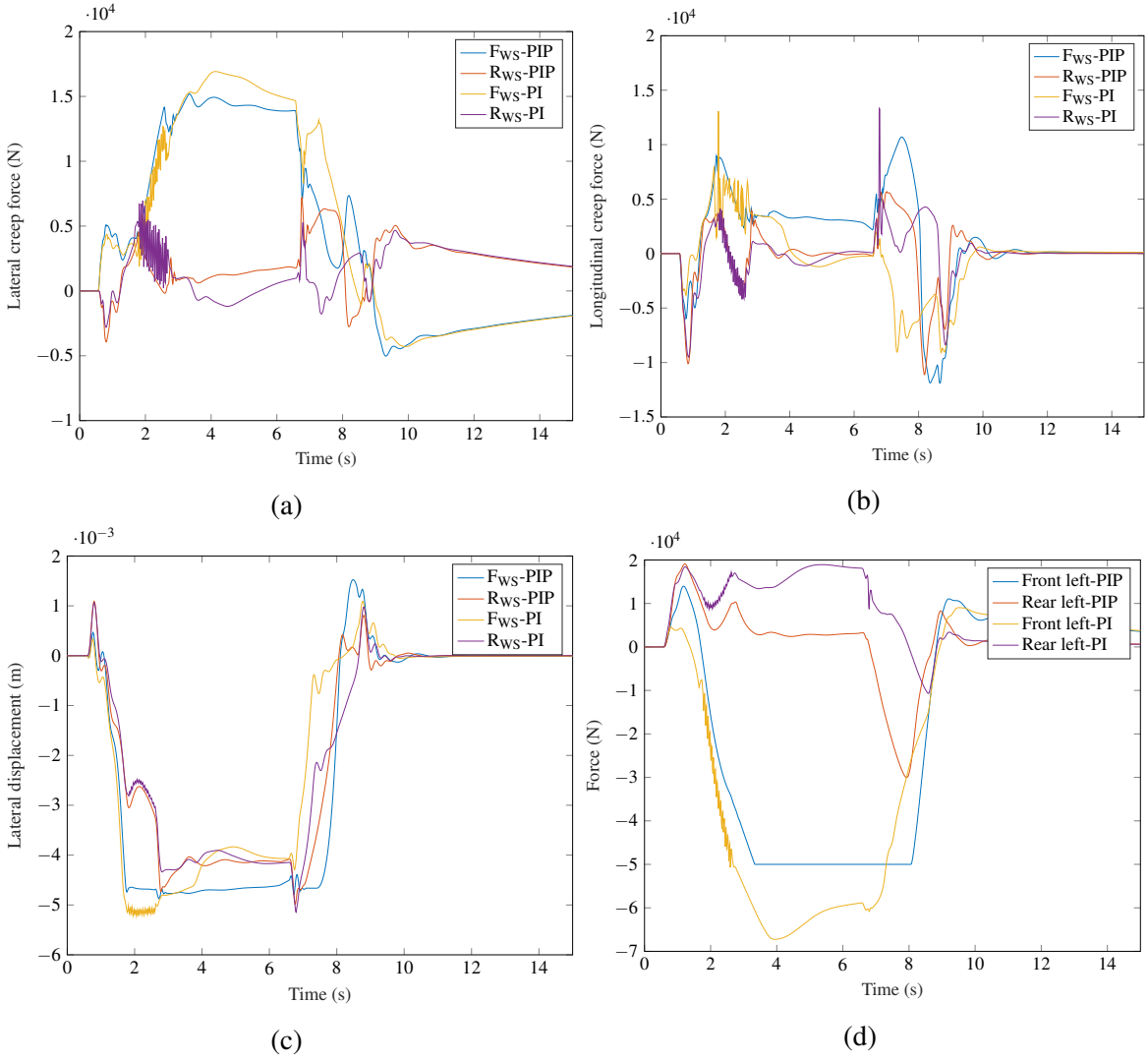

Figure 5.37: Lateral creep force, longitudinal creep force and lateral displacement response of the ASW vehicle using classical and PIP controllers on the **curved track with radius = 535 m, cant = 4° and vehicle speed = 30 m/s**. The notations F_{WS}, R_{WS} and psv used in the graph labels mean 'front wheelset', 'rear wheelset' and 'passive' respectively. Figure 5.37d shows the left ASW actuator forces on the front and rear wheelsets of the front bogie.

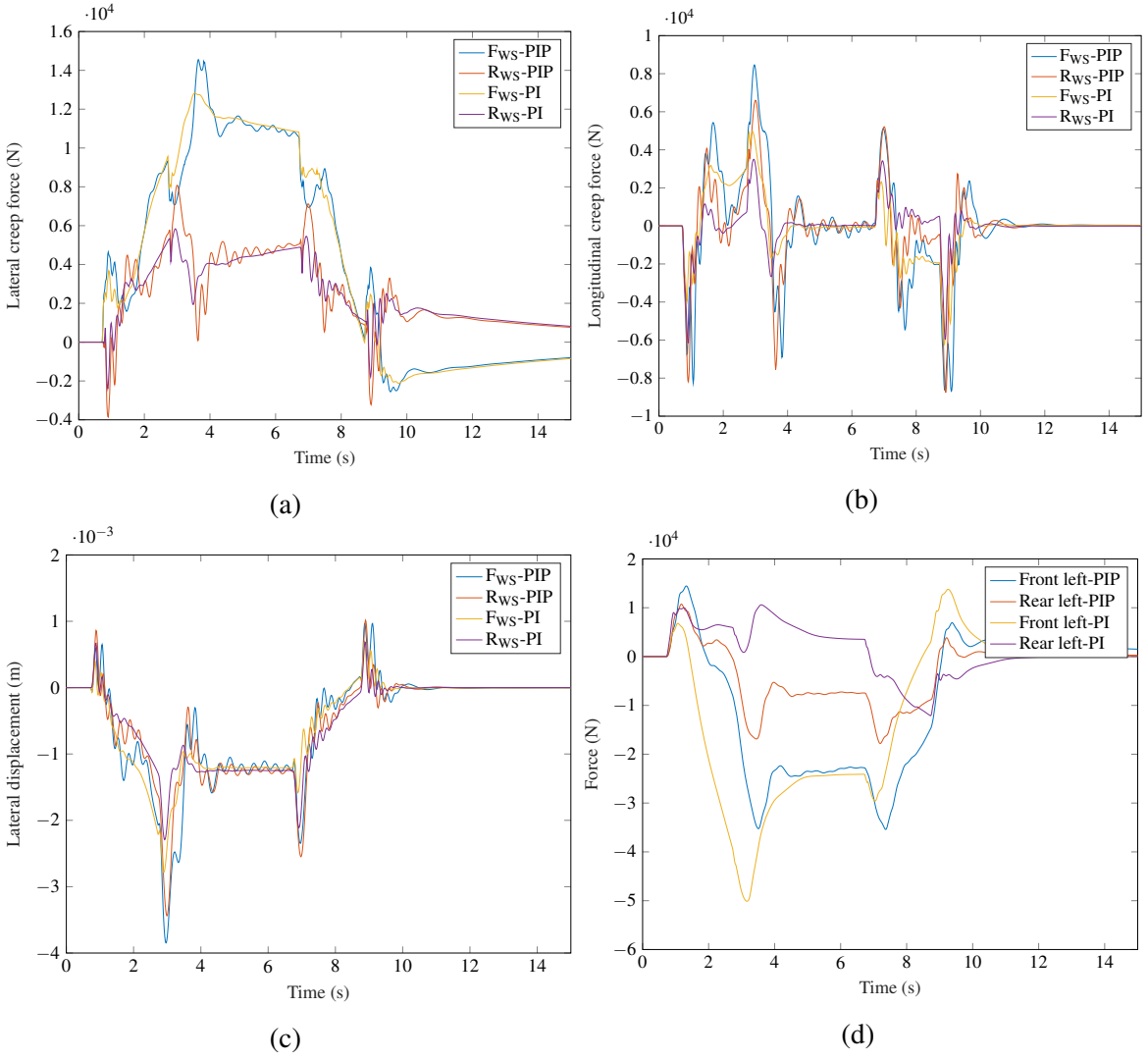

Figure 5.38: Lateral creep force, longitudinal creep force and lateral displacement response of the ASW vehicle using classical and PIP controllers on the **curved track with radius = 1200 m, cant = 4° and vehicle speed = 45 m/s**. The notations F_{WS}, R_{WS} and psv used in the graph labels mean 'front wheelset', 'rear wheelset' and 'passive' respectively. Figure 5.38d shows the left ASW actuator forces on the front and rear wheelsets of the front bogie.

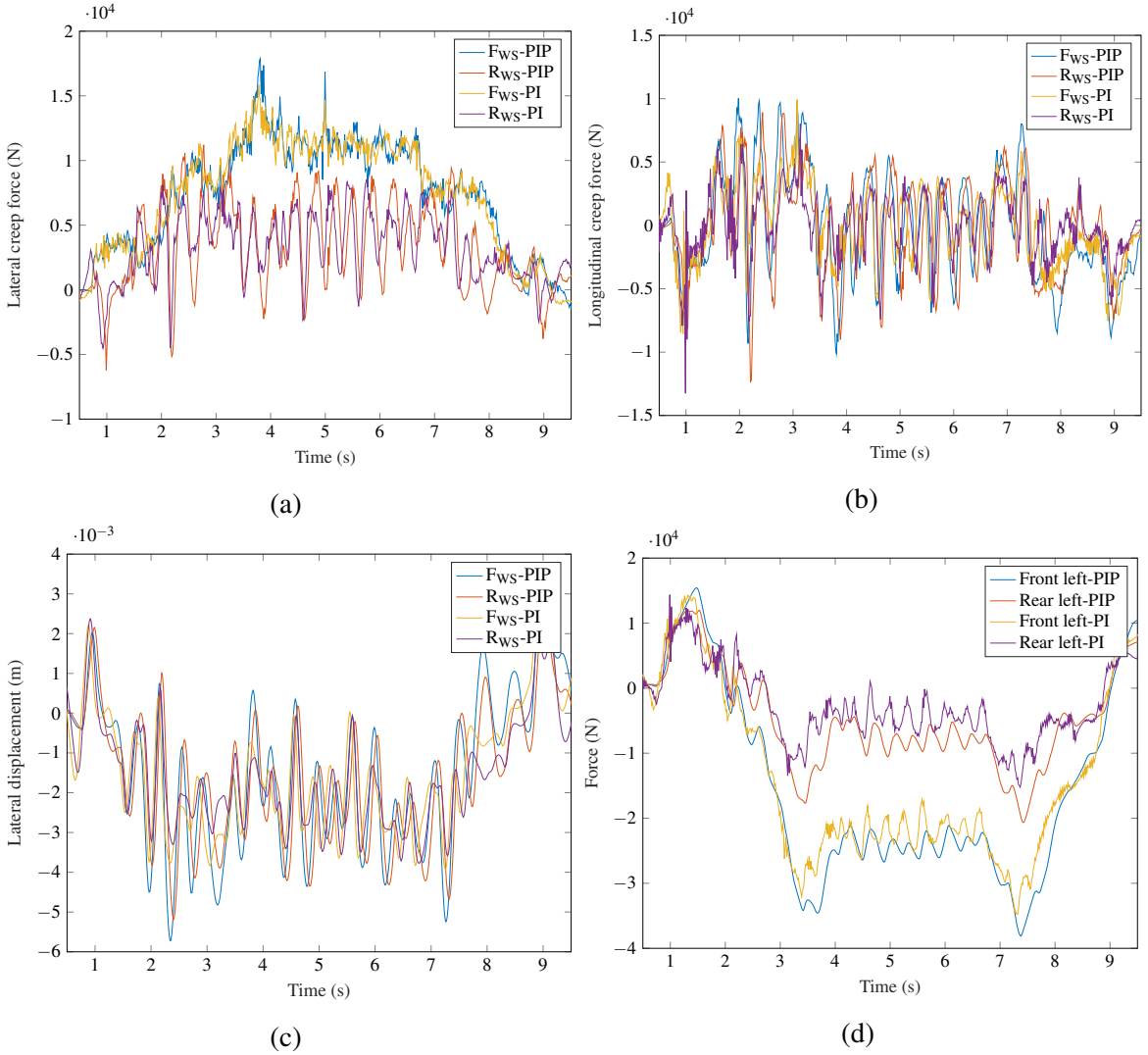

Figure 5.39: Lateral creep force, longitudinal creep force and lateral displacement response of the ASW vehicle using classical and PIP controllers on the **curved track with radius = 1200 m, cant = 4° and vehicle speed = 45 m/s, with lateral, vertical and gauge width stochastics**. The notations F_{WS}, R_{WS} and psv used in the graph labels mean 'front wheelset', 'rear wheelset' and 'passive' respectively. Figure 5.39d shows the left ASW actuator forces on the front and rear wheelsets of the front bogie.

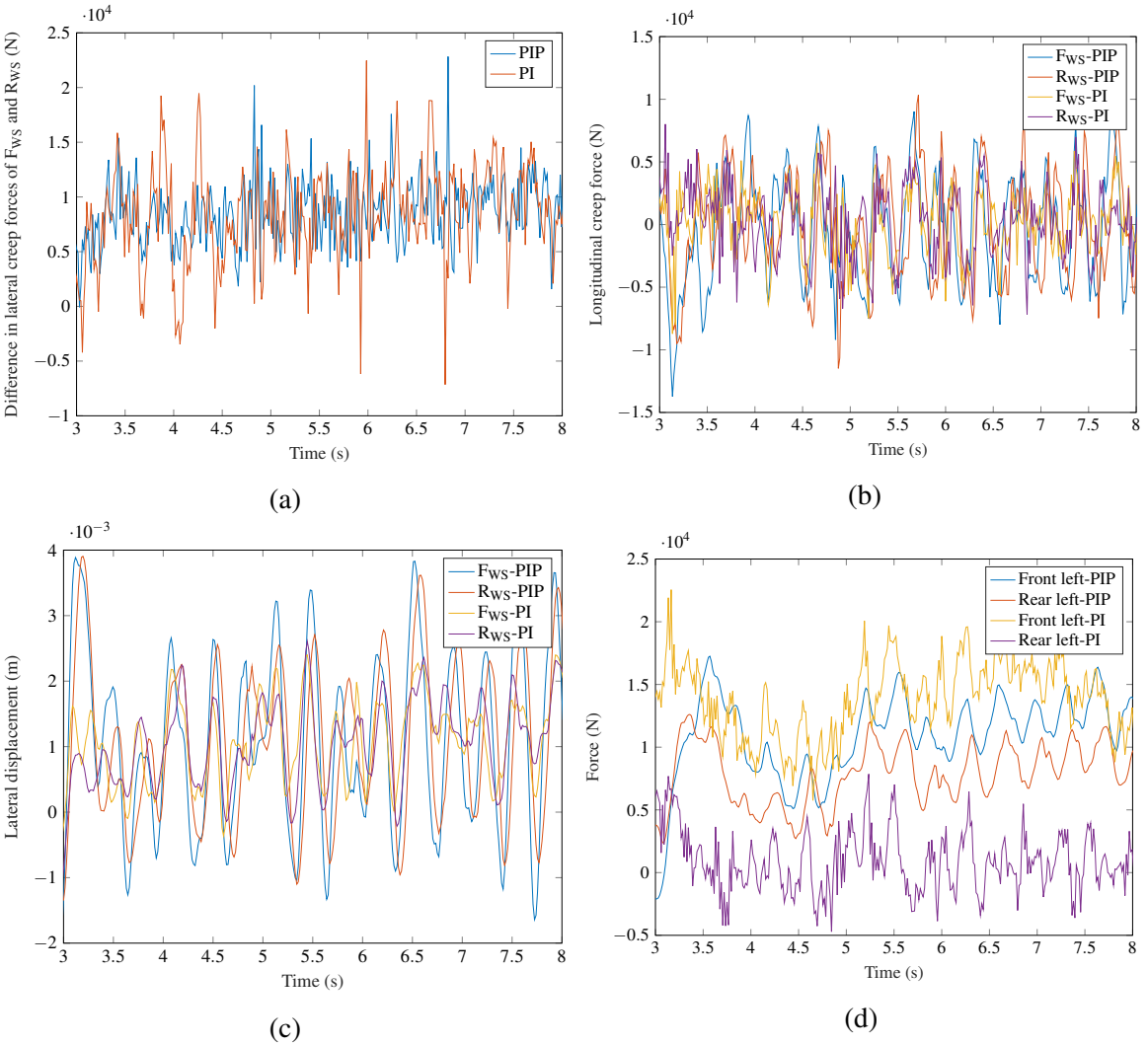

Figure 5.40: Longitudinal creep force and lateral displacement response of the ASW vehicle using classical and PIP controllers on the **straight track with stochastic disturbances**. The notations F_{WS}, R_{WS} and psv used in the graph labels mean 'front wheelset', 'rear wheelset' and 'passive' respectively. Figure 5.40a compares the difference in the lateral creep forces of the front and rear wheelsets of the ASW and passive vehicles. Figure 5.40d shows the left ASW actuator forces on the front and rear wheelsets of the front bogie.

5.6.3 DIRW

Figures 5.41 to 5.44 show the creep forces, wheelset lateral displacement and motor torque response of the DIRW vehicle using the PIP controller and the classical PA plus I controller on the four track profiles considered.

On the curved track with radius = 535 m, cant = 4° and vehicle speed = 30 m/s, the lateral creep force in Figure 5.41a shows that both controllers give a similar response during the curve and the transitions, however after the transition onto straight track i.e. after approximately 10 s, there is a residual lateral creep force on both wheelsets. The longitudinal creep force of both wheelsets using the PIP controller is lower during the curve transitions but higher on the steady states as shown in Figure 5.41b. The torque requirement is also higher using the PIP controller during the steady states as shown in Figure 5.41d. This is because the torque is used to generate the higher longitudinal creep forces which provide a greater steering action than the classical controller. For this reason the wheelset lateral displacement in the steady state is smaller using the PIP controller as can be seen from Figure 5.41c.

The responses are very similar for the high speed curve and the curved track profile with stochastics as shown in Figures 5.42 and 5.43 respectively.

On the straight track profile with stochastics, it can be seen from Figure 5.44a that the PIP controller reduces the lateral creep force difference between the two wheelsets more effectively than the PA plus I controller. The longitudinal creep forces, wheelset lateral displacements and motor torques using both controllers look very similar as shown in Figures 5.44b, 5.44c and 5.44d.

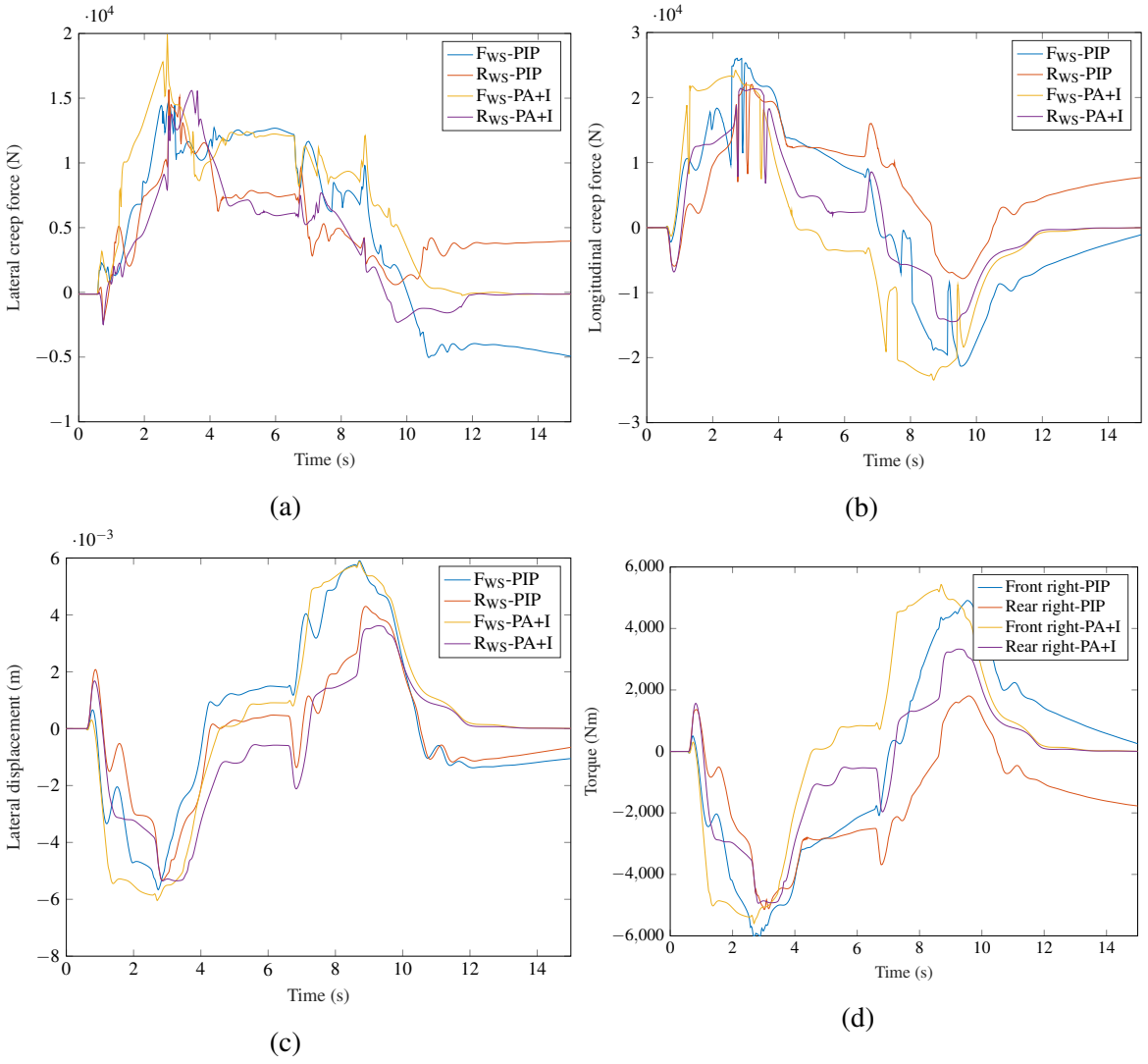

Figure 5.41: Lateral creep force, longitudinal creep force and lateral displacement response of the DIRW vehicle using classical and PIP controllers on the **curved track with radius = 535 m, cant = 4° and vehicle speed = 30 m/s**. The notations F_{WS}, R_{WS} and psv used in the graph labels mean 'front wheelset', 'rear wheelset' and 'passive' respectively. Figure 5.41d shows the right DIRW motor forces on the front and rear wheelsets of the front bogie.

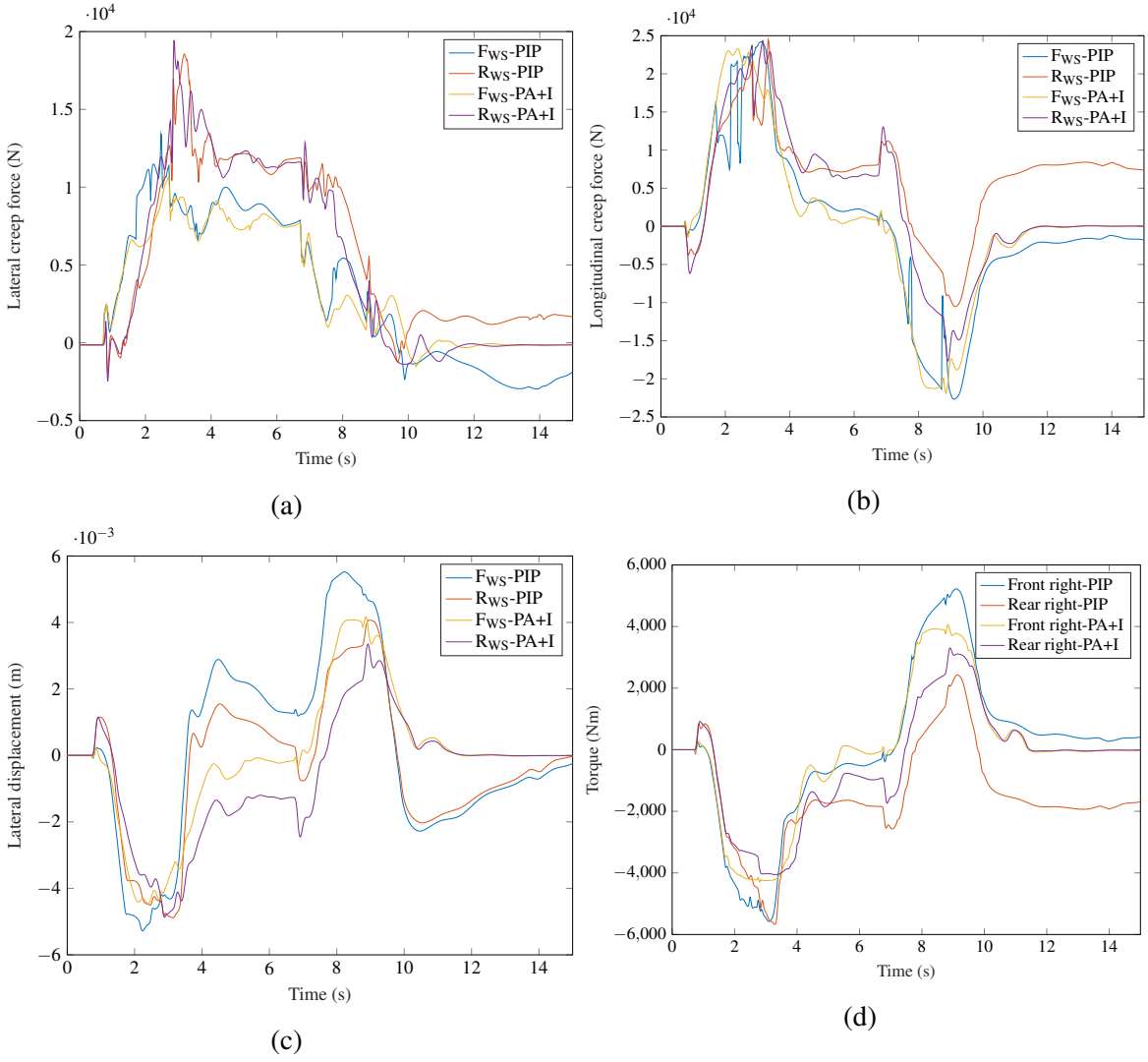

Figure 5.42: Lateral creep force, longitudinal creep force and lateral displacement response of the DIRW vehicle using classical and PIP controllers on the **curved track with radius = 1200 m, cant = 4° and vehicle speed = 45 m/s**. The notations F_{WS}, R_{WS} and psv used in the graph labels mean 'front wheelset', 'rear wheelset' and 'passive' respectively. Figure 5.42d shows the right DIRW motor forces on the front and rear wheelsets of the front bogie.

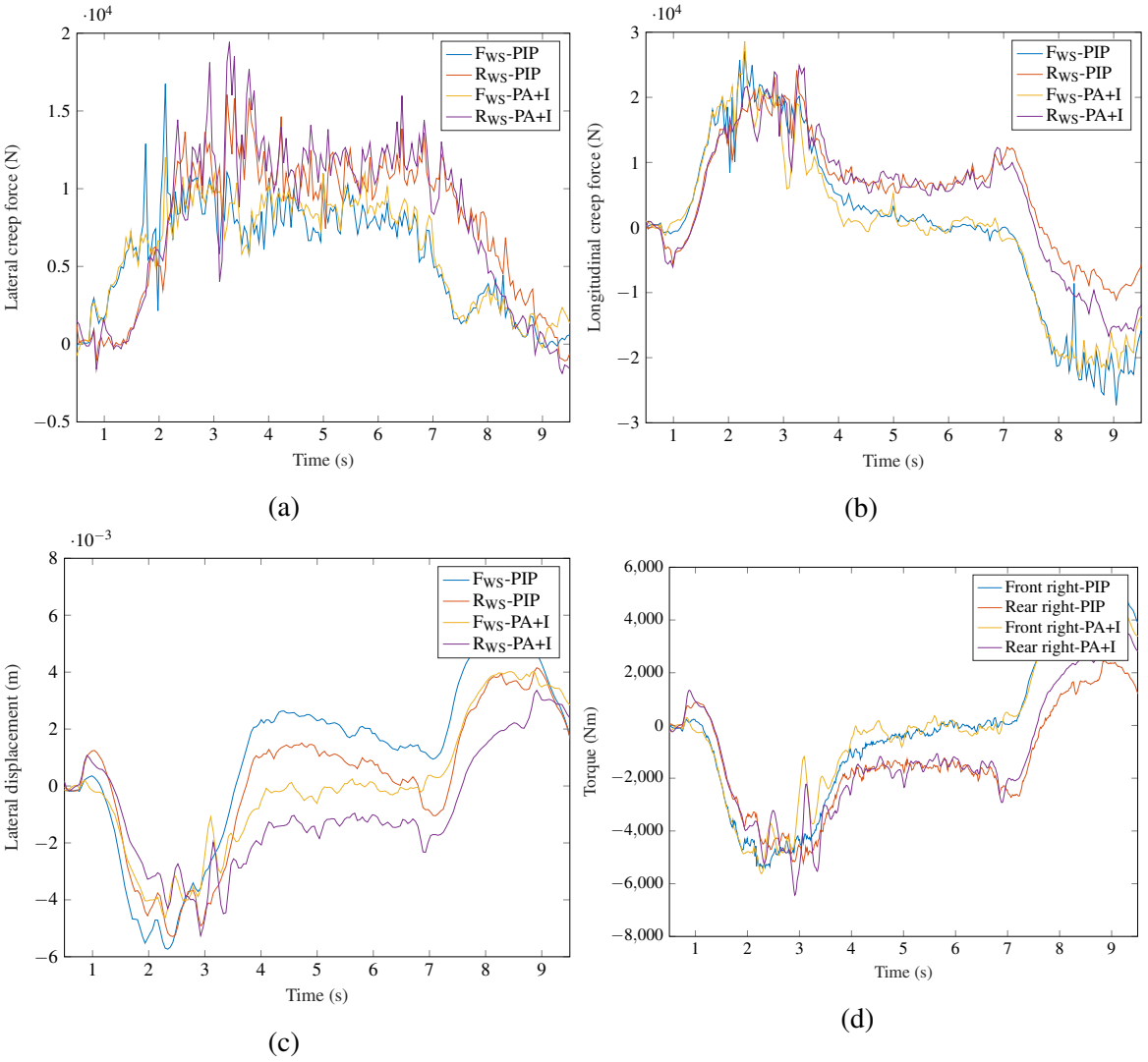

Figure 5.43: Lateral creep force, longitudinal creep force and lateral displacement response of the DIRW vehicle using classical and PIP controllers on the **curved track with radius = 1200 m, cant = 4° and vehicle speed = 45 m/s, with lateral, vertical and gauge width stochastics**. The notations F_{WS}, R_{WS} and psv used in the graph labels mean 'front wheelset', 'rear wheelset' and 'passive' respectively. Figure 5.43d shows the right DIRW motor forces on the front and rear wheelsets of the front bogie.

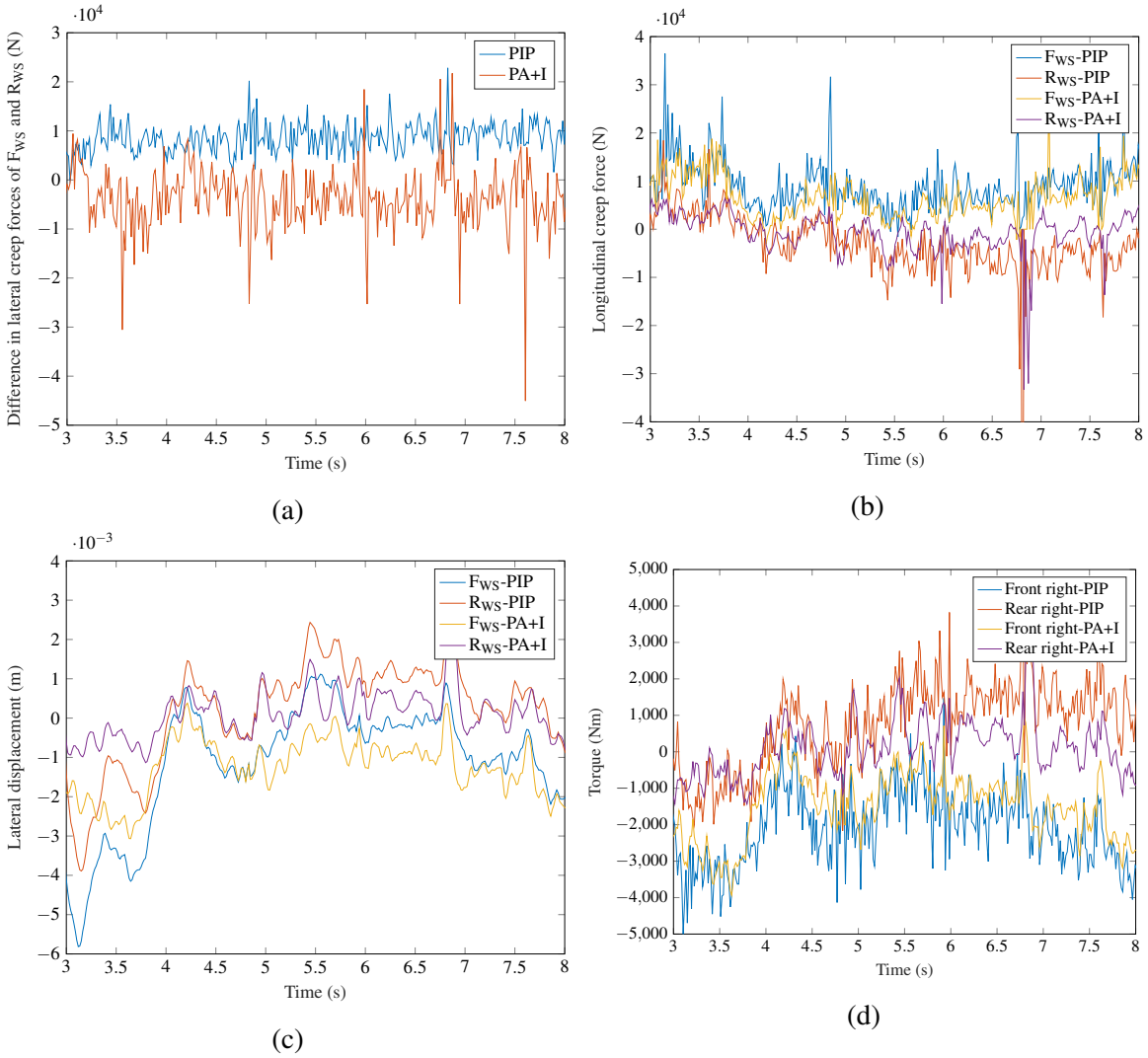

Figure 5.44: Longitudinal creep force and lateral displacement response of the DIRW vehicle using classical and PIP controllers on the **straight track with stochastic disturbances**. The notations F_{WS}, R_{WS} and psv used in the graph labels mean 'front wheelset', 'rear wheelset' and 'passive' respectively. Figure 5.44a compares the difference in the lateral creep forces of the front and rear wheelsets of the DIRW and passive vehicles. Figure 5.44d shows the right DIRW motor forces on the front and rear wheelsets of the front bogie.

5.6.4 Wheel-rail wear

Table 5.5 lists the difference in $T\gamma$ values using the classical and those from using PIP controllers. The negative values indicate the decrease in wear using the PIP controllers compared to using the classical controllers. The sum total reduction in wear using the PIP controller is expressed as a percentage of the wear of the passive vehicle. So for example a value of -45.29 % means that the PIP controller reduces the wear by 45.29 % of the wear on the passive vehicle. Likewise, a value of 5.96 % means that the PIP controller increases the wear by 5.96 % of the wear on the passive vehicle.

Figure 5.45 presents the key tabular data pictorically. As can be seen, the PIP controllers produce an overall reduction in wear in the SYC and ASW vehicles on all the track profiles under consideration. There is a marginal increase of 5-7% using the PIP controller on the DIRW vehicle in some of the track scenarios. This is not considered to be significant and the overall performance using the PIP controller is better than using the classical controllers.

Table 5.5: The table provides the difference between the $T\gamma$ values using the classical and PIP controllers. Note that the units for the $T\gamma$ values is J/m.

Curved track at R=1200 m, v=45 m/s			
	SYC	ASW	DIRW
Front bogie front WS	-15.06	-3.81	-0.10
Front bogie rear WS	3.69	-0.36	3.00
Rear bogie front WS	-24.75	-0.36	0.58
Rear bogie rear WS	16.17	-4.10	-0.84
Total $T\gamma$ on all WSs	-19.96	-8.64	2.63
Percentage of passive	-45.29	-19.61	5.96
Curved track at R=534.52 m, v=30 m/s			
	SYC	ASW	DIRW
Front bogie front WS	-9.64	-5.27	0.55
Front bogie rear WS	0.55	0.54	0.23
Rear bogie front WS	-20.08	0.02	-7.56
Rear bogie rear WS	0.00	-9.56	0.25
Total $T\gamma$ on all WSs	-29.17	-14.27	-6.53
Percentage of passive	-18.82	-9.20	-4.21
Curved track with stochastics at R=1200 m, v=45 m/s			
	SYC	ASW	DIRW
Front bogie front WS	-13.84	-4.08	-0.22
Front bogie rear WS	4.43	-0.29	2.98
Rear bogie front WS	-27.95	-0.69	0.38
Rear bogie rear WS	11.93	-3.23	0.07
Total $T\gamma$ on all WSs	-25.43	-8.29	3.20
Percentage of passive	-58.40	-19.05	7.36

Straight track with stochastics			
	SYC	ASW	DIRW
Front bogie front WS	-8.54	-3.30	6.01
Front bogie rear WS	-1.83	1.69	-0.32
Rear bogie front WS	-11.72	-0.64	-1.86
Rear bogie rear WS	-22.10	-0.35	-1.76
Total $T\gamma$ on all WSs	-44.19	-2.60	2.08
Percentage of passive	-117.75	-6.93	5.54

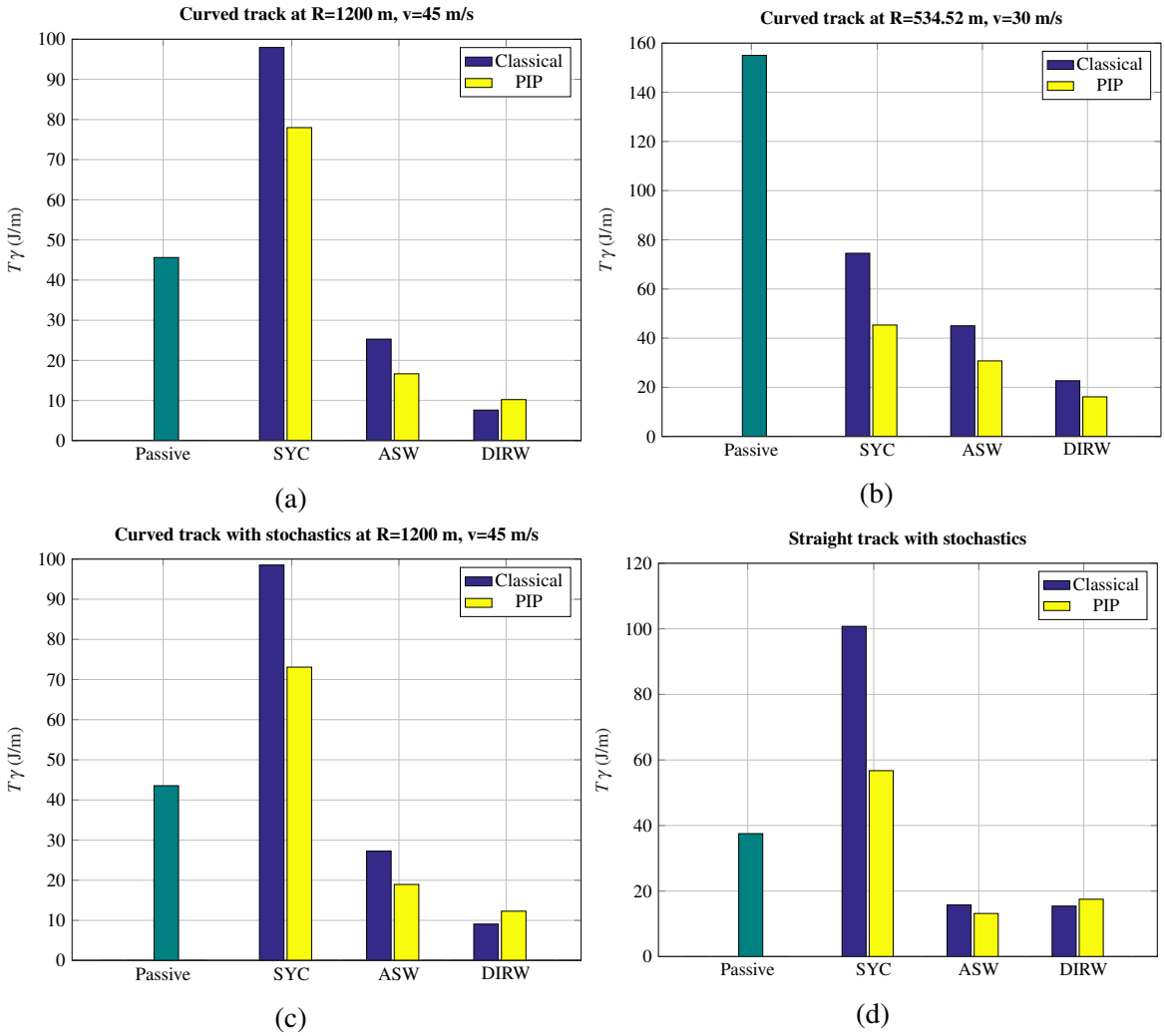

Figure 5.45: Trends in $T\gamma$ using classical and PIP controllers

5.7 Discussion of results

This section draws the main points of discussion from the graphical results presented in sections 5.4, 5.5 and 5.6.

SYC

- Both the controllers effectively reduce the difference in the lateral creep forces at the front and rear wheelsets to zero on all the track profiles considered. The front wheelset lateral creep force is lower than that of the passive vehicle, however the rear wheelset lateral creep force is higher. This is expected, in order to equalise the lateral creep forces on both wheelsets.

- The wheelsets have a larger lateral displacement on the SYC vehicle than the passive vehicle, with the front wheelset making flange contact at $\approx$ 6 mm on all the track simulations. This results in higher or similar longitudinal creep forces to the passive vehicle.

- The $T\gamma$ values for the SYC vehicle are nearly double that of the passive in most of the simulations due to the higher longitudinal creep forces and higher lateral creep force on the rear wheelsets.

- Although the controllers are effective in satisfying one of the conditions for “ideal curving" which is to equalise the lateral creep forces, the overall performance is worse than that of the passive vehicle. This suggests that the SYC configuration does not provide a good steering mechanism.

ASW

- The longitudinal creep forces are reduced to zero by both the controllers in the steady states in all the track profiles considered.

- The lateral creep force difference between the front and rear wheelsets are lower than the passive vehicle. Both wheelsets stay well clear of the flange and the lateral displacements are significantly lower than the passive vehicle.

- The lower creep forces result in lower $T\gamma$ values than the passive vehicle on all the track profiles considered. The % decrease in $T\gamma$ using a PIP controller ranges from $\approx$ 20% to 40%.

- The overall performance of the ASW vehicle is better than the passive vehicle due to the reduction in creep forces and wheelset lateral displacements.

DIRW

- The DIRW configuration works by providing a guidance mechanism to the wheelsets by controlling their lateral displacement to follow the track. From all the results using either controller, it can be seen that the wheelset lateral displacement of the DIRW vehicle is significantly lower than the passive vehicle.
- As a result of the guidance and due to the absence of a solid-axle wheelset, the longitudinal creep forces are significantly reduced. The lateral creep force difference between the front and rear wheelsets are also reduced.
- The lower creep forces result in lower $T\gamma$ values than the passive vehicle on all the track profiles considered. Using a PIP controller, the % decrease in $T\gamma$ achieved ranges from $\approx$ 10% to 50%.
- The overall performance of the DIRW vehicle is significantly better than the passive vehicle. It also performs the best compared to the other two steering mechanisms considered using either controller.

5.8 Conclusions

In this chapter two important comparisons were drawn. Firstly, the active vehicles were compared to the conventional passive vehicle and to each other. The vehicles are run on four different track profiles described and analysed in terms of creep forces, $T\gamma$ values, wheelset lateral displacement and actuation force/ torque. Secondly, the classical and PIP controllers designed in the previous chapter are compared on all of the track profiles described.

Amongst the active steering mechanisms under consideration, the DIRW vehicle shows the best performance with a significant reduction in wear on straight and curved track, using either controller. In the ASW and SYC vehicles the control action interferes with the natural behaviour of a solid-axle wheelset which requires a higher actuation power and is also detrimental to the wheel-rail wear. The DIRW vehicle requires the most radical change in terms of the mechanical configuration, but promises the best performance.

The controller comparisons show that the PIP controller generally gives a better performance than the simpler classical controllers. The reason for this is that it is a state-feedback controller unlike a PI or PA controller which uses a single feedback signal. So the use of a more complex control algorithm in this case gives an improvement in performance.

Ideal sensing and actuation is assumed with the idea that further work is needed to consider the practical implementation of these active steering strategies. Although simple

calculations based on actuator force and velocity have been done to determine the approximate actuator power required, a more detailed study needs to be done which takes into account the actuator dynamics.

In the next chapter, the DIRW vehicle is controlled using a PIP controller on switches and crossings.

Chapter 6

Track switch modelling and simulations

From the analysis in Chapter 5, it is clear that the Driven Independently-Rotating Wheelset (DIRW) vehicle shows the best performance compared to the other active steering mechanisms considered on a range of operating conditions and metrics. In this chapter, the DIRW vehicle is simulated on two conventional track switches to compare its performance to that of the passive vehicle model. The objective is to firstly establish whether an active vehicle can generate the guidance forces necessary to travel on an S&C. This has been hypothesised but not proved yet. Secondly, this chapter also aims to set a benchmark for the performance improvement that can be expected when applying active steering on conventional S&Cs.

The different switches and crossings under consideration are described in terms of their geometric layout and their modelling process in Simpack. Although the DIRW vehicle is used with a PIP controller, the controller gains may need to be re-tuned because of the absence of track cant on the diverging routes of switches. The vehicle speeds on S&Cs are restricted by the maximum allowable turnout speed. In reality, gain scheduling method would likely need to be employed for different operating conditions, as used in aircraft flight control.

In this chapter, two different S&Cs are under consideration. The results presented here aim to show the benefits of active vehicles on conventional switches which have been been designed only for passive solid-axle vehicles. The longer term view is that switches can be redesigned to further improve the performance.

6.1 Switch modelling

Track switches are manufactured in standard dimensions ranging from tight curves of only 140 m radius to shallow curves with a 3000 m radius. The letters A to H are used in switch

nomenclature in the UK to denote the radius and the corresponding variations in maximum permissible speed with A having the lowest turnout radius.

In plain line track in Britain, the rails have a nominal inclination of 1 in 20 towards the track centre line [89]. S&Cs are permitted to be either vertical or inclined. However, an inclination is usually present because in the absence of track cant, the wheel-rail contact geometry is affected such that it increases the stress on the turnout structure [103]. If the S&C is vertical, the switch type has a 'V', for example AV for a vertical A switch. Typically, switches are manufactured at a shallow depth which is indicated with an 'S', for example AVS. Special bearers of a larger height are used to maintain the same rail height as the rest of the track.

In this study, two types of track switches are modelled to study the active vehicle at different maximum allowable speeds. The running rails are inclined by 1:20 in both switch models. In practice, they could be either shallow or full depth. A C switch is chosen because it is the most commonly occurring switch, accounting for nearly half of the switch population on the UK mainline [11]. It is usually located at or near stations due to its relatively tight radius of ≈245 m on the diverging route. The maximum allowable speed on this switch is 25 mph ≈11 m/s. A high speed H type turnout is chosen to study the behaviour at speeds of 90 mph ≈40 m/s. This switch has a curve radius of ≈3000 m on the diverging route and consequently a shallow diverging angle of 1 in 32. This makes the gap at the crossing over 4 m long which necessitates the use of a moveable crossing nose, also known as a swingnose crossing. Table 6.1 lists some of the main dimensions of each switch. A track gauge of 1432 mm is maintained throughout. On plain track the nominal gauge is 1435 mm, but no special measures are required when it abuts with the narrower switch gauge as a variation of 3 mm is within acceptable limits [104]. The curvature variation of the C and H switches is shown in Figure 6.1.

The stock, switch and check rail profiles used for both switches are CEN56 E1, CEN54 E1A1 and CEN33 C1 respectively. The stock rail and switch rail profile is described in detail in British Standards [88], [105]. The check rail profile and its relationship with the running rail is described in the Network Rail Track Design Handbook [104].

In the case of the C switch, the machining of the switch rail at different distances from the toe is described in detail in the RE/PW/1602 B drawings. The crossing nose profile detail is given in RE/PW/1769 drawing. For the H switch, the machining of the switch rail is similar to that of a C switch but spread across a longer planing length. The swingnose geometry details are given in the Track Switch Handbook [104].

As the rail profiles are constantly changing at switches and crossings, Simpack modelling of an S&C involves specifying the rail profile at different cross sections along the forward

Table 6.1: Table listing key C and H turnout details. Note that IP is the intersection point where the two rails cross just before the crossing gap.

Dimension	Switch type	
	C	H
Toe to IP length (mm)	24877	89693
Radius of curvature (mm)	245767	3000716
Divergence angle (1 in -)	9.25	32.365
Gap length (mm)	148	4118
Maximum turnout speed (mph)	25	90

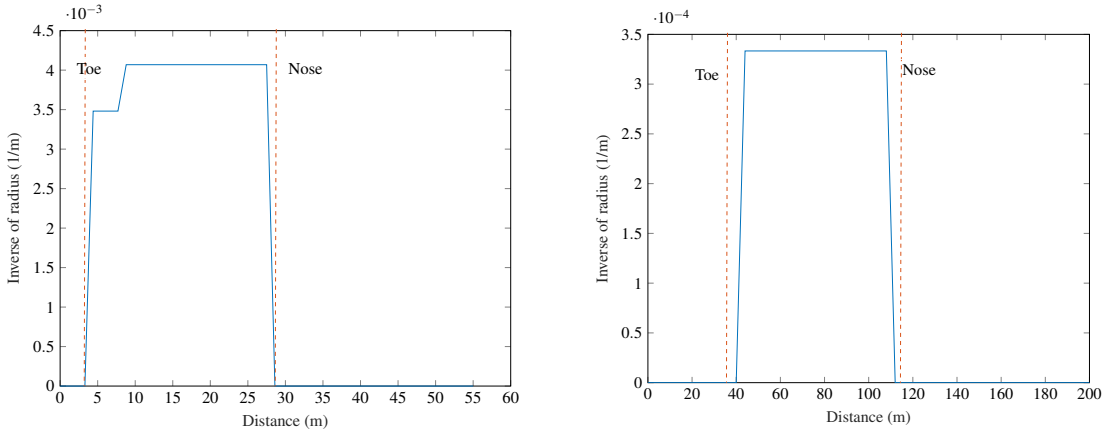

(a) (b)

Figure 6.1: Curvature variation of the diverging routes of C and H switches

running direction of the rail vehicle [106]. Figure 6.2 shows the process used to model an S&C in Simpack. The cross sections are generated from CAD models of the switches which are developed from the rail profile geometries described in British Standards and the RE/PW drawings. MATLAB is used to slice the CAD model to generate the cross-sectional profiles. The profiles are specified using a Cartesian coordinate system where the origin is at the top centre of the rail head as shown in Figure 6.3.

The z axis is positive in the downward direction and the y axis is positive towards the right. The third axis is the s axis along the direction of the track, which is also the forward running direction of the rail vehicle. The contours are specified in Simpack in the form of .prr files which specify the y,z coordinates at a particular value of s. Figure 6.4 illustrates some of these cross-sectional profiles at different points along the C switch.

Simpack performs an interpolation between consecutive cross sections to form a continuous rail. Although this has its advantages, the interpolation can produce undesirable effects at certain points in the switch model which have sudden drastic changes in profile shape such

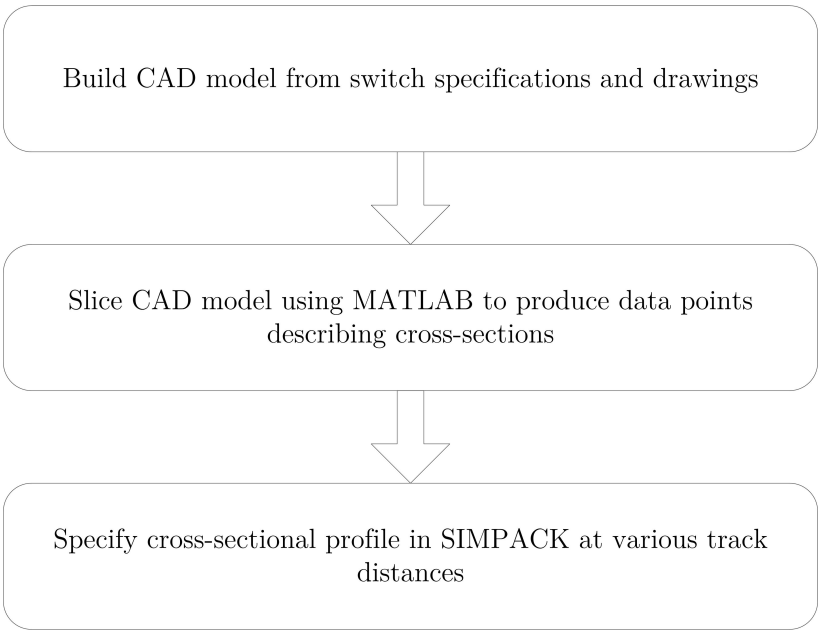

Figure 6.2: Rail wheel profile axes

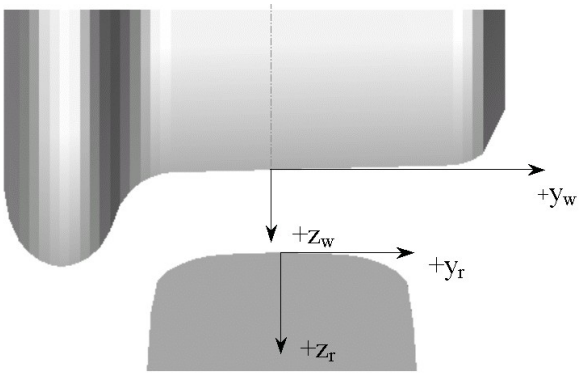

Figure 6.3: Rail wheel profile axes

as at the nose. Discontinuities are introduced in the switch model by specifying the same distance or the same ‘s’ value for two different consecutive profiles. This forces Simpack to not interpolate between successive prr files. Figure 6.4a shows the profile at the switch toe and 6.4b shows the profile where the contact patch shifts from the stock rail to switch rail. Figures 6.4c and 6.4d illustrate the profiles at the crossing gap and nose respectively. For a left-handed switch, these profiles occur on the left rail for the through-route and on the right rail for the diverging-route. The opposite rail i.e. the right rail in this case, has a stock rail profile with the check rail appearing at the crossing as shown in Figure 6.5. The check rail makes flange contact to laterally displace the wheelset so that the vehicle is guided across the

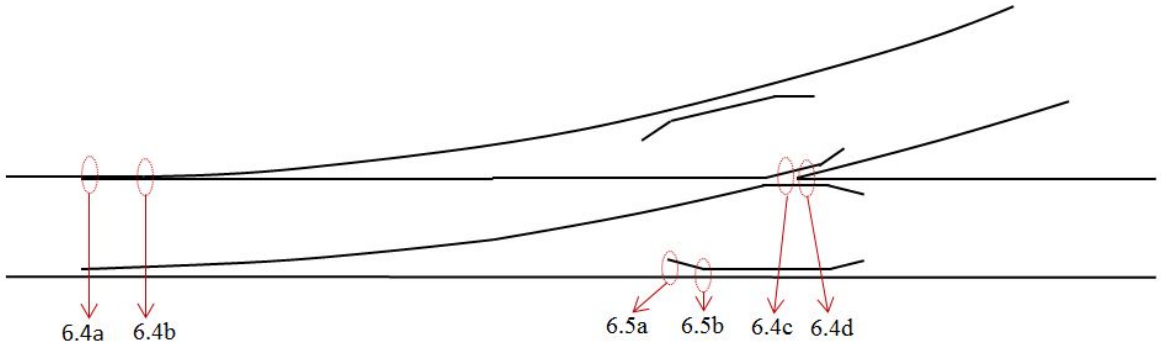

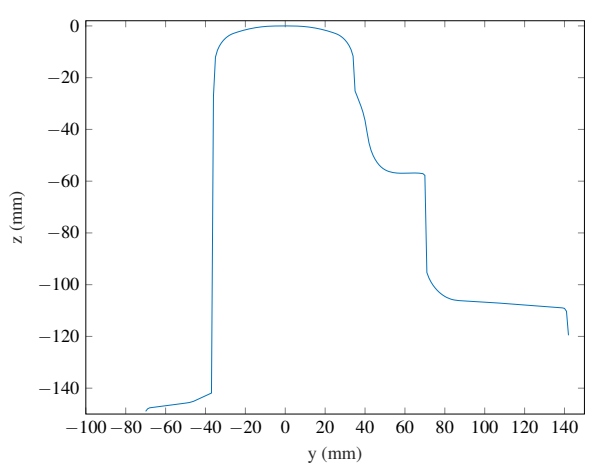

(a) Switch toe at 3.1 m from start of switch model.

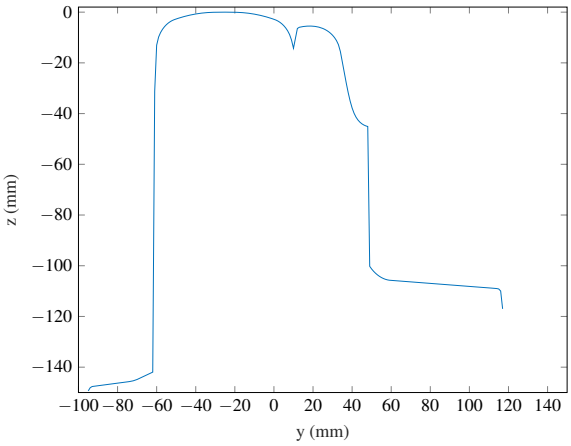

(b) Change in contact from stock to switch rail at 5.5 m from start of switch model.

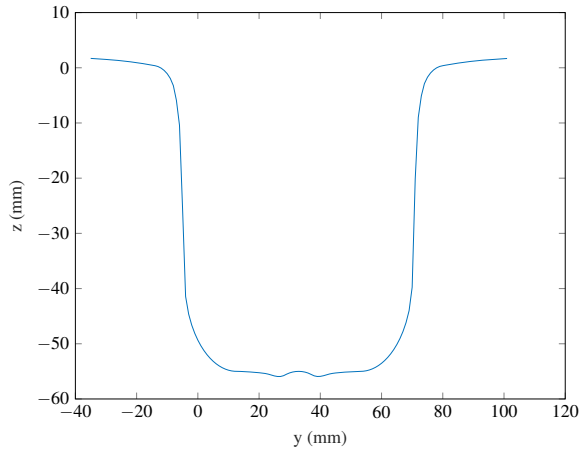

(c) Crossing gap at 28 m from start of switch model.

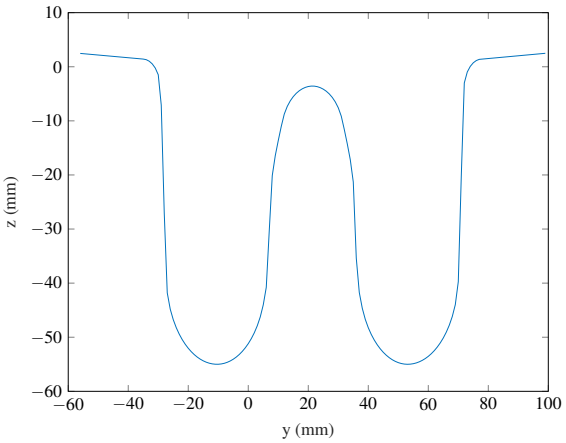

(d) Crossing nose at 28.3 m from start of switch model.

Figure 6.4: Different cross sections in the Simpack C switch model

crossing gap onto the nose. In the absence of the check rail, the wheelset has a tendency to follow the diverging rail and become derailed.

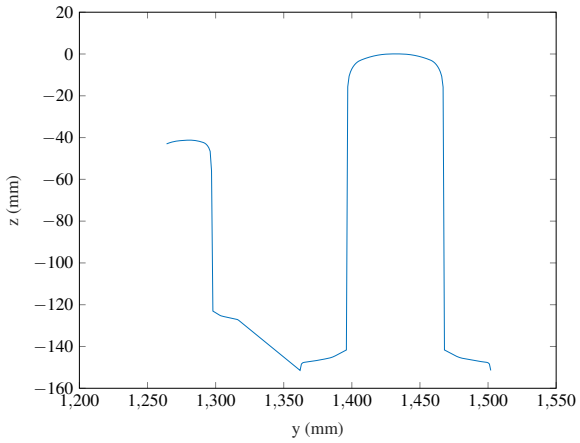

(a) First profile of check rail at 21.18 m from start of switch model.

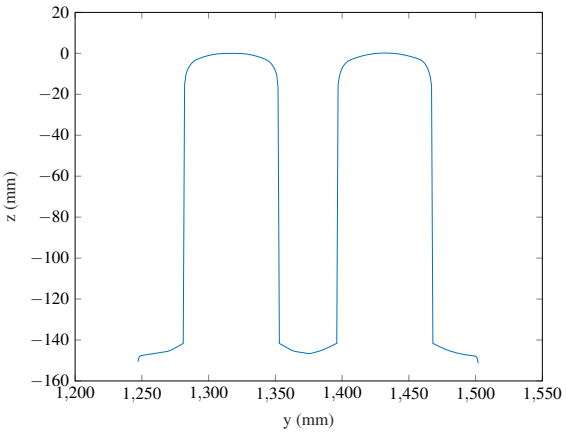

(b) Check rail profile at crossing nose at 28.3 m from start of switch model.

Figure 6.5: Check rail in relation to the stock rail in the Simpack C switch model

The cross-sections of the H switch at the switch blades is exactly the same as that of the C switch, simply spread across a longer planing length due to the vehicle running speed being significantly higher. The swingnose crossing ensures a smooth transition at the nose without any crossing gaps which are a feature of low and moderate speed switches. Figure 6.6 shows the variation in the swingnose profile across a running distance of 1 m.

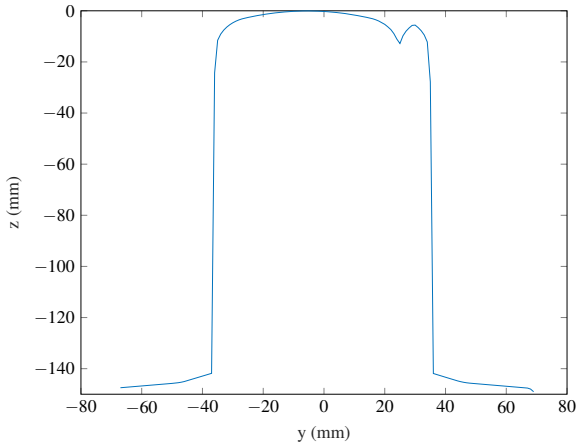

(a) Swingnose at 89.063 m from start of switch model.

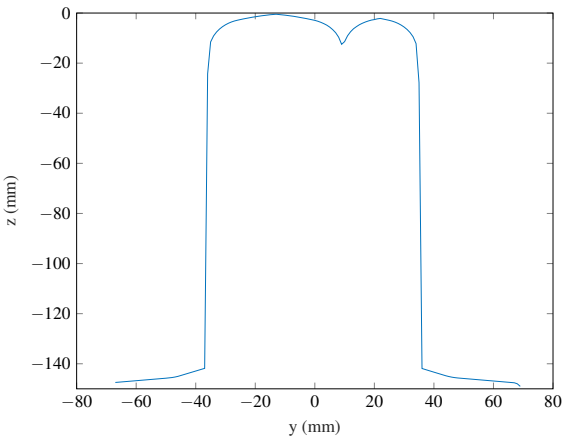

(b) Change in contact from stock to swingnose at 90.063 m from start of switch model.

Figure 6.6: Swingnose profiles in the Simpack H switch model

6.2 Controller design for switch simulations

The controller designed in Chapter 4, based on the linear model identified at a maximum line speed of 45 m/s is used on the C and H switch simulations in the next section. However, the C switch has a relatively tight curve radius on the diverging route and there is no cant on either of the switch curves. Moreover, steering on the diverging routes is likely to require higher motor torques than guidance on the through routes. The PIP controller could be re-tuned by changing the W_y, W_u and W_z weightings to give a higher or lower output motor torque. If the motor torques are too high, the wheels could be slipping, leading to excessive longitudinal creep forces, which in turn would increase the wear or $T\gamma$ values. If the motor torques are too low, insufficient guidance could cause flange contact, which would again increase wear. Therefore the controllers need to be tuned to provide sufficient but in-excessive motor torque for a particular switch scenario.

A higher controller gain matrix is calculated by minimising the PIP cost function with the weightings $W_y = 1 \times 10^{-3}, W_u = 1 \times 10^{-6}$ and $W_z = 2 \times 10^{6}$.

$k = 1 \times 10^{9}$ [-0.7 1.2 -0.4 -0.1 0.2 -0.1 0.1 0.0 0.0 0.0 0.0 ... 0.0 0.0 0.0 0.0]

Figure 6.7 shows the uncompensated open loop frequency response, and the response with the high gain PIP controller, which is labelled as 'Controller 1'. The uncompensated open loop response is from the motor torque in kNm to the wheelset lateral displacement in millimeters. The uncompensated open loop system has a GM of 29.1 dB and a PM of 63.1 degrees. 'Controller 1' with the higher gains reduces the gain and phase margins to 24.1 dB and 60.3 degrees. These margins are slightly lower than the those with the controller designed in Chapter 4 which will be called 'Controller 2'. The margins are not pushed excessively so as to keep the control force/ torque required to practically realisable levels between 5 to 6 kNm.

Both controllers are applied in the next section on the through and diverging routes of the C and H switches to determine the relative performance variation and with respect to a conventional passive vehicle. The higher controller gains should give a better performance on the diverging routes which will require higher motor torques for steering.

6.3 Simulation results

In this section the DIRW vehicle is compared against the passive vehicle on the through and diverging routes of the C and H switches designed in section 6.1. The wheelset lateral displacement and the contact patch frictional energy are being used, as before, to analyse the

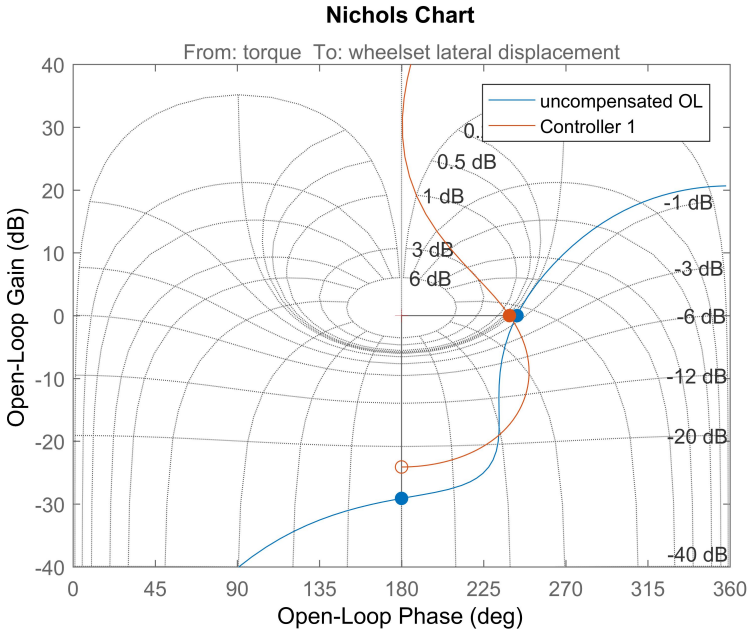

Figure 6.7: Nichols plot for PIP controller design.

performance of the vehicles. In addition it is necessary to determine whether the ride quality is compromised by using the DIRW vehicle on conventional track switches. So the following indicators are used to assess ride comfort.

- $\ddot{y}_v$, lateral acceleration in the middle of the vehicle body floor. The maximum allowable acceleration is 1 m/s^2 to maintain ride quality standards [107].

- P_{DE}, ride comfort index on discrete events. It indicates the percentage of dissatisfied passengers and is calculated as a continuous time-variant signal. The comfort index is calculated as

$$P_{DE} = 100 \times [a.\ddot{y}_{pp}(t) + b.|\ddot{y}_{2s}(t)| - c] \tag{6.1}$$

  where $|\ddot{y}_{2s}(t)|$ is the absolute mean value of the lateral acceleration of the vehicle body expressed in m/s^2 over a 2 s averaging window and $\ddot{y}_{pp}(t)$ is the maximum corresponding peak to peak lateral acceleration [107]. The constants a,b and c are 0.1662, 0.2701 and 0.37 respectively for standing passengers. Only the P_{DE} for standing passengers is considered because the comfort quality when standing is worse than that when seated. A higher P_{DE} indicates poorer passenger comfort. If the P_{DE} value is negative because c is bigger than the a and b terms combined, the P_{DE} can be considered to be zero, indicating good ride quality with no dissatisfied passengers.

6.3.1 C switch through route

Figure 6.8a shows the lateral displacements of the front and rear wheelsets with respect to the track centre-line on the through route of a C switch using 'Controller 1'. At the switch toe, the lateral displacement of the DIRW wheelsets are much lower than that of the passive vehicle. At the nose, although the initial displacement is similar, the DIRW vehicle guidance responds quicker than the passive vehicle. This improvement in performance can also be seen from the average $T\gamma$ values in Table 6.2 which are reduced to less than a quarter of the passive vehicle. The main peaks in the $T\gamma$ responses in Figure 6.8c occur when the rear bogie wheelsets travel over the switch toe and crossing nose. The car body lateral acceleration is similar to that of the passive vehicle as shown in Figure 6.8b. The maximum P_{DE} values for both vehicles are negative which means that there are no dissatisfied passengers which is indicative of good ride quality. These results indicate that the through route performance of the DIRW vehicle is significantly better than the passive vehicle.

Using 'Controller 2' the average $T\gamma$ values are worse than using 'Controller 2' as shown in Table 6.2 and very similar to a passive vehicle. This is because of insufficient guidance which can be clearly seen from the wheelset lateral displacement in Figure 6.9a. The lateral displacement is higher than that observed using 'Controller 1' which has higher gains. The settling time after the nose is also longer than the passive vehicle. This contributes to the higher wear as indicated in the table. The spikes in the $T\gamma$ responses in Figure 6.9c occur at the transition from stock to switch rail past the toe and at the nose. The vehicle body lateral acceleration shown in Figure 6.9b is very similar to the passive vehicle. Overall, the results indicate that the performance is similar to the passive vehicle but worse than using 'Controller 1'.

Table 6.2: $T\gamma$ values in J/m on the through route of a C switch. The values under 'Controller 1' column are obtained from simulations with higher controller gains than that in 'Controller 2' column.

	Passive	Controller 1	Controller 2
Front bogie front WS	1.2198	0.4725	2.3853
Front bogie rear WS	0.9762	0.4552	1.3445
Rear bogie front WS	1.3267	0.3723	1.7970
Rear bogie rear WS	2.9491	0.1740	1.1718
Total $T\gamma$ on all WSs	6.4718	1.4740	6.6986
Percentage of passive		22.7757	103.5044

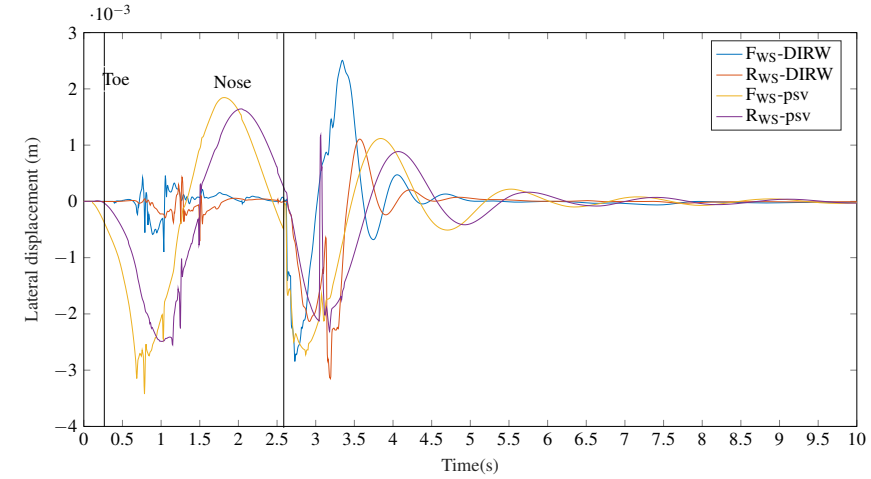

(a)

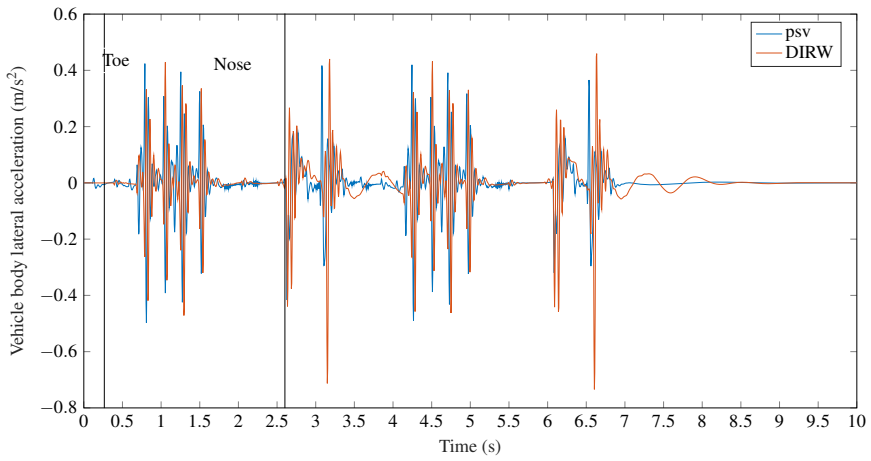

(b)

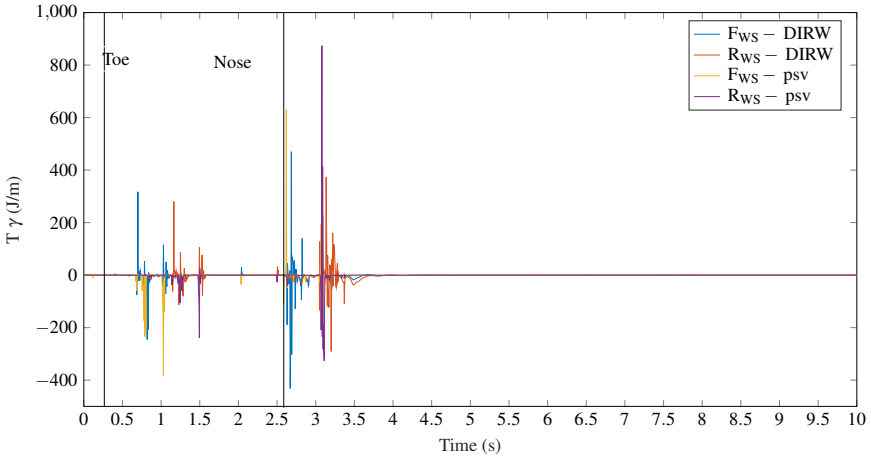

(c)

Figure 6.8: Response of the DIRW vehicle compared to the passive vehicle on the **through route of a C switch using 'Controller 1'** at v=11 m/s. The notations F_{WS}, R_{WS} and psv used in the graph labels mean 'front wheelset', 'rear wheelset' and 'passive' respectively.

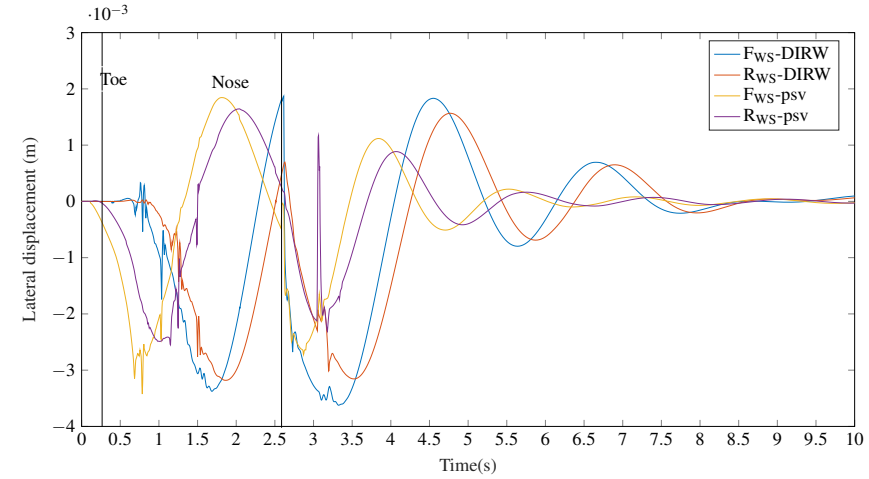

(a)

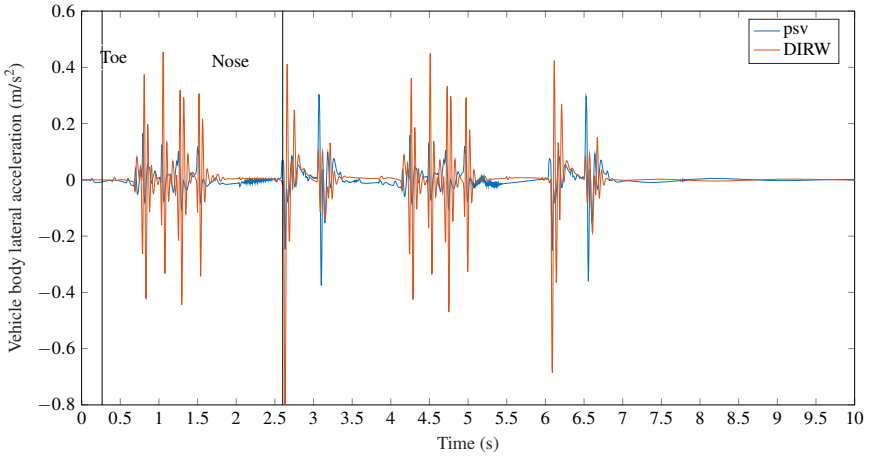

(b)

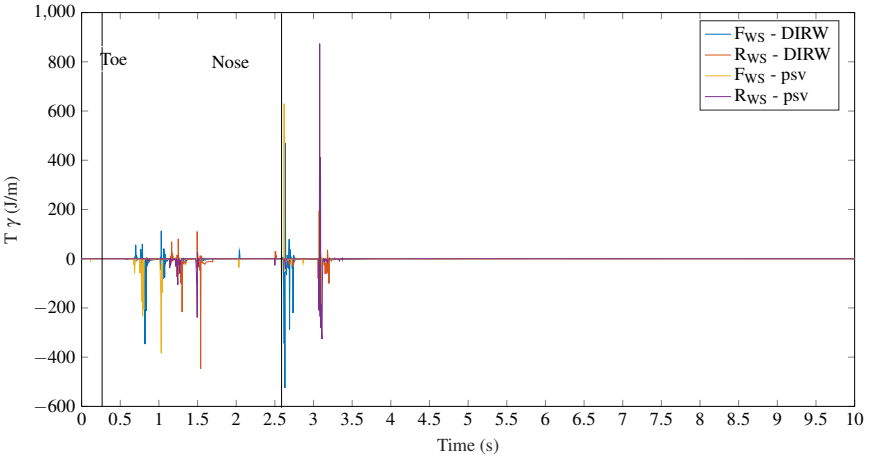

(c)

Figure 6.9: Response of the DIRW vehicle compared to the passive vehicle on the **through route of a C switch using 'Controller 2'** at v=11 m/s. The notations F_{WS}, R_{WS} and psv used in the graph labels mean 'front wheelset', 'rear wheelset' and 'passive' respectively.

6.3.2 C switch diverging route

The diverging route has a tight curve radius where both passive and DIRW vehicles make flange contact to generate enough lateral creep forces to balance the centripetal forces on the curve. Previous switch simulation studies have shown that the wheelsets of a conventional vehicle make flange contact when travelling on the divergent routes of moderate and high speed turnouts [108], [109]. The DIRW vehicle using 'Controller 1' gives a very similar performance to the passive vehicle in terms of lateral displacement as shown in Figure 6.10a. The wear is reduced by approximately a third of that of the passive vehicle as indicated by the $T\gamma$ values in Table 6.3. From the $T\gamma$ response in Figure 6.10c it can be seen that the majority of the wear occurs on the curve which is expected from all the lateral creep forces generated during curve negotiation. The wear on the front wheelset of the passive vehicle is the highest, which is the case on conventional vehicles at present and this usually sets the limiting speed on a curve. Although the average wear on the front wheelset of the front bogie of the DIRW vehicle is marginally higher than the passive vehicle, the maximum $T\gamma$ value is lower as the wear is spread across a greater distance. This means that the DIRW vehicle could allow a higher turnout speed than is currently recommended. The DIRW vehicle body acceleration is less than that of the passive vehicle at the switch nose, but is otherwise similar as shown in Figure 6.10b. The maximum P_{DE} values for both vehicles are negative which means that the percentage of dissatisfied passengers is zero. Overall, on the diverging route, using 'Controller 1', the DIRW vehicle shows a considerable improvement in performance than the passive vehicle.

Table 6.3: $T\gamma$ values in J/m on the diverging route of a C switch. The values under 'Controller 1' column are obtained from simulations with higher controller gains than that in 'Controller 2' column.

	Passive	Controller 1	Controller 2
Front bogie front WS	22.6880	32.1984	40.6996
Front bogie rear WS	5.1924	1.2658	2.1731
Rear bogie front WS	30.4560	0.1647	3.8114
Rear bogie rear WS	1.7047	8.4680	6.5279
Total $T\gamma$ on all WSs	60.0411	42.1269	53.2120
Percentage of passive		70.1634	88.6260

Using 'Controller 2' with the lower gains, the wheelset lateral displacement takes longer than the passive vehicle to return to the track centre-line after travelling through the crossing nose, as shown in Figure 6.11a. This indicates that the guidance torque is not sufficiently high. As a consequence the vehicle body lateral acceleration is also marginally higher than using 'Controller 1'. The $T\gamma$ values in Table 6.3 and the graphs in Figure 6.11c indicate that the wear is largely similar to the passive vehicle.

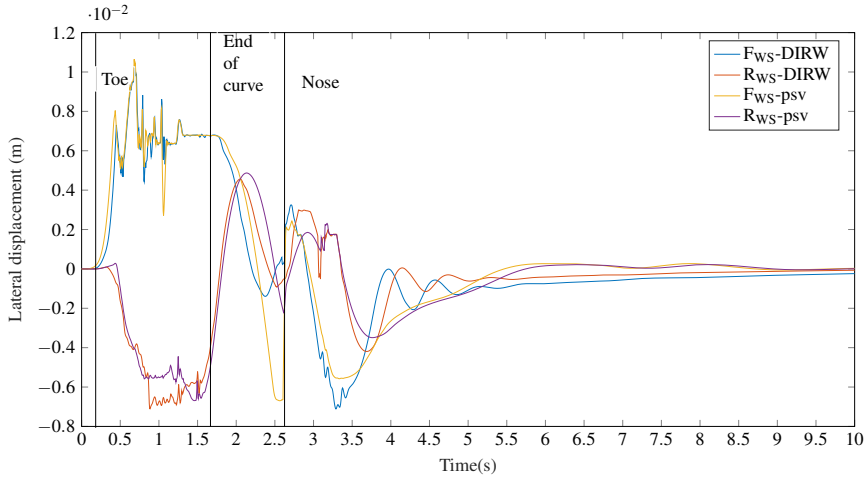

(a)

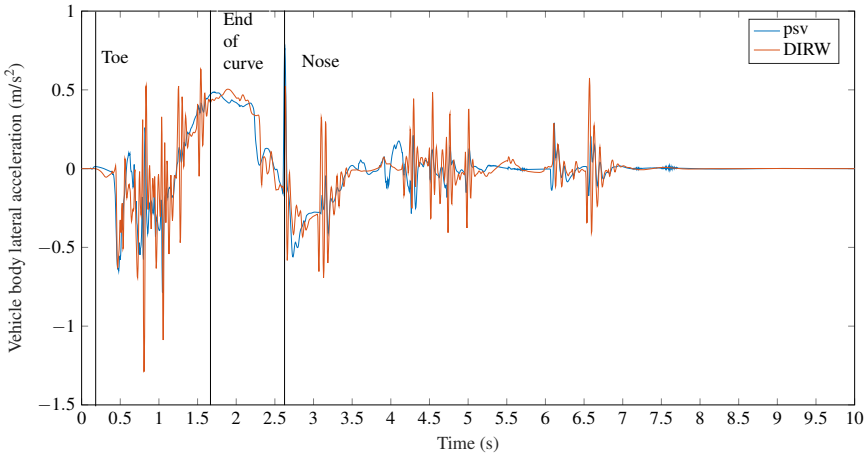

(b)

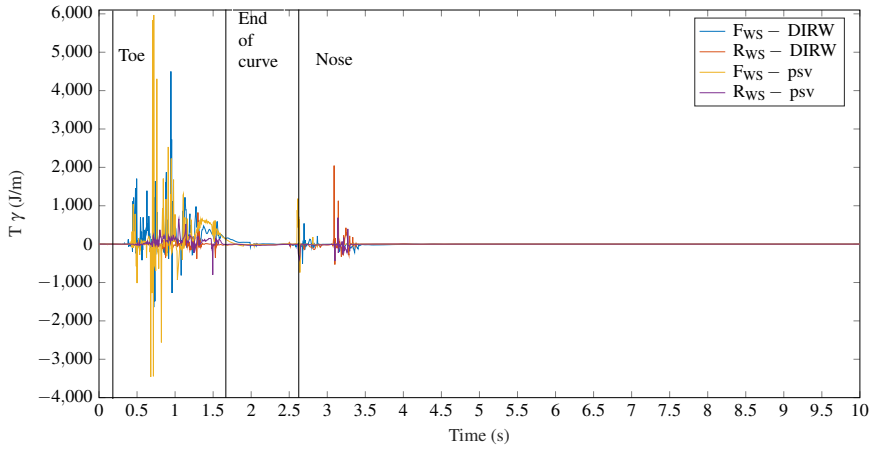

(c)

Figure 6.10: Response of the DIRW vehicle compared to the passive vehicle on the **diverging route of a C switch using 'Controller 1'** at v=11 m/s. The notations F_{WS}, R_{WS} and psv used in the graph labels mean 'front wheelset', 'rear wheelset' and 'passive' respectively.

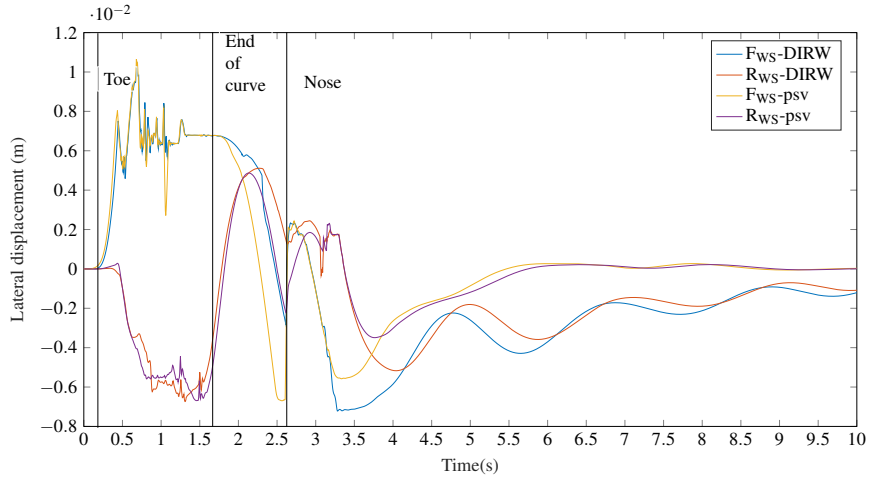

(a)

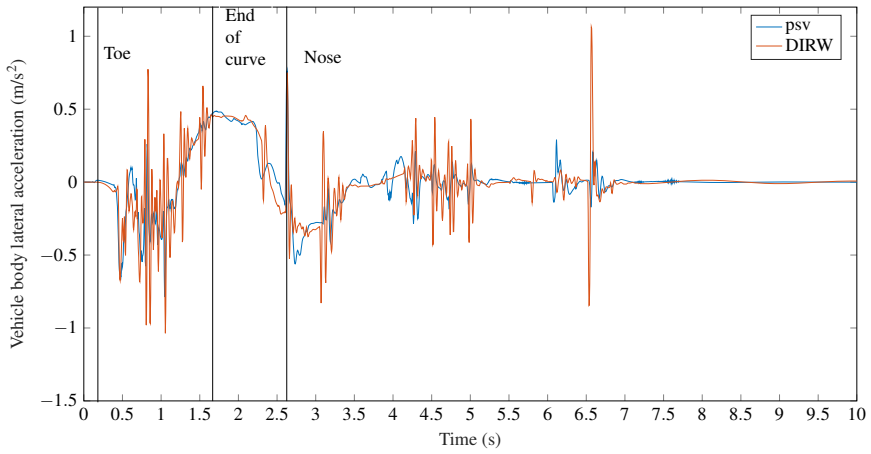

(b)

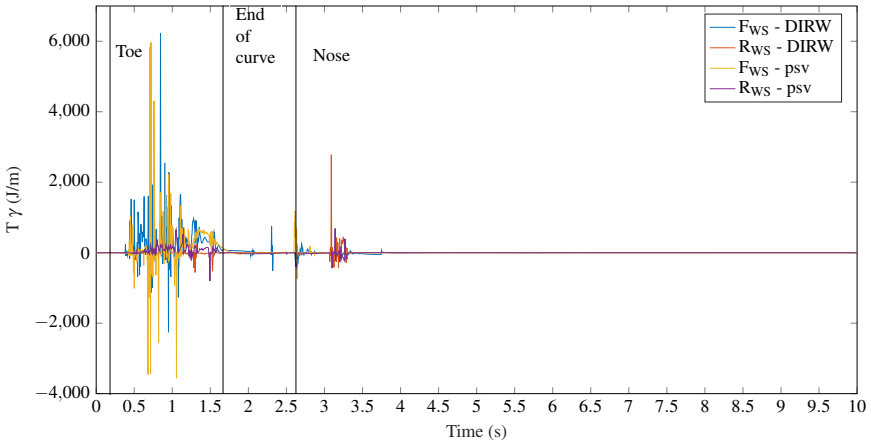

(c)

Figure 6.11: Response of the DIRW vehicle compared to the passive vehicle on the **diverging route of a C switch using 'Controller 2'** at v=11 m/s. The notations F_{WS}, R_{WS} and psv used in the graph labels mean 'front wheelset', 'rear wheelset' and 'passive' respectively.

From the results it can be concluded that the higher gains on 'Controller 1', provide the required motor torques to minimise flange contact and therefore reduce wear indicating an overall improvement in performance. However using 'Controller 2' produces more wear due to the lower guidance action.

6.3.3 H switch through route

On the through-route of the H switch using 'Controller 1', the lateral displacement of the DIRW vehicle is significantly smaller than that of the passive case as shown in Figure 6.12a. The vehicle body acceleration is also lower than the passive vehicle as shown in Figure 6.12b. However the longitudinal creep forces generated are high as shown in Figure 6.12c. This results in higher average $T\gamma$ values as listed in Table 6.4. The change in $T\gamma$ through the switch is shown in Figure 6.14. From the figure it can be seen that there is a sudden spike just past the toe at ≈ 1.2 s. This occurs when the wheel-rail contact patch shifts from the stock to the switch rail. The high wear can be explained by the high longitudinal creep forces generated due to excessive motor torques.

Table 6.4: $T\gamma$ values in J/m on the through route of a H switch. The values under 'Controller 1' column are obtained from simulations with higher controller gains than that in 'Controller 2' column.

	Passive	Controller 1	Controller 2
Front bogie front WS	0.0285	0.0414	0.0290
Front bogie rear WS	0.0641	0.1550	0.0220
Rear bogie front WS	0.0430	0.0337	0.0297
Rear bogie rear WS	0.0766	0.1497	0.0239
Total $T\gamma$ on all WSs	0.2122	0.3798	0.1046
Percentage of passive		178.9821	49.2931

Using lower gains with 'Controller 2', the wheelset lateral displacement is as shown in Figure 6.13a. The maximum lateral displacement is still quite small. The car body lateral acceleration is also smaller than that of the passive vehicle as shown in Figure 6.13b and smaller than using 'Controller 1'. The maximum P_{DE} values using either controller are negative indicating good ride quality. This shows that the controller could be re-tuned to reduce the creep forces and resultant wear while not having any significantly adverse effects on the wheelset lateral displacement or the ride quality. The longitudinal creep forces generated by using the re-tuned controller are lower than with 'Controller 1'. The average $T\gamma$ values are significantly lower than the passive vehicle as listed in the 'Controller 2' values in Table 6.4. Figure 6.15 shows the $T\gamma$ response of the DIRW vehicle compared to the passive vehicle.

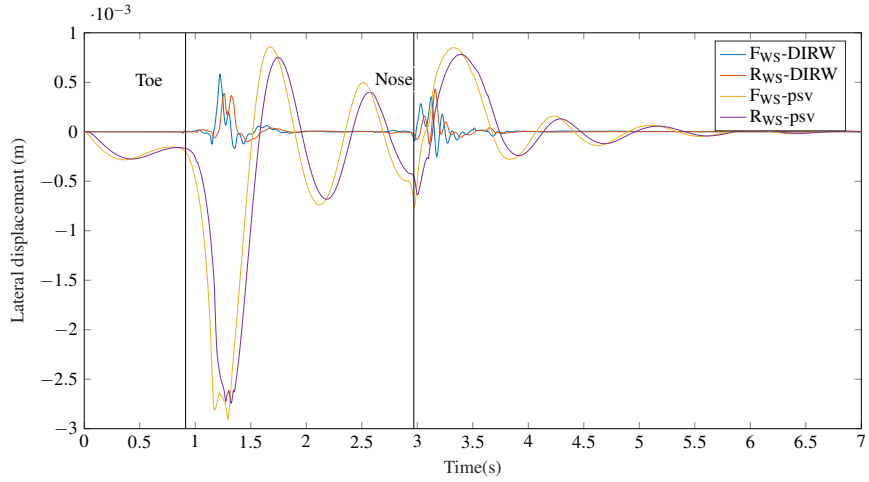

(a)

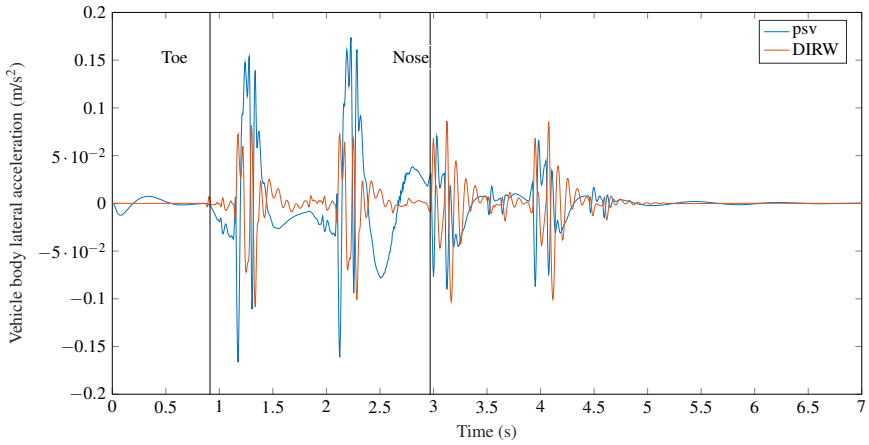

(b)

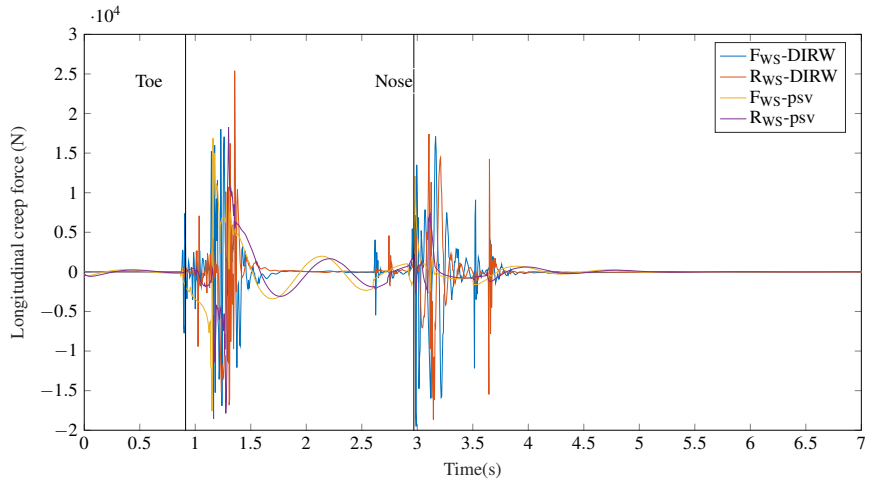

(c)

Figure 6.12: Response of the DIRW vehicle compared to the passive vehicle on the **through route of a H switch using 'Controller 1'** at v=40 m/s. The notations F_{WS}, R_{WS} and psv used in the graph labels mean 'front wheelset', 'rear wheelset' and 'passive' respectively.

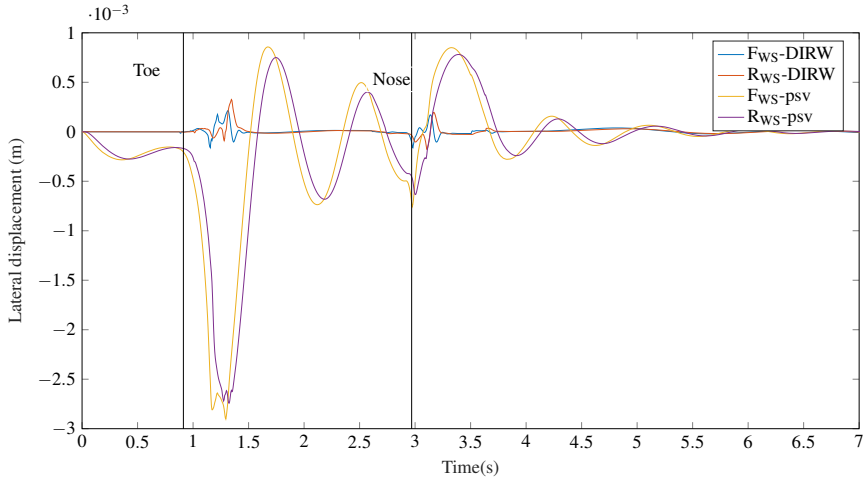

(a)

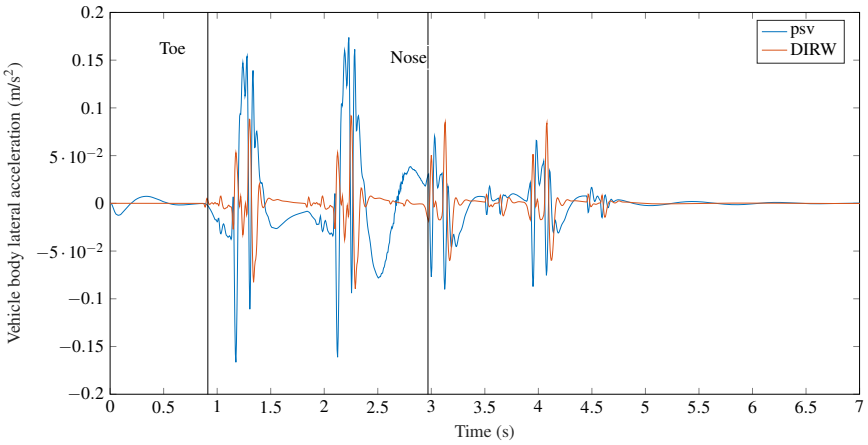

(b)

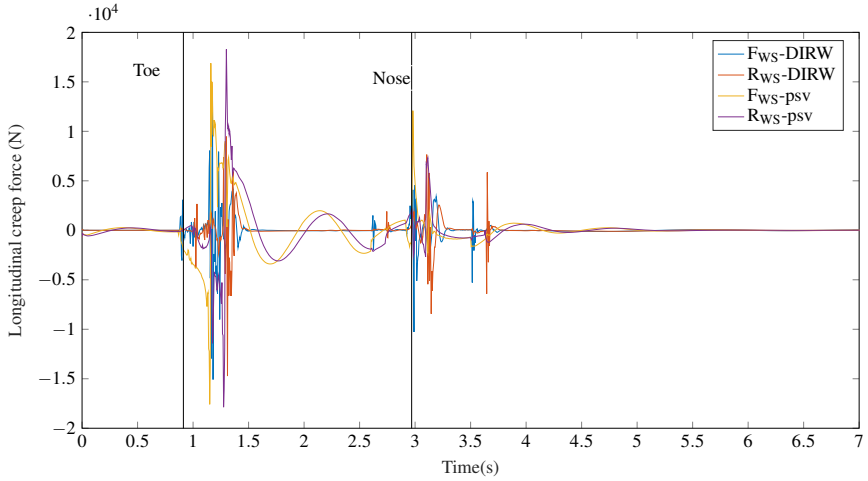

(c)

Figure 6.13: Response of the DIRW vehicle compared to the passive vehicle on the **through route of a H switch using 'Controller 2'** at v=40 m/s. The notations F_{WS}, R_{WS} and psv used in the graph labels mean 'front wheelset', 'rear wheelset' and 'passive' respectively.

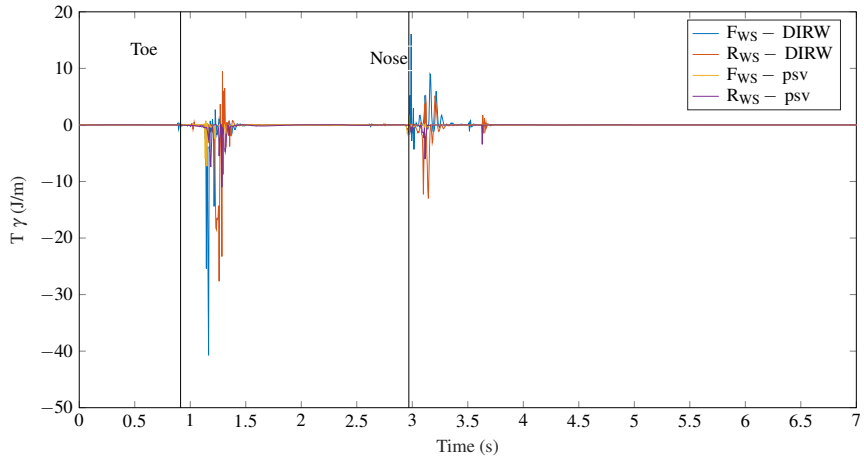

Figure 6.14: $T\gamma$ response of the DIRW vehicle compared to the passive vehicle on the **through route of a H switch using 'Controller 1'** at v=40 m/s. The notations F_{WS}, R_{WS} and psv used in the graph labels mean 'front wheelset', 'rear wheelset' and 'passive' respectively.

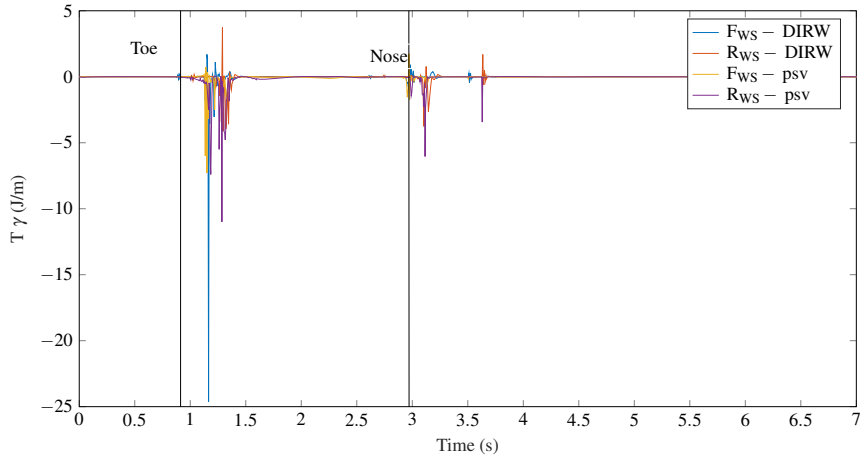

Figure 6.15: Tγ response of the DIRW vehicle compared to the passive vehicle on the **through route of a H switch using 'Controller 2'** at v=40 m/s. The notations F_{WS}, R_{WS} and psv used in the graph labels mean 'front wheelset', 'rear wheelset' and 'passive' respectively.

Comparing the overall performance of 'Controller 1' with higher gains and 'Controller 2' with lower gains on the through route, it can be concluded that the high gains result in more "slippage" or higher longitudinal creep forces giving larger Tγ values, indicating more wear. The main difference in the through routes of both C and H switches is the presence of a crossing gap in the C switch which is absent in the H switch due to the swingnose. This means that a larger guidance torque is required on the C switch which is the reason a significant reduction in wear is achieved using 'Controller 1'. The H switch through route is essentially similar to a straight track with stochastics. Therefore this track scenario does not require a large guidance torque and consequently 'Controller 1' produces excessive longitudinal creep forces leading to high wear.

6.3.4 H switch diverging route

On the diverging-route of the H switch, only the passive vehicle makes flange contact on the curve radius as shown in Figure 6.16a. These results are from using 'Controller 1'. The DIRW vehicle has a much lower lateral displacement at both the toe and the crossing nose than the passive vehicle. The control action also guides it back to the track centre-line which is not the case for the passive vehicle which remains displaced by ≈2 mm in the steady state. The vehicle body acceleration of the DIRW vehicle is lower at the toe and nose as shown in Figure 6.16b. The DIRW vehicle generates high longitudinal creep forces on the diverging route as shown in Figure 6.16c in order to generate a steering action. An overall reduction in the average $T\gamma$ values is observed due to the minimal flange contact. The average $T\gamma$ values are listed under the 'Controller 1' column in Table 6.5. Figure 6.18 shows the $T\gamma$ response of the DIRW vehicle compared to the passive vehicle using 'Controller 1' . From the figure it can be seen that there is a sudden increase in the $T\gamma$ value just past the toe where the contact patch shifts from the stock to the switch rail.

Table 6.5: $T\gamma$ values in J/m on the diverging route of a H switch. The values under 'Controller 1' column are obtained from simulations with higher controller gains than that in 'Controller 2' column.

	Passive	Controller 1	Controller 2
Front bogie front WS	0.8139	1.1833	2.5698
Front bogie rear WS	1.9583	1.12536	2.0834
Rear bogie front WS	0.2296	0.9245	1.9981
Rear bogie rear WS	2.3670	0.6610	0.8610
Total $T\gamma$ on all WSs	5.3688	2.5228	7.5123
Percentage of passive		72.5320	139.9251

With 'Controller 2' which has lower gains, the wheelset lateral displacement is much higher as shown in Figure 6.17a. This is because the re-tuned controller does not provide sufficient guidance forces to maintain minimal flange contact. The car body lateral acceleration is similar to that with 'Controller 1' as shown in Figure 6.17b. The maximum P_{DE} values using either controller are negative indicating good ride quality. The longitudinal creep forces are lower at the nose and on the curve than that in the 'DIRW 1' case as shown in Figure 6.17c due to the lower controller gains. However the $T\gamma$ values are higher as shown by the values under the 'Controller 2' column in Table 6.5 because of the flange contact. These results show an overall degradation in performance with the re-tuned controller compared to the previous controller. Figure 6.19 shows the $T\gamma$ responses of the passive and DIRW vehicles.

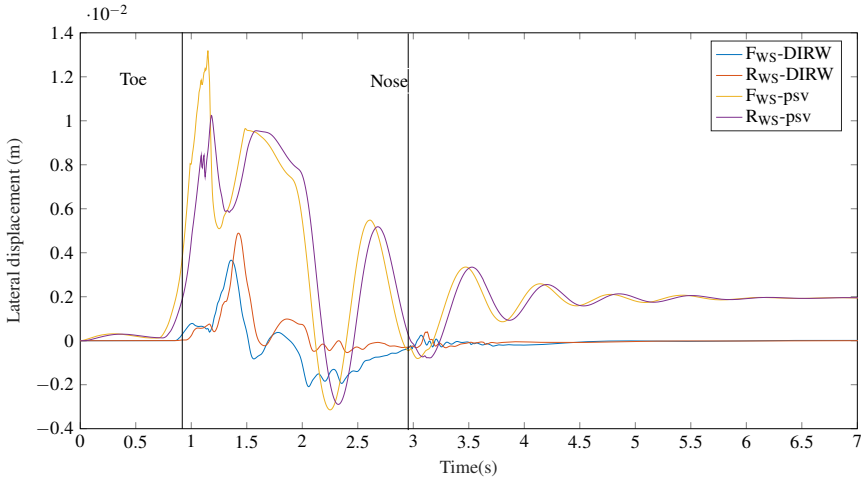

(a)

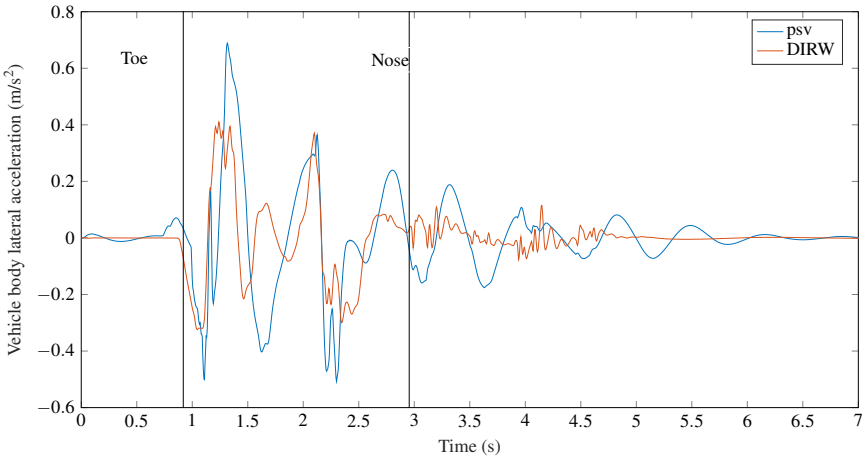

(b)

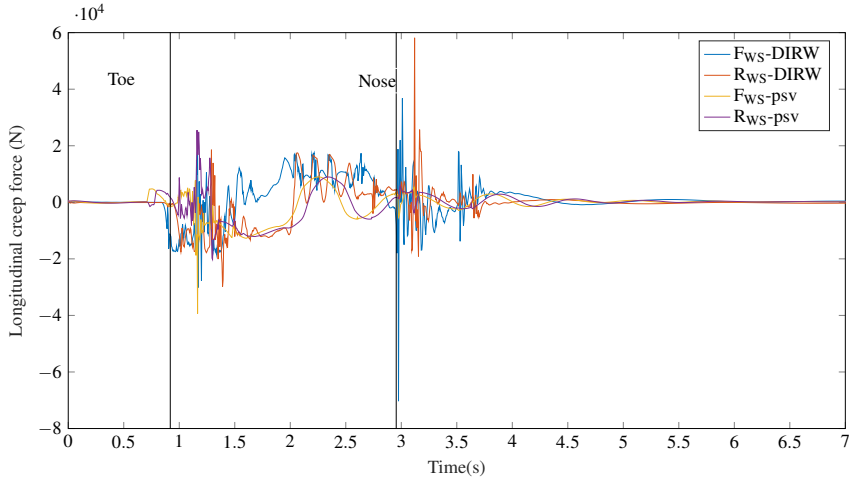

(c)

Figure 6.16: Response of the DIRW vehicle compared to the passive vehicle on the **diverging route of a H switch using the 'Controller 1'** at v=40 m/s. The notations F_{WS}, R_{WS} and psv used in the graph labels mean 'front wheelset', 'rear wheelset' and 'passive' respectively.

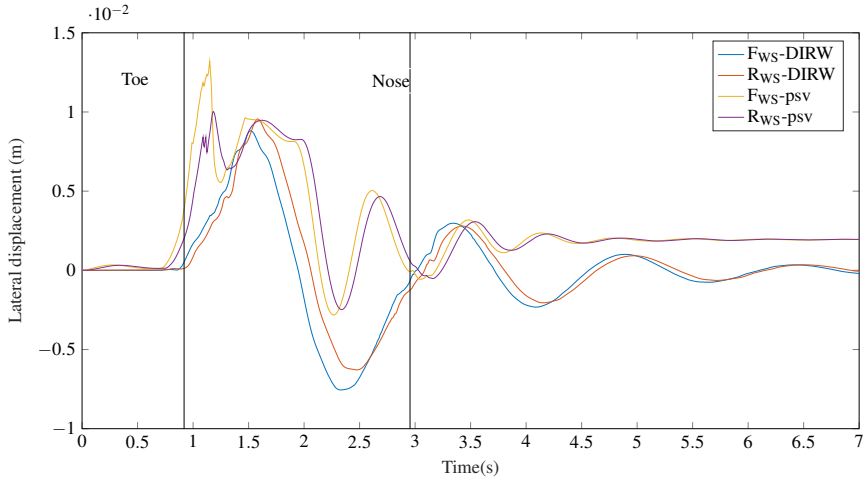

(a)

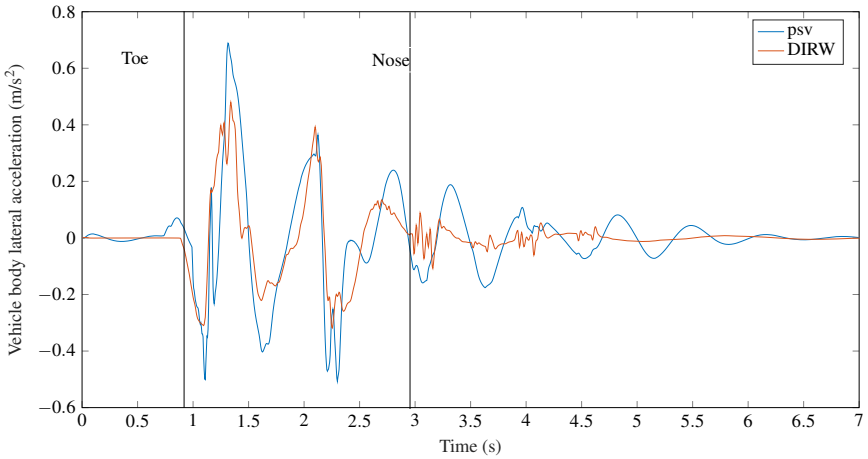

(b)

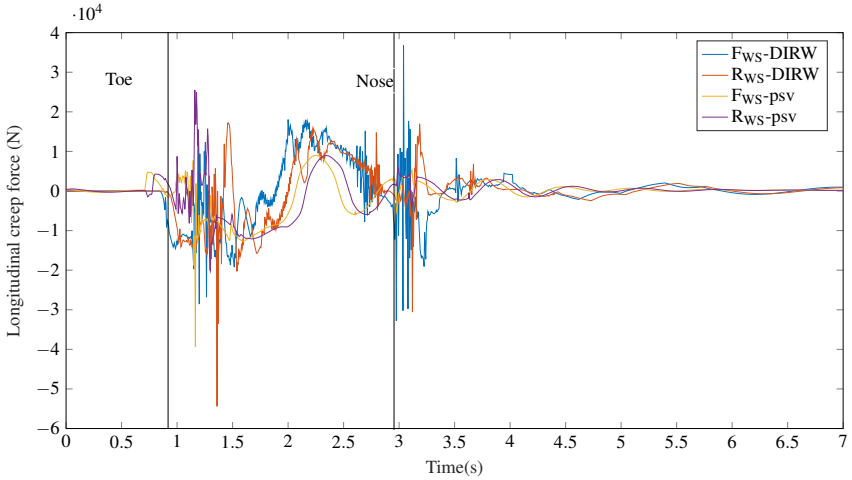

(c)

Figure 6.17: Response of the DIRW vehicle compared to the passive vehicle on the **diverging route of a H switch using 'Controller 2'** at v=40 m/s. The notations F_{WS}, R_{WS} and psv used in the graph labels mean 'front wheelset', 'rear wheelset' and 'passive' respectively.

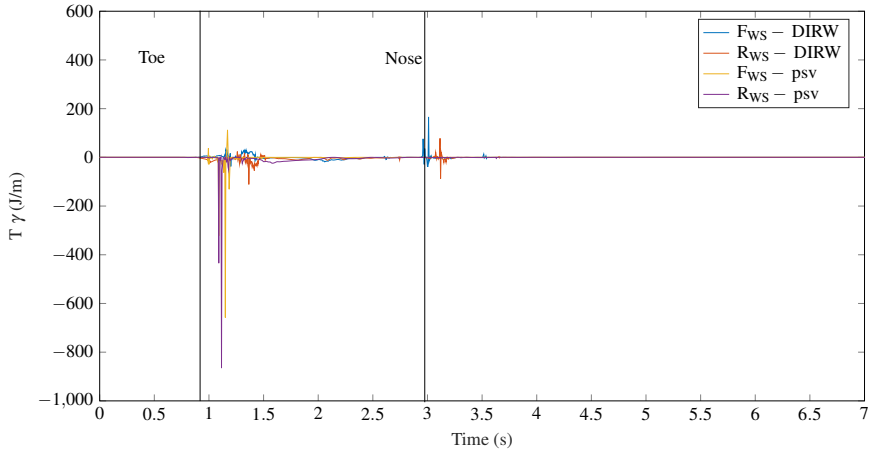

Figure 6.18: Tγ response of the DIRW vehicle compared to the passive vehicle on the **diverging route of a H switch using 'Controller 1'** at v=40 m/s. The notations F_{WS}, R_{WS} and psv used in the graph labels mean 'front wheelset', 'rear wheelset' and 'passive' respectively.

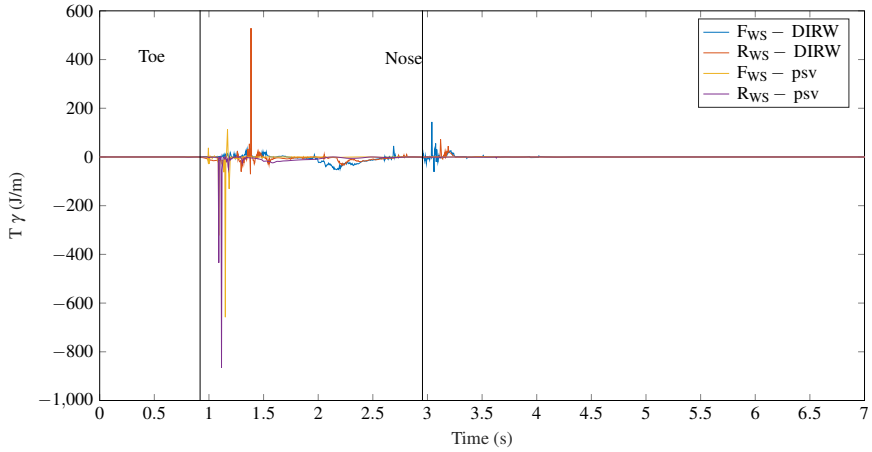

Figure 6.19: Tγ response of the DIRW vehicle compared to the passive vehicle on the **diverging route of a H switch using 'Controller 2'** at v=40 m/s. The notations F_{WS}, R_{WS} and psv used in the graph labels mean 'front wheelset', 'rear wheelset' and 'passive' respectively.

Comparing the overall performance of 'Controller 1' with higher gains and 'Controller 2' with lower gains on the diverging route, it can be concluded the former gives the necessary guidance forces to the wheelsets to maintain minimal flange contact. This in turn results in lower Tγ values. The longitudinal creep forces with higher controller gains is higher, which is expected due to the larger steering action.

6.4 Conclusions

This chapter discussed the modelling of a moderate speed C switch and a high speed H switch in Simpack. The results from running the DIRW vehicle on both switches are presented using the PIP controller designed in Chapter 4 called 'Controller 2' and another PIP controller with higher gains called 'Controller 1'. The results show that an actively-guided vehicle with independently-rotating wheelsets can be used on conventional S&Cs. The following key observations can be made from the simulation results.

- The active vehicle shows a significant improvement in performance in comparison to a conventional passive vehicle in the following scenarios - on both routes of the C switch using 'Controller 1', using 'Controller 2' on the through route of the H switch and 'Controller 1' on the diverging route of the H switch. The improvement is enough to suggest a large potential benefit even when the practicalities of sensing and actuation are taken into consideration.

- Both C and H switch diverging routes show an improvement from using higher controller gains because steering necessitates higher motor torques, especially due to the absence of track cant on switches. Insufficient control action will increase flange contact and consequently increase wear as observed by using 'Controller 2'.

- Although guidance on through routes may be perceived to require less torque than on divergent curves, the presence of a crossing gap necessitates sufficiently high torque. For this reason, the through route of the C switch shows significantly lesser wear with 'Controller 1' than 'Controller 2'.

- The through route of the H switch, which does not have a crossing gap, shows higher $T\gamma$ values using 'Controller 1'. This is due to high longitudinal creep forces generated from high motor torques. Through re-tuning the controller, the $T\gamma$ values have shown a significant reduction. So gain scheduling would be needed on the through route of different switches based on vehicle speed and length of the crossing gap.

- From the two switch simulations under consideration in this study, it can be concluded that the controller gains need to be rescheduled for different switches based on speed-restriction and for different routes. A more detailed analysis comparing the performance of the active vehicle with a conventional vehicle on different switches, A through H, is necessary to determine whether the gain scheduling is necessary for all switches.

Similar to the previous simulations on straight and curved sections of track in Chapter 5, ideal sensing and actuation is assumed here in order to establish the performance improvements before more detailed research can be considered on the practical implementation.

The next chapter will draw some important conclusions on the work presented in this thesis with some suggestions for further work needed to address the gaps in the technology route-map outlined in Chapter 1.

Chapter 7

Conclusion

This chapter draws conclusions on the key research results presented in this thesis. Some recommendations for how this research could be used in academia and industry are provided. Finally future research work in this area is discussed.

7.1 Conclusion on key research results

The contributions of this thesis as discussed in Chapter 1 were to analyse the performance of MBS models of actively controlled vehicle against a conventional vehicle on different track profiles and to establish a benchmark performance improvement for active vehicles on track switches. Although such comparisons have been drawn previously on simpler vehicle models, this thesis assesses the performance of the actie steering concepts in a non-linear simulation environment which take into account complex vehicle dynamics and provide a better representation of a real rail vehicle.

The simulation results on the straight and curved track profiles presented in Chapter 5 show that the SYC vehicle successfully reduces the lateral creep forces but approaches the wheel flanges leading to significantly higher wear than the passive vehicle on almost all the track profiles considered. Both the ASW and DIRW vehicles have lower wear, creep forces, wheelset lateral displacement than the passive vehicle. The DIRW vehicle performs better than the ASW vehicle and requires lower actuation torque due to the fact that the wheels can be driven independently. Compared to the classical controllers, the PIP controllers reduce wear on the curved track profile for the SYC and ASW vehicles. Although the wear is marginally higher in the DIRW vehicle, it is still lower than the SYC and ASW vehicles. The PIP controller also reduces the actuation torque required compared to the classical controllers.

Simulation studies in previous literature have used slightly different track profiles, but the responses achieved are similar indicating that the results presented in this thesis support

previous research on actively steered vehicles. Previous research on the SYC mechanism [29] have shown a good balance between the lateral creep forces at the front and rear wheelsets, which is achieved using the controllers in this study as well. However, steering the bogies does not affect the angle of attack of the individual wheelsets and is therefore less effective as a steering mechanism. For the ASW configuration, previous studies [32] have shown a similar reduction in wheelset lateral displacement on a high speed curve (of radius = 1357 m, cant = 6°, speed = 230 kmph ≈ 63 m/s) as has been observed in this study (where radius = 1200 m, cant = 4°, speed = 45 m/s). In the DIRW vehicle, the simulation results from a curved track profile (with radius = 300 m, cant = 6°, speed=25 m/s) using optimal state feedback control [27] is similar to that achieved in this study on a (radius = 535 m, cant = 4°, speed=30 m/s) curve using classical controllers. Minimal flange contact was achieved on both studies on a track with stochastic disturbances, although the disturbances applied were different.

For the track switch simulations, the switch types considered in this thesis were chosen based on the different maximum allowable turnout speeds. At a maximum speed of 25 mph ≈ 11 m/s, the C switch is mostly found at or near stations while the H switch allows a train to travel at a maximum of 90 mph ≈ 40 m/s. This makes the two switch layouts very different and the DIRW vehicle was studied on both to demonstrate the performance improvement compared to a conventional passive vehicle. The novelty of the work presented in this thesis lies in firstly, proving that active vehicles can negotiate a track switch that has been optimised only for passive vehicles, and secondly, establishing a benchmark improvement in performance that can be expected compared to a passive vehicle. On the through route of the C switch, a 22% reduction in wear was shown while on the diverging route it was 70%. On the through and diverging routes of the H switch, the percentage reduction in wear achieved was 50% and 73% respectively.

Although, the improvement on the diverging routes is less substantial, it is important to remember that the active vehicle allows a trade-off during the running of the vehicle between the wheel-rail wear and the wheelset lateral displacement. A control torque optimised for a particular switch scenario could reduce wheel-rail wear and minimise flange contact. This is a functionality not possible on a passive vehicle. Moreover, track switches account for less than 0.1% of the rail network length, which means that with the significant improvements on straight/ curved track profiles and the through-route of track switches, active vehicles promise a radical shift in the way railways operate. Lower wear would mean that track switch maintenance costs and the service downtime could be reduced, contributing towards the vision of a 24/7 railway.

7.2 Recommendations

The results in this thesis show that a significant reduction in wheel and track wear is achievable on plain track and on switches using the driven independently-rotating wheelset vehicle. The conceptual benefits of the mechanism are clear from decades of related research from simulation studies and experimental roller rig testing. Full-scale testing of the mechanism has been more recent with the first applications on a tram. The issue of the estimation of the feedback signals can be addressed using kalman filters. In Germany, the DIRW mechanism is being investigated on a high speed vehicle. The recommendation therefore is for train operating companies to invest in a prototype for the DIRW vehicle. The use of this modern rolling stock on existing track infrastructure would enable an analysis of the vertical and lateral track impact forces. This could then be used to establish the reduction in both wheel and track wear compared to conventional vehicles.

The recommendation for academia is to investigate whether the controllers are robust enough to cope with the phase lag introduced due to sensing and estimation when the concept is implemented in practice. It will also be useful to study different controllers to further improve the performance of the DIRW vehicle. Cascaded control strategies with different feedback signals such as yaw velocity or differential wheel speeds could offer a better vehicle performance and reduce the difficulty of obtaining the required feedback signals.

These steps will develop an intermediary solution in the technology route-map shown in Figure 1.2. To establish the system level benefits of VBS, it will be necessary to mature the concept itself. The ultimate objective is to design a self-steering vehicle on a track switch without any moving components. As this is a conceptual realisation in the lower Technology Readiness Level (TRL), the development of VBS research will be mainly academic initially. An overview of how the VBS concept could be developed through further work is presented in the next section.

7.3 Further work

Developing VBS as a concept requires thinking about the wheel-rail interaction as a single system, instead of considering the running gear and the track infrastructure as separate systems. As an initial design, the conventional track switch design could be altered such that at the switch toe, if the switch rails are not touching the stock rails on either side, the wheel-rail interface at the nose could be replicated at the toe, therefore introducing a flange gap. The active mechanism could then be used to provide the additional guidance torque. This would be possible on a low speed turnout but not on a high speed turnout due to the

shallow divergence angle. On a high speed turnout, a feed-forward controller could be used which calculates the required wheelset lateral displacement from a track geometry database or an inductive metal detector at the front of the vehicle.

In order to introduce a continuous running rail at switches and crossings, it will be necessary to investigate the use of retractable flanges or flange-less wheels which would remove the need for gaps and moveable switch toes at switches and crossings. The vehicle could be controlled such that they are able to self-steer while the track is purely passive i.e. it does not have any moving rails or components.

The system-level benefits can be established once the wheel-rail contact geometry has been optimised for a passive track infrastructure. Then the reduction in wear using VBS can be analysed and the consequent increase in the lifetime of S&C assets can be predicted. This would quantify the system benefits in terms of reliability. Cost function algorithms for railway timetable operation could be used to quantify the systemic benefits possible by reducing the distance between consecutive trains due to increased switch reliability. The development of the concept will contribute to an increase in capacity and a decrease in operating costs, which are two among the four key areas of improvement identified in the 2012 Rail Technical Strategy.

References

[1] C4R Capacity for Rail. Operational failure modes of switches and crossings, 2015.

[2] HS2. High speed 2. Online; accessed 23-July-2018, https://www.hs2.org.uk/.

[3] Shift2Rail. About the initiative. Online; accessed 23-July-2018, https://shift2rail.org/.

[4] S-code. Switch and crossing optimal design and evaluation. Online; accessed 23-July-2018, http://www.s-code.info/.

[5] B. Pålsson and J. Nielsen. Track gauge optimisation of railway switches using a genetic algorithm. *Vehicle system dynamics*, 50(sup1):365–387, 2012.

[6] P. Wang, X. Ma, J. Wang, J. Xu, and R. Chen. Optimization of rail profiles to improve vehicle running stability in switch panel of high-speed railway turnouts. *Mathematical Problems in Engineering*, 2017, 2017.

[7] D. Nicklisch, E. Kassa, J. Nielsen, M. Ekh, and S. Iwnicki. Geometry and stiffness optimization for switches and crossings, and simulation of material degradation. *Proceedings of the Institution of Mechanical Engineers, Part F: Journal of Rail and Rapid Transit*, 224(4):279–292, 2010.

[8] Office of Road and Rail ORR. Online data portal - total journey count reporting. Online; accessed 13-February-2018; https://dataportal.orr.gov.uk/, 2018.

[9] S. Bemment, R. Goodall, R. Dixon, and C. Ward. Improving the reliability and availability of railway track switching by analysing historical failure data and introducing functionally redundant subsystems. *IMechE Part F. JRRT*, July 2017.

[10] A. T. Cornish. *Lifetime monitoring of in service switches and crossings through field experimentation*. PhD thesis, Imperial College London, 2014.

[11] H. Lindner. Railway switch for vignoles rails, June 25 1974. US Patent 3,819,935.

[12] Caterpillar. Partial flange bearing frog no. 9. Online; accessed 04-January-2018; http://s7d2.scene7.com/is/content/Caterpillar/C10670254, 2018.

[13] S. S. Hsu. Rail technology magazine, why are s&c layouts failing? Online; accessed 22-December-2018, http://www.railtechnologymagazine.com/Comment/Page-8/why-are-S&C-layouts-failing.

[14] E. Grey and S. Iwnicki. Railway technology, run2rail: Bringing 3d printing to rail design. Online; accessed 22-December-2018, https://www.railway-technology.com/features/run2rail-bringing-3d-printing-rail-design/.

[15] RailEngineer. Track inspection at 125 mph. Online; accessed 19-January-2018; https://www.railengineer.uk/2012/11/28/track-inspection-at-125mph/, 2012.

[16] H. M. Yusof. *Technologies and control strategies for active railway suspension actuators*. PhD thesis, Loughborough University, 2013.

[17] V. K. Garg and R. V. Dukkipatti. *Dynamics of Railway Vehicle Systems*. Academic press, Ontario, Canada, 1984.

[18] F. W. Carter. On the action of locomotive driving wheel. *Proc. R. Soc. London*, 112:151–157, 1926.

[19] A. O. Gilchrist. The long road to solution of the railway hunting and curving problems. *Proceedings of the Institution of Mechanical Engineers*, 212(3):219, 1998.

[20] A. H. Wickens. The dynamics of railway vehicles—from stephenson to carter. *Proceedings of the Institution of Mechanical Engineers, Part F: Journal of Rail and Rapid Transit*, 212(3):209–217, 1998.

[21] T. X. Mei and R. M. Goodall. Recent Development in Active Steering of Railway Vehicles. *Vehicle System Dynamics*, 39(6):415–436, jun 2003.

[22] D. Boocock. Steady-state motion of railway vehicles on curved track. *Archive: Journal of Mechanical Engineering Science 1959-1982 (vols 1-23)*, 11:556–566, 12 1969.

[23] C. P. Ward, T. X. Mei, P. Hubbard, and M. Mirzapour. Half cost trains: Design for Control. *RRUKA (produced by Loughborough University and University of Salford)*, 2013.

[24] R. M. Goodall. *System Dynamics and Long-Term Behaviour of Railway Vehicles, Track and Subgrade*, chapter Active Suspension Technology and its Effect upon Vehicle-Track Interaction, pages 35–50. Springer Berlin Heidelberg, 2003.

[25] R. V. Dukkipati, S. N. Swamy, and M. O. M. Osman. Independently rotating wheel systems for railway vehicles-a state of the art review. *Vehicle System Dynamics*, 21(1):297–330, 1992.

[26] T. X. Mei and R. M. Goodall. Practical Strategies for Controlling Railway Wheelsets Independently Rotating Wheels. *Journal of Dynamic Systems, Measurement, and Control*, 125(3):354–360, sep 2003.

[27] G. Diana, S. Bruni, F. Cheli, and F. Resta. Active control of the running behaviour of a railway vehicle: stability and curving performances. *Vehicle System Dynamics*, 37(11):157–170, 2002.

[28] F. Braghin, S. Bruni, and F. Resta. Active yaw damper for the improvement of railway vehicle stability and curving performances: simulations and experimental results. *Vehicle System Dynamics*, 44(11):857–869, 2006.

[29] R. M. Goodall, C. P. Ward, D. Prandi, and S. Bruni. Railway bogie stability control from secondary yaw actuators. In *24th International Symposium on Dynamics of Vehicles on Roads and Tracks (IAVSD 2015)*, Graz, Austria, Aug 2015.

[30] G. Shen and R. Goodall. Active yaw relaxation for improved bogie performance. *Vehicle System Dynamics*, 28(4-5):273–289, 1997.

[31] J. Pérez, J. M. Busturia, and R. M. Goodall. Control strategies for active steering of bogie-based railway vehicles. *Control Engineering Practice*, 10(9):1005–1012, sep 2002.

[32] T. X. Mei and R. M. Goodall. Wheelset control strategies for a two-axle railway vehicle. *Vehicle System Dynamics*, 33(10):653–664, 1999.

[33] J. T. Pearson, R. M. Goodall, T. X. Mei, and G. Himmelstein. Active stability control strategies for a high speed bogie. *Control Engineering Practice*, 12(11):1381–1391, nov 2004.

[34] Bombardier. Flexx tronic technology. Online; accessed 24-December-2018, https://www.bombardier.com/content/dam/Websites/bombardiercom/supporting-documents/BT/Bombardier-Transportation-ECO4-FLEXX_Tronic-EN.pdf.

[35] R. Schneider. Combining capacity with track-friendly technology: Flexx tronic wako and ars from bombardier. Online; accessed 24-December-2018, https://www.globalrailwayreview.com/article/5797/combining-capacity-with-track-friendly-technology-flexx-tronic-wako-and-ars-from-bombardier/.

[36] R. Goodall and H. Li. Solid Axle and Independently-Rotating Railway Wheelsets - A Control Engineering Assessment of Stability. *Vehicle System Dynamics*, aug 2010.

[37] J. Perez, L. Mauer, and J. M. Busturia. Design of Active Steering Systems for Bogie-Based Railway Vehicles with Independently Rotating Wheels. *Vehicle System Dynamics*, 37(sup1):209–220, jan 2002.

[38] T. X. Mei and R. M. Goodall. Robust control for independently rotating wheelsets on a railway vehicle using practical sensors. *IEEE Transactions on Control Systems Technology*, 9(4):599–607, 2001.

[39] M. Gretzschel and L. Bose. A mechatronic approach for active influence on railway vehicle running behaviour. *Vehicle System Dynamics*, 33:418–430, 1999.

[40] M. Gretzschel and L. Bose. A new concept for integrated guidance and drive of railway running gears. *Control Engineering Practice*, 10:1013–1021, 2002.

[41] B. Kurzeck and L. Valente. A novel mechatronic running gear: concept, simulation and scaled roller rig testing. In *9th World Congress on Railway Research*, May 2011.

[42] J. Pérez, J. M. Busturia, T.X. Mei, and J. Vinolas. Combined active steering and traction for mechatronic bogie vehicles with independently rotating wheels. *Annual Reviews in Control*, 28(2):207–217, Jan 2004.

[43] SET Ltd. Wheelmotor project. Online; accessed 23-May-2016; http://www.set.gb.com/innovation.php, 2013.

[44] J. Stow, N. Cooney, R.M. Goodall, and R. Sellick. The use of wheelmotors to provide active steering and guidance for a light rail vehicle. *The Stephenson Conference: Research for Railways*, April 2017.

[45] T. X. Mei, H. Li, R. M. Goodall, and A. H. Wickens. Dynamics and control assessment of rail vehicles using permanent magnet wheel motors. *Vehicle System Dynamics*, 37:326–337, 2002.

[46] R. Melnik and B. Sowinski. Analysis of dynamics of a metro vehicle model with differential wheelsets. *Transport Problems*, 12:113–124, 09 2017.

[47] DLR. Dlr at innotrans 2012: High-tech research for tomorrow's rail transport. Online; accessed 24-December-2018, https://www.dlr.de/dlr/desktopdefault.aspx/tabid-10081/151_read-5246//year-all/gallery/7608.

[48] Green Car Congress. Dlr team advises concept for next-gen rail cargo transport: automated, intelligent freight wagons. Online; accessed 24-December-2018, https://www.greencarcongress.com/2017/04/dlr-team-devises-concept-for-next-gen-rail-cargo-transport-automated-intelligent-freight-wagons.html.

[49] A. J. Powell. On the dynamic stability of actively steered railway vehicles. *Vehicle System Dynamics*, 33:442–452, 1999.

[50] A. H. Wickens. Dynamic stability of articulated and steered railway vehicles guided by lateral displacement feedback. *Vehicle System Dynamics*, 23:541–553, 1994.

[51] Y. Michitsuji and Y. Suda. Running performance of power-steering railway bogie with independently rotating wheels. *Vehicle System Dynamics*, 44(sup1):71–82, Jan 2006.

[52] T. X. Mei, S. Shen, R. M. Goodall, and J. T. Pearson. Active steering control for railway bogies based on displacement measurements. *IFAC Proceedings Volumes*, 38(1):586 – 591, 2005. 16th IFAC World Congress.

[53] R. M. Goodall and W. Kortüm. Mechatronic developments for railway vehicles of the future. *Control Engineering Practice*, 10(8):887 – 898, 2002.

[54] T. X. Mei and R. M. Goodall. Modal controllers for active steering of railway vehicles with solid axle wheelsets. *Vehicle System Dynamics*, 34:25–41, 2000.

[55] J. M. Maciejowski. *Multivariable Feedback Design*. Addison-Wesley Publishers Ltd., 1989.

[56] H. Selamat, A. Alimin, and M. A. Zawawi. Optimal control of railway vehicle system. 02 2009.

[57] A. Qazizadeh and S. Stichel. Improved curving performance for two-axle rail vehicles with actuated solid wheelsets using h-infinity control. In *Proceedings of the ASME Joint Rail Conference 2016*. AMER SOC Mechanical engineers, May 2016.

[58] T. X. Mei and H. Li. Control design for the active stabilization of rail wheelsets. *Journal of Dynamic Systems Measurement and Control-transactions of The Asme - J DYN SYST MEAS CONTR*, 130, 01 2008.

[59] T. X. Mei, R. M. Goodall, and H. Li. Kalman filter for the state estimation of a 2-axle railway vehicle. In *Control Conference (ECC), 1999 European*, pages 2431–2435, Aug 1999.

[60] T. X. Mei and R. M. Goodall. LQG and GA solutions for active steering of railway vehicles. *IEEE Proceedings - Control Theory and Applications*, 147(1):111–117, jan 2000.

[61] L. Ljung. Asymptotic behavior of the extended kalman filter as a parameter estimator for linear systems. *IEEE Transactions on Automatic Control*, 24(1):36–50, Feb 1979.

[62] S. Shuiwen, T. X. Mei, R. M. Goodall, and J. T. Pearson. A novel control strategy for active steering of railway bogies. In *International Control Conference*, September 2004.

[63] S. Bruni, R. Goodall, T. X. Mei, and H. Tsunashima. Control and monitoring for railway vehicle dynamics. *Vehicle System Dynamics*, 45(7-8):743–779, 2007.

[64] M. Mirzapour, T. X. Mei, and I. Hussain. Assessment of fault tolerance for actively controlled railway wheelset. In *Control (CONTROL), 2012 UKACC International Conference on*, pages 631–636, sep 2012.

[65] J. P. Sutherland. Fly-by-wire flight control systems. In *Joint meeting of flight mechanics and guidance and control panels of AGARD*. Air Force Base, September 1968.

[66] BBC. Nissan steer-by-wire cars set for showrooms by 2013. Online; accessed 24-December-2018, https://www.bbc.co.uk/news/technology-19979380.

[67] C. Fox. The railway: British track since 1804, pen and sword transport. In *Andrew Dow*, 1836.

[68] Rail Technology Magazine. High performance switch system update. Online; accessed 5-March-2018; http://www.railtechnologymagazine.com/Rail-News/high-performance-switch-system-update.

[69] M. Pletz, W. Daves, and H. Ossberger. A wheel set/crossing model regarding impact, sliding and deformation—explicit finite element approach. *Wear*, 294-295:446 – 456, 2012.

[70] B. A. Pålsson. Design optimisation of switch rails in railway turnouts. *Vehicle System Dynamics*, 51(10):1619–1639, 2013.

[71] Alpinestrasse 1 8740 Zeltweg Austria. voestalpine vae gmbh. Online; accessed 6-March-2018; www.voestalpine.com/vae/.

[72] R. F. Lagos, A. Alonso, J. Vinolas, and X. Perez. Rail vehicle passing through a turnout: analysis of different turnout designs and wheel profiles. *Proceedings of the Institution of Mechanical Engineers Part F-Journal of Rail and Rapid Transit*, 226(F6):587–602, 2012.

[73] M. R. Bugarín and J. M. García Díaz de Villegas. Improvements in railway switches. *Proceedings of the Institution of Mechanical Engineers, Part F: Journal of Rail and Rapid Transit*, 216(4):275–286, 2002.

[74] S. D. Bemment, E. Ebinger, R. M. Goodall, C. P. Ward, and R. Dixon. Rethinking rail track switches for fault tolerance and enhanced performance. *Proceedings of the Institution of Mechanical Engineers, Part F: Journal of Rail and Rapid Transit*, 231(9):1048–1065, 2017.

[75] In2track. Project details. Online; accessed 23-July-2018, https://shift2rail.org/project/in2track/.

[76] J. Rivington. Self-acting railway switches, 1838.

[77] T. Koseki, Z. P. Yang, Y. Ujihara, and S. Sone. On-board turnout in a flexible operation of rail-guided transport system. *IFAC Control in Transportation Systems*, 33(9):535–540, 2000.

[78] D. A. Bushko, T. M. Clark, and R. D. Thornton. Vehicle guidance and switching via magnetic forces. https://encrypted.google.com/patents/EP1042152A1?cl=nl, October 11 2000. EP Patent App. EP19,980,966,064.

[79] Dassault Systemes. Simpack. Online; accessed 12-March-2018; http://www.simpack.com/.

[80] O. Polach, M. Berg, and S. Iwnicki. *Handbook of Railway Vehicle dynamics*, chapter Simulation, pages 360–404. Taylor & Francis, 2006.

[81] S. Iwnicki. Manchester Benchmarks for Rail Vehicle Simulation. *Vehicle System Dynamics*, 30(3):295–313, jan 1998.

[82] R. M. Goodall and C. P. Ward. Active control of railway bogies – assessment of control strategies. In *The International Symposium on Speed-up and Sustainable Technology for Railway and Maglev Systems*, Chiba, Japan, November 2015.

[83] O. Polach. Characteristic parameters of nonlinear wheel/rail contact geometry. *Vehicle System Dynamics*, 48(sup1):19–36, 2010.

[84] J. J. Kalker. Wheel-rail rolling contact theory. *Wear*, 144:243–261, 1991.

[85] M. Spiryagin, O. Polach, and C. Cole. Creep force modelling for rail traction vehicles based on the fastsim algorithm. *Vehicle System Dynamics*, 51(11):1765–1783, 2013.

[86] Rail Safety and Standards Board. Railway Group Standards, Railway Wheelsets. Standard, Rail Safety and Standards Board, 2017.

[87] Network Rail. BS EN 13674-1:2011+A1:2017 - Railway applications. Track. Rail. Vignole railway rails 46 kg/m and above. Standard, British Standards Online, March 2017.

[88] Track system requirements. Online; accessed 14-February-2017, https://www.rssb.co.uk/rgs/standards/GCRT5021%20Iss%203.pdf, February 2007.

[89] P. Hubbard, C. Ward, R. Dixon, and R. Goodall. Real time detection of low adhesion in the wheel/rail contact. *Proceedings of the Institution of Mechanical Engineers, Part F: Journal of Rail and Rapid Transit*, 227(6):623–634, 2013.

[90] I. Hussain and T. X. Mei. Multi kalman filtering approach for estimation of wheel-rail contact conditions. In *UKACC International Conference on Control 2010*, pages 1–6, Sept 2010.

[91] C. P. Ward, R. M. Goodall, R. Dixon, and G. A. Charles. Adhesion estimation at the wheel-rail interface using advanced model-based filtering. *Vehicle System Dynamics*, 50(12):1797–1816, Dec 2012.

[92] A. H. Wickens. *Fundamentals of Rail Vehicle dynamics, Guidance and Stability*, chapter The bogie vehicle, page 174. Swets & Zeitlinger, Lisse, Netherlands, 2003.

[93] P. Young, M. A. Behzadi, C. L. Wang, and A. Chotai. Direct digital and adaptive control by input-output state variable feedback pole assignment. *International Journal of Control*, 46(6):1867–1881, 1987.

[94] Mathworks. Assessing gain and phase margins. Online; accessed 19-March-2018; https://uk.mathworks.com/help/control/examples/assessing-gain-and-phase-margins.html.

[95] Simpack 9.10.2 Documentation. Multi domain interfaces/ model export, simat, 2016.

[96] Y. Bezin, C. Funfschilling, S. Kraft, and L. Mazzola. Virtual testing environment tools for railway vehicle certification. *Proceedings of the Institution of Mechanical Engineers, Part F: Journal of Rail and Rapid Transit*, 229(6):755–769, 2015.

[97] M. Burstow. Vtac calculator: Guidance notes for determining $t\gamma$ values. https://cdn.networkrail.co.uk/wp-content/uploads/2016/12/VTAC-calculator-Guidance-note-for-determining-Tgamma-values.pdf, 2012.

[98] M. Hiensch. *Rail damage issues*, chapter Wheel-rail interface components, pages 2–51. University of Birmingham Press, 2010.

[99] M. Burstow. Improving track geometry alignment to reduce rolling contact fatigue (rcf). In *9 World congress on railway research*, May 2011.

[100] MTS. Series 244 hydraulic actuators. Online; accessed 3-January-2018, https://www.mts.com/cs/groups/public/documents/library/dev_002093.pdf.

[101] Moog. A085 series hydraulic servo actuators. Online; accessed 3-January-2018, http://www.moog.com/products/actuators-servoactuators/industrial/hydraulic/a085-series-hydraulic-servo-actuators.html.

[102] Alstom. Motor catalogue. Online; accessed 3-January-2018, http://www.alstom.com/Global/Transport/Resources/Documents/brochure2014/Alstom%20Motors%20Catalogue%202015%20-%20English.pdf?epslanguage=en-GB.

[103] L. Raif, B. Puda, J. Havlík, and M. Smolka. Design of high-speed turnouts and crossings. *IOP Conference Series: Materials Science and Engineering*, 236(1):012044, 2017.

[104] Network Rail. Nr/l2/trk/2049 level 2 track design handbook. Handbook, Network Rail, March 2010.

[105] Network Rail. BS EN 13674-2:2006+A1:2010 - Railway applications. Track. Rail. Switch and crossing rails used in conjunction with Vignole railway rails 46 kg/m and above. Standard, British Standards Online, March 2006.

[106] G. Schupp, C. Weidemann, and L. Mauer. Modelling the contact between wheel and rail within multibody system simulation. *Vehicle System Dynamics*, 41(5):349–364, 2004.

[107] British Standards. BS EN 12299:2009 - Railway applications - Ride comfort for passengers - Measurement and evaluation. Standard, British Standards Online, May 2009.

[108] R. F. Lagos, A. Alonso, J. Vinolas, and X. Pérez. Rail vehicle passing through a turnout: analysis of different turnout designs and wheel profiles. *Proceedings of the Institution of Mechanical Engineers, Part F: Journal of Rail and Rapid Transit*, 226(6):587–602, 2012.

[109] M. R. Bugarin, M. Novales, and A. Orro. Modelling high speed turnouts. *World Congress on Railway Research (WCRR) 2006, Montreal, Canada*, 2006.

Appendix A

Vehicle modelling

A.1 Passive vehicle model in Simpack

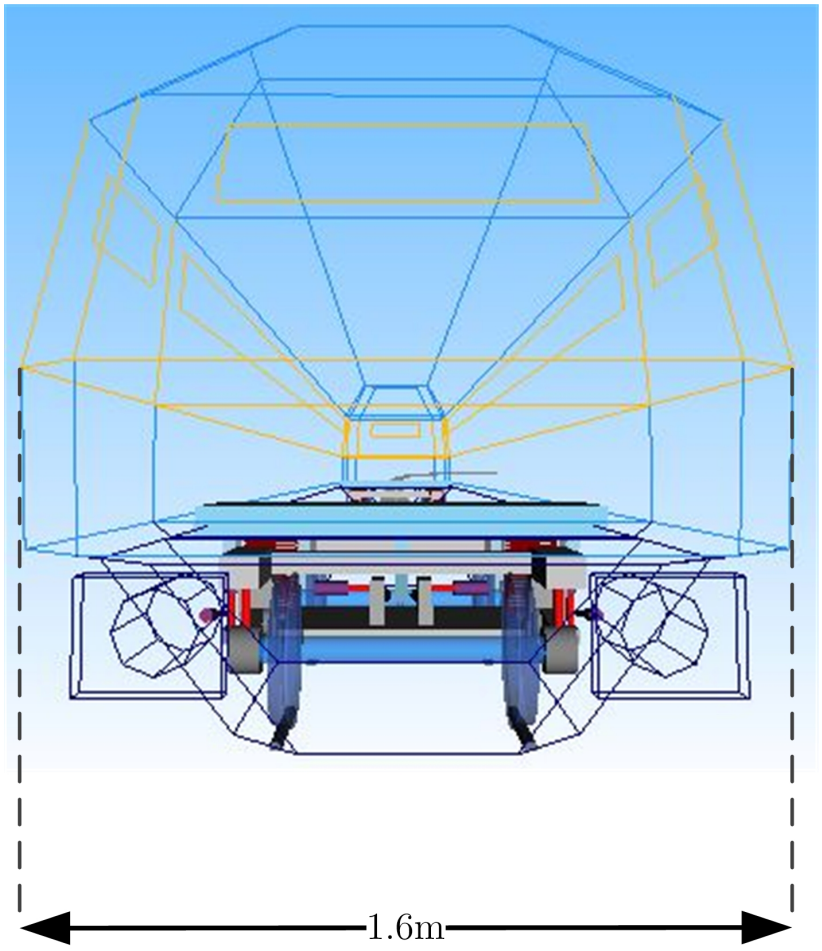

Figure A.1: Front view of passive vehicle

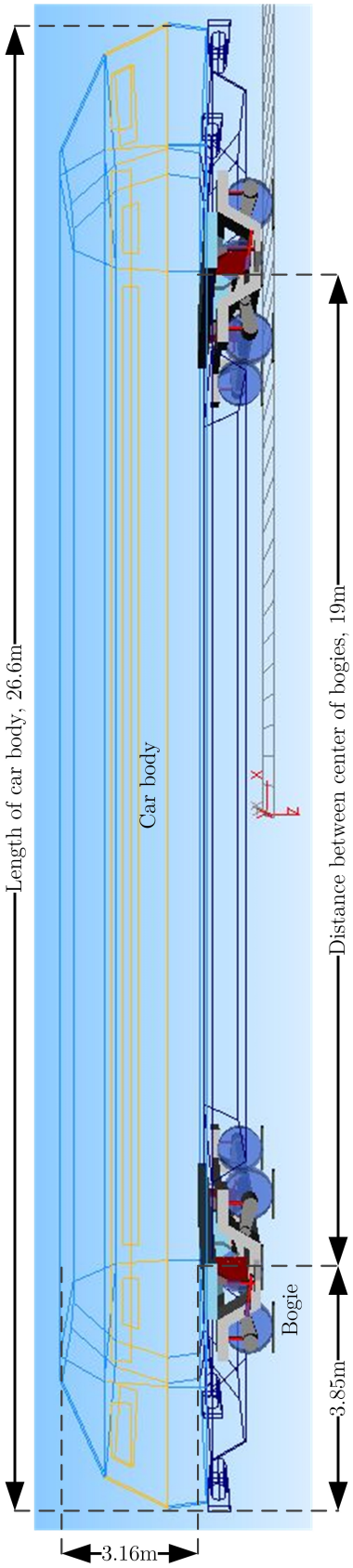

Figure A.2: Side view of passive vehicle

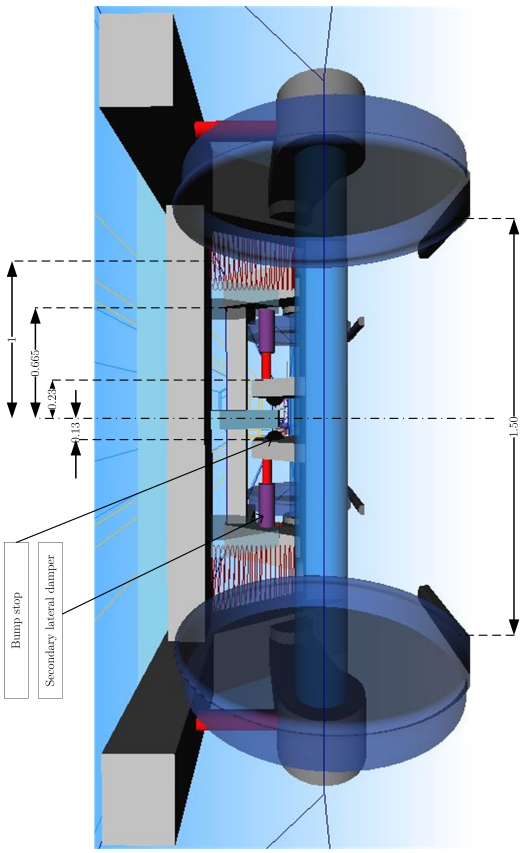

Figure A.3: Front view of passive bogie

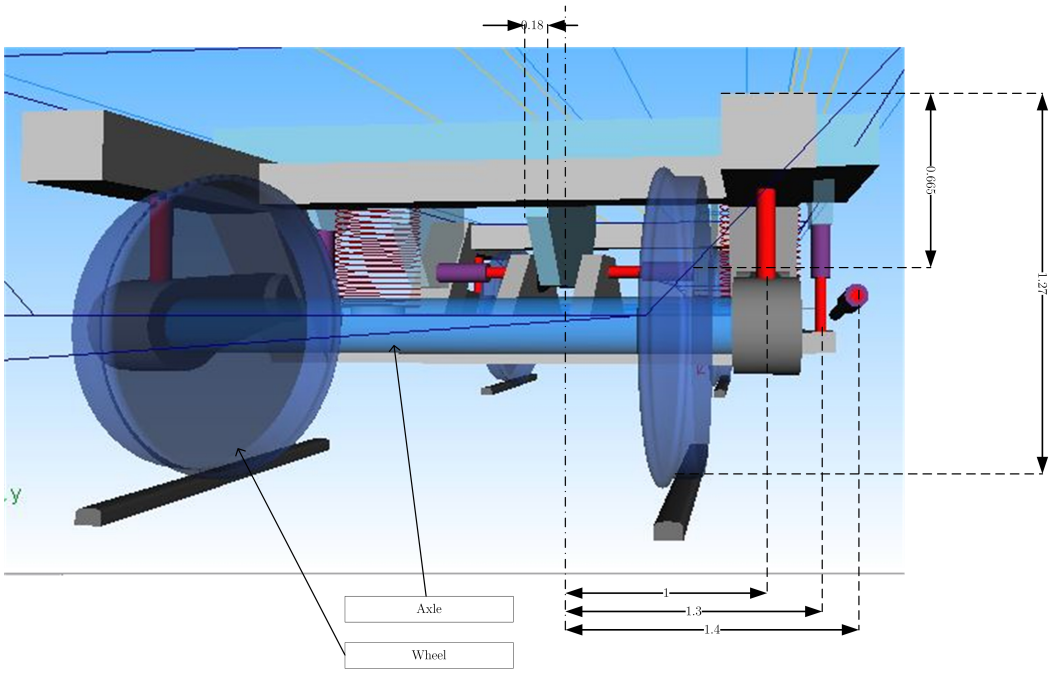

Figure A.4: Front view of passive bogie

Table A.1: Simpack vehicle parameters

Car body	Value	Units
Mass	2e4	kg
Inertia xx	2.9998e4	kg m^2
Inertia yy	1.23e6	kg m^2
Inertia zz	1.23e6	kg m^2
Centre of gravity	(0,0,-1.8)	m
Dummy bolster	**Value**	**Units**
Mass	1e-6	kg
Inertia xx	1e-6	kg m^2
Inertia yy	1e-6	kg m^2
Inertia zz	1e-6	kg m^2
Centre of gravity	(0,0,-1.25)	m
Bogie frame	**Value**	**Units**
Mass	2.615e3	kg
Inertia xx	1.722e3	kg m^2
Inertia yy	1.476e3	kg m^2
Inertia zz	3.076e3	kg m^2
Centre of gravity	(0,0,-0.6)	m

Radius arm	Value	Units
Mass	1.6e2	kg
Inertia xx	1.469	kg m^2
Inertia xz	-1.38	kg m^2
Inertia yy	8.85	kg m^2
Inertia zz	7.758	kg m^2
Centre of gravity	(-0.185,0,-0.037)	m
Axle-box	**Value**	**Units**
Longitudinal stiffness	1.22e7	N/m
Lateral stiffness	6e6	N/m
Vertical stiffness	1.2e7	N/m
Roll stiffness	1.5e3	Nm/rad
Pitch stiffness	2e3	Nm/rad
Yaw stiffness	1.5e3	Nm/rad
Longitudinal damping	1e4	Ns/m
Lateral damping	1e4	Ns/m
Vertical damping	3e3	Ns/m
Roll damping	5e1	Nms/rad
Pitch damping	5e1	Nms/rad
Yaw damping	6e1	Nms/rad
Primary spring	**Value**	**Units**
longitudinal parallel stiffness	3.14e7	N/m
lateral parallel stiffness	6.5e5	N/m
vertical parallel stiffness	1.22e6	N/m
longitudinal series stiffness	6e7	N/m
lateral series stiffness	7.5e6	N/m
spring length	0.42	m
Primary damper	**Value**	**Units**
longitudinal series damping	1.5e5	Ns/m
lateral series damping	2e3	Ns/m
longitudinal parallel damping	1.22e6	Ns/m
lateral parallel damping	6e5	Ns/m
vertical parallel damping	6e5	Ns/m
Secondary spring	**Value**	**Units**
longitudinal stiffness	1.6e5	N/m
lateral stiffness	1.6e5	N/m
vertical stiffness	4.3e5	N/m
roll stiffness	1.05e4	Nm/rad
pitch stiffness	1.05e4	Nm/rad
yaw stiffness	3.75e5	N/m
spring length	0.6	m
Secondary damper	**Value**	**Units**
lateral stiffness	1e6	N/m
vertical stiffness	6e6	N/m
vertical damping	2.5e4	Ns/m

Traction rod	Value	Units
stiffness	5e6	N/m
damping	2.5e4	Ns/m
length	1.12	m
Wheelset	**Value**	**Units**
Mass	1.2e3	kg
Inertia xx	7e2	kg m^2
Inertia yy	7.4e1	kg m^2
Inertia zz	7e2	kg m^2
Axle length	2	m
Axle diameter	0.18	m
Wheel radius	0.46	m
Young's modulus	2.1e11	N/m^2
Poisson number	2.8e-1	
Contact damping	1e5	Ns/m
Friction coefficient	4e-1	

Note: The centre of gravity of the bodies are defined with respect to their individual body reference markers. The reference marker of the car body is shown in Figure A.2 using the red axis marker. The reference markers for the bogie frames are displaced only along the x-axis by $\pm 8.5m$. The reference markers for the corresponding dummy bolsters for each bogie are displaced only along the z-axis wrt the relevant bogie by -1.25 m. The reference marker of the right radius arm of the front wheelset of the front bogie is at (x,y,z)=(0.78,1,-0.56) m wrt the front bogie reference marker. Likewise that of the left radius arm of the same wheelset will be at (x,y,z)=(-0.78,1,-0.56) m.

A.2 Active vehicle models in Simpack

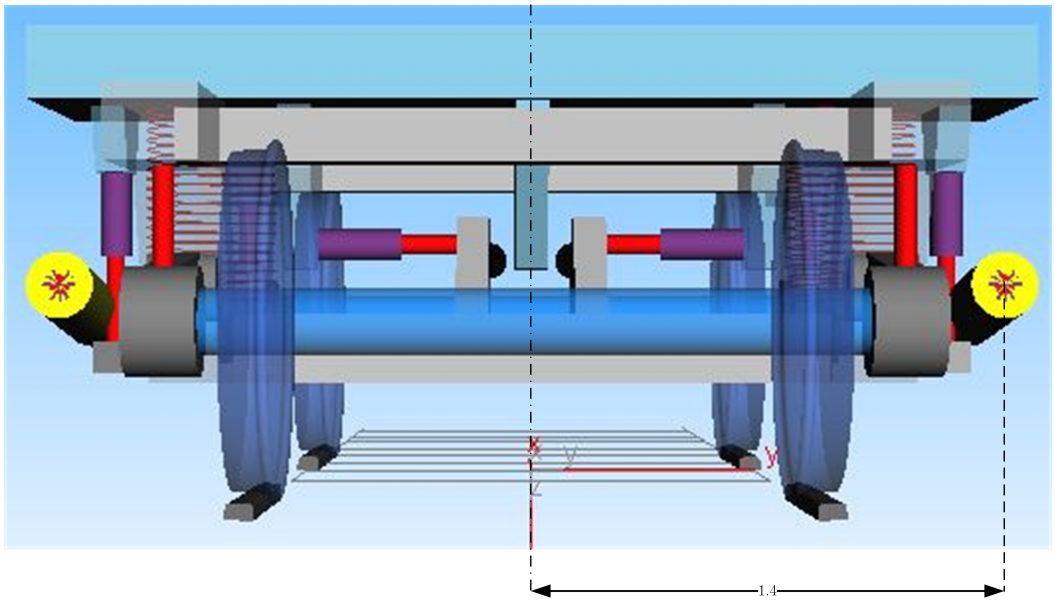

Figure A.5: Front view of SYC bogie

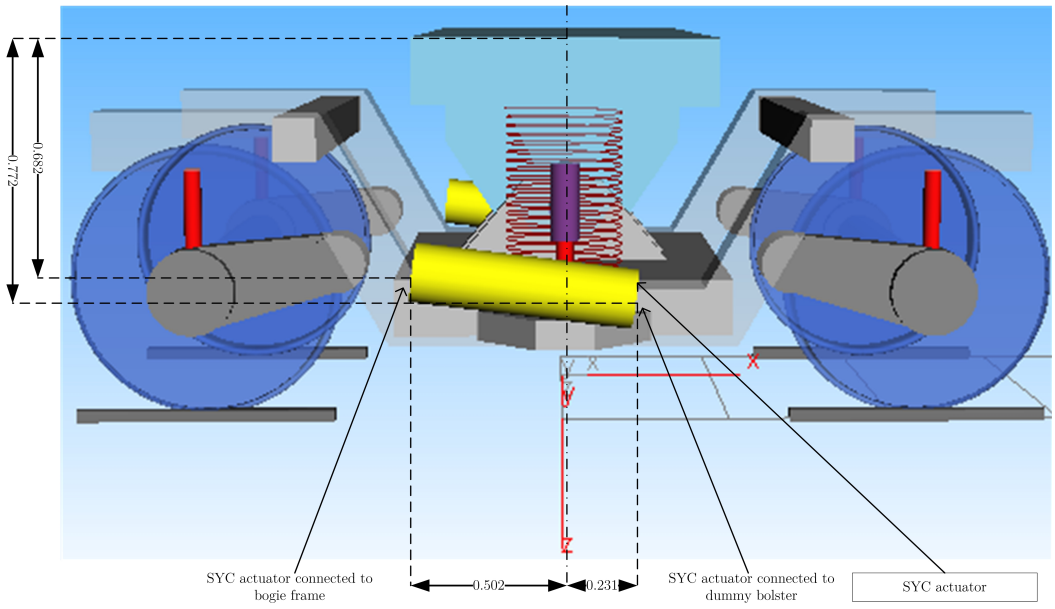

Figure A.6: Side view of SYC bogie

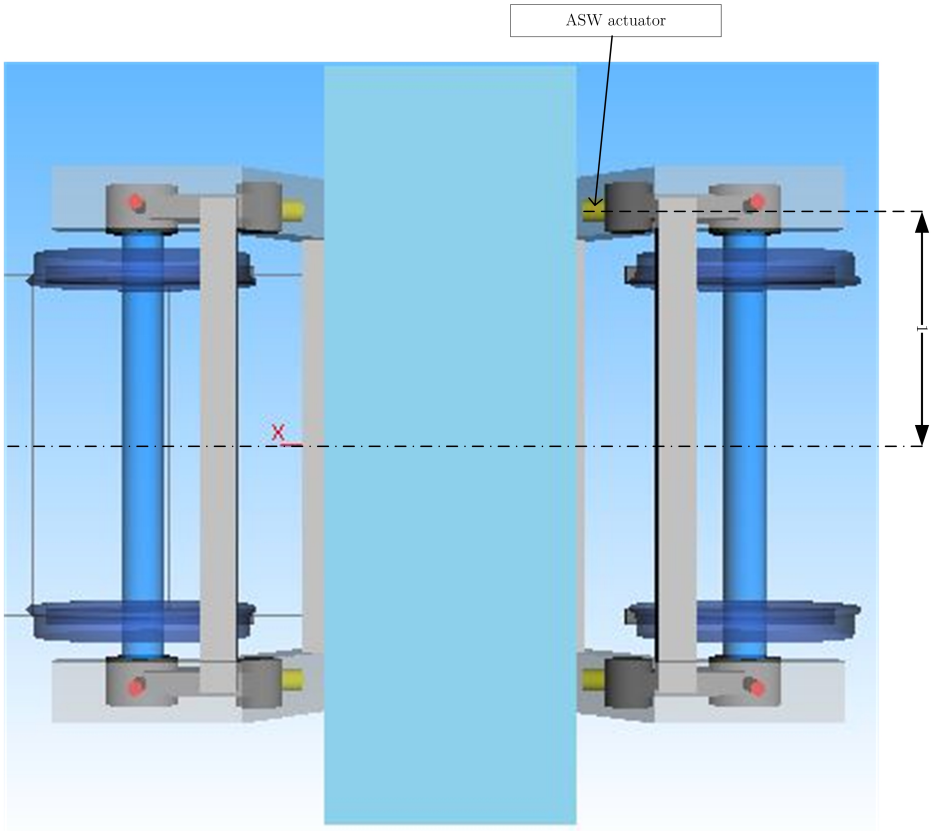

Figure A.7: Plan view of ASW bogie

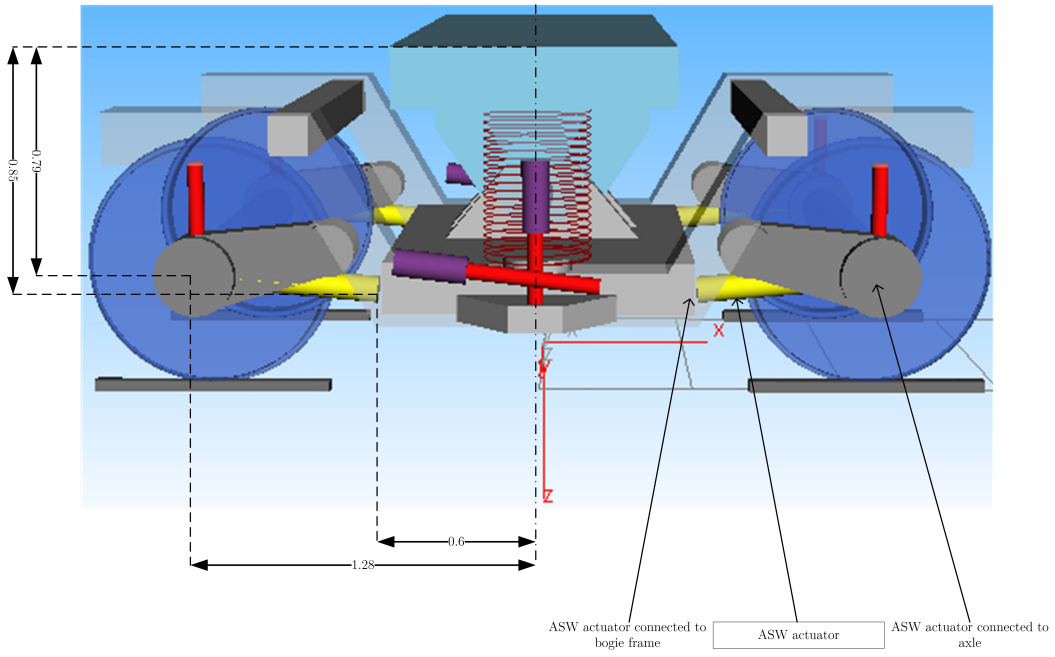

Figure A.8: Side view of ASW bogie

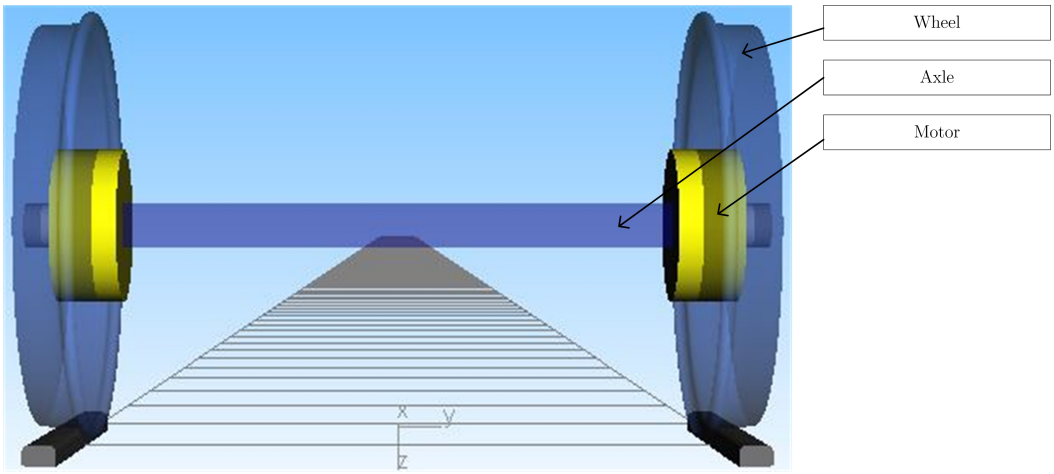

Figure A.9: DIRW wheelset

Note: The active element in each vehicle is defined as a force element of type 93 “Force/Torque by u(t) Cmp". This allows the user to use co-simulation to give a force/ torque input from MATLAB/ Simulink along all 6 degrees of freedom.

A.3 Transfer functions of models at different speeds

Table A.2: Transfer function of the linear ASW model at different vehicle speeds.

Speed	Transfer function
20 m/s	$G(z) = \frac{0.02526z^{-2} - 0.3298z^{-3} + 0.314z^{-4}}{1 - 1.641z^{-1} + 1.116z^{-2} - 0.702z^{-3} + 0.2623z^{-4}}$
30 m/s	$G(z) = \frac{0.3867z^{-2} - 0.9845z^{-3} + 0.6369z^{-4}}{1 - 1.185z^{-1} + 0.3823z^{-2} - 0.2997z^{-3} + 0.1612z^{-4}}$
40 m/s	$G(z) = \frac{0.883z^{-2} - 1.828z^{-3} + 1.033z^{-4}}{1 - 0.5528z^{-1} - 0.6355z^{-2} + 0.3876z^{-3} - 0.08809z^{-4}}$
50 m/s	$G(z) = \frac{0.5692z^{-2} - 1.255z^{-3} + 0.7784z^{-4}}{1 - 0.8667z^{-1} - 0.1333z^{-2} + 0.09351z^{-3} + 0.0277z^{-4}}$

Table A.3: Transfer function of the linear SYC model at different vehicle speeds.

Speed	Transfer function
20 m/s	$G(z) = \frac{0.06761z^{-1} + 0.04395z^{-2} - 0.06236z^{-3} - 0.04243z^{-4} - 0.0586z^{-5}}{1 - 1.48z^{-1} + 0.5353z^{-2} - 0.2717z^{-3} - 0.2206z^{-4} + 0.3963z^{-5}} \cdots$ $\frac{-0.02212z^{-6} + 0.02642z^{-7} + 0.01313z^{-8} + 0.0345z^{-9}}{0.04838z^{-6} + 0.04596z^{-7} + 0.04107z^{-8} - 0.05118z^{-9} - 0.03964z^{-10}}$
30 m/s	$G(z) = \frac{0.05599z^{-1} + 0.03411z^{-2} - 0.03973z^{-3} - 0.06815z^{-4} + 0.002734z^{-5}}{1 - 1.727z^{-1} + 0.7577z^{-2} - 0.1889z^{-3} + 0.07996z^{-4} - 0.1246z^{-5}} \cdots$ $\frac{-0.0459z^{-6} + 0.02674z^{-7} - 0.01117z^{-8} + 0.04526z^{-9}}{0.3676z^{-6} - 0.06859z^{-7} - 0.1576z^{-8} + 0.09917z^{-9} - 0.03168z^{-10}}$
40 m/s	$G(z) = \frac{0.05489z^{-1} + 0.03234z^{-2} - 0.02534z^{-3} - 0.07787z^{-4} - 0.002995z^{-5}}{1 - 1.659z^{-1} + 0.6422z^{-2} - 0.2205z^{-3} + 0.1221z^{-4} + 0.1209z^{-5}} \cdots$ $\frac{-0.04667z^{-6} + 0.02038z^{-7} + 0.0006235z^{-8} + 0.04438z^{-9}}{0.09053z^{-6} + 0.07729z^{-7} - 0.2364z^{-8} + 0.02423z^{-9} + 0.05026z^{-10}}$
50 m/s	$G(z) = \frac{0.03481z^{-1} + 0.05066z^{-2} - 0.02144z^{-3} - 0.07489z^{-4} - 0.02298z^{-5}}{1 - 1.722z^{-1} + 0.5744z^{-2} + 0.06177z^{-3} + 0.06428z^{-4} + 0.05274z^{-5}} \cdots$ $\frac{-0.009337z^{-6} - 0.0152z^{-7} + 0.04586z^{-8} + 0.01276z^{-9}}{0.1485z^{-6} - 0.1827z^{-7} + 0.007843z^{-8} - 0.06279z^{-9} + 0.0761z^{-10}}$

Table A.4: Transfer function of the linear DIRW model at different vehicle speeds.

Speed	Transfer function
20 m/s	$G(z) = \frac{-4.505e-10z^{-1} - 6.529e-10z^{-2} + 4.034e-10z^{-3} + 3.198e-10z^{-4}}{1 - 2.423z^{-1} + 1.989z^{-2} - 0.7965z^{-3} + 0.2782z^{-4} + 0.001532z^{-5}} \ldots \frac{+2.465e-10z^{-5}}{-0.04945z^{-6}}$
30 m/s	$G(z) = \frac{-5.804e-10z^{-1} - 9.722e-10z^{-2} + 2.725e-10z^{-3} + 5.43e-10z^{-4}}{1 - 2.255z^{-1} + 1.539z^{-2} - 0.4366z^{-3} + 0.1845z^{-4} + 0.06947z^{-5}} \ldots \frac{+5.685e-10z^{-5}}{-0.1011z^{-6}}$
40 m/s	$G(z) = \frac{-5.973e-10z^{-1} - 1.096e-09z^{-2} + 1.095e-10z^{-3} + 4.703e-10z^{-4}}{1 - 2.271z^{-1} + 1.591z^{-2} - 0.6248z^{-3} + 0.473z^{-4} - 0.07631z^{-5}} \ldots \frac{+9.854e-10z^{-5}}{-0.09201z^{-6}}$
50 m/s	$G(z) = \frac{-3.715e-10z^{-1} - 1.375e-09z^{-2} + 1.795e-10z^{-3} + 5.075e-10z^{-4}}{1 - 2.328z^{-1} + 1.651z^{-2} - 0.5989z^{-3} + 0.5002z^{-4} - 0.163z^{-5}} \ldots \frac{+9.509e-10z^{-5}}{0.06089z^{-6}}$

Appendix B

Supplementary graphs from Chapter 5 simulations

The graphs in this appendix have several notations in the labels which are defined as follows.

F_{WS}	Front wheelset
R_{WS}	Rear wheelset
psv	Passive
SYC	Secondary Yaw Control
ASW	Actuated Solid-axle Wheelset
DIRW	Driven Independently-Rotating Wheelset

B.1 Rear bogie graphs

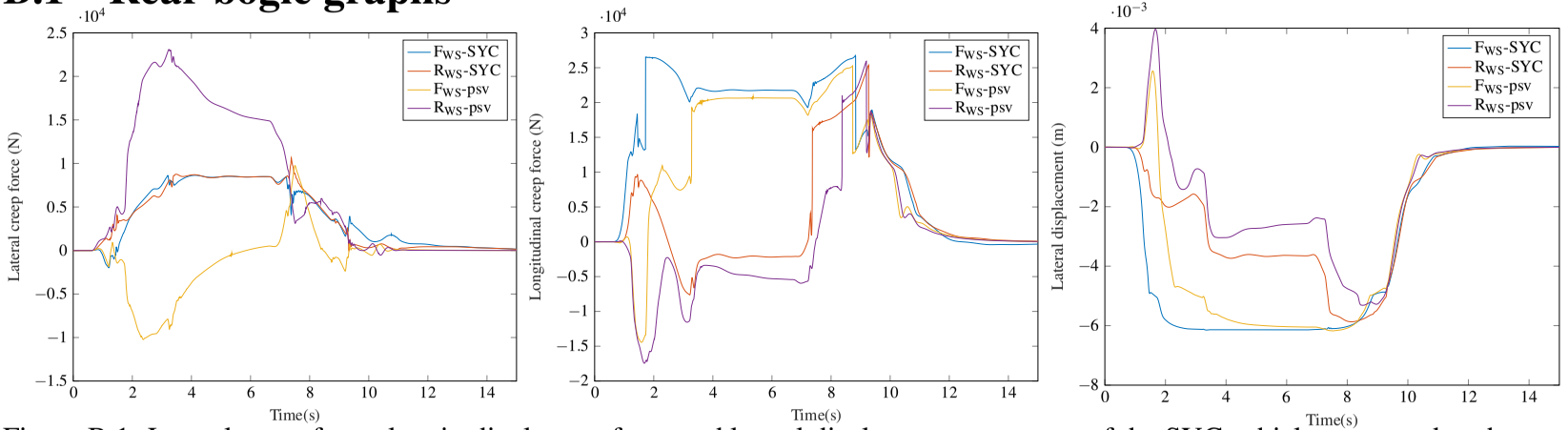

Figure B.1: Lateral creep force, longitudinal creep force and lateral displacement response of the SYC vehicle compared to the passive vehicle on the **curved track with radius = 535 m, cant = 4° and vehicle speed = 30 m/s**.

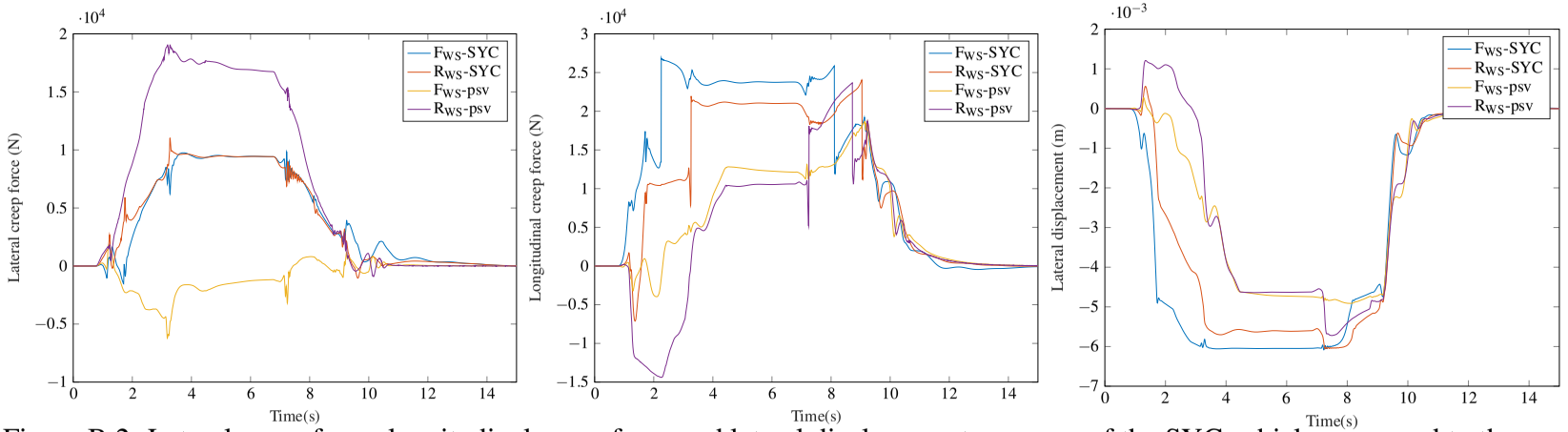

Figure B.2: Lateral creep force, longitudinal creep force and lateral displacement response of the SYC vehicle compared to the passive vehicle on **curved track with radius = 1200 m, cant = 4° and vehicle speed = 45 m/s**.

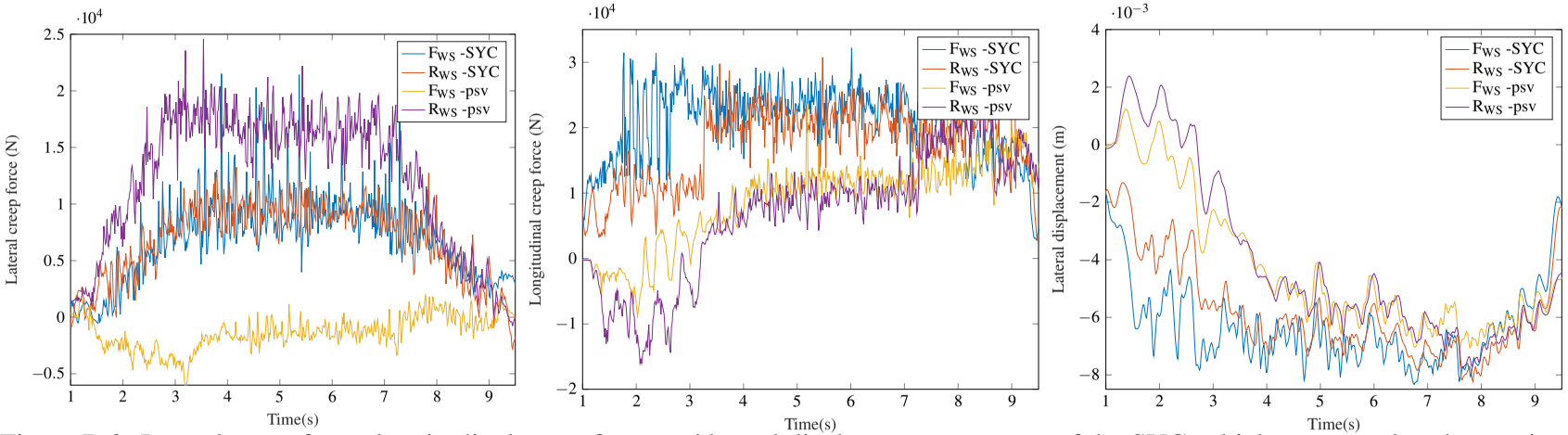

Figure B.3: Lateral creep force, longitudinal creep force and lateral displacement response of the SYC vehicle compared to the passive vehicle on **curved track with radius = 1200 m, cant = 4° and vehicle speed = 45 m/s, with lateral, vertical and gauge width stochastics**.

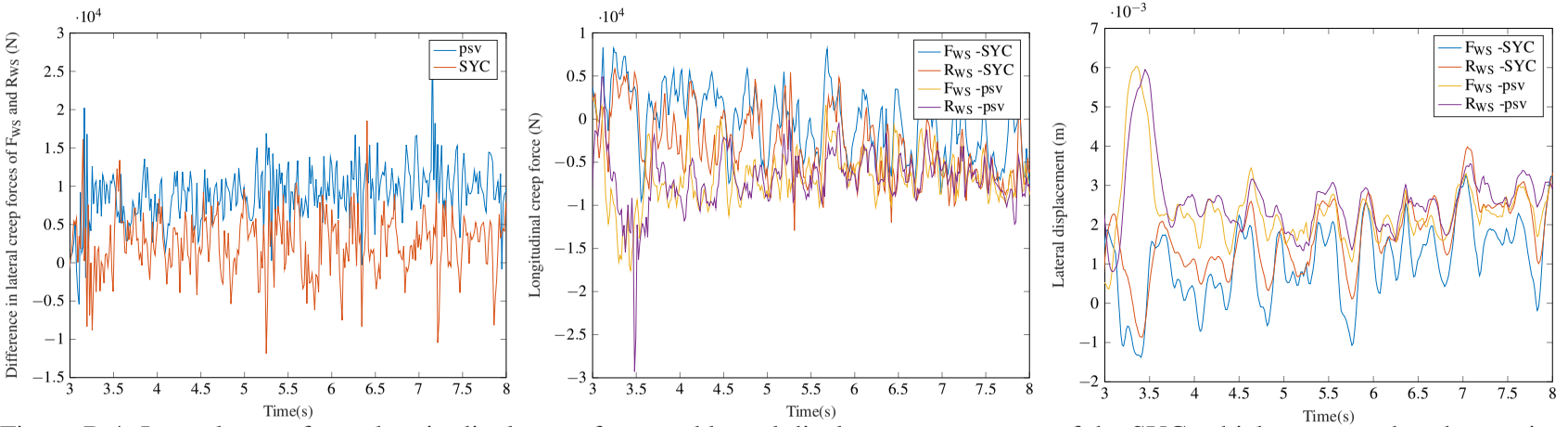

Figure B.4: Lateral creep force, longitudinal creep force and lateral displacement response of the SYC vehicle compared to the passive vehicle on **straight track with lateral, vertical and gauge width stochastics**.

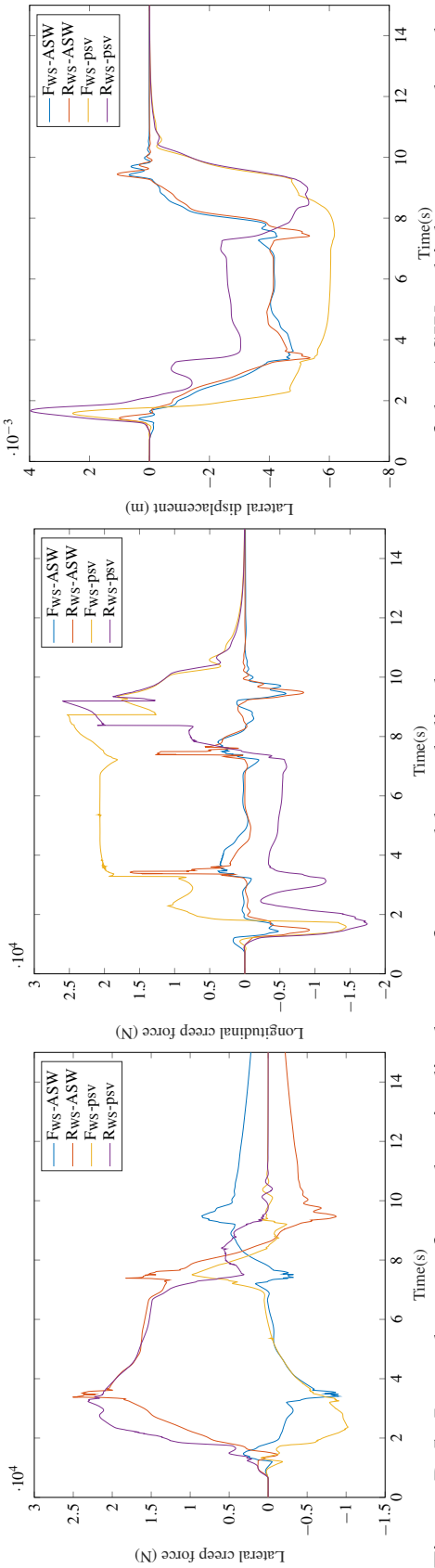

Figure B.5: Lateral creep force, longitudinal creep force and lateral displacement response of the ASW vehicle compared to the passive vehicle on **curved track with radius = 535 m, cant = 4° and vehicle speed = 30 m/s.**

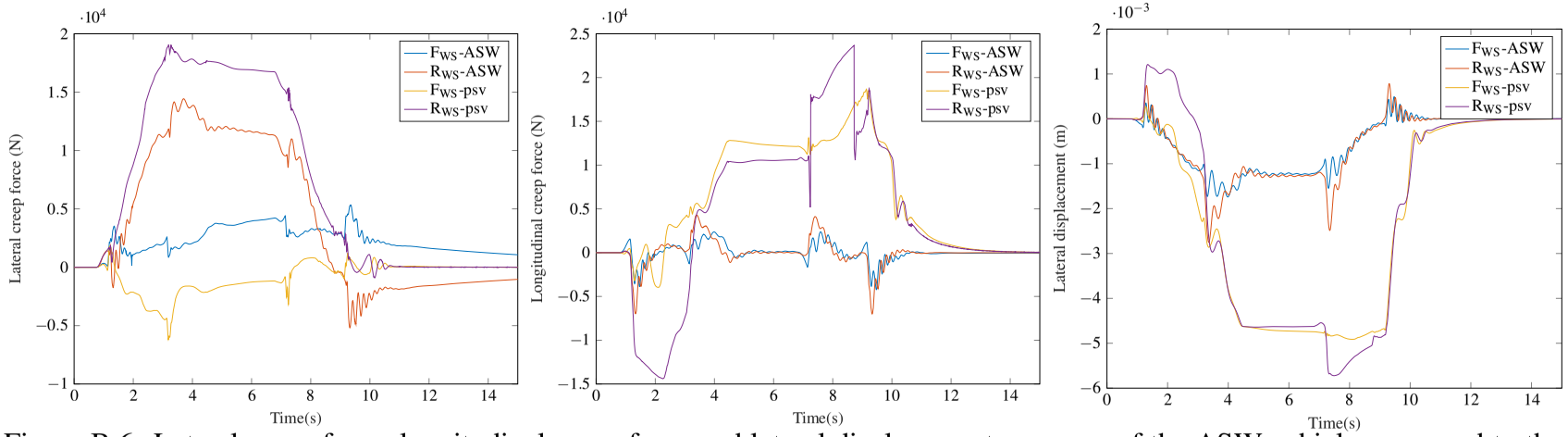

Figure B.6: Lateral creep force, longitudinal creep force and lateral displacement response of the ASW vehicle compared to the passive vehicle on **curved track with radius = 1200 m, cant = 4° and vehicle speed = 45 m/s**.

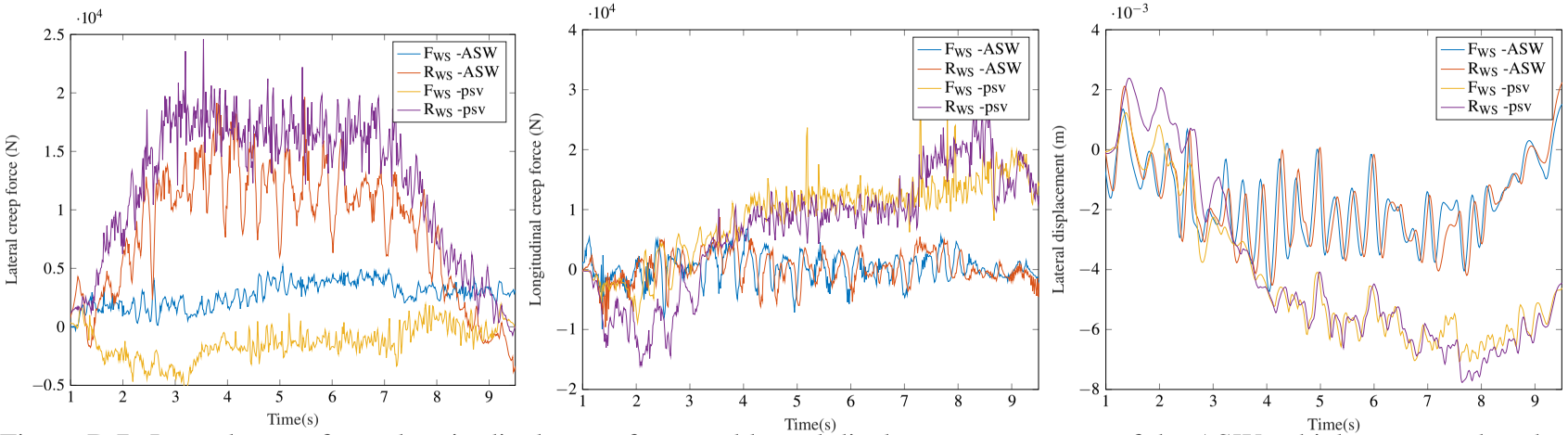

Figure B.7: Lateral creep force, longitudinal creep force and lateral displacement response of the ASW vehicle compared to the passive vehicle on **curved track with radius = 1200 m, cant = 4° and vehicle speed = 45 m/s, with lateral, vertical and gauge width stochastics**.

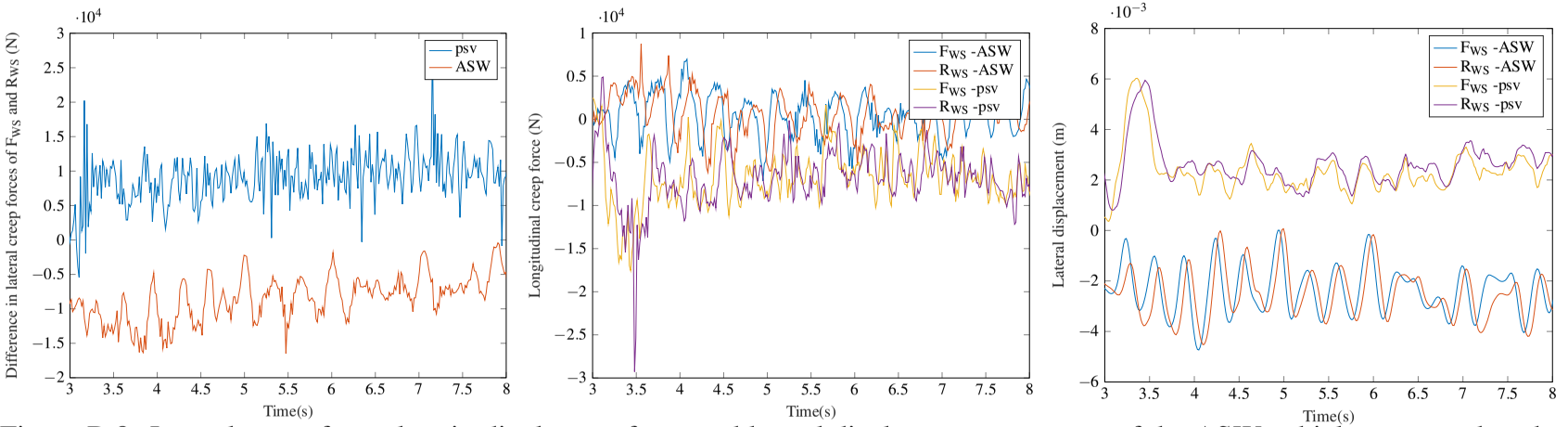

Figure B.8: Lateral creep force, longitudinal creep force and lateral displacement response of the ASW vehicle compared to the passive vehicle on **straight track with lateral, vertical and gauge width stochastics**.

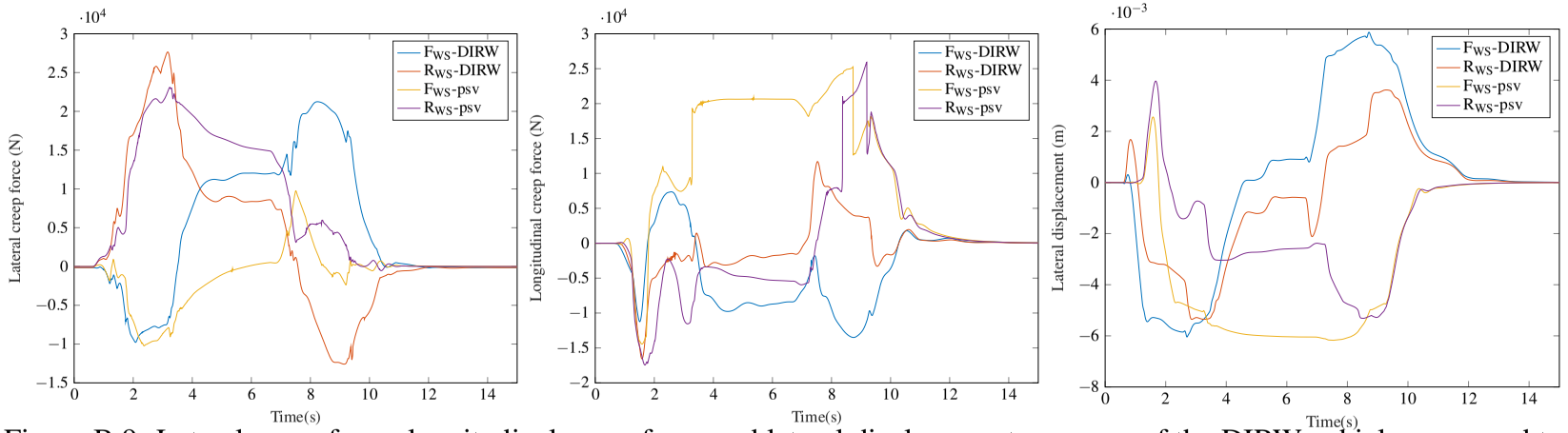

Figure B.9: Lateral creep force, longitudinal creep force and lateral displacement response of the DIRW vehicle compared to the passive vehicle on the **curved track with radius = 535 m, cant = 4° and vehicle speed = 30 m/s**.

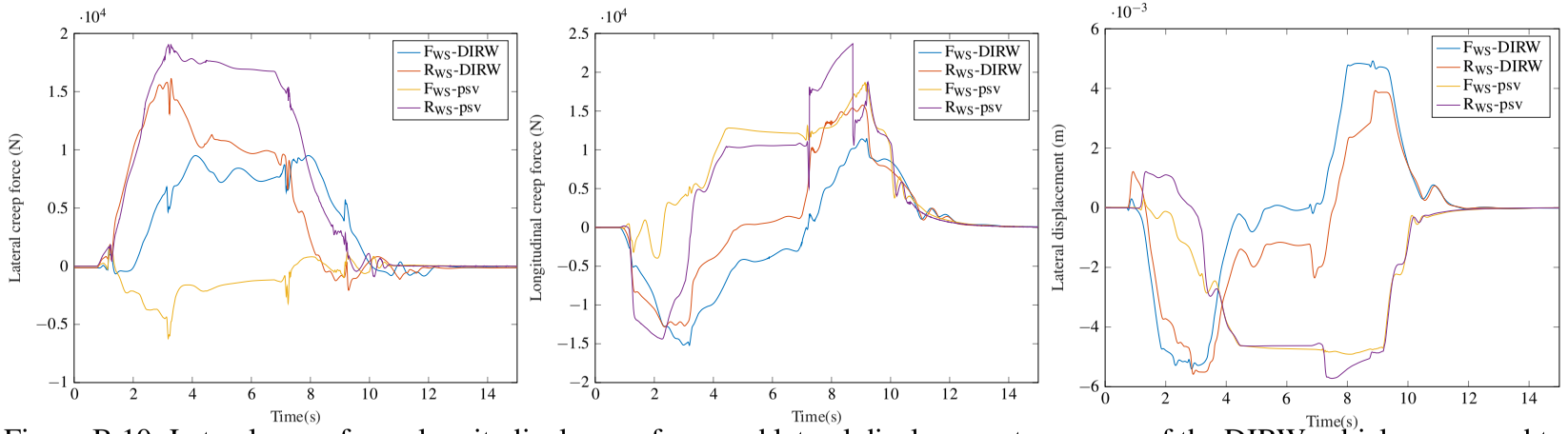

Figure B.10: Lateral creep force, longitudinal creep force and lateral displacement response of the DIRW vehicle compared to the passive vehicle on the **curved track with radius = 1200 m, cant = 4° and vehicle speed = 45 m/s**.

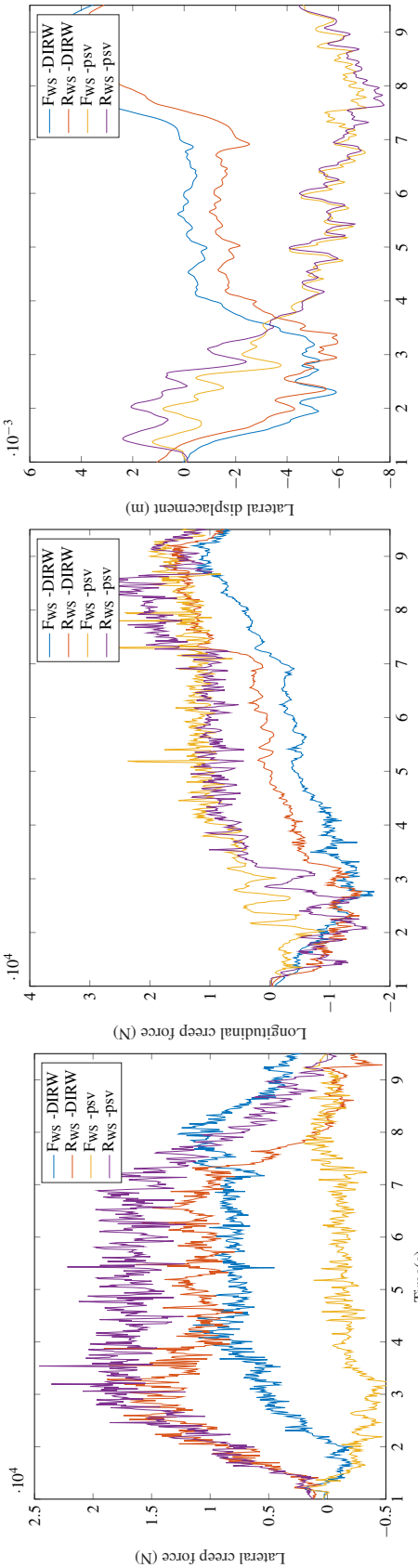

Figure B.11: Lateral creep force, longitudinal creep force and lateral displacement response of the DIRW vehicle compared to the passive vehicle on the **curved track with radius = 1200 m, cant = 4° and vehicle speed = 45 m/s, with lateral, vertical and gauge width stochastics.**

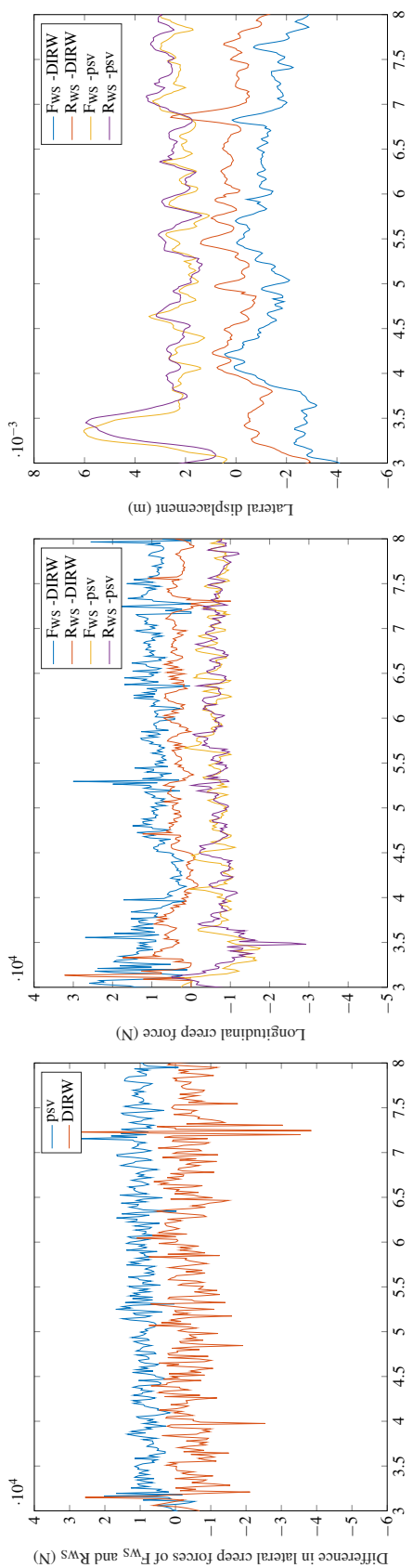

Figure B.12: Lateral creep force, longitudinal creep force and lateral displacement response of the DIRW vehicle compared to the passive vehicle on **straight track with lateral, vertical and gauge width stochastics.**

B.2 Tγ graphs

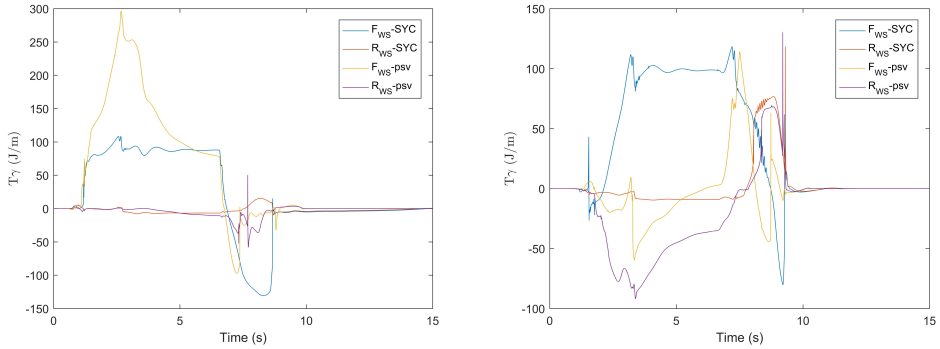

(a) Front bogie (b) Rear bogie

Figure B.13: Tγ on curved track with radius = 535 m, cant = 4° and vehicle speed = 30 m/s

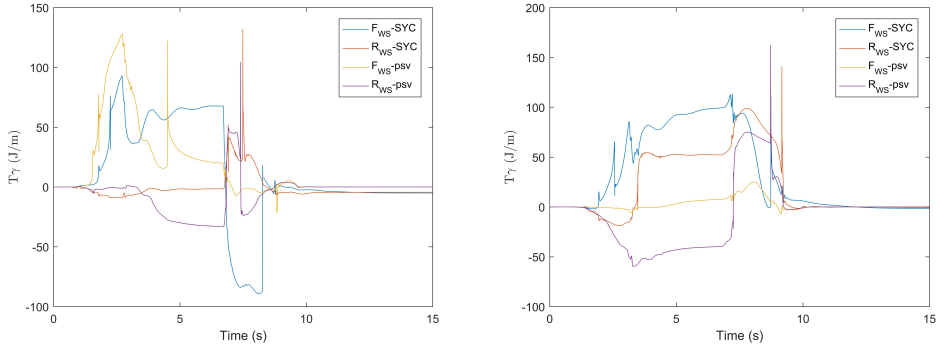

(a) Front bogie (b) Rear bogie

Figure B.14: Tγ on curved track with radius = 1200 m, cant = 4° and vehicle speed = 45 m/s

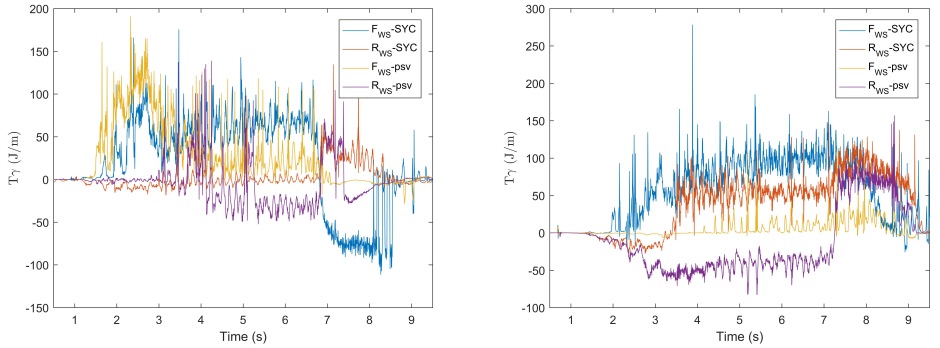

(a) Front bogie (b) Rear bogie

Figure B.15: Tγ on curved track with radius = 1200 m, cant = 4° and vehicle speed = 45 m/s, with lateral, vertical and gauge width stochastics

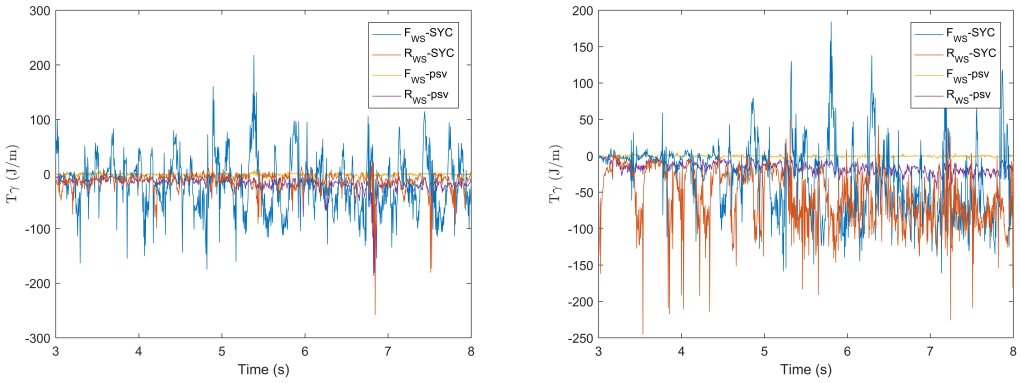

(a) Front bogie (b) Rear bogie

Figure B.16: Tγ on straight track with lateral, vertical and gauge width stochastics

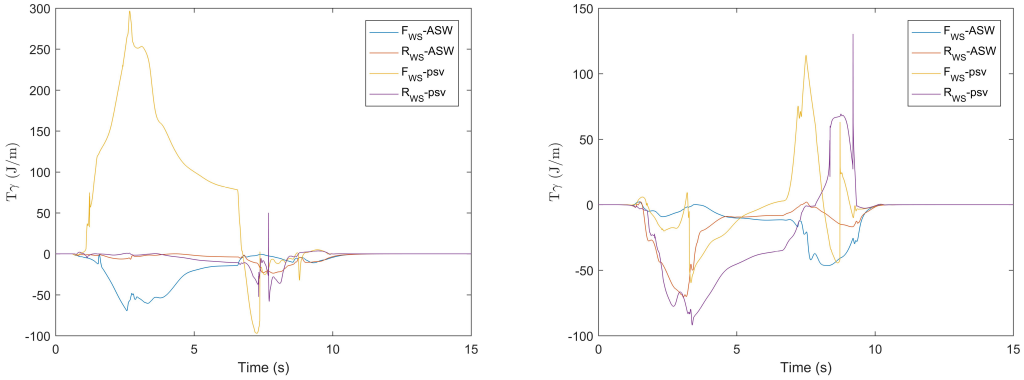

(a) Front bogie (b) Rear bogie

Figure B.17: Tγ on curved track with radius = 535 m, cant = 4° and vehicle speed = 30 m/s

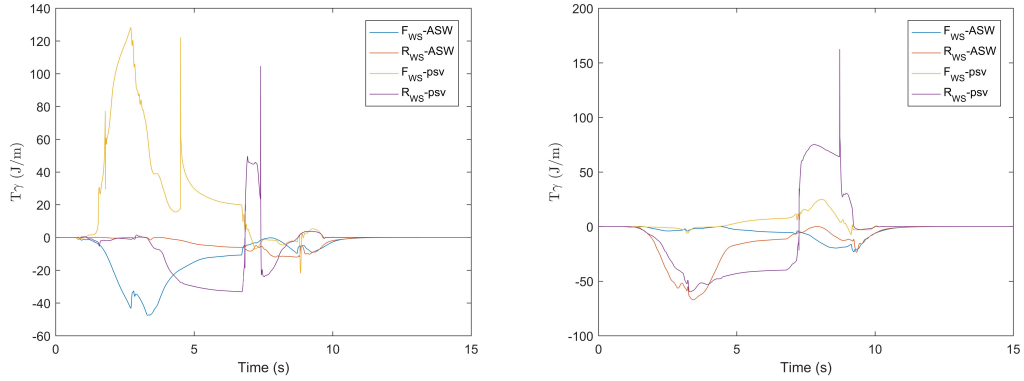

(a) Front bogie (b) Rear bogie

Figure B.18: Tγ on curved track with radius = 1200 m, cant = 4° and vehicle speed = 45 m/s

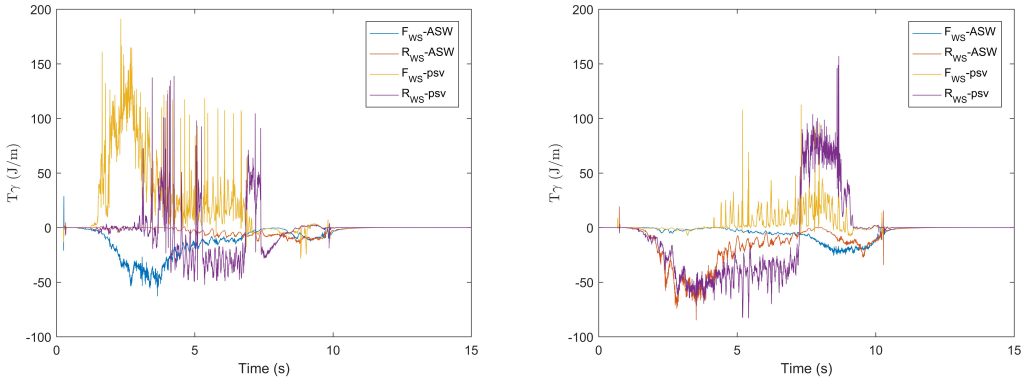

(a) Front bogie (b) Rear bogie

Figure B.19: Tγ on curved track with radius = 1200 m, cant = 4° and vehicle speed = 45 m/s, with lateral, vertical and gauge width stochastics

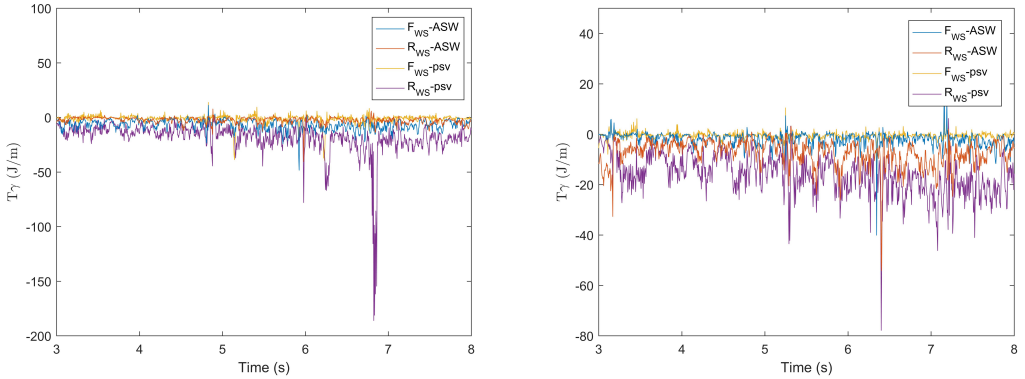

(a) Front bogie (b) Rear bogie

Figure B.20: Tγ on straight track with lateral, vertical and gauge width stochastics

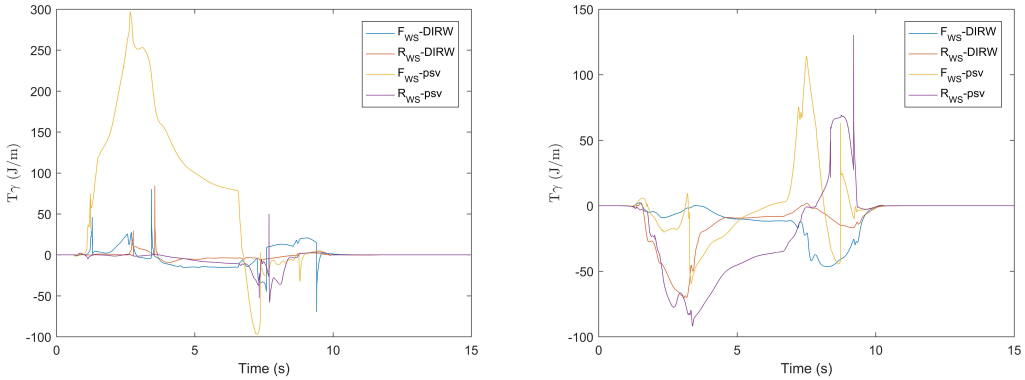

(a) Front bogie (b) Rear bogie

Figure B.21: Tγ on curved track with radius = 535 m, cant = 4° and vehicle speed = 30 m/s

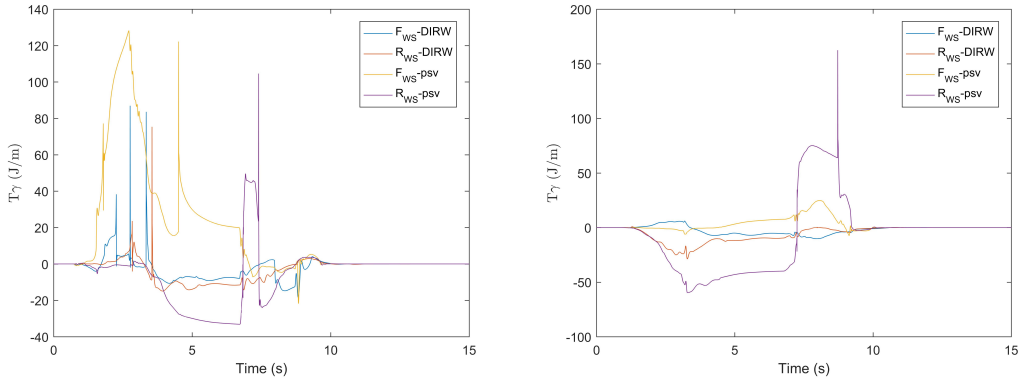

(a) Front bogie (b) Rear bogie

Figure B.22: Tγ on curved track with radius = 1200 m, cant = 4° and vehicle speed = 45 m/s

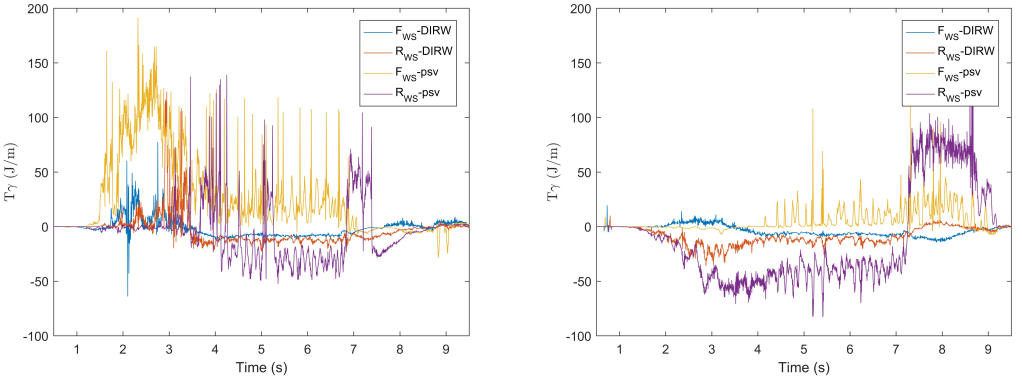

(a) Front bogie (b) Rear bogie

Figure B.23: Tγ on curved track with radius = 1200 m, cant = 4° and vehicle speed = 45 m/s, with lateral, vertical and gauge width stochastics

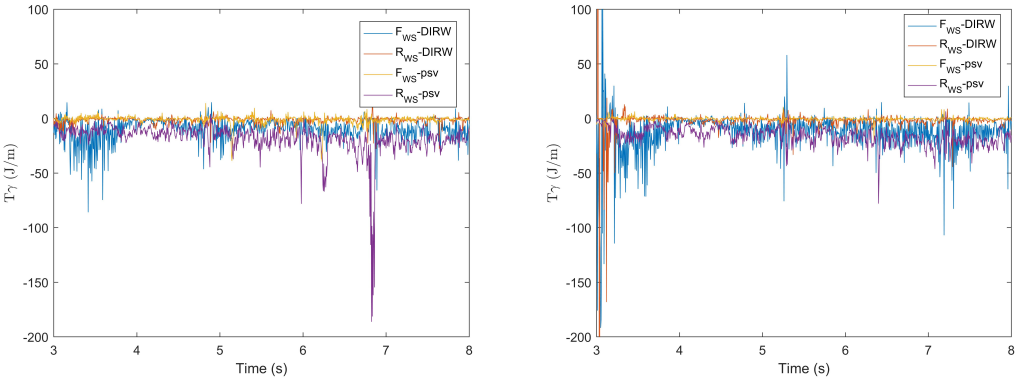

(a) Front bogie (b) Rear bogie

Figure B.24: Tγ on straight track with lateral, vertical and gauge width stochastics